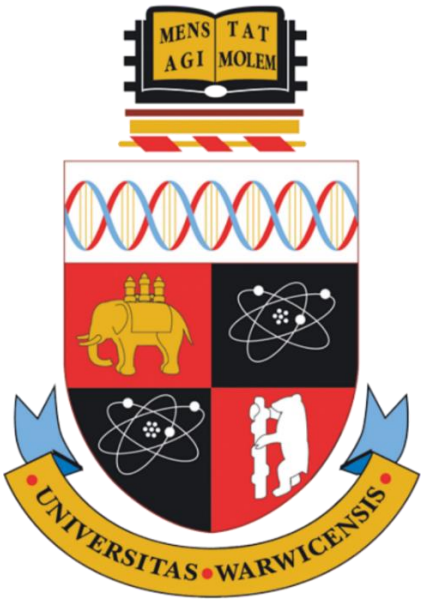

The development of nickel-catalysed coordination polymerisation-induced self-assembly (NiCCo-PISA) of helical copolymers for asymmetric organocatalytic nanoreactors

Sètuhn Ismaël Seddamin Chris JIMAJA

Submitted for the degree of Doctor of Philosophy

University of Warwick

Department of Chemistry

July 2020

WARWICK
THE UNIVERSITY OF WARWICK

THÈSE EN COTUTELLE PRÉSENTÉE

POUR OBTENIR LE GRADE DE

DOCTEUR DE

L'UNIVERSITÉ DE BORDEAUX
ET DE L'UNIVERSITÉ DE WARWICK

École doctorale des Sciences Chimiques de l'Université de Bordeaux

Doctoral College of Warwick

Spécialité : Polymères

Par Sètuhn Ismaël Seddamin Chris JIMAJA

Le développement de l'auto-assemblage induit par la polymérisation de coordination catalysée par le nickel (NiCCo-PISA) de copolymères hélicoïdaux pour nanoréacteur organocatalytiques asymétriques

Sous la direction de Daniel TATON et de Andrew P. DOVE

Soutenue le 29 Juillet 2020

Membres du jury :

Dr TOPHAM Paul	Université de Akron	Président/Rapporteur
Dr WILLCOCK Helen	Université de Loughborough	Rapporteur
Dr WILSON Paul	Université de Warwick	Examinateur
Dr BONDUELLE Colin	Université de Bordeaux (LCPO)	Examinateur

Pour mon grand-père, Jean-Jacques Asper

« Per Aspera Ad Astra »

Table of contents

Lists of figures, tables and schemes

Figures

Schemes

Tables

Acknowledgments

Firstly, I would like to thank my supervisors Andrew Dove, Rachel O'Reilly and Daniel Taton for their guidance over all those years and the opportunity to work and learn in their respective group. I am grateful for the high expectations that you set for my PhD which has encouraged me to succeed and find pride in my work. Thank you to the SUSPOL network and all its members – professors and students – that welcomed me with open arms.

I would like to thank the members past and present of the Dove and O'Reilly groups that have made the experience of being a joined student more manageable. Thank you to Benoît without whom the NiCCo-PISA project might have never started. Thanks to the team PISA and especially Jeff for his help with the management of my projects. A special thanks to Noé and Panos for their help in my entry in the SUSPOL network. Thanks to Gordon for his constant questioning that kept me alert for three years. Special thanks to the "French mafia": Anissa, Marjolaine, Hélène and Matthieu who made the home-sick feeling a tad more bearable. A big thanks to my Las Iguanas buddies: Siobhan, Kayla, Chiara, Connor and Zac who cheered me up when I most needed it. A massive thank you to Andrew Weems my "lab-husband" who supported me through most of my PhD for everything science- and life-related. This PhD has been paid with blood, sweat and tears but thanks to all of you mostly tears of laughter.

I also would like to thank the Nzalé's and my family for their infallible encouragements. Thank you to my partner, Sofia, who stuck with me through this challenging period of my life even though I am still wondering why. I am forever indebted to my parents, that gave me the education and support that allowed me to achieve this new step in my life. Finally, a huge thanks to my

brother Wedali who is always here to remind that one should shoot for the stars, but a little gaming night won't hurt.

This thesis went through a move, a flood, and a global pandemic but wherever I was, I remembered the motto of my birthplace:

« Post Tenebras Lux »

Declaration of authorship

This thesis is submitted to the University of Warwick in support of my application for the degree of Doctor of Philosophy. It has been composed by myself and has not been submitted in any previous application for any degree. The work presented (including data generated and data analysis) was carried out by the author except in the cases outlined below:

- The TEM images in Chapters 2, 4 and 5 were obtained by Mr Spyridon Varlas (University of Birmingham).
- The spectrophotometer data in Chapters 2 and 3 were obtained by Ms Yujie Xie (University of Warwick).
- The aminochlormaleimide dye (ACM) in Chapter 3 was synthesised and analysed by Ms Yujie Xie (University of Warwick).
- The AEE compound in Chapter 4 was synthesised and analysed by Dr Maria Chiara Arno (University of Birmingham).
- The HRMS data in Chapter 7 were obtained by Dr Christopher Williams (University of Birmingham).

Publications

1. *Stereochemical enhancement of polymer properties,* Josh C. Worch, Hannah Prydderch, Sètuhn Jimaja, Panagiotis Bexis, Matthew L. Becker, Andrew P. Dove, *Nat. Rev. Chem.*, 2019, *3*, 514–535. (Chapter 1)
2. *Nickel-Catalyzed Coordination Polymerization-Induced Self-Assembly of Helical Poly(aryl isocyanide)*s, Sètuhn Jimaja, Spyridon Varlas, Yujie Xie, Jeffrey C. Foster, Daniel Taton, Andrew P. Dove and Rachel K. O'Reilly, *ACS Macro Lett.* 2020, *9*, 226-232. (Chapter 2)
3. *Functional nanostructures by NiCCo-PISA of helical poly(aryl isocyanide) copolymers*, Sètuhn Jimaja, Yujie Xie, Jeffrey C. Foster, Daniel Taton, Andrew P. Dove and Rachel K. O'Reilly, *Polym. Chem.*, *Submitted.* (Chapter 3)
4. *Stimulus-responsive nanostructures by NiCCo-PISA*, Sètuhn Jimaja, Spyridon Varlas, Jeffrey C. Foster, Daniel Taton, Andrew P. Dove and Rachel K. O'Reilly, *In Preparation.* (Chapter 4)

Summary of thesis

This thesis reports the use of helical polymers for the development of helix containing nano-objects through self-assembly of polyisocyanide block copolymers, and their post-polymerisation modification (PPM) to try and achieve enzyme-like enantioselective nanoreactors.

Chapter 2 presents the nickel-catalysed coordination polymerisation-induced self-assembly (NiCCo-PISA) of helical amphiphilic block copolymers of polyisocyanide, the exploration of the resulting morphologies and the effect of the helical core an encapsulated dye.

Chapter 3 describes the development of functionalisable NiCCo-PISA micelles and their PPM with primary diamines that contain easily detectable moieties which allow the assessment of the substitution reaction and assess the effect on the nanostructures' stability of the change in pendant groups' polarity

In Chapter 4 further investigation into the PPM of NiCCo-PISA micelles by diamine cross-linkers with a view towards the formation of stimulus-responsive nano-objects.

Chapter 5 builds upon the previous chapters and presents the PPM of polyisocyanide block copolymers and NiCCo-PISA micelles with DMAP derivatives and their use as catalyst and nanoreactor respectively in acetylation reactions.

Chapter 6 provides a summary of the key findings of Chapters 2 – 5 and perspectives for the methodology designed in this thesis.

Chapter 7 presents the experimental methods of this thesis.

Résumé de la thèse

Cette thèse explore l'utilisation de polymère hélicoïdaux pour le développement de nano-objets contenant des hélices par l'autoassemblage de copolymère bloc de polyisocyanures et leur modification post-polymérisation (MPP) pour essayer d'achever des nano-réacteurs imitant les enzymes.

Le Chapitre 2 présente l'autoassemblage induit par polymérisation de coordination catalysée au nickel (AAIP-CoCNi) de copolymères bloc amphiphile, l'exploration des morphologies résultante et l'effet du cœur hélicoïdal sur un colorant encapsulé.

Le Chapitre 3 décrit le développement de micelles fonctionalisables synthétisées par AAIP-CoCNi et leur MPP avec des diamines primaires qui contiennent qui contiennent des fragments facilement détectables qui permettent d'évaluer la réaction de substitution et d'évaluer l'effet sur la stabilité des nanostructures du changement de polarité des groupes latéraux.

Dans le chapitre 4, une étude plus approfondie de la MPP des micelles synthétisées par AAIP-CoCNi par des diamines réticulantes en vue de la formation de nano-objets sensibles au stimulus.

Le chapitre 5 s'appuie sur les chapitres précédents et présente la MPP des copolymères blocs de polyisocyanure et des micelles synthétisées par AAIP-CoCNi avec des dérivés DMAP et leur utilisation comme catalyseur et nano-réacteur respectivement dans des réactions d'acétylation.

Le chapitre 6 résume les principales conclusions des chapitres 2 à 5 et les perspectives de la méthodologie conçue dans cette thèse.

Le chapitre 7 présente les méthodes expérimentales de cette thèse.

Abbreviations

A_2	Second virial coefficient
ACM	Aminochloromaleimide
AEE	2-[1-(2-Amino-ethoxy)-1-methyl-ethoxy]-ethylamine
A_{fast}	Relative amplitude of the fast mode in light scattering
ATRP	Atom transfer radical polymerisation
A_{slow}	Relative amplitude of the slow mode in light scattering
BINAP	2,2′-Bis(diphenylphosphino)-1,1′-binaphthyl
BCP	Block copolymer
BDA	1,4-Butanediamine
Boc	*Tert*-butyloxycarbonyl
br	Broad peak in ^{1}H NMR spectrum
°C	Celsius degree
c	Concentration
CA	Cystamine
cat.	Catalyst
CD	Circular dichroism
CDSA	Crystallisation-driven self-assembly
C_{fast}	Contribution to the signal intensity from the fast mode
CPL	Circularly polarised luminescence
CPP	Cell penetrating peptide
C_{slow}	Contribution to the signal intensity from the slow mode
CSP	Chiral stationary phase
CuAAC	copper(I)-catalysed azide alkyne cycloaddition
D	Translational diffusion coefficient
d	Doublet peak in ^{1}H NMR spectrum
DCR	derived count rate

D_{DLS}	Diameter measured by dynamic light scattering
D_{h}	Hydrodynamic diameter
DIPAMP	Ethane-1,2-diylbis[(2-methoxyphenyl)phenylphosphane]
DLS	Dynamic light scattering
$Đ_{\mathrm{M}}$	Molecular weight dispersity
DMAP	4-Dimethylaminopyridine
DMAP-OH	2-(Methyl(pyridin-4-yl)amino)ethan-1-ol
$\mathrm{DMAP(OH)_2}$	2,2'-(Pyridin-4-ylazanediyl)bis(ethan-1-ol)
DMSO	Dimethyl sulfoxide
$\mathrm{d}n/\mathrm{d}c$	Refractive index increment
DNA	Deoxyribonucleic acid
DOSY	Diffusion ordered spectroscopy
DP	Degree of polymerisation
D_{TEM}	Diameter measured by transmission electron microscopy
EDA	1,2-Ethanediamine
EDC	1-Ethyl-3-(3-dimethylaminopropyl)carbodiimide
ee%	Enantiomeric excess
em	Emission
EOA	Ethanolamine
equiv.	Equivalent
ESI	Electrospray ionisation
ex	Excitation
FAIC	Pentafluorophenyl 4-isocyanobenzoate
FT-IR	Fourier transform infrared
$g_2(q, t)$	Scattering intensity autocorrelation function
GC	Gas chromatography
GO	Graphene oxide
GSH	L-Glutathione

HBPPI	Hydrophobic poly(phenyl isocyanide)
HDA	1,6-hexanediamine
HPLC	High-performance liquid chromatography
HPPPI	Hydrophilic poly(phenyl isocyanide)
I_{sample}	Intensity of light scattered from the sample
I_{solvent}	Intensity of light scattered from the solvent
I_{standard}	Intensity of light scattered from the standard
IPA	Isopropyl alcohol
J	Coupling constant from ^{1}H NMR spectroscopy
K	Optical contrast constant
k_{B}	Boltzmann constant
LCST	Lower critical solution temperature
LWHH	Line width at half height
M	Molarity (moles·litre^{-1})
m	Multiplet peak in ^{1}H NMR spectrum
MAIC	Menthyl 4-isocyanobenzoate
MADLS	Multi-angle dynamic light scattering
MALS	Multi-angle light scattering
MCR	Multi component reaction
M_{LS}	Molecular weight measured by light scattering
M_{n}	Number average molecular weight
mPEG	Methoxypolyethylene glycol
MS	Mass spectrometry
MW	Molecular weight
M_{w}	Weight average molecular weight
MWD	Molecular weight distribution
m/z	Mass to charge ratio
n	Refractive index

N_A	Avogadro's constant
N_{agg}	Aggregation number
NiCCo-PISA	Nickel-catalysed coordination PISA
NIR	Near infrared
NMP	Nitroxide-mediated radical polymerisation
NMR	Nuclear magnetic resonance
NP	Nanoparticle
NR	Nile Red
p	Packing parameter
P	Product
PAIC	mPEGyl 4-isocyanobenzoate
PD	Dispersity (light scattering)
PEG	Poly(ethylene glycol)
PFP	Pentafluorophenol
PFPMA	Pentafluorophenyl methacrylate
PFPA	Pentafluorophenyl acrylate
PIC	Polyisocyanide
PISA	Polymerisation-induced self-assembly
PLLA	Poly(L-lactic acid)
PPI	poly(phenyl isocyanide)
PPM	Post-polymerisation modification
ppm	Parts per million
PS	Polystyrene
PTFE	Polytetrafluorethylene
q	Quartet peak in ^{1}H NMR spectrum
q	Scattering wave vector
R^2	Coefficient of determination
RAFT	Reversible addition-fragmentation chain transfer

R_h	Hydrodynamic radius
R_g	Gyration radius
RI	Refractive index
RM	Reaction mixture
ROCOP	Ring-opening copolymerisation
ROMP	Ring-opening metathesis polymerisation
ROMPISA	Ring-opening metathesis polymerisation-induced self-assembly
ROP	Ring-opening polymerisation
rROP	Radical ring-opening polymerization
r.t.	Room temperature
R_ϑ	Rayleigh ratio
$R_{\vartheta,\,standard}$	Rayleigh ratio of the standard
s	Singlet peak in ^{1}H NMR spectrum
SAXS	Small angle X-ray scattering
SCPNP	Single-chain polymeric nanoparticles
SE	Solvent-exchange
SEC	Size exclusion chromatography
SEM	Scanning electron microscopy
SLS	Static light scattering
SM	Starting material
T	Temperature
t	Time
t	Triplet peak in ^{1}H NMR spectrum
TEM	Transmission electron microscopy
TFA	Trifluoroacetic acid
TFEA	Trifluoroethylamine
THF	Tetrahydrofuran
T_m	Melting transition temperature

TERP	Organotellurium-mediated radical polymerisation
UV/Vis	Ultraviolet
v	Volume
Vis	Visible
wt%	Weight percentage
[M]/[Cat]	Monomer/catalyst ratio
Δ_λ	Wavelength difference
δ	Chemical shift in NMR spectroscopy
Γ	Decay rate
η	Intrinsic viscosity
λ	Wavelength
ν	Wavenumber
τ	Relaxation time
ϑ	Angle
1p1e	1-Phenyl-1-ethanol
1p1p	1-Phenyl-1-propanol

Chapter 1 Introduction

1.1. Declaration of authorship

Parts of this Chapter have been published in *Nature Reviews Chemistry:*

Stereochemical enhancement of polymer properties, Josh C. Worch, Hannah Prydderch, Sètuhn Jimaja, Panagiotis Bexis, Matthew L. Becker, Andrew P. Dove, *Nat. Rev. Chem.*, 2019, *3*, 514–535

1.2. Enantioselective catalysts

The homochirality found throughout nature is a special, yet mysterious feature that has not been completely explained. The study of the origin of the enantiomerically pure amino acids is an active field, where numerous theories[1] have been proposed but there is no apparent reason, other than chance, that justifies the configuration of the molecules found in nature. In living organisms two enantiomers - molecules with identical chemical composition but different spatial arrangement - can have divergent effects on metabolism even though they are chemically similar. A very simple example of this concept is exemplified in the different odour profiles (quality and threshold) for various enantiomers of terpenes (Figure 1.1).[2]

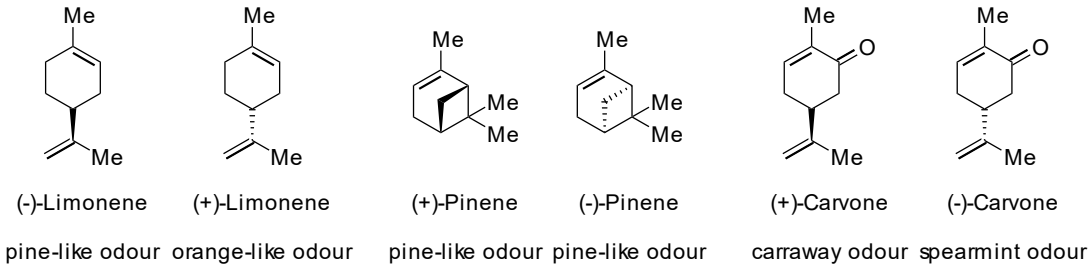

Figure 1.1. Terpene enantiomers of different fragrances: Limonene (*S*/-, *R*/+), Pinene (*R*/+, *S*/-) and Carvone (*S*/+, *R*/-).

Another well-known illustration of the effect of stereochemistry on reactivity and metabolism that had a tremendous impact on the chemical industry and on the lives of tens of thousands of people was the molecule thalidomide (anti-morning sickness treatment for pregnant women), which was sold under the brand name *Immunoprin*. Unfortunately, while the *R* enantiomer was therapeutically active and prevented nausea associated with morning sickness, the *S* enantiomer was teratogenic (Figure 1.2). Since the drug was marketed and sold as a racemic mixture of the two enantiomers, it led to numerous reports of malformations in new-borns that forced the US Federal Drug Administration (FDA) to recall the drug from the market. After this episode,

the FDA decreed that all new molecular entities (drugs) must be approved as single enantiomers. This has led the pharmaceutical industry to move towards enantiomerically pure drugs, which created a large demand for enantioselective reactions, chiral catalysts, biocatalysis and means to separate respective enantiomers.

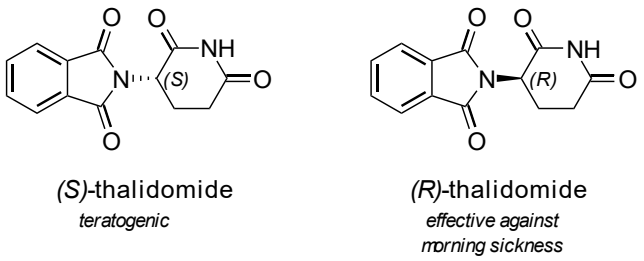

Figure 1.2. Enantiomers have different biological properties: example of the thalidomide where one enantiomer (*R*) has a positive effect against morning sickness and the other (*S*) is teratogenic.

Over the last 50 years, there have been a number of pioneers in the field of catalytic and enantioselective synthesis, among them: Sharpless,[3] Noyori,[4] Knowles,[5] Corey,[6] Evans,[7, 8] Carreira,[9] Overman,[10] Breslow,[11] Feringa,[12, 13] Jacobsen,[14] Fu,[15] Macmillan[16, 17] and Bode[18]. A validation of the importance of this field, a number of Nobel prizes related to stereochemistry and asymmetric catalysis have been awarded in the past few decades: Derek Barton and Odd Hassel (1969), John Cornforth and Vladimir Prelog (1975), Donald Cram, Jean-Marie Lehn and Charles Pedersen (1987), and William Knowles, Ryoji Noyori and Barry Sharpless (2001).

The first recognised enantioselective reactions all required transition metal catalysts which featured chiral ligands as described in the highlighted reactions of the three Nobel awardees of 2001: the epoxidation of Sharpless (titanium and diethyltartrate),[3] the hydrogenation of Noyori (ruthenium and BINAP)[4] and the hydrogenation of Knowles (rhodium and DIPAMP).[5] In parallel to metal-based asymmetric catalysts, the use of organocatalysts in asymmetric transformations has been contemporaneous with metal-based catalysis,[19, 20]

with the first reports which used proline (Figure 1.3) in the asymmetric aldol reaction called the Hajos–Parrish–Eder–Sauer–Wiechert reaction in the 1970s.[21, 22] Although proline is a structurally simple and naturally occurring amino acid, it has been shown to be a versatile organocatalyst which is used extensively in asymmetric catalysis.[23] Another class of cyclic amines, imidazolidinones, have been developed by MacMillan for various asymmetric reactions. The original work was inspired by phenylalanine[16] which proved that nature is a good resource for asymmetric catalysis. Recently, thioureas have attracted attention for asymmetric catalysis as demonstrated in the work of Jacobsen with a catalytically active thiourea in the Strecker reaction.[14] Interesting asymmetric catalysts that do not employ simple point asymmetry (*i.e.* chiral atoms) are chiral 4-dimethylaminopyridines (DMAPs).[24] Yu and co-workers have developed a class of catalytical DMAPs that derive their enantioselective properties from planar chirality. DMAP, which is planar, needs to be de-symmetrised in order to allow enantioselectivity and in the case of Yu's catalyst, this was accomplished by derivatisation with ferrocene.[15, 25, 26]

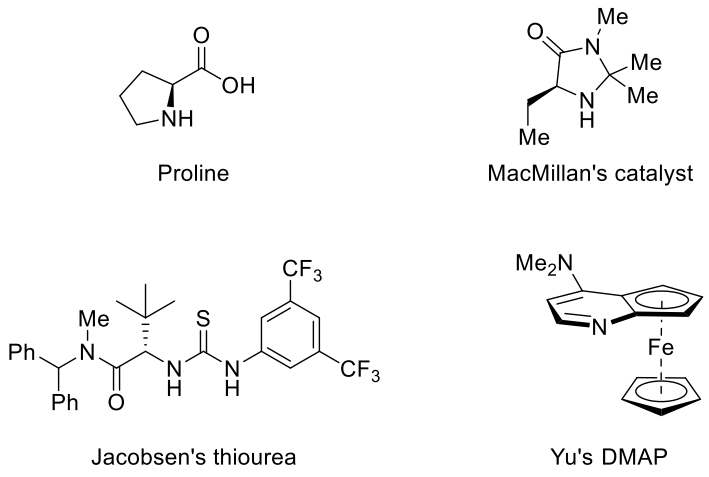

Figure 1.3. Different amine-based organocatalysts: L-proline, MacMillan's catalyst, Jacobsen's thiourea and Yu's planar-chiral derivative of DMAP.

These synthetically derived catalysts essentially mimic the action of enzymes. Enzymes are the catalysts that allow for the existence of life since they increase

the kinetics in a multitude of chemical reactions that would otherwise be too slow to create, develop and sustain life. Enzymes are sequence-specific, monodisperse polypeptides (*i.e.* proteins). The specific sequence of amino acids that composes the enzyme is crucial for its overall structure. Thus, the enzyme will fold in accordance with this sequence and the resulting three-dimensional structure will have an important role in the recognition of substrate and catalytic activity of the enzyme. The so called "active-site" is usually hydrophobic in nature and displays remarkable selectivity for certain substrates. Enzymes are biomacromolecules comprised of two main components that result from the specific layout of the amino acids: α-helices and β-sheets (Figure 1.4). The application of enzymes in synthetic chemistry for applications for which they have not evolved is called biocatalysis.[27] The most recent developments in this field include directed evolution, which is the modification through repeated mutation of an enzyme (*via* an *in vitro* version of Darwinian evolution) to orient its catalytic scope towards a given substrate.[28] An example is the work by Savile *et al.* where a transaminase was designed by directed evolution to afford a catalyst for a targeted reaction (Scheme 1.1).[29]

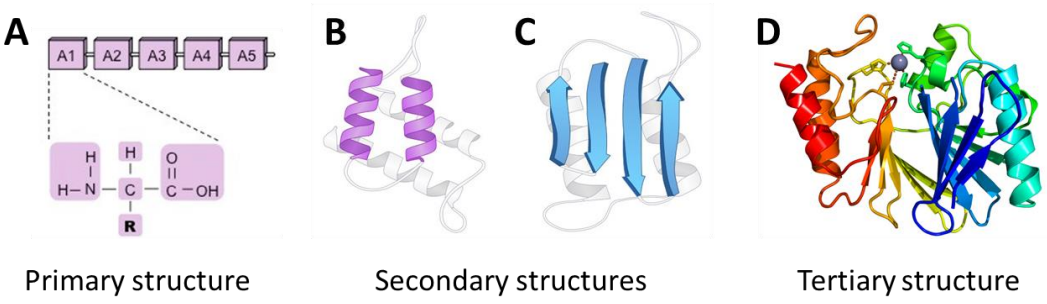

Figure 1.4. (A) Primary structure: sequence of amino acids which defines the enzyme. (B) α-helix and (C) β-sheet secondary structure. (D) Tertiary structure: 3D configuration of the folded amino acid sequence subdivided into α-helices, β-sheets and random coils.

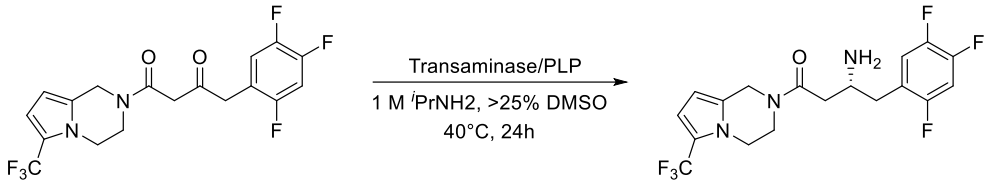

Scheme 1.1. Transamination reaction with an enzyme modified by directed evolution to catalyse a reaction on a substrate that was out of its original scope and that is performed under harsh conditions for an enzyme.[29]

Metal-based catalysts tend to have a wide substrate scope and high catalytic activity, but are often air- and water-sensitive compounds that are hard to remove from end products (this is an especially troublesome issue for the pharmaceutical and electronic industries) and can pollute the environment. On the other hand, enzymes often display very high selectivity and/or catalytic activity under mild and environmentally acceptable conditions. However, they have a limited substrate scope, can usually only be found in one enantiomeric form and are more suited for aqueous based reactions since the loss of configuration of enzymes in organic solvents makes them unsuitable for such environments. Finally, organocatalysts are usually derived from the nature chiral pool, display a high degree of robustness and, through immobilisation, are quite easily recyclable. Nevertheless, they tend to also have a limited substrate scope, though not as narrow as the substrate pool for enzymes and are generally employed in toxic organic solvent. Currently, there exists an expansive library of asymmetric transformations and some of the corresponding catalysts are commercially available. However, many robust chiral catalysts require multiple synthetic steps and the costs are often prohibitive.

1.3. Helical polymers

Helices are fascinating chiral objects that are present in nature of which the double-stranded helix of DNA as the support for genetic information[30] and the α-helices in proteins[31] are prominent examples. Historically, the first synthetic helical polymer was exposed by Natta when he discovered that highly isotactic polypropylene in the crystalline state had a helical conformation.[32, 33] However, this polymer could not maintain its conformation in solution. After this discovery, investigations into synthetic helical polymers grew, but stable helical conformations were scarce and most of them suffered from frequent helix reversion (defects in the backbone itself).

More recently, synthetic helical polymers have attracted polymer chemists' attention because of their possible applications in catalysis, nanomaterials, chiral recognition and the study of biological helices.[34-38] One interesting property of helical polymers is that they can display optical activity solely due to their helicity, as it was found by Nolte *et al.* who separated two enantiomers of poly(*tert*-butyl isocyanide).[39] Optical activity originates from that molecule exhibit chirality which can come from point, axial or planar asymmetry (Figure 1.5). The inherent chirality of helical polymers is an axial chirality that comes from atropisomerism - steric related stereoisomerism induced by hindered rotation about a single bond - therefore they can be classified as polymers with backbone stereochemistry without chiral atoms in the backbone.

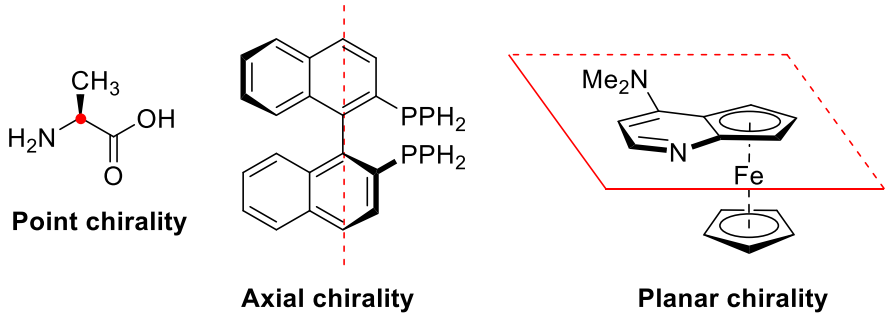

Figure 1.5. Illustration of the different types of chirality: point, axial and planar.

The analysis of the helicity of macromolecules can be done with circular dichroism (CD) spectroscopy which is an absorption spectroscopy method based on the differential absorption of left and right circularly polarised light by the analyte (Figure 1.6). UV CD spectroscopy is commonly used to determine aspects of protein secondary structure (β-sheets or α-helices) but has also been employed in the confirmation of molecules' secondary structures especially for helical polymers, where the presence of a CD signal indicates the presence of an enriched screw-sense selective helix. CD is generally employed to compare the helicity of similar polymer helices.

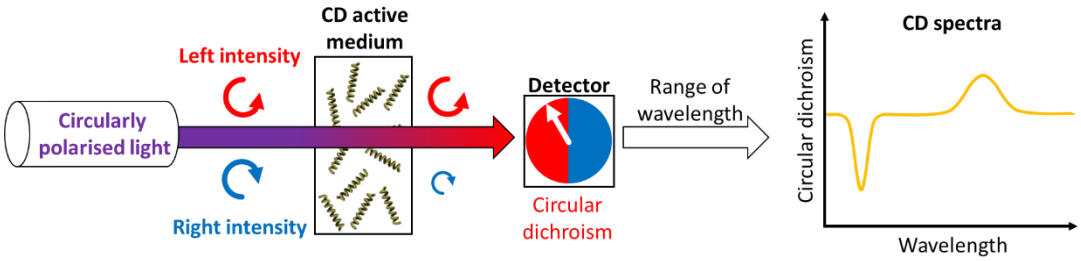

Figure 1.6. Illustration of circular dichroism (CD) spectroscopy where the differential absorption between left and right circularly polarised intensity absorptions of a CD active sample is measured over a range of wavelengths which yields the CD spectrum.

1.3.1. Dynamic *vs* static synthetic helical polymers

Helices can be divided in two major groups - static and dynamic helices – which depends on the helix inversion energy (*i.e.* the energy it takes to completely reverse the helical handedness).[34] Polymers with low inversion barriers are called "dynamic helices" and have a backbone that undergoes fast helix inversion in solution between the left-handed (M) and right-handed (P) conformations. This flexibility in their conformation makes them ideal candidates to create chiral structures that are responsive to various stimuli (*e.g.*, light, heat, pH and other environment changes). On the other hand, when

the helix inversion barrier of the polymer is high, they are referred to as "static helices", where the helical conformation is formed under kinetic conditions. In this situation, each monomer addition to the growing chain is sterically 'locked' into conformation which gives helices that are stable in solution and suffer only minor helix inversion. Thus, a fixed helical architecture can be used as a molecular scaffold for controlled special alignment of functional groups or chromophores, and ordered molecular alignment in the solid phase such as that in liquid crystalline materials. Nevertheless, some classes of polymers can be categorised as either dynamic or static which depends on the substituents present on the chain.

For all helical polymers, when the polymerisation occurs with achiral or racemic side-chains, the resulting M and P helices are enantiomers and equally distributed which leads to no optical activity. However, when the side chains consist of only one enantiomer or is enantioenriched, M and P are diastereoisomers and one screw-sense is favoured over the other. In the case of static helices, this process is kinetically favoured whereas dynamic helices form under thermodynamic control as discovered by Green *et al.* while they studied polyisocyanate.[40, 41] Side-chain stereochemistry in static polymers is not as important as in dynamic polymers since helicity is locked after the synthesis; thus, there is no need for a constant chirality along the chain to retain the favoured screw-sense. However, chiral side-chains can be significant for the environment they form around the helix.

When the screw-sense selection does not originate from the chirality of the monomer (side-chain), it can be induced by the catalyst[32, 42, 43], the solvent[44, 45], metal cation[46-48] or chiral additive as demonstrated by Chen *et al.* in a study where they made an optically active polyisocyanide from achiral monomers and chiral lactide additive.[49, 50] An improvement in the field of helicity production,

is the work by Yashima *et al.,* where the induction of helicity by an achiral small molecule is followed by its replacement with an achiral molecule that led to the retention of the helicity which showed a good case of macromolecular helical memory.[51] Examples of dynamic helical polymers are polyisocyanates, chiral π-conjugated polymers, polysilanes and polyacetylenes (Figure 1.7).[34, 35, 52] Among static helical polymers there are sterically restricted polymethacrylates, polymethacrylamides, phthalocyaninatopolysiloxane, polyaldehydes, binaphthyl-based polymers, polyisocyanides and polyguanidines. Some classes of polymers can be categorised as either dynamic or static as is the case for polycarbodiimides, poly(quinoxaline-2,3-diyl)sand polychlorals. [34, 35, 52]

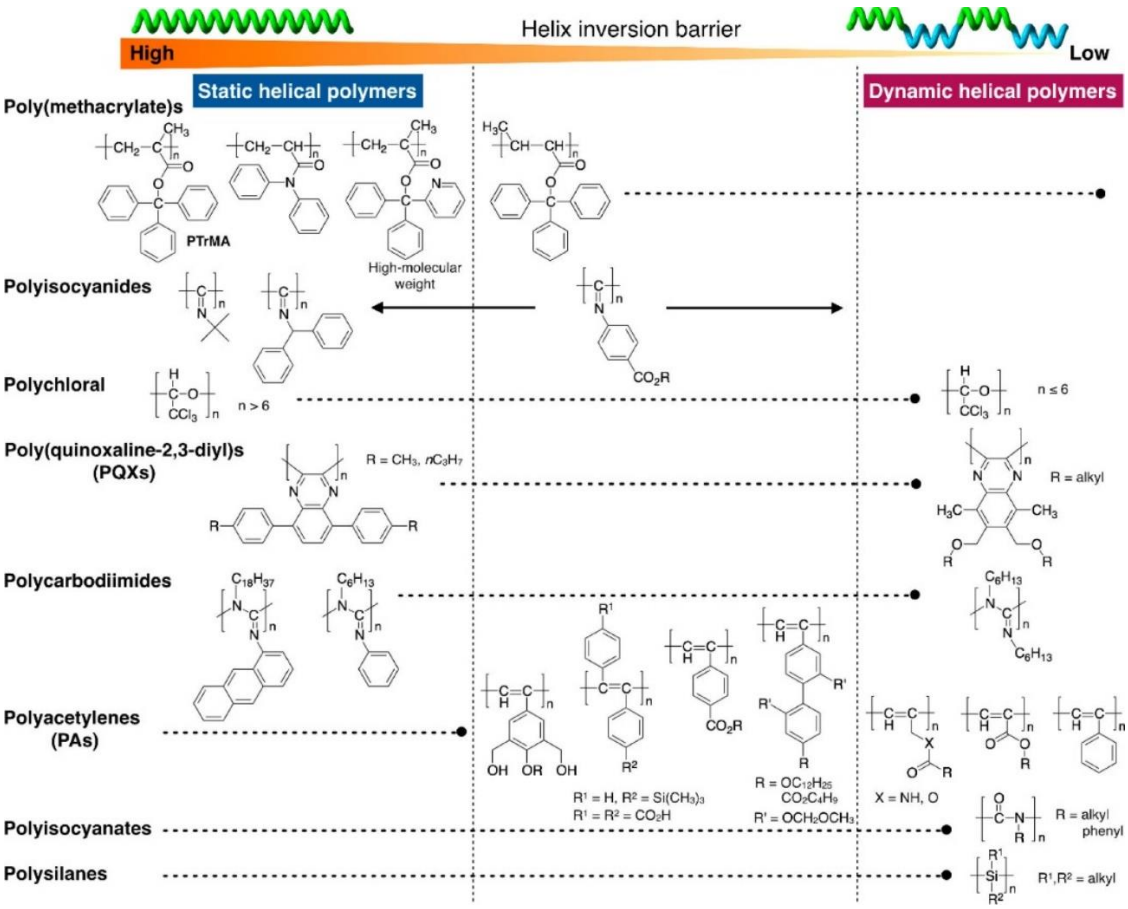

Figure 1.7. Representative examples of static and dynamic helical polymers that differ through their helix inversion barriers. Reproduced from the work of Yashima *et al.* published in ACS, Chemical Reviews.[35]

Helical copolymers are remarkable because of the rules that govern their helicity. The "Sergeant-Soldiers" rule applies if a dynamic copolymer is mainly composed of optically inactive monomer with small amount of optically active monomer. This rule comes from observation made by Green *et al.* that showed a minor quantity of chiral monomer could greatly influence the optical activity of polymers which made it possible to have optical activities similar to that of a homopolymer of chiral monomer with only a slight excess of chiral monomer among achiral monomer.[53] The Majority rule is observed with copolymers of enantiomeric monomers. It has been shown that a slight enantiomeric excess could lead to similar optical activities than homopolymers of the chiral monomer in excess.[54] The Sergeant-Soldier rule permits the use of a very small amount of chiral units among achiral units to allow an optimal transfer of chirality while the Majority rule discards the obligation to make use of enantiopure monomers to attain high enantiomeric excess (Scheme 1.2). Combined together, they open the road to facile synthesis of high-purity chiral molecules and high-quality purification materials/process from cheap and low-quality components.

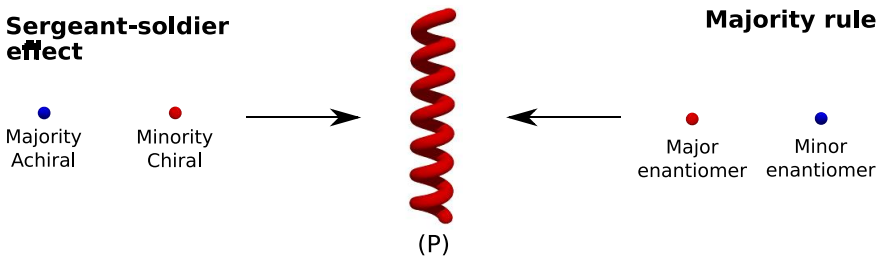

Scheme 1.2. Illustration of the sergeant-soldier effect (left) and the majority rule (right) which induce screw-sense selectivity (P) in a helical polymer.

1.3.1.1. Polyisocyanides

Among the different helical polymers, polyisocyanides (PICs) are of interest as a consequence of their high density of pendant groups – one for each repeating unit (Figure 1.8) – and their high inversion energy that produces very stable

helices.[28] PICs have a backbone structure that contains four repeating units per turn (denoted as 4_1) and a helical pitch of 4.1-4.2 Å. PICs started to attract attention in the late 1970's when it was discovered that they form helices when bulky side groups are present.[29–32]

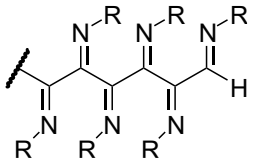

Figure 1.8. Hexamer of polyisocyanide which shows the high density of pendant groups along the main backbone.

The isocyanides' polymerisation is usually catalysed by nickel(II) complexes[55, 56] or ethynyl palladium(II) complexes,[49, 57] with the nickel catalyst preferred for the polymerisation of alkyl isocyanides and the palladium complexes used primarily for phenyl isocyanides (Scheme 1.3). Additionally, dinuclear μ-ethynediyl palladium(II)-platinum(II) complexes[58, 59] and organorhodium(I) complexes[60-62] have shown catalytic activity in the polymerisation of isocyanides, as well as an acid-initiated polymerisation.[63] The nickel-catalysed polymerisation of isocyanides has been thoroughly studied and is believed to follow a "merry-go-round" mechanism.[64, 65] The initiation steps consists in a fast insertion of isocyanide into the Ni–allyl bond followed by the reduction of the nickel(II) centre by isocyanide into nickel(I) which have been detected by EPR. The next steps (propagation steps) involves the coordination of a new isocyanide moiety onto nickel complex followed by its insertion into the polyiminic growing chain (Scheme 1.4).

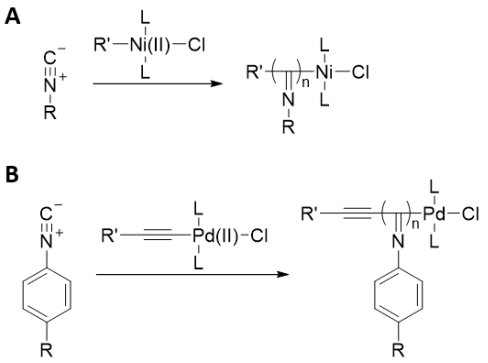

Scheme 1.3. Polymerisation of isocyanide with a (A) nickel(II) and (B) ethynyl palladium(II) complex.

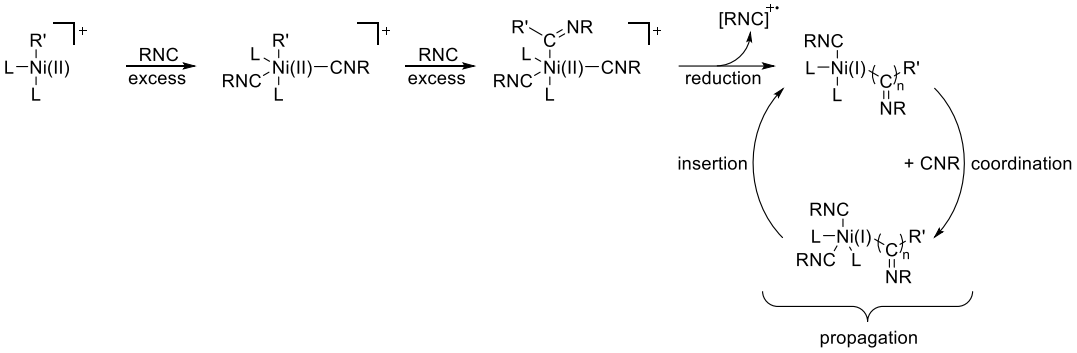

Scheme 1.4. Mechanism of the nickel(II)-catalysed polymerisation of isocyanides. Inspired from the work of Ribeiro *et al.* published in Elsevier, Polyhedron.[65]

1.3.2. Applications

Chiral recognition is an obvious application of helical polymers.[66] They have been employed in enantioselective adsorption[48, 67] and enantioselective permeation (membranes)[68, 69] with some success. Moreover, chiral recognition can be exploited in the case of chiral stationary phases (CSPs) for HPLC columns where static helical polymers like polyisocyanide[70, 71] and poly(triphenylmethyl methacrylate) (PTrMA)[72-74] have already been used for this application. The dynamic and helical memory properties of polyacetylene have been leveraged for the same application but with the possibility to switch

the chirality of the CSP which allows for the choice of the elution order of the enantiomers.[75]

An interesting property of helical polymers is the amplification of the optical activity from monomer to polymer as a result of the synergetic effect of the helical backbone. This property seems to extend to the chirality induction properties of catalysts attached onto helical polymers. In the case of helical polymers complexed to metal, an induced enantioselectivity can be observed.[76, 77] This property of dynamic helical polymers allows the possibility to make asymmetric catalysts with switchable enantioselectivity.[78] In the case of organocatalysts, the enantioselectivity can be improved[79-82] or even entirely induced[83, 84] by the helical polymer scaffold. This use of helical polymers that are similar to α-helices found in proteins might well be a step towards the mimicry of one of the most specialised tools in nature - enzymes - while retaining high adjustability.

In the area of synthetic material, a class of polyisocyanide grafted with peptide side-chains developed by Cornelissen *et al.* and which exhibited a fascinating structure that consisted of β-sheet-like side-chain attached along an α-helix-like backbone[85] has been modified to give a biomimetic polymer gel which displayed stress-stiffening response similar to that of biological tissues.[86] This property might well be a way to create materials that can be effectively used to repair or replace body parts. In the domain of optical data storage, polyisocyanate[87] and polysilane[88] were studied for their dynamic properties. It would be possible to make materials that store the ones and zeroes of our computers' memory as chiral information – P and M – and to dynamically modify them with stimuli like light and/or heat to implement a re-writable (RW) mode. This opens more applications of polymers in electronics and

modern information technology which could lead maybe to a higher recyclability of future hardware.

1.4. Solution self-assembly of amphiphilic block copolymers

The cell membrane is certainly one of the most interesting examples of the use by nature of self-assembly to create ordered structures.[89] They are mainly composed of phospholipids, which are amphiphilic molecules – comprised of a hydrophobic tail and a charged phosphate head – that self-assemble in water as a result of the hydrophobic effect.[90, 91] Non-polar molecules are unable to form hydrogen bonds with water and this leads to a disruption of the hydrogen bonding network. When they aggregate together, hydrophobic molecules reduce their exposure to water and minimise the disruption which leads to the formation of organised structures. A model has been developed by Israelachvili *et al.* to predict the type of structure achieved by the self-assembly of molecular amphiphilic species.[92] The model is based on the geometry of the molecules and the most stable curvature of the resulting aggregate is established by a packing parameter, $p = v/l{\cdot}a$, where v and l are the volume and the length of the hydrophobic chains, and a is the surface area of the charged headgroup. Different values of p correspond to different morphologies: species with a $p \leq ⅓$ achieve spherical micelles while $⅓ < p \leq ½$ yields cylindrical micelles (*i.e.* worm- or rod-like micelles) and $½ < p \leq 1$ results in vesicle or bilayer structures (Figure 1.9). Interestingly, this approach assumes the structures are at thermodynamic equilibrium achieved by exchange of unimers between the aggregates. Similarly to phospholipids, amphiphilic block copolymers (BCPs) that contained two or more blocks spontaneously self-assemble when dispersed into a selective solvent and can achieve a range of structures on the nanoscale such as spherical micelles or vesicles (*i.e.* polymersomes).[93-96] However, as a consequence of the lower mobility of BCPs in the solvent milieu, the exchange of unimer chains between the aggregates can be slow comparatively to the

experimental timescale, which means that these BPC aggregates are formed under kinetic control which leads to the constitution of "frozen" micelles.[97, 98] The type of structures achieved by BCP can therefore diverge from the ones presented earlier as they can be far from equilibrium which allows a rich range of nanostructures[99] such as Janus nanodiscs,[100] helical assemblies,[101] framboidal vesicles,[102] "hamburger" micelles,[103] jellyfish-like micelles[104] and diamond platelets[105] (Figure 1.10).

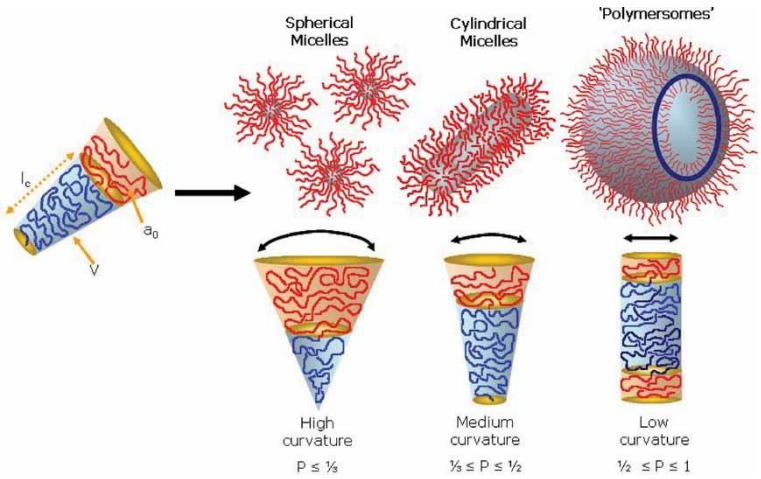

Figure 1.9. Different aggregate morphologies predicted by the packing parameter (p). Reproduced from the work of Blanazs *et al.* published in Wiley-VCH, Macromolecular Rapid Communication.[106]

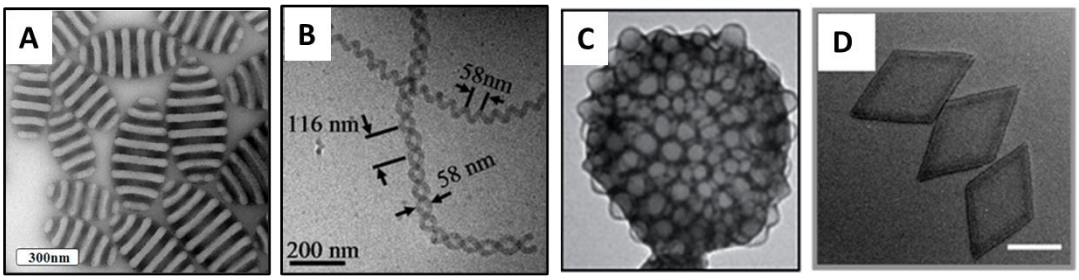

Figure 1.10. Examples of out-of-equilibrium morphologies achieved by BCPs self-assembly: (A) Janus nanodiscs,[103] (B) helical micelles,[101] (C) framboidal vesicles[102] and (D) diamond platelets.[105]

1.4.1. Formulations

Various techniques can be employed to achieve nanostructures from BCPs[107] such as direct dissolution, solvent exchange, thin-film rehydration, and crystallisation-driven self-assembly (CDSA). Direct dissolution is a straightforward approach where a selective solvent for the corona block is added to the dry BCPs, which leads to the assembly while in the solvent exchange process, the copolymer is first dissolved in a non-selective solvent before slow addition of the selective solvent and removal of the non-selective solvent at the end of the process. In the thin film rehydration approach, the copolymer is also dissolved in a non-selective solvent but the solution is first dried to leave a thin film of the copolymer before slow addition of a selective solvent under vigorous stirring to allow nanostructures formation. Crystallisation-driven self-assembly necessitates BCPs with a crystalline core-forming block. The crystalline-coil BCP is heated in a selective solvent above the melting temperature (T_m) of the crystalline block then allowed to cool down which leads the unimers to rearrange as the solvophobic blocks recrystallise and aggregate, which produces nanostructures.[108-112] These approaches will yield different morphologies and sizes that depend on the method chosen but also on several other parameters such as the solvent, BCP and stirring employed. As mentioned above, BCP self-assemblies are usually formed under kinetic control and are out of thermodynamic equilibrium which makes the prediction of the resulting morphology for a given approach complicated.

The aforementioned techniques are time- and resource-consuming, give solutions with a relatively low content of polymer and lead to mixtures of morphology especially when nanostructures that are not spherical micelles are targeted. As an additional drawback, CDSA requires the solvoophobic block to

be crystalline and have a T_m achievable in the selective solvent. A technique that has gained traction for its capacity to achieve pure phase of nanostructures with high concentration of copolymer and simple experimental procedures is the polymerisation-induced self-assembly (PISA) of BCPs.

1.4.1.1. Polymerisation-induced self-assembly

PISA was first reported in 2002 by Ferguson *et al.* in a seminal work where they demonstrated the practical polymerisation *via* reversible addition-fragmentation chain transfer (RAFT) of well-defined poly(acrylic acid)-*b*-poly(butyl acrylate) amphiphilic diblock copolymers in water under emulsion conditions which led to spherical micelles of 60 nm in size.[113] In a typical PISA experiment, a solvophilic monomer is polymerised in the selective solvent that produces a macroinitiator which is chain-extended with a different monomer by either dispersion[114] or emulsion[115] polymerisation which forms the solvophobic block (Scheme 2.1). In the case of dispersion PISA, the second monomer needs to be solvophilic as a small molecule, but the polymer becomes insoluble once it reached a certain DP which drives the self-assembly. For the PISA methodology any type of living polymerization can be employed and many types of polymerisation methods have been employed in PISA[116] such as nitroxide-mediated polymerisation (NMP),[117, 118] organotellurium-mediated radical polymerisation (TERP),[119, 120] cobalt-mediated radical polymerisation,[121] anionic polymerisation,[122] ring-opening polymerisation (ROP),[123-125] atom transfer radical polymerisation (ATRP),[126-130] ring-opening metathesis polymerisation (ROMP)[131-134] and RAFT;[135-139] the latter is the most used currently in the PISA community. The wide variety of polymerisation types and therefore monomers available for PISA gives access to a range of different solvents with various polarity such as: water,[139-142] DMSO,[143] alcohols,[144-146] ethylene glycol,[147] alkanes,[148-151] ionic liquids[152] and critical CO_2.[153, 154]

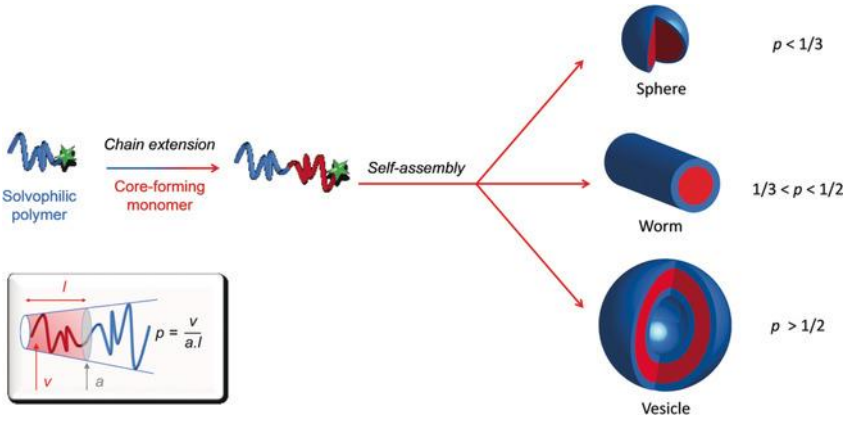

Scheme 1.5. General model for polymerisation-induced self-assembly (PISA). Reproduced from the work of D'Agosto *et al.* published in Wiley-VCH, Angewandte Chemie International Edition.[135]

PISA is a reproducible technique and the morphology which results from self-assembly can be changed when the solvophilic and/or solvophobic block length, solid content and temperature are varied. A common observation is the formation of higher order morphologies (sphere → worm-like → polymersome) when the solvophobic block length or solid content are increased. The completion and analysis of several PISA experiments at different concentrations and/or block lengths allow to map and predict the morphology of the nanostructures with a phase diagrams (Figure 1.11).[155-157]

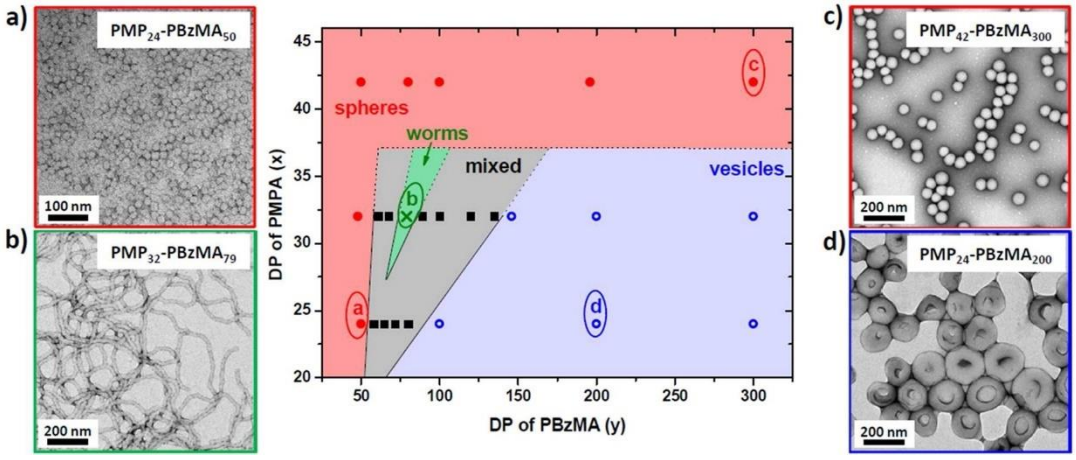

Figure 1.11. Phase diagram constructed by varying the solvophobic (abscissa) and solvophilic (ordinate) block length for poly(methacryloyloxymethyl dimethylphosphonate)$_x$-*b*-poly(benzyl methacrylate)$_y$ diblock copolymer nano-objects: spherical micelles (red), worm-like micelles (green), polymersomes (blue) and mixed morphologies (grey). Reproduced from the work of Hanisch *et al.* published in ACS, Macromolecules.[157]

1.4.2. Applications

As a consequence of their wide range of synthetic methodologies and structures, self-assembled nanostructures find applications in various areas[158, 159] such as nanomedicine,[160-163] sensing,[164] antimicrobial agents,[165] stimuli-responsive "smart" nanomaterials,[166, 167] lubricant,[168] composite reinforcement[169] and catalysis with nanoreactors.[170] In most applications, the confinement of a specific compound and its controlled access by diffusion or controlled release is the key role of the nanostructures. For example, nano-object drug delivery vehicles in aqueous medium require the encapsulation of a therapeutic compounds in either the hydrophobic core in the case of a micelle, or the aqueous lumen or hydrophobic membrane in the case of polymersomes, which protects the cargo during its journey to the targeted organ which facilitates controlled release. In the case of catalysis applications, the nano-objects shield the active sites from the surrounding milieu which requires the reagent to diffuse inside the hydrophobic core or the aqueous lumen to reach the catalytic units, and, in the case of micellar objects, increase the reaction concentration within the catalytic core. Among all these fields, synthetic nanoreactors are the objects that are of interest for the scope of this work.

1.4.2.1. Nanoreactors

Nanoreactors are nanometre-sized reaction vessels[171] that can take many forms such as polymersomes[172], gels[173] or micelles[174] with micellar nanoreactors that are similar to enzymes with the presence of a solvophobic pocket that contains the active sites. They are commonly formed by self-assembly of amphiphilic BCPs and because of their amphiphilic construction, it is possible to conduct organic reactions in aqueous media. Furthermore, these reactions can not only occur inside the nanoreactors but can even occur between the structures.[175]

Additionally, a catalyst can be directly tethered to the solvophobic core, which makes it easily recoverable. For example, Liu *et al.* used shell cross-linked micelles (SCM) that contain Co(III) Salen as catalysts for the hydrolytic kinetic resolution of various terminal epoxides and showed that because of their nanoparticles' size and stability, they were able to recover and reuse the catalyst after up to 8 cycles.[176] This feature is even more attractive when taking into account the "concentrator effect" – discovered by Helms *et al.*[177] with dendrimers that contained core-confined catalyst – where catalytic reactions performed in confined environments display faster kinetics and sometimes better overall efficiencies. Finally, nanoreactors have been shown to achieve specific molecular recognition. Cotanda *et al.* synthesised poly(styrenic-DMAP)-*b*-poly(*N*-isopropylacrylamide) micelles for use in competitive acylation of alcohols with different anhydrides and demonstrated a specific substrate recognition which was able to alter the selectivity of the reactions (Scheme 1.6).[178, 179]

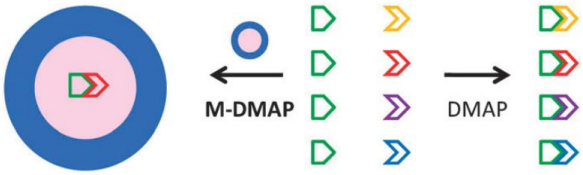

Scheme 1.6 Illustration of specific reaction of one substrate (from a pool of 4) with a polymeric nanoreactor (M-DMAP) as a reaction vessel (green = anhydride compound; yellow, red, purple and blue = 4 different alcohol compounds). Reproduced from the work of Cotanda *et al.* published in RSC, Chemical Communications.[178]

1.4.3. Analysis

The analysis of solution self-assembled copolymers can be conducted with a wide range of techniques[180] such as scattering, microscopy, zeta potential and DOSY NMR. Scattering methods with laser light, X-rays, or neutrons can be conducted *in situ* and provide information on the particles such as their corona,

core and total size, size distribution, aggregation number (*i.e.* how many polymer chains compose one particle), molecular weight and morphology. These techniques inform on the sample as a whole and the data are often analysed with a model developed within the boundaries of particular assumptions (*e.g.* spherical morphology with homogeneous distribution of the mass inside the particles). Therefore, these techniques are difficult to employ for samples that are widely heterogeneous and/or contain unknown structures. Laser light equipment is nowadays affordable and can be stored on the benchtop which gives this technique an edge in terms of ease of use. On the other hand, microscopic techniques such as transmission electron microscopy (TEM) and scanning electron microscopy (SEM) are very costly techniques that produce images of individual particles and allow to establish the shape and size of the particles. These are destructive methods that can require conditions such as drying or vacuum that can alter the particles' structure and the number of particles analysed through these method makes for poor statistics compared to scattering methods. The images taken need to be numerous enough to select representative images and avoid the analysis of impurities or minor populations moreover, unlike scattering techniques, they do not give quantitative information about the particles' size in solution (for dry-state microscopy), aggregation number or molecular weight. TEM and SEM will give different information on the analysed nanostructure. SEM analyses the electrons that interact with the surface of the nanoparticles and are re-emitted which gives information on the topography and elemental composition of the nanostructure. For TEM, the electron beam goes through the sample which yields a negative image of the nano-objects which is useful in the determination the inner structure. Microscopy and scattering techniques generate complementary information about the analysed particles, and it is

preferable to combine both scattering and microscopy to achieve the more reliable information on the nanostructures.

1.4.3.1. Laser light-scattering

In scattering techniques, the solution analysed is illuminated with an electromagnetic radiation of known wavelength and the intensity scattered by the sample at a given angle is measured. The data can be analysed as a function of time for dynamic light-scattering (DLS) or averaged over the time scale for static light-scattering (SLS), which provides different information about the particles. The angle mentioned earlier is important when the size of the particles analysed is considered. Indeed, the length scale achievable is inversely proportional to the scattering wave vector q (the difference between the incident wave vector and the scattered wave vector) which is a function of the scattering angle (*i.e.* the detection angle, ϑ) and the wavelength of the incident laser light (λ) (Scheme 1.7). Therefore, the length scale can be adapted by either a change in ϑ or λ. The sample analysed must be dilute enough to avoid inter-particle scattering of light and the solvent employed should be filtered to avoid contributions from dust or other impurities present. This is because scattering intensity is related to the square of the mass of the particle and so very small numbers of large particles (*e.g.* dust/muck) tend to dominate the measured scattering profile. The different nanostructures present in solution scatter the light differently which depends on the angle chosen therefore a multi-angle experiment allows to achieve a more accurate determination by extrapolation of the various quantities measured (size, distribution, morphology, *etc.*).

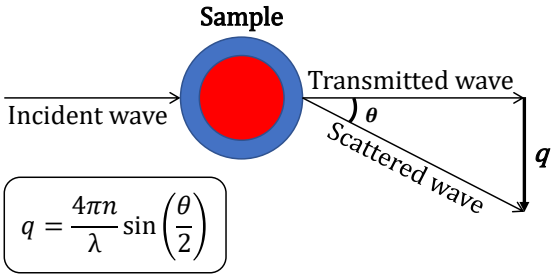

Scheme 1.7. Illustration of the scattering wave vector (q) and its associated equation where λ is the wavelength of the incident wave, ϑ is the scattering angle and n is the refractive index of the solvent.

Dynamic light scattering (DLS) uses the fact that particles in solution move under Brownian motion and their diffusion coefficient D can be related to their hydrodynamic size (R_h) by the Stokes–Einstein equation (Equation 1.1) where k_B is Boltzmann's constant, T the absolute temperature and η the viscosity of the solvent. In a typical DLS experiment, the sample is illuminated with a known wavelength (Figure 1.12A) and the scattered light intensity is recorded over time at a fixed angle (Figure 1.12B). The autocorrelation function at a specific angle (g_2) which measures how fast the scattered intensity changes with time is then determined (Figure 1.12C). For monodisperse assemblies, the autocorrelation function can be modelled as a monoexponential decay which exhibits a single relaxation time τ. The apparent value of D (D_{app}) can then be calculated from τ (Equation 1.2). However, like synthetic polymers, polymeric nanostructures are rarely monodisperse and in this case, the cumulant method,[181, 182] the CONTIN algorithm[183] or the REPES algorithm[184] can be employed to fit the data and generate a continuous distribution of relaxation times that permit the analysis of multiple broad distributions. From the relaxation time distribution, D can be determined and as mentioned earlier, D is related to R_h by the Stokes-Einstein equation which allows the retrieval of the nano-structures intensity-weighted size distribution (Figure 1.12D).

$$R_{\mathrm{h}} = \frac{k_{\mathrm{B}}T}{6\pi\eta D} \tag{1.1}$$

$$\tau^{-1} = D_{\mathrm{app}}q^2 \tag{1.2}$$

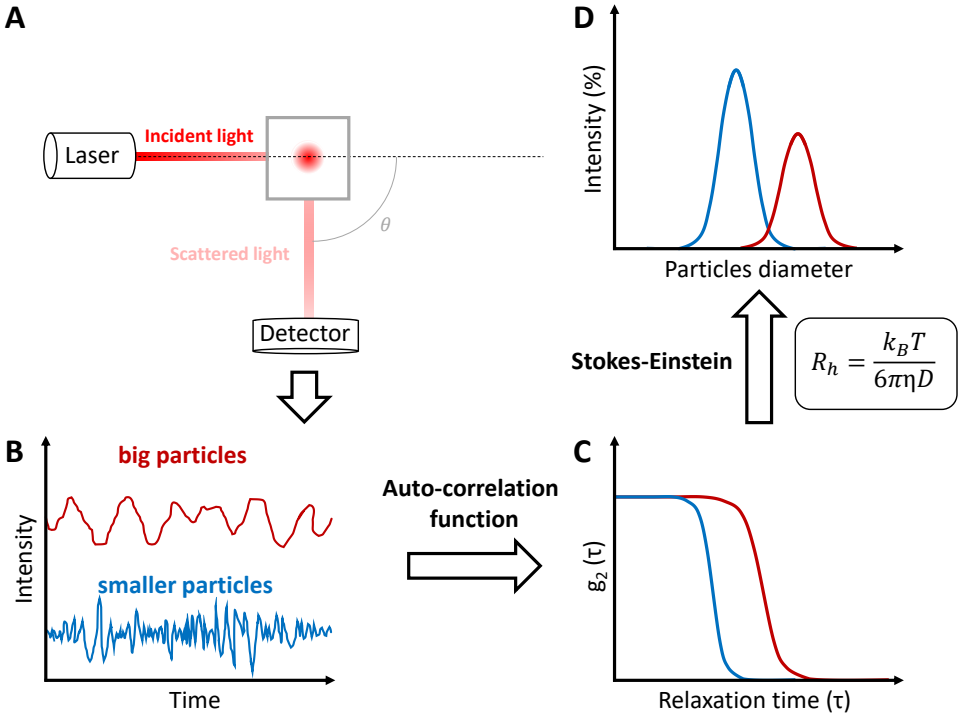

Figure 1.12. Illustration of the dynamic light scattering analysis: (A) instrument layout, (B) scattered intensity over time, (C) correlation function g_2 and (D) intensity-weighed size distribution. The Stokes-Einstein equation is given between step (C) and (D).

In static light scattering, instead of the intensity variation over time employed in DLS, the mean intensity is employed in the calculations which is obtained from the average of the intensity over the time scale. This intensity is measured for a standard, usually toluene (I_{standard}), the solvent (I_{solvent}) and the sample (I_{sample}). These allow to compute the Rayleigh ratio of the sample (R_θ) which is the normalised contribution of the sample to the total scattering intensity (1.3) where $R_{\theta,\mathrm{standard}}$ is the known Rayleigh ratio of the standard. Therefore, the contribution by the sample container and the solvent to the measurements are both mitigated. Three main models are employed to fit the data from SLS:

Zimm,[185] Berry[186] and Debye.[187] They differ in the quantity used on the ordinate where Zimm uses $\frac{Kc}{R_\theta}$ (1.4) , Berry $\sqrt{\frac{Kc}{R_\theta}}$ and Deby $\frac{R_\theta}{Kc}$ but the abscissa is always q^2. The value on the ordinate can be computed from the optical contrast constant (K) (1.5) where n_0 is the refractive index of the solvent, $\frac{\mathrm{d}n}{\mathrm{d}c}$ is the refractive index increment that can be measured with a differential refractometer and N_A is the Avogadro number. It is important to note that if the refractive index of the polymer solution is the same as the solvent, $\frac{\mathrm{d}n}{\mathrm{d}c} = 0$, there is no scattering and another solvent should be selected. The intensity measurements are conducted at different concentration (c) and angles which allows extrapolation of the data to $c = 0$ and $q^2 = 0$. Extrapolation to zero concentration allows to remove the contribution of the interactions between the particles represented by the term A_2 while extrapolation to $q^2 = 0$ removes the contribution of length scale which allows calculations of the average particle's size. Fitting the data with one of the models at $c = 0$ yields the average molecular weight of the particles (M_w) at the intercept and the gyration radius (R_g) from the slope at $q^2 = 0$ (Table 1.1). Choosing the right method depends on the experiment and the expected particle size and morphology that latter can be determined by microscopy. Andersson *et al.* suggest the Berry model as the most general procedure when there is no prior information on the particles' morphology or size.[188] While Patterson *et al.* suggest that the Zimm method may not be employed for nanostructures with $R_\mathrm{g} < 80$ nm.[180] The molecular weight calculated by light scattering can be used to determine the aggregation number (N_agg) which is an estimate of the number of polymer chains per particles (1.6) where $M_\mathrm{w,polymer}$ is determined by size exclusion chromatography (SEC). The N_agg can be an indicator of the nanostructure morphology where micelles will have N_agg in the tens to the hundreds while the polymersomes will display much higher values in the

thousands or hundreds of thousands. For cylindrical morphologies, this number would vary with the dimensions of the nanostructures.

$$R_\theta = \frac{I_{\text{sample}} - I_{\text{solvent}}}{I_{\text{standard}}} R_{\theta,\text{standard}} \quad 1.3$$

$$\frac{Kc}{R_\theta} = \frac{{R_g}^2}{3M_w} q^2 + \frac{1}{M_w} + 2A_2 c \quad 1.4$$

$$K = \frac{(2\pi n_0)^2 \left(\frac{dn}{dc}\right)^2}{N_A \lambda^4} \quad 1.5$$

Table 1.1. Overview of the equations for the intercept and slope for the different method (Zimm, Berry and Debye).

Method	Intercept	Slope[a]
Zimm	M_w	$\frac{{R_g}^2}{3M_w}$
Berry	${M_w}^{-1}$	$\frac{{R_g}^2}{6{M_w}^{1/2}}$
Debye	${M_w}^{-1/2}$	$-\frac{M_w {R_g}^2}{3}$

[a]At $q^2 = 0$

$$N_{agg} = \frac{M_{w,particle}}{M_{w,polymer}} \quad 1.6$$

DLS and SLS are complementary techniques and together they can give information on the morphology of the analysed particles. Indeed, the ratio between the R_h calculated from DLS and the R_g calculated from SLS is an indication on the nanostructure's morphology. A ratio $\frac{R_g}{R_h} = 1$ indicates that the mass is distributed along the hydrodynamic radius of the particles therefore the morphology represented is a hollow sphere *i.e.* a polymersome (Figure 1.13). Ratios larger than one can be indicative of an elongated cylindrical morphology while a ratio of 0.775 indicates homogeneous spheres *i.e.* micelles.

Moreover, DLS and SLS can also be combined to remove the signal contribution from spurious scatterers (*i.e.* very large particles like dust or particles' aggregates) present in small quantities in a sample that contains mainly small particles when the unwanted particles are not easily removed (by filtration or centrifugation for example). This method necessitates to measure DLS and SLS simultaneously on the sample. The contribution to the signal intensity from the fast mode (C_{fast}) *i.e.* the small scatterers and slow mode (C_{slow}) *i.e.* the larger population is determined by DLS with one of the algorithms cited above which allows to separate these two populations during the analysis. The contribution from the fast mode is then employed to modify the SLS analysis where R_θ of the sample is replaced by $R_{\theta,\text{fast}} = C_{\text{fast}} R_\theta$.

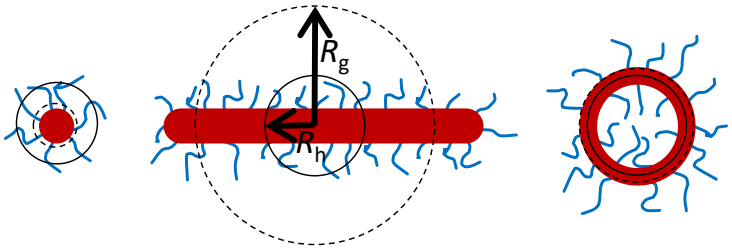

Figure 1.13. Scheme that indicates how the different morphologies would have a different R_g/R_h ratio where R_g is indicated by the dashed line and R_h is indicated by the solid line.

1.5. Conclusion and aims

As presented, the development of green and water-based enantioselective catalysts is hindered by the multi-step reactions and toxic solvent necessary for their synthesis and operation respectively. Micellar nanoreactors are able to mimic the enzyme hydrophobic pocket and have already shown selectivity towards the type of species that can access their active core. Making this selectivity applicable to enantiomers could be effective with helical polymers that are chiral objects similar to the α-helices present in enzymes and are already employed in enantioselective organocatalysts.

This project took enzymes as an inspiration for the development of water-based nanoreactors for transesterification reactions. Employing a bottom-up strategy[189] to engineer enzyme-like systems that would replicate the behaviour of enzymes with the objective to achieve asymmetric reactions in water.

The aim of this work is to develop micelles with a chiral core that can easily be functionalised to allow the introduction of a simple achiral catalyst moiety. The chiral environment of the core is thought to enable enantioselective catalysis by kinetic resolution.

1.6. References

1. Breslow, R.; Cheng, Z.-L., *Proc. Natl. Acad. Sci. U.S.A.* 2009, 23, 9144-9146.
2. Barham, P.; Skibsted, L. H.; Bredie, W. L. P.; Bom Frøst, M.; Møller, P.; Risbo, J.; Snitkjær, P.; Mortensen, L. M., *Chem. Rev.* 2010, 4, 2313-2365.
3. Katsuki, T.; Sharpless, K. B., *J. Am. Chem. Soc.* 1980, 18, 5974-5976.
4. Noyori, R.; Ohkuma, T.; Kitamura, M.; Takaya, H.; Sayo, N.; Kumobayashi, H.; Akutagawa, S., *J. Am. Chem. Soc.* 1987, 19, 5856-5858.
5. Vineyard, B. D.; Knowles, W. S.; Sabacky, M. J.; Bachman, G. L.; Weinkauff, D. J., *J. Am. Chem. Soc.* 1977, 18, 5946-5952.
6. Ensley, H. E.; Parnell, C. A.; Corey, E. J., *J. Org. Chem.* 1978, 8, 1610-1612.
7. Hoveyda, A. H.; Evans, D. A.; Fu, G. C., *Chem. Rev.* 1993, 4, 1307-1370.
8. Evans, D. A.; Kim, A. S.; Metternich, R.; Novack, V. J., *J. Am. Chem. Soc.* 1998, 24, 5921-5942.
9. Evans, D. A.; Chapman, K. T.; Carreira, E. M., *J. Am. Chem. Soc.* 1988, 11, 3560-3578.
10. Overman, L. E.; McCready, R. J., *Tetrahedron Lett.* 1982, 23, 2355-2358.
11. Breslow, R.; Cheng, Z.-L., *Proc. Natl. Acad. Sci. U.S.A.* 2010, 13, 5723-5725.
12. Zhao, D.; Neubauer, T. M.; Feringa, B. L., *Nat. Commun.* 2015, 1, 6652.
13. López, F.; Harutyunyan, S. R.; Minnaard, A. J.; Feringa, B. L., *J. Am. Chem. Soc.* 2004, 40, 12784-12785.
14. Zuend, S. J.; Coughlin, M. P.; Lalonde, M. P.; Jacobsen, E. N., *Nature* 2009, 7266, 968-970.
15. Fu, G. C., *Acc. Chem. Res.* 2004, 8, 542-547.
16. Ahrendt, K. A.; Borths, C. J.; MacMillan, D. W. C., *J. Am. Chem. Soc.* 2000, 17, 4243-4244.
17. Northrup, A. B.; MacMillan, D. W. C., *J. Am. Chem. Soc.* 2002, 24, 6798-6799.
18. Kaeobamrung, J.; Mahatthananchai, J.; Zheng, P.; Bode, J. W., *J. Am. Chem. Soc.* 2010, 26, 8810-8812.
19. MacMillan, D. W. C., *Nature* 2008, 7211, 304-308.
20. Dalko, P. I.; Moisan, L., *Angew. Chem. Int. Ed.* 2001, 20, 3726-3748.
21. Hajos, Z. G.; Parrish, D. R., *J. Org. Chem.* 1974, 12, 1615-1621.
22. Eder, U.; Sauer, G.; Wiechert, R., *Angew. Chem. Int. Ed.* 1971, 7, 496-497.
23. Gaunt, M. J.; Johansson, C. C. C.; McNally, A.; Vo, N. T., *Drug Discovery Today* 2007, 1, 8-27.
24. Wurz, R. P., *Chem. Rev.* 2007, 12, 5570-5595.

25. Ruble, J. C.; Fu, G. C., *J. Org. Chem.* 1996, 21, 7230-7231.
26. Ruble, J. C.; Latham, H. A.; Fu, G. C., *J. Am. Chem. Soc.* 1997, 6, 1492-1493.
27. Schmid, A.; Dordick, J. S.; Hauer, B.; Kiener, A.; Wubbolts, M.; Witholt, B., *Nature* 2001, 6817, 258-268.
28. Bornscheuer, U. T.; Huisman, G. W.; Kazlauskas, R. J.; Lutz, S.; Moore, J. C.; Robins, K., *Nature* 2012, 7397, 185-194.
29. Savile, C. K.; Janey, J. M.; Mundorff, E. C.; Moore, J. C.; Tam, S.; Jarvis, W. R.; Colbeck, J. C.; Krebber, A.; Fleitz, F. J.; Brands, J.; Devine, P. N.; Huisman, G. W.; Hughes, G. J., *Science* 2010, 5989, 305-309.
30. Pauling, L.; Corey, R. B.; Branson, H. R., *Proc. Natl. Acad. Sci. U.S.A.* 1951, 4, 205-211.
31. Watson, J. D.; Crick, F. H. C., *Nature* 1953, 4356, 737-738.
32. Nakano, T.; Okamoto, Y., *Chem. Rev.* 2001, 12, 4013-4038.
33. Natta, G.; Pino, P.; Corradini, P.; Danusso, F.; Mantica, E.; Mazzanti, G.; Moraglio, G., *J. Am. Chem. Soc.* 1955, 6, 1708-1710.
34. Yashima, E.; Maeda, K.; Iida, H.; Furusho, Y.; Nagai, K., *Chem. Rev.* 2009, 11, 6102-6211.
35. Yashima, E.; Ousaka, N.; Taura, D.; Shimomura, K.; Ikai, T.; Maeda, K., *Chem. Rev.* 2016, 22, 13752-13990.
36. Cornelissen, J. J. L. M.; Rowan, A. E.; Nolte, R. J. M.; Sommerdijk, N. A. J. M., *Chem. Rev.* 2001, 12, 4039-4070.
37. Leigh, T.; Fernandez-Trillo, P., *Nat. Rev. Chem.* 2020, 6, 291-310.
38. Yashima, E., *Polym. J.* 2010, 1, 3-16.
39. Nolte, R. J. M.; Van Beijnen, A. J. M.; Drenth, W., *J. Am. Chem. Soc.* 1974, 18, 5932-5933.
40. Green, M. M.; Peterson, N. C.; Sato, T.; Teramoto, A.; Cook, R.; Lifson, S., *Science* 1995, 5219, 1860-1866.
41. Green, M. M.; Park, J.-W.; Sato, T.; Teramoto, A.; Lifson, S.; Selinger, R. L. B.; Selinger, J. V., *Angew. Chem. Int. Ed.* 1999, 21, 3138-3154.
42. Okamoto, Y.; Nakano, T., *Chem. Rev.* 1994, 2, 349-372.
43. Nishimura, T.; Ichikawa, Y.; Hayashi, T.; Onishi, N.; Shiotsuki, M.; Masuda, T., *Organometallics* 2009, 16, 4890-4893.
44. Nagata, Y.; Yamada, T.; Adachi, T.; Akai, Y.; Yamamoto, T.; Suginome, M., *J. Am. Chem. Soc.* 2013, 27, 10104-10113.
45. Nagata, Y.; Nishikawa, T.; Suginome, M., *J. Am. Chem. Soc.* 2014, 45, 15901-15904.
46. Freire, F.; Seco José, M.; Quiñoá, E.; Riguera, R., *Angew. Chem. Int. Ed.* 2011, 49, 11692-11696.
47. Freire, F.; Seco, J. M.; Quiñoá, E.; Riguera, R., Helical Polymer–Metal Complexes: The Role of Metal Ions on the Helicity and the Supramolecular

Architecture of Poly(phenylacetylene)s. In *Hierarchical Macromolecular Structures: 60 Years after the Staudinger Nobel Prize II*, Springer, Cham: 2013; pp 123-140.

48. Miyabe, T.; Iida, H.; Banno, M.; Yamaguchi, T.; Yashima, E., *Macromolecules* 2011, 21, 8687-8692.

49. Chen, J.-L.; Su, M.; Jiang, Z.-Q.; Liu, N.; Yin, J.; Zhu, Y.-Y.; Wu, Z.-Q., *Polym. Chem.* 2015, 26, 4784-4793.

50. Chen, J.-L.; Yang, L.; Wang, Q.; Jiang, Z.-Q.; Liu, N.; Yin, J.; Ding, Y.; Wu, Z.-Q., *Macromolecules* 2015, 21, 7737-7746.

51. Yashima, E.; Maeda, K.; Okamoto, Y., *Nature* 1999, 6735, 449-451.

52. Yashima, E.; Maeda, K.; Furusho, Y., *Acc. Chem. Res.* 2008, 9, 1166-1180.

53. Green, M. M.; Reidy, M. P.; Johnson, R. D.; Darling, G.; O'Leary, D. J.; Willson, G., *J. Am. Chem. Soc.* 1989, 16, 6452-6454.

54. Green, M. M.; Garetz, B. A.; Munoz, B.; Chang, H.; Hoke, S.; Cooks, R. G., *J. Am. Chem. Soc.* 1995, 14, 4181-4182.

55. Asaoka, S.; Joza, A.; Minagawa, S.; Song, L.; Suzuki, Y.; Iyoda, T., *ACS Macro Lett.* 2013, 10, 906-911.

56. Lee, J.; Shin, S.; Choi, T.-L., *Macromolecules* 2018, 19, 7800-7806.

57. Xue, Y.-X.; Chen, J.-L.; Jiang, Z.-Q.; Yu, Z.; Liu, N.; Yin, J.; Zhu, Y.-Y.; Wu, Z.-Q., *Polym. Chem.* 2014, 22, 6435-6438.

58. Onitsuka, K.; Yanai, K.; Takei, F.; Joh, T.; Takahashi, S., *Organometallics* 1994, 10, 3862-3867.

59. Takei, F.; Onitsuka, K.; Takahashi, S.; Terao, K.; Sato, T., *Macromolecules* 2007, 15, 5245-5254.

60. Yamamoto, M.; Onitsuka, K.; Takahashi, S., *Organometallics* 2000, 23, 4669-4671.

61. Onitsuka, K.; Mori, T.; Yamamoto, M.; Takei, F.; Takahashi, S., *Macromolecules* 2006, 21, 7224-7231.

62. Onitsuka, K.; Yamamoto, M.; Mori, T.; Takei, F.; Takahashi, S., *Organometallics* 2006, 5, 1270-1278.

63. Metselaar, G. A.; Cornelissen, J. J. L. M.; Rowan, A. E.; Nolte, R. J. M., *Angew. Chem. Int. Ed.* 2005, 13, 1990-1993.

64. Deming, T. J.; Novak, B. M., *J. Am. Chem. Soc.* 1993, 20, 9101-9111.

65. Ribeiro, A. F. G.; Gomes, P. T.; Dias, A. R.; Ferreira da Silva, J. L.; Teresa Duarte, M.; Henriques, R. T.; Freire, C., *Polyhedron* 2004, 17, 2715-2724.

66. Okamoto, Y.; Nakano, T.; Habaue, S.; Shiohara, K.; Maeda, K., *J. Macromol. Sci. Part A* 1997, 10, 1771-1783.

67. Song, C.; Zhang, C.; Wang, F.; Yang, W.; Deng, J., *Polym. Chem.* 2013, 3, 645-652.

68. Liu, L.; Zang, Y.; Hadano, S.; Aoki, T.; Teraguchi, M.; Kaneko, T.; Namikoshi, T., *Macromolecules* 2010, 22, 9268-9276.
69. Nakano, T.; Satoh, Y.; Okamoto, Y., *Macromolecules* 2001, 8, 2405-2407.
70. Tamura, K.; Miyabe, T.; Iida, H.; Yashima, E., *Polym. Chem.* 2011, 1, 91-98.
71. Miyabe, T.; Iida, H.; Ohnishi, A.; Yashima, E., *Chem. Sci.* 2012, 3, 863-867.
72. Yuki, H.; Okamoto, Y.; Okamoto, I., *J. Am. Chem. Soc.* 1980, 20, 6356-6358.
73. Okamoto, Y.; Honda, S.; Okamoto, I.; Yuki, H.; Murata, S.; Noyori, R.; Takaya, H., *J. Am. Chem. Soc.* 1981, 23, 6971-6973.
74. Okamoto, Y., *Proc Jpn Acad Ser B Phys Biol Sci* 2015, 6, 246-261.
75. Shimomura, K.; Ikai, T.; Kanoh, S.; Yashima, E.; Maeda, K., *Nat Chem* 2014, 5, 429-434.
76. Yamamoto, T.; Murakami, R.; Komatsu, S.; Suginome, M., *J. Am. Chem. Soc.* 2018.
77. Reggelin, M.; Doerr, S.; Klussmann, M.; Schultz, M.; Holbach, M., *Proc. Natl. Acad. Sci. U.S.A.* 2004, 15, 5461-5466.
78. Yoshinaga, Y.; Yamamoto, T.; Suginome, M., *ACS Macro Lett.* 2017, 705-710.
79. Zhou, L.; Chu, B.-F.; Xu, X.-Y.; Xu, L.; Liu, N.; Wu, Z.-Q., *ACS Macro Lett.* 2017, 824-829.
80. Zhang, D.; Ren, C.; Yang, W.; Deng, J., *Macromol. Rapid Commun.* 2012, 8, 652-657.
81. Tang, Z.; Iida, H.; Hu, H.-Y.; Yashima, E., *ACS Macro Lett.* 2012, 2, 261-265.
82. Zhang, H.; Yang, W.; Deng, J., *J. Polym. Sci. A Polym. Chem.* 2015, 15, 1816-1823.
83. Miyabe, T.; Hase, Y.; Iida, H.; Maeda, K.; Yashima, E., *Chirality* 2009, 1, 44-50.
84. Yamamoto, T.; Murakami, R.; Suginome, M., *J. Am. Chem. Soc.* 2017, 7, 2557-2560.
85. Cornelissen, J. J. L. M.; Donners, J. J. J. M.; Gelder, R. d.; Graswinckel, W. S.; Metselaar, G. A.; Rowan, A. E.; Sommerdijk, N. A. J. M.; Nolte, R. J. M., *Science* 2001, 5530, 676-680.
86. Kouwer, P. H. J.; Koepf, M.; Le Sage, V. A. A.; Jaspers, M.; van Buul, A. M.; Eksteen-Akeroyd, Z. H.; Woltinge, T.; Schwartz, E.; Kitto, H. J.; Hoogenboom, R.; Picken, S. J.; Nolte, R. J. M.; Mendes, E.; Rowan, A. E., *Nature* 2013, 7434, 651-655.
87. Mayer, S.; Zentel, R., *Macromol. Rapid Commun.* 2000, 13, 927-930.

88. Ohira, A.; Okoshi, K.; Fujiki, M.; Kunitake, M.; Naito, M.; Hagihara, T., *Adv. Mater.* 2004, 18, 1645-1650.
89. Alberts, B.; Bray, D.; Lewis, J.; Raft, M.; Roberts, K.; Watson, J. D., *Molecular biology of the cell.* Garland Pub: New York, 1983; p 1146.
90. Tanford, C., *The hydrophobic effect: formation of micelles and biological membranes.* Wiley: New York, 1973; p 200.
91. Chandler, D., *Nature* 2005, 7059, 640-647.
92. Israelachvili, J. N.; Mitchell, D. J.; Ninham, B. W., *J. Chem. Soc., Faraday Trans. 2* 1976, 0, 1525-1568.
93. Riess, G., *Progress in Polymer Science* 2003, 7, 1107-1170.
94. Mai, Y.; Eisenberg, A., *Chem. Soc. Rev.* 2012, 18, 5969-5985.
95. Bates, C. M.; Bates, F. S., *Macromolecules* 2017, 1, 3-22.
96. Konishcheva, E.; Daubian, D.; Gaitzsch, J.; Meier, W., *HCA* 2018, 2, e1700287.
97. Nicolai, T.; Colombani, O.; Chassenieux, C., *Soft Matter* 2010, 14, 3111-3118.
98. Jain, S.; Bates, F. S., *Macromolecules* 2004, 4, 1511-1523.
99. Tritschler, U.; Pearce, S.; Gwyther, J.; Whittell, G. R.; Manners, I., *Macromolecules* 2017, 9, 3439-3463.
100. Jang, S. G.; Audus, D. J.; Klinger, D.; Krogstad, D. V.; Kim, B. J.; Cameron, A.; Kim, S.-W.; Delaney, K. T.; Hur, S.-M.; Killops, K. L.; Fredrickson, G. H.; Kramer, E. J.; Hawker, C. J., *J. Am. Chem. Soc.* 2013, 17, 6649-6657.
101. Zhong, S.; Cui, H.; Chen, Z.; Wooley, K. L.; Pochan, D. J., *Soft Matter* 2008, 1, 90-93.
102. Mable, C. J.; Warren, N. J.; Thompson, K. L.; Mykhaylyk, O. O.; Armes, S. P., *Chem. Sci.* 2015, 11, 6179-6188.
103. Li, Z.; Hillmyer, M. A.; Lodge, T. P., *Macromolecules* 2006, 2, 765-771.
104. Blanazs, A.; Madsen, J.; Battaglia, G.; Ryan, A. J.; Armes, S. P., *J. Am. Chem. Soc.* 2011, 41, 16581-16587.
105. Inam, M.; Jones, J. R.; Pérez-Madrigal, M. M.; Arno, M. C.; Dove, A. P.; O'Reilly, R. K., *ACS Cent. Sci.* 2018, 1, 63-70.
106. Blanazs, A.; Armes, S. P.; Ryan, A. J., *Macromol. Rapid Commun.* 2009, 4-5, 267-277.
107. Dionzou, M.; Morère, A.; Roux, C.; Lonetti, B.; Marty, J. D.; Mingotaud, C.; Joseph, P.; Goudounèche, D.; Payré, B.; Léonetti, M.; Mingotaud, A. F., *Soft Matter* 2016, 7, 2166-2176.
108. Inam, M.; Cambridge, G.; Pitto-Barry, A.; Laker, Z. P. L.; Wilson, N. R.; Mathers, R. T.; Dove, A. P.; O'Reilly, R. K., *Chem. Sci.* 2017.

109. Finnegan, J. R.; He, X.; Street, S. T. G.; Garcia-Hernandez, J. D.; Hayward, D. W.; Harniman, R. L.; Richardson, R. M.; Whittell, G. R.; Manners, I., *J. Am. Chem. Soc.* 2018, 49, 17127-17140.
110. Massey, J. A.; Temple, K.; Cao, L.; Rharbi, Y.; Raez, J.; Winnik, M. A.; Manners, I., *J. Am. Chem. Soc.* 2000, 47, 11577-11584.
111. Hudson, Z. M.; Boott, C. E.; Robinson, M. E.; Rupar, P. A.; Winnik, M. A.; Manners, I., *Nat Chem* 2014, 10, 893-898.
112. Wang, X.; Guerin, G.; Wang, H.; Wang, Y.; Manners, I.; Winnik, M. A., *Science* 2007, 5838, 644.
113. Ferguson, C. J.; Hughes, R. J.; Pham, B. T. T.; Hawkett, B. S.; Gilbert, R. G.; Serelis, A. K.; Such, C. H., *Macromolecules* 2002, 25, 9243-9245.
114. Wang, K.; Wang, Y.; Zhang, W., *Polym. Chem.* 2017, 41, 6407-6415.
115. Siirilä, J.; Häkkinen, S.; Tenhu, H., *Polym. Chem.* 2019, 6, 766-775.
116. Liu, C.; Hong, C.-Y.; Pan, C.-Y., *Polym. Chem.* 2020.
117. Darabi, A.; Shirin-Abadi, A. R.; Jessop, P. G.; Cunningham, M. F., *Macromolecules* 2015, 1, 72-80.
118. Nicolaÿ, R.; Marx, L.; Hémery, P.; Matyjaszewski, K., *Macromolecules* 2007, 17, 6067-6075.
119. Okubo, M.; Sugihara, Y.; Kitayama, Y.; Kagawa, Y.; Minami, H., *Macromolecules* 2009, 6, 1979-1984.
120. Kitayama, Y.; Moribe, H.; Minami, H.; Okubo, M., *Polymer* 2011, 13, 2729-2734.
121. Cordella, D.; Ouhib, F.; Aqil, A.; Defize, T.; Jérôme, C.; Serghei, A.; Drockenmuller, E.; Aissou, K.; Taton, D.; Detrembleur, C., *ACS Macro Lett.* 2017, 2, 121-126.
122. Tanaka, H.; Yamauchi, K.; Hasegawa, H.; Miyamoto, N.; Koizumi, S.; Hashimoto, T., *Physica B: Condensed Matter* 2006, 742-744.
123. Guégain, E.; Zhu, C.; Giovanardi, E.; Nicolas, J., *Macromolecules* 2019, 10, 3612-3624.
124. Lecommandoux, S.; Grazon, C.; Salas-Ambrosio, P.; Ibarboure, E.; Buol, A.; Garanger, E.; Grinstaff, M. W.; Bonduelle, C., *Angew. Chem. Int. Ed.* 2019, ja, doi:10.1002/anie.201912028.
125. Yoon, K.-Y.; Lee, I.-H.; Kim, K. O.; Jang, J.; Lee, E.; Choi, T.-L., *J. Am. Chem. Soc.* 2012, 35, 14291-14294.
126. Li, W.; Min, K.; Matyjaszewski, K.; Stoffelbach, F.; Charleux, B., *Macromolecules* 2008, 17, 6387-6392.
127. Sugihara, S.; Sugihara, K.; Armes, S. P.; Ahmad, H.; Lewis, A. L., *Macromolecules* 2010, 15, 6321-6329.
128. Sugihara, S.; Armes, S. P.; Lewis, A. L., *Angew. Chem. Int. Ed.* 2010, 20, 3500-3503.

129. Wang, G.; Schmitt, M.; Wang, Z.; Lee, B.; Pan, X.; Fu, L.; Yan, J.; Li, S.; Xie, G.; Bockstaller, M. R.; Matyjaszewski, K., *Macromolecules* 2016, 22, 8605-8615.
130. Kim, K. H.; Kim, J.; Jo, W. H., *Polymer* 2005, 9, 2836-2840.
131. Zhang, L.; Song, C.; Yu, J.; Yang, D.; Xie, M., *J. Polym. Sci. A Polym. Chem.* 2010, 22, 5231-5238.
132. Wright, D. B.; Touve, M. A.; Adamiak, L.; Gianneschi, N. C., *ACS Macro Lett.* 2017, 9, 925-929.
133. Foster, J. C.; Varlas, S.; Blackman, L. D.; Arkinstall, L. A.; O'Reilly, R. K., *Angew. Chem. Int. Ed.* 2018, 33, 10672-10676.
134. Varlas, S.; Foster, J. C.; O'Reilly, R. K., *Chem. Commun.* 2019, 62, 9066-9071.
135. D'Agosto, F.; Rieger, J.; Lansalot, M., *Angew. Chem. Int. Ed.* 2020, 22, 8368-8392.
136. Warren, N. J.; Armes, S. P., *J. Am. Chem. Soc.* 2014, 29, 10174-10185.
137. Charleux, B.; Delaittre, G.; Rieger, J.; D'Agosto, F., *Macromolecules* 2012, 17, 6753-6765.
138. Sun, J.-T.; Hong, C.-Y.; Pan, C.-Y., *Polym. Chem.* 2013, 4, 873-881.
139. Li, Y.; Armes, S. P., *Angew. Chem. Int. Ed.* 2010, 24, 4042-4046.
140. Boissé, S.; Rieger, J.; Belal, K.; Di-Cicco, A.; Beaunier, P.; Li, M.-H.; Charleux, B., *Chem. Commun.* 2010, 11, 1950-1952.
141. Tan, J.; Sun, H.; Yu, M.; Sumerlin, B. S.; Zhang, L., *ACS Macro Lett.* 2015, 11, 1249-1253.
142. Doncom, K. E. B.; Warren, N. J.; Armes, S. P., *Polym. Chem.* 2015, 41, 7264-7273.
143. Couturaud, B.; Georgiou, P. G.; Varlas, S.; Jones, J. R.; Arno, M. C.; Foster, J. C.; O'Reilly, R. K., *Macromol. Rapid Commun.* 2019, 2, 1800460.
144. Lowe, A. B., *Polymer* 2016, 161-181.
145. Yeow, J.; Xu, J.; Boyer, C., *ACS Macro Lett.* 2015, 9, 984-990.
146. Pei, Y.; Lowe, A. B., *Polym. Chem.* 2014, 7, 2342-2351.
147. Gao, C.; Zhou, H.; Qu, Y.; Wang, W.; Khan, H.; Zhang, W., *Macromolecules* 2016, 10, 3789-3798.
148. Houillot, L.; Bui, C.; Farcet, C.; Moire, C.; Raust, J.-A.; Pasch, H.; Save, M.; Charleux, B., *ACS Appl. Mater. Interfaces* 2010, 2, 434-442.
149. Fielding, L. A.; Derry, M. J.; Ladmiral, V.; Rosselgong, J.; Rodrigues, A. M.; Ratcliffe, L. P. D.; Sugihara, S.; Armes, S. P., *Chem. Sci.* 2013, 5, 2081-2087.
150. Pei, Y.; Thurairajah, L.; Sugita, O. R.; Lowe, A. B., *Macromolecules* 2015, 1, 236-244.
151. Derry, M. J.; Mykhaylyk, O. O.; Armes, S. P., *Angew. Chem. Int. Ed.* 2017, 7, 1746-1750.

152. Zhang, Q.; Zhu, S., *ACS Macro Lett.* 2015, 7, 755-758.
153. Alzahrani, A.; Zhou, D.; Kuchel, R. P.; Zetterlund, P. B.; Aldabbagh, F., *Polym. Chem.* 2019, 21, 2658-2665.
154. Derry, M. J.; Fielding, L. A.; Armes, S. P., *Progress in Polymer Science* 2016, 1-18.
155. Blanazs, A.; Ryan, A. J.; Armes, S. P., *Macromolecules* 2012, 12, 5099-5107.
156. Warren, N. J.; Mykhaylyk, O. O.; Mahmood, D.; Ryan, A. J.; Armes, S. P., *J. Am. Chem. Soc.* 2014, 3, 1023-1033.
157. Hanisch, A.; Yang, P.; Kulak, A. N.; Fielding, L. A.; Meldrum, F. C.; Armes, S. P., *Macromolecules* 2016, 1, 192-204.
158. Schacher, F. H.; Rupar, P. A.; Manners, I., *Angew. Chem. Int. Ed.* 2012, 32, 7898-7921.
159. Truong, N. P.; Quinn, J. F.; Whittaker, M. R.; Davis, T. P., *Polym. Chem.* 2016, 26, 4295-4312.
160. Karagoz, B.; Esser, L.; Duong, H. T.; Basuki, J. S.; Boyer, C.; Davis, T. P., *Polym. Chem.* 2014, 2, 350-355.
161. Mitragotri, S.; Anderson, D. G.; Chen, X.; Chow, E. K.; Ho, D.; Kabanov, A. V.; Karp, J. M.; Kataoka, K.; Mirkin, C. A.; Petrosko, S. H.; Shi, J.; Stevens, M. M.; Sun, S.; Teoh, S.; Venkatraman, S. S.; Xia, Y.; Wang, S.; Gu, Z.; Xu, C., *ACS Nano* 2015, 7, 6644-6654.
162. Ge, Z.; Liu, S., *Chem. Soc. Rev.* 2013, 17, 7289-7325.
163. Elsabahy, M.; Wooley, K. L., *Chem. Soc. Rev.* 2012, 7, 2545-2561.
164. Hu, J.; Liu, S., *Macromolecules* 2010, 20, 8315-8330.
165. Li, Y.; Hindi, K.; Watts, K. M.; Taylor, J. B.; Zhang, K.; Li, Z.; Hunstad, D. A.; Cannon, C. L.; Youngs, W. J.; Wooley, K. L., *Chem. Commun.* 2010, 1, 121-123.
166. Rodríguez-Hernández, J.; Chécot, F.; Gnanou, Y.; Lecommandoux, S., *Prog. Polym. Sci.* 2005, 7, 691-724.
167. Stuart, M. A. C.; Huck, W. T. S.; Genzer, J.; Müller, M.; Ober, C.; Stamm, M.; Sukhorukov, G. B.; Szleifer, I.; Tsukruk, V. V.; Urban, M.; Winnik, F.; Zauscher, S.; Luzinov, I.; Minko, S., *Nat Mater* 2010, 2, 101-113.
168. Zheng, R.; Liu, G.; Devlin, M.; Hux, K.; Jao, T.-c., *Tribology Transactions* 2009, 1, 97-107.
169. Dean, J. M.; Verghese, N. E.; Pham, H. Q.; Bates, F. S., *Macromolecules* 2003, 25, 9267-9270.
170. Vriezema, D. M.; Comellas Aragonès, M.; Elemans, J. A. A. W.; Cornelissen, J. J. L. M.; Rowan, A. E.; Nolte, R. J. M., *Chem. Rev.* 2005, 4, 1445-1490.
171. O'Reilly, R. K., *Philos. Trans. R. Soc. Lond. Math. Phys. Eng. Sci.* 2007, 1861, 2863-2878.

172. Gaitzsch, J.; Huang, X.; Voit, B., *Chem. Rev.* 2016, 3, 1053-1093.
173. Díaz, D. D.; Kühbeck, D.; Koopmans, R. J., *Chem. Soc. Rev.* 2010, 1, 427-448.
174. Sorella, G. L.; Strukul, G.; Scarso, A., *Green Chem.* 2015, 2, 644-683.
175. Hecht, S., *Nat Nano* 2016, 1, 6-7.
176. Liu, Y.; Wang, Y.; Wang, Y.; Lu, J.; Piñón, V.; Weck, M., *J. Am. Chem. Soc.* 2011, 36, 14260-14263.
177. Helms, B.; Liang, C. O.; Hawker, C. J.; Fréchet, J. M. J., *Macromolecules* 2005, 13, 5411-5415.
178. Cotanda, P.; O'Reilly, R. K., *Chem. Commun.* 2012, 83, 10280-10282.
179. Cotanda, P.; Lu, A.; Patterson, J. P.; Petzetakis, N.; O'Reilly, R. K., *Macromolecules* 2012, 5, 2377-2384.
180. Patterson, J. P.; Robin, M. P.; Chassenieux, C.; Colombani, O.; O'Reilly, R. K., *Chem. Soc. Rev.* 2014, 8, 2412-2425.
181. Koppel, D. E., *The Journal of Chemical Physics* 1972, 11, 4814-4820.
182. Frisken, B. J., *Appl. Opt.* 2001, 24, 4087-4091.
183. Provencher, S. W., *Computer Physics Communications* 1982, 3, 229-242.
184. Jakeš, J., *Collection of Czechoslovak Chemical Communications* 1995, 11, 1781-1797.
185. Zimm, B. H., *The Journal of Chemical Physics* 1948, 12, 1099-1116.
186. Berry, G. C., *The Journal of Chemical Physics* 1966, 12, 4550-4564.
187. Debye, P., *The Journal of Physical and Colloid Chemistry* 1947, 1, 18-32.
188. Andersson, M.; Wittgren, B.; Wahlund, K.-G., *Anal. Chem.* 2003, 16, 4279-4291.
189. Schwille, P., *Science* 2011, 6047, 1252.

Chapter 2 Nickel-catalysed coordination polymerisation-induced self-assembly of helical poly(aryl isocyanide)s

2.1. Declaration of authorship

Transmission electron microscopy was conducted by Mr Spyridon Varlas and spectrophotometry was performed by Ms Yujie Xie at the University of Birmingham.

This work was published in *ACS Macro Letters*:

Nickel-Catalyzed Coordination Polymerization-Induced Self-Assembly of Helical Poly(aryl isocyanide)s, Sètuhn Jimaja, Spyridon Varlas, Yujie Xie, Jeffrey C. Foster, Daniel Taton, Andrew P. Dove and Rachel K. O'Reilly, *ACS Macro Lett.* 2020, *9*, 226-232

2.2. Introduction

Helices and helical assemblies are important structures in bio-macromolecules (Figure 2.1) that are employed in many roles in nature from a structural function in the case of collagen to the storage of information (*i.e.*, DNA) to the many purposes the α-helix has in protein assembly and function.[1] One of the most remarkable attributes of the helical architecture is its inherent chirality – right- and left-handed helices are the mirror image of one another, but are not superimposable. The chirality of the helical structures gives it a potential role in the recognition of other chiral compounds such as other helices for example, which is well demonstrated by the α-helices present in the zinc finger motif for its binding to DNA double helix or proteins.[2-4] Moreover, helical polymer chains can form rigid rods,[5-9] which gives these types of polymers interesting properties in terms of structural applications. Collagen, as the most abundant structural proteins found in the extracellular matrix of vertebrates, is a good example of helical polymers for structural purpose, where three helical polypeptide chains are twisted around each other and form a triple helix.[10-12]

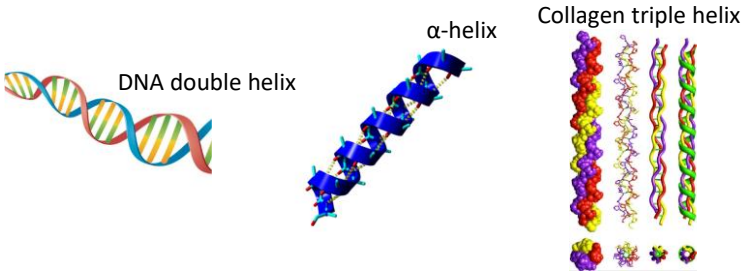

Figure 2.1. Helices found in nature: DNA double helix, protein α-helix and collagen triple helix.

The wide variety of applications of the helical structure in nature was an inspiration that chemists have applied in the development of synthetic helices in different areas[13-15] such as nanomaterials,[16-18] chiral recognition,[19-22] catalysis,[23-27] and data storage.[13-15] For instance, silica nanoparticles (NPs) grafted with helical polymers have been successfully employed as chiral

stationary phases (CSPs) for HPLC columns.[19, 28, 29] Helical polymers have also been investigated in optical data storage devices. It is theorised that the binary chiral information which arises from the helicity (right- or left-handed) could be used as an analogue to the binary system used currently (0 and 1).[30, 31]

In the field of nanomaterials, the self-assembly of helical polymers has been extensively explored.[26, 27, 32-43] Lecommandoux and coworkers used nature's building blocks (*i.e.* amino acids) to investigate the synthesis and self-assembly of polypeptide-based diblock copolymers into different nanostructures and studied their possible application as stimuli-responsive materials.[44-46] Diblock copolymer polypeptide assemblies were shown to respond to variations in pH and ionic force, as a consequence of the pH-sensitivity of polypeptides' secondary structure, which transitioned from α-helix to random coil which thereby altered amphiphilic packing.[45, 47-51] Pioneers in the self-assembly of polyisocyanides (PICs), Nolte and coworkers developed rod-coil diblock polyisocyanopeptide copolymers that self-assembled into polymersome which proved the feasibility of helix that contained PIC nano-structures.[52-54] In chiral recognition, Wu and coworkers employed self-assembled helical PICs. These helical-core micelles showed a difference in uptake between two enantiomers of a racemic mixture of a chiral dye or alcohol.[21, 22] To replicate the properties of cell penetrating peptides (CPP), which have excellent membrane permeability in part as a consequence of their helical shape[55], Cheng *et al.* showed that cationic, α-helical, poly(arginine) mimics displayed enhanced cellular internalisation and were employed as molecular transporters to mediate intracellular delivery of DNA and siRNA.[56] Building on this, Wu and coworkers reported that rapid cellular internalisation was observed with PEGylated left-handed helical PIC corona micelles.[57, 58] These last examples demonstrate the already advanced research conducted in nanomaterials for PICs. However, such assemblies are usually prepared by methods that are time- and resource-

consuming and give solutions with a relatively low content of polymer. An alternative route to prepare nanostructures is polymerisation-induced self-assembly (PISA, Scheme 2.1), which is an efficient approach to achieve nanostructures with different morphologies at high solids concentrations (up to 50 wt%) with simple experimental procedures.[59-65] Recently, Grazon *et al.* have demonstrated the PISA of helical polymers with the ring-opening PISA (ROPISA) of *N*-carboxyanhydrides where they chain-extended a PEG macroinitiator with γ-benzyl-L-glutamate *N*-carboxyanhydrides which produced a hydrophobic helical polypeptide block that self-assembled into well-defined micelles.[64]

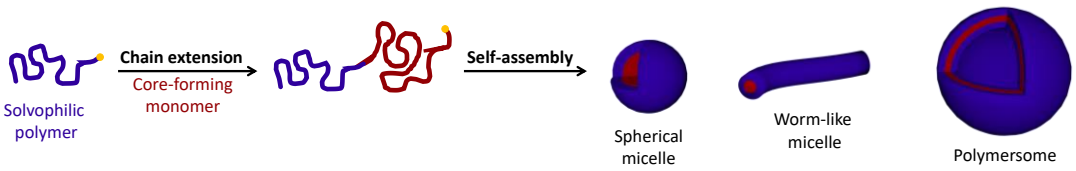

Scheme 2.1. General model for polymerisation-induced self-assembly (PISA) showing the three most common morphologies: spherical micelles, worm-like micelles and polymersomes.

While PISA is usually conducted by radical polymerisation techniques (RAFT, ATRP, NMP, *etc.*)[59, 60, 66-77] that rely heavily on methacrylate monomers, metal-catalysed coordination polymerisation methodologies for PISA provide entirely new possible backbone and side-chain chemistry. Such methodologies have been reported but have yet to be fully explored to the same degree as their radical counterparts. For instance, a ROMP-mediated PISA (ROMPISA) was recently described and extended the possibility of PISA to norbornene monomers.[78-82] PISA also has the advantage that encapsulation of small molecules can be accomplished *in situ* during polymerisation. Since the polymerisation of PIC can occur at room temperature, there is little risk of damage to thermolabile compounds like dyes, drugs or enzymes. Moreover, for nanoparticles prepared from helical polymers, the chiral induction effect of the

nanoparticle cores can be probed by measuring the circular dichroism (CD) of an encapsulated dye. Chiral induction of CD for an achiral dye embedded in helical assemblies has been observed before, where the chiral supramolecular architecture contributed to the induction effect.[83-88] However, it has not been reported for achiral supramolecular nano-objects such as micelles, where the overall architecture of the nanoparticle isn't helical and has therefore no effect on the CD absorption of encapsulated compounds. In this Chapter, the *in situ* synthesis and self-assembly of helical PICs into different nanostructures *via* a nickel-catalysed coordination polymerisation-induced self-assembly (NiCCo-PISA) and their chiral induction effect on an encapsulated achiral dye (Nile Red) was investigated. It is anticipated that such nanostructures will be useful in nanomedicine for the accessible synthesis of helix-containing delivery systems, while the chiral core could be leveraged for chiral recognition or asymmetric catalysis.

2.3. Nickel-catalysed polymerisation of poly(arylisocyanide)s

2.3.1. Solvophobic and solvophilic homopolymers

The common methodology to conduct dispersion PISA is through the chain-extension of a solvophilic block with a solvent-miscible monomer whose corresponding homopolymer is solvophobic. The growing polymer block gradually becomes insoluble in the reaction media, forming an amphiphilic diblock copolymer that self-assembles *in situ*.[60] In the early attempts to synthesise poly(isocyanide)s with chiral L-menthol side-chains, precipitation of the growing polymer was observed in DMSO during polymerisation. Thus, it was reasoned that menthyl-ester arylisocyanide (MAIC)[89, 90] could be utilised as the core-forming monomer in PISA formulations (Scheme 2.2). Toward this end, a DMSO-soluble PEG-ester aryl isocyanide (PAIC) monomer was synthesised as the corona block. A PEG side-chain was chosen because of the expected solubility in both water and DMSO of the monomer and homopolymer as well as its known biocompatibility. The catalyst developed by Lee *et al.*, *o*-Tol(dppe)NiCl, was selected because of its ease of synthesis (2 steps), stability towards air and water, and the speed of the polymerisation it catalyses.[91] In their investigation, Lee *et al.* reported the synthesis of a PIC pentablock copolymer in 1 minute by sequential addition of monomers, the different growing blocks were analysed by SEC which showed the increase in molecular weight as the different monomers feeds were added.

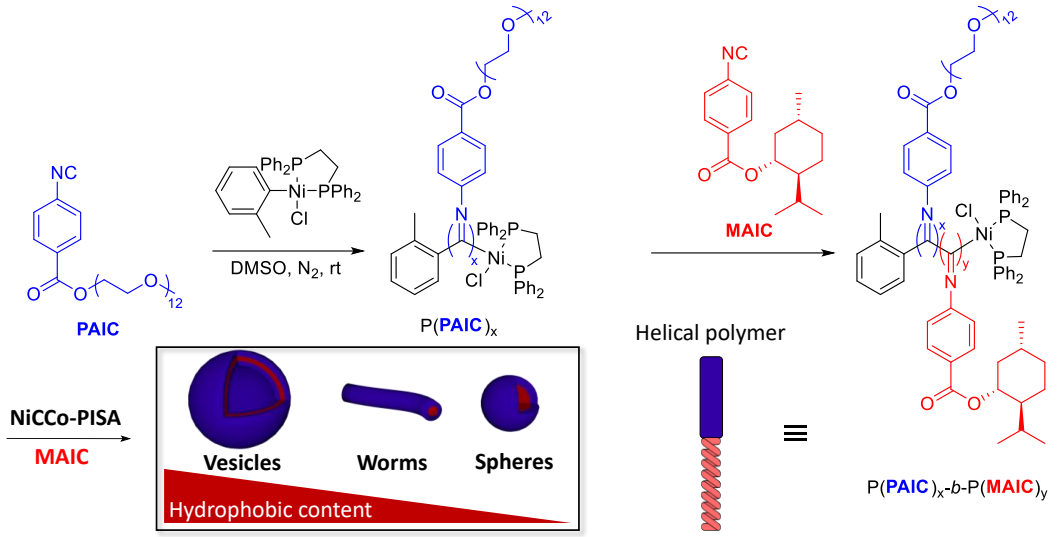

Scheme 2.2. Synthetic route followed for the preparation of diblock copolymers *via* NiCCo-PISA of P(PAIC)$_x$-*b*-P(MAIC)$_y$.

Both PAIC and MAIC were homopolymerised *via* a coordination polymerisation catalysed by *o*-Tol(dppe)NiCl. PAIC was polymerised in DMSO (Figure 2.2) as it is the solvent in which the NiCCo-PISA will be conducted while MAIC was polymerised in THF (Figure 2.3), as the homopolymer was not soluble in DMSO. Excellent control over the polymerisation process was observed in both cases, and polymers were obtained with low-to-moderate dispersities ($Đ_M$ <1.2) and number-average molecular weight (M_n) values (Table 2.1). The reported M_n values obtained by SEC were lower than the theoretical values calculated from the monomers molecular weight. These values were deduced from a polystyrene standard which assumes a globular shape from a coiled polymer. PICs are rigid-rod polymers; therefore, the PS standard is not an accurate model to calculate M_n. The measured M_n evolution was similar to what has been reported previously.[91]

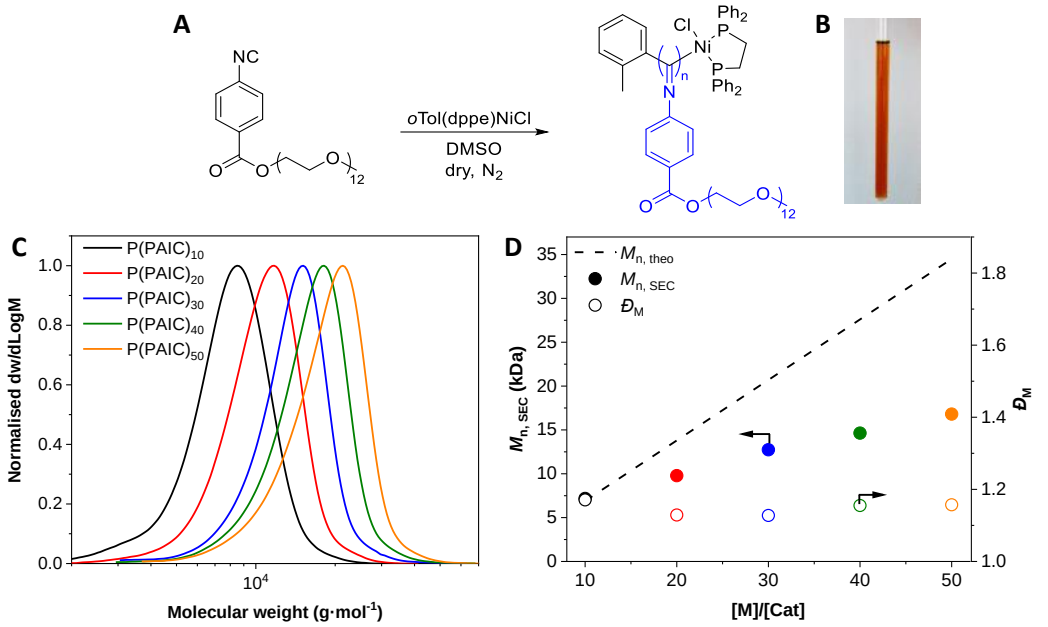

Figure 2.2. (A) Scheme of the homopolymerisation of PAIC. (B) The NMR tube contains P(PAIC) $DP_{PAIC} = 10$ in DMSO which shows the solubility of the homopolymer in DMSO. (C) Normalised SEC RI molecular weight distributions (THF + 2% v/v NEt_3, 40 °C, PS standards) of the different DPs of $P(PAIC)_x$ homopolymer. (D) $M_{n,SEC}$ (filled circles) and $Đ_M$ (hollow circles) as a function of monomer over catalyst ratio.

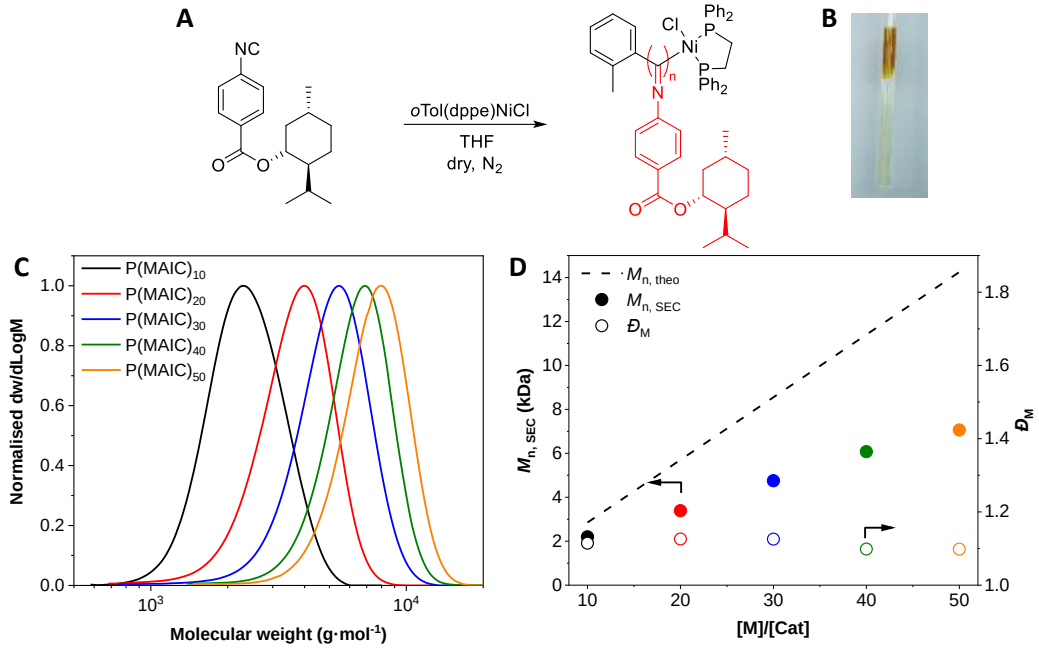

Figure 2.3. (A) Scheme of the homopolymerisation of MAIC. (B) The NMR tube contains P(MAIC) $DP_{MAIC} = 10$ in DMSO which shows the insolubility of the homopolymer in DMSO. (C) Normalised SEC RI molecular weight distributions (THF + 2% v/v NEt_3, 40 °C, PS standards) of the different DPs of $P(MAIC)_y$ homopolymer. (D) $M_{n,SEC}$ (filled circles) and $Đ_M$ (hollow circles) as a function of monomer over catalyst ratio.

Table 2.1. Characterisation by SEC of synthesised homopolymers P(PAIC)$_x$ and P(MAIC)$_x$ homopolymers (x = 10, 20, 30, 40, 50).

$DP_{P(PAIC)}$ [a]	$M_{n,\,theo}$ (kDa) [b]	$M_{n,\,SEC}$ (kDa) [c]	$Đ_M$ [c]
10	6.9	7.2	1.17
20	13.8	9.8	1.13
30	20.7	12.8	1.13
40	27.6	14.7	1.16
50	34.5	16.8	1.16
$DP_{P(MAIC)}$ [a]	$M_{n,\,theo}$ (kDa) [b]	$M_{n,\,SEC}$ (kDa) [c]	$Đ_M$ [c]
10	2.9	2.2	1.11
20	5.7	3.4	1.13
30	8.6	4.8	1.13
40	11.4	6.1	1.10
50	14.3	7.1	1.10

[a]All conversions were > 99%, as determined by ^{1}H NMR spectroscopy in $CDCl_3$. [b]Calculated from conversion with the monomer's MW and feed ratio. [c]Determined by SEC (THF + 2% v/v NEt_3) using polystyrene (PS) standards.

PICs are inherently helical in nature, and this helicity can be detected by circular dichroism (CD) spectroscopy. Moreover, these helices are static, which means that changes in helicity at room temperature are seldom observed.[14] However, in the absence of a driving force to influence the equilibrium during polymerisation between both screw-senses, they are present in equal quantities (*i.e.* a racemic helical mixture) and the overall CD signal is null. On the contrary, in P(MAIC), the chiral moiety on the side chain kinetically favours one of the helix screw-senses and this excess can be measured by CD (Figure 2.4).[90] In the case of MAIC, the CD signal is null and for P(MAIC)$_x$ the signal increases with M_n until it reaches a plateau at $DP_{P(MAIC)} = 20$. The CD

signal for the homopolymer P(PAIC) is also null as there is no chiral side chain to drive the screw-sense selectivity.

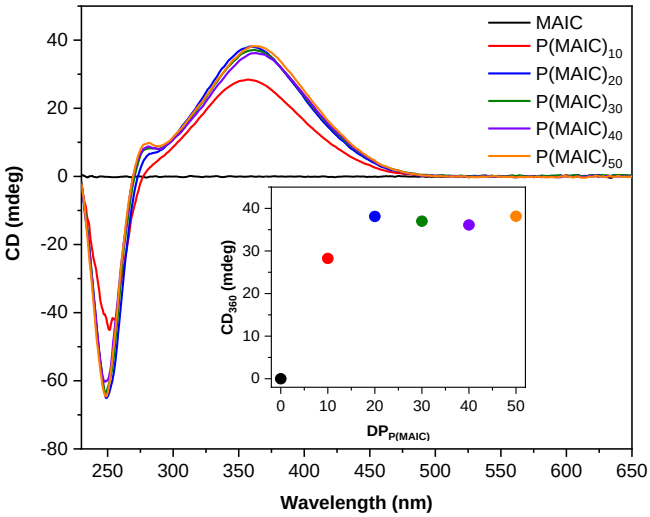

Figure 2.4. CD spectra of MAIC monomer and P(MAIC) homopolymers ($DP_{P(MAIC)}$ = 10, 20, 30, 40 and 50) in THF at 0.5 mg·mL^{-1}. *Inset*: CD signal at λ = 360 nm *vs* $DP_{P(MAIC)}$.

2.3.2. Amphiphilic P(PAIC)$_x$-*b*-P(MAIC)$_y$ block copolymers

Block copolymerisation of PAIC and MAIC was conducted by the *in-situ* chain-extension of a P(PAIC)$_x$ macroinitiator with MAIC as the core-forming monomer in DMSO, which yielded diblock copolymers P(PAIC)$_x$-*b*-P(MAIC)$_y$. The control over the polymerisation was verified by targeting different degrees of polymerisation (DPs) of both the solvophilic and solvophobic blocks and constructing M_n *vs* $DP_{P(MAIC)}$ plots (Figure 2.5, Figure 2.6 and Figure 2.7). A linear relationship between targeted DP and M_n indicated the polymerisation process was controlled (Table 2.3). However, when high $DP_{P(MAIC)}$ were targeted, high molecular weight shoulders were observed. The SEC measurement was repeated in $CHCl_3$ and the high molecular weight shoulders were still present which indicated the secondary population presence was not caused by the solvent or the solvent-specific column employed. Moreover, when the chain-extension of the macroinitiator

was conducted in a good solvent, namely THF, no shoulder was observed, which suggested that the apparition of high molecular weight population most likely originated from the PISA process itself (Figure A2.20). The reported M_n obtained by SEC were lower than the theoretical values (*vide supra*).

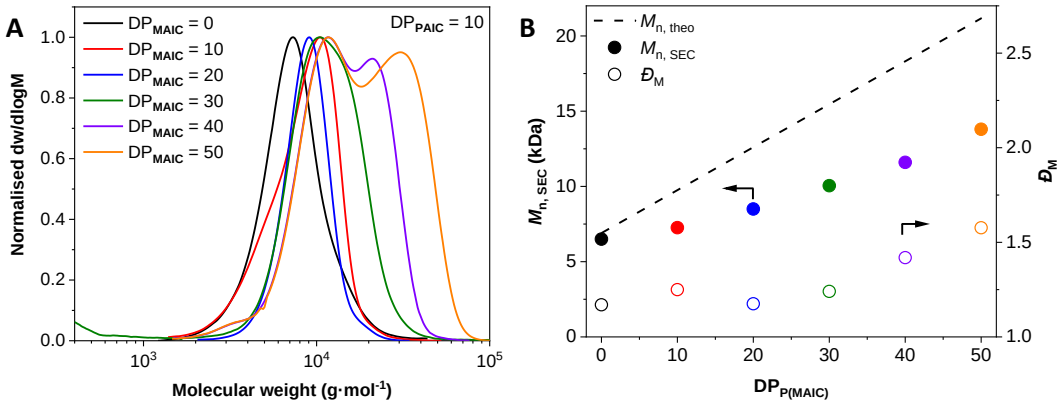

Figure 2.5. (A) Normalised SEC RI molecular weight distributions (THF + 2% v/v NEt_3, 40 °C, PS standards) of the chain extensions of macroinitiator $P(PAIC)_{10}$ with MAIC targeting different $DP_{P(MAIC)}$. (B) Evolution of $M_{n,\,SEC}$ (filled circle) and $Đ_M$ (hollow circle) values measured by SEC as a function of targeted $DP_{P(MAIC)}$. The $M_{n,\,theo}$ (dashed line) calculated from the monomer molecular weight and feed ratio is displayed as reference

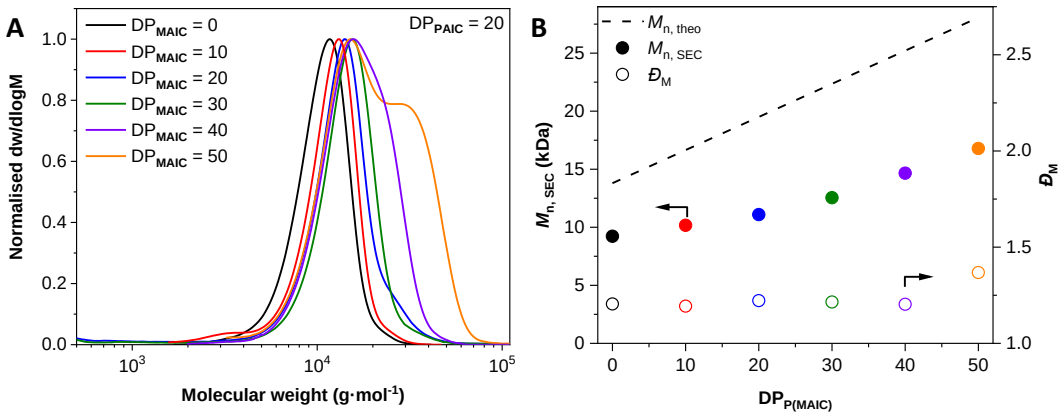

Figure 2.6. (A) Normalised SEC RI molecular weight distributions (THF + 2% v/v NEt_3, 40 °C, PS standards) of the chain extensions of macroinitiator $P(PAIC)_{20}$ with MAIC targeting different $DP_{P(MAIC)}$. (B) Evolution of $M_{n,\,SEC}$ (filled circle) and $Đ_M$ (hollow circle) values measured by SEC as a function of targeted $DP_{P(MAIC)}$. The $M_{n,\,theo}$ (dashed line) calculated from the monomer molecular weight and feed ratio is displayed as reference

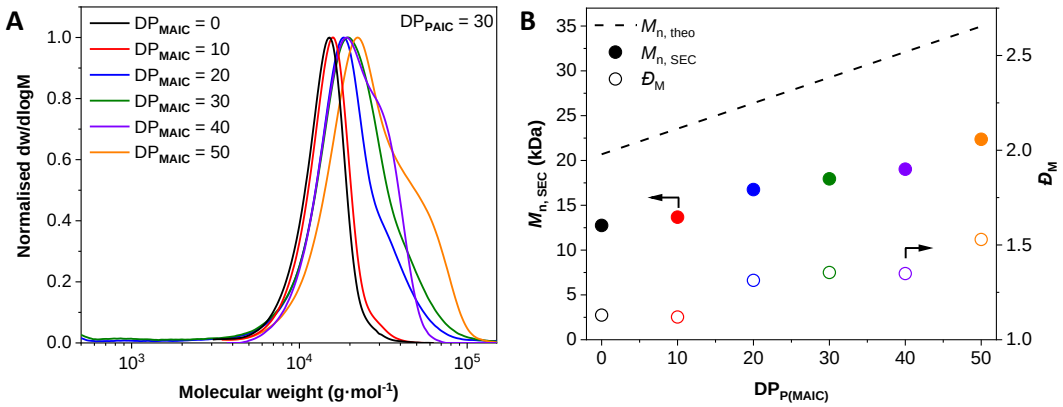

Figure 2.7. (A) Normalised SEC RI molecular weight distributions (THF + 2% v/v NEt_3, 40 °C, PS standards) for chain extensions of macroinitiator $P(PAIC)_{30}$ with MAIC targeting different $DP_{P(MAIC)}$. (B) Evolution of $M_{n,\,SEC}$ (filled circle) and $Đ_M$ (hollow circle) values measured by SEC as a function of targeted $DP_{P(MAIC)}$. The $M_{n,\,theo}$ (dashed line) calculated from the monomer molecular weight and feed ratio is displayed as reference

In PISA, the solids content can have a dramatic impact on the nanostructures produced by the self-assembly reaction.[62] When the solids contents is increased, the nano-objects can progress to higher morphologies (*i.e.* spherical micelles to worm-like micelles or worm-like micelles to vesicles). NiCCo-PISA of $P(PAIC)_{20}$-*b*-$P(MAIC)_{30}$ was conducted with 0.5, 1, 3.5, 5 and 10 wt% to assess the influence of the solids content on the resulting nano-objects. This solids contents screening showed no change in the resulting spherical morphologies by DLS over the studied range (Table 2.2; all the size distributions are found in the Appendix: Figure A2.21). Since there was no apparent influence of concentration on the size distribution, the concentration was held constant at 5 wt% throughout the study and the block length was varied (Figure 2.8).

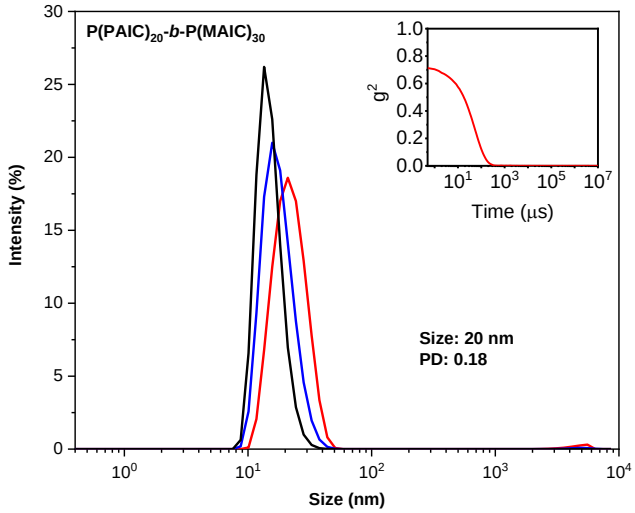

Figure 2.8. Intensity-weighted size distributions of NiCCo-PISA mixture conducted at 5 wt% of P(PAIC)$_{20}$-*b*-P(MAIC)$_{30}$ in DMSO obtained by DLS. The intensity (red line), volume (blue line) and number (black line) distributions are displayed *Inset:* Correlogram.

Table 2.2. DLS characterisation of the NiCCo-PISA mixture of P(PAIC)$_{20}$-*b*-P(MAIC)$_{30}$ in DMSO conducted at different solids contents

Solids contents (%)	Size (nm)
0.5	26 (0.16)
1	20 (0.18)
3.5	27 (0.19)
5	20 (0.18)
10	25 (0.35)

To determine whether the diblock copolymers obtained from NiCCo-PISA exhibited helicity, P(PAIC)$_x$-*b*-P(MAIC)$_y$ copolymers of different block ratios were analysed by CD spectroscopy after dissolution in a good solvent for both blocks, namely THF, to circumvent the possible interferences emerging from light-scattering by the nano-objects (example with the $DP_{P(PAIC)} = 20$ series Figure 2.9; all the series are in the Appendix: Figure A2.22 to Figure A2.24). While the P(PAIC) homopolymers did not display any signal, the diblock copolymers showed a clear signal at $\lambda = 360$ nm, consistent

with previous literature reports.[89-91] By comparing the change in the intensity of this signal for the different solvophobic block lengths, a linear increase of signal response with the $DP_{P(MAIC)}$ was observed, which confirmed the helical nature of the nanostructures' core for all the DPs and ratios studied (Table 2.3). Importantly, as a consequence of the static nature of the helix, the CD spectrum of the copolymer unimers dissolved in THF was expected to be similar to that of the nanoparticles in DMSO. The slope of the CD *vs* $DP_{P(MAIC)}$ plot became more gradual as the PAIC content was increased, concurrent with the increased content of opposite screw-sense helices present in the P(PAIC) block (Figure 2.10).

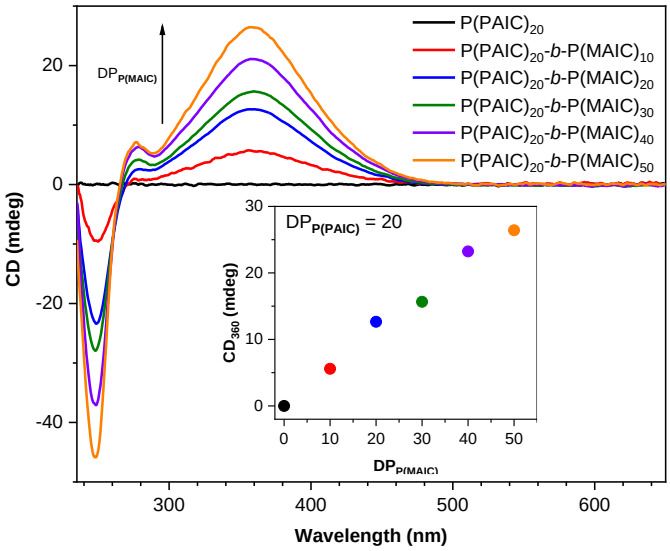

Figure 2.9. CD (THF, 0.5 mg·mL^{-1}) spectra of PAIC monomer and P(PAIC)$_{10}$-*b*-P(MAIC)$_x$ copolymers (x = 0, 10, 20, 30, 40, 50). *Inset*: CD signal at λ = 360 nm plotted *vs* $DP_{P(MAIC)}$.

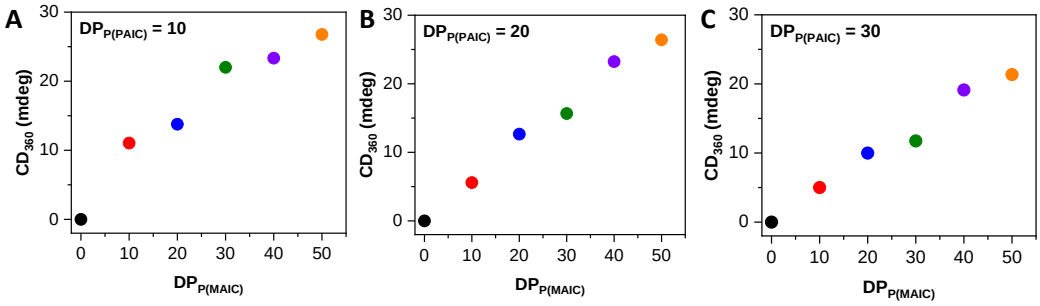

Figure 2.10. CD signal at $\lambda = 360$ nm plotted *vs* $DP_{P(MAIC)}$ for $P(PAIC)_x$-*b*-$P(MAIC)_y$ copolymers with $DP_{P(PAIC)}$ = (A) 10, (B) 20 and (C) 30 and $DP_{P(MAIC)}$ = 0, 10, 20, 30, 40, 50. The different colours correspond to the $DP_{P(MAIC)}$ = 0 (black), 10 (red), 20 (blue), 30 (green), 40 (purple), 50 (orange).

Table 2.3. Characterisation of synthesised P(PAIC)$_x$-*b*-P(MAIC)$_y$ diblock copolymers.

Sample[a]	$M_{n,\,theo}$ (kDa)[b]	$M_{n,\,SEC}$ (kDa)[c]	$Đ_M$[c]	CD_{360}[d] (mdeg)
P(PAIC)$_{10}$	6.9	6.5	1.24	0
P(PAIC)$_{10}$-*b*-P(MAIC)$_{10}$	9.8	7.3	1.25	11
P(PAIC)$_{10}$-*b*-P(MAIC)$_{20}$	12.6	8.5	1.17	14
P(PAIC)$_{10}$-*b*-P(MAIC)$_{30}$	15.5	10.1	1.25	22
P(PAIC)$_{10}$-*b*-P(MAIC)$_{40}$	18.3	11.6	1.42	23
P(PAIC)$_{10}$-*b*-P(MAIC)$_{50}$	21.1	13.8	1.58	27
P(PAIC)$_{20}$	13.8	9.2	1.20	0
P(PAIC)$_{20}$-*b*-P(MAIC)$_{10}$	16.7	10.2	1.19	6
P(PAIC)$_{20}$-*b*-P(MAIC)$_{20}$	19.5	11.1	1.22	13
P(PAIC)$_{20}$-*b*-P(MAIC)$_{30}$	22.4	12.5	1.21	16
P(PAIC)$_{20}$-*b*-P(MAIC)$_{40}$	25.2	14.7	1.20	23
P(PAIC)$_{20}$-*b*-P(MAIC)$_{50}$	28.1	16.8	1.37	26
P(PAIC)$_{30}$	20.7	12.8	1.13	0
P(PAIC)$_{30}$-*b*-P(MAIC)$_{10}$	23.6	15.7	1.28	5
P(PAIC)$_{30}$-*b*-P(MAIC)$_{20}$	26.4	16.8	1.31	10
P(PAIC)$_{30}$-*b*-P(MAIC)$_{30}$	29.3	18.0	1.35	12
P(PAIC)$_{30}$-*b*-P(MAIC)$_{40}$	32.1	18.4	1.45	19
P(PAIC)$_{30}$-*b*-P(MAIC)$_{50}$	35.0	18.5	1.53	21
P(MAIC)$_{50}$	14.3	7.1	1.16	38

[a]All conversions were >99%, as determined by ^{1}H NMR spectroscopy in $CDCl_3$. [b]Calculated from conversion using the monomer's MW and feed ratio: $M_{n,\,theo}$ = MW × [M]/[I]. [c]Determined by SEC (THF + 2% v/v NEt_3, 40 °C, PS standards). [d]CD signal at λ = 360 nm.

2.4. Nickel-catalysed coordination polymerisation-induced self-assembly of helical poly(arylisocyanide)s

As a consequence of the insolubility of P(MAIC) in DMSO, chain-extension of a P(PAIC) macroinitiator with MAIC led to the formation of self-assembled nanostructures. Dynamic light scattering (DLS) was used to measure the size (or hydrodynamic diameter, D_h) of the nano-objects in the various block copolymer solutions targeting different DPs (the size distributions can be found in the Appendix, Table 2.4). For the P(PAIC)$_x$-*b*-P(MAIC)$_{20}$ series, single populations of nano-objects were observed, with sizes ranging from 16 to 25 nm which depended on $DP_{P(PAIC)}$. As the targeted $DP_{P(MAIC)}$ was increased, multiple nano-object populations were detected, consistent with the evolution of mixed morphologies that contains both spherical and worm-like micelles. At high $DP_{P(MAIC)}$, primarily mixed morphologies were obtained with the exception of P(PAIC)$_{10}$-*b*-P(MAIC)$_{50}$, which exhibited a single population of particles with D_h = 630 nm.

Transmission electron microscopy (TEM) was employed to determine the obtained morphologies. To prepare TEM samples, the crude NiCCo-PISA reaction mixtures were diluted in DMSO to 0.1-0.02 mg·mL^{-1} and deposited onto graphene oxide-coated (GO) copper grids prior to staining and imaging. Spheres, worm-like micelles and polymersomes were achieved. In brief, the $DP_{P(MAIC)}$ = 20 series consisted of spherical micelles with D_{TEM} = 18, 17, and 21 nm for P(PAIC)$_{10}$-*b*-(PMAIC)$_{20}$, P(PAIC)$_{20}$-*b*-(PMAIC)$_{20}$, and P(PAIC)$_{30}$-*b*-(PMAIC)$_{20}$, respectively, in good agreement with the data obtained from DLS (Table 2.4, TEM images for each diblock copolymer can be found in the Appendix: Figure A2.25 to Figure A2.36). Mixed morphologies that contained both spherical and worm-like micelles occupied an

intermediate DP range in the phase space. For the P(PAIC)$_{10}$-*b*-P(MAIC)$_{40}$ sample, a pure phase of worm-like micelles was apparent in the TEM images. Upon further increasing the $DP_{P(MAIC)}$ to 50, polymersomes were obtained with D_{TEM} = 490 nm. The observed difference in diameter between DLS and TEM analysis is most possibly attributed to drying effects during the sample preparation process prior to TEM imaging that would induce shrinkage of the particle. When taken as a whole, the morphology for the different pairs of $DP_{P(PAIC)}$ and $DP_{P(MAIC)}$, and their transitions from one phase to another were combined to form a full phase diagram (Figure 2.11). Overall, decreasing the length of the P(PAIC) stabiliser block or increasing the length of the P(MAIC) core block resulted in the formation of higher-order morphologies such as worm-like micelles or polymersomes. Importantly, these higher-order morphologies were also demonstrated to retain their core helicity, which extended the breadth of possible nanostructures that can be synthesised in one step using a simple PISA methodology.

Table 2.4. Characterisation by DLS and TEM of the nanostructures obtained by NiCCo-PISA of P(PAIC)$_x$-*b*-P(MAIC)$_y$ diblock copolymers.

Sample	Morphologies	D_{DLS} (nm)[a]	D_{TEM} (nm)[b]
P(PAIC)$_{10}$-*b*-P(MAIC)$_{20}$	Spheres	18 (0.16)	18 ± 5
P(PAIC)$_{10}$-*b*-P(MAIC)$_{30}$	Spheres/worms	-[c]	17± 5[d]
P(PAIC)$_{10}$-*b*-P(MAIC)$_{40}$	Worms	-[e]	-[e]
P(PAIC)$_{10}$-*b*-P(MAIC)$_{50}$	Vesicles	630 (0.21)	490 ± 290
P(PAIC)$_{20}$-*b*-P(MAIC)$_{20}$	Spheres	16 (0.24)	17 ± 5
P(PAIC)$_{20}$-*b*-P(MAIC)$_{30}$	Spheres	20 (0.18)	21 ± 7
P(PAIC)$_{20}$-*b*-P(MAIC)$_{40}$	Spheres/worms	-[c]	24 ± 5[d]
P(PAIC)$_{20}$-*b*-P(MAIC)$_{50}$	Spheres/worms	-[c]	20 ± 5[d]
P(PAIC)$_{30}$-*b*-P(MAIC)$_{20}$	Spheres	25 (0.18)	14 ± 5
P(PAIC)$_{30}$-*b*-P(MAIC)$_{30}$	Spheres	26 (0.23)	20 ± 5
P(PAIC)$_{30}$-*b*-P(MAIC)$_{40}$	Spheres	42 (0.15)	54 ± 24
P(PAIC)$_{30}$-*b*-P(MAIC)$_{50}$	Spheres/worms	-[c]	26 ± 12[d]

[a]Spherical particles size measured by DLS with dispersity (PD) in parenthesis. [b]Spherical particles size calculated by TEM. [c]Mixed morphologies did not have one population by DLS. [d]Size of the spherical particles in the spheres/worms mixed phase. [e]No spherical particles present.

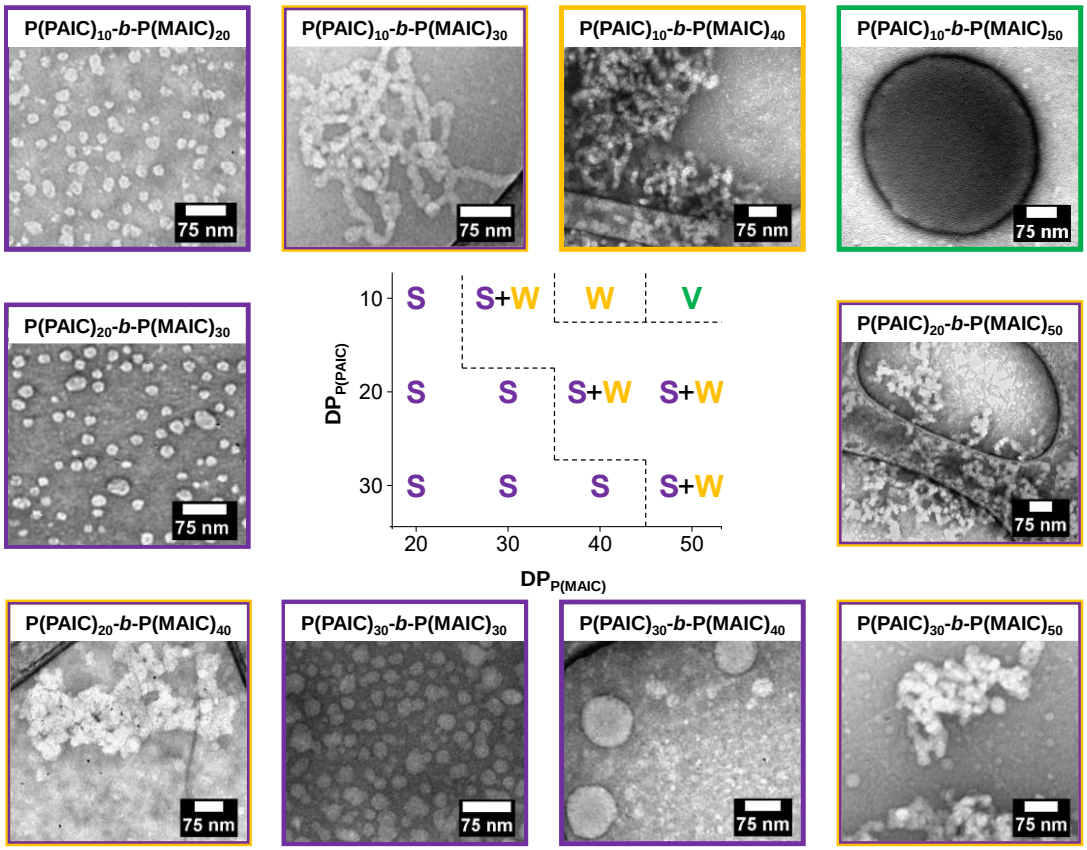

Figure 2.11. Phase diagram for $P(PAIC)_x$-*b*-$P(MAIC)_y$ diblock copolymer nano-objects prepared *via* NiCCo-PISA (5 wt% solids content) by varying the $DP_{P(PAIC)}$ and $DP_{P(MAIC)}$, along with representative dry-state TEM images of different formulations.

The polymersome morphology was not apparent given the previous analysis (DLS and TEM). DLS does not discriminate between spherical morphologies and no clear membrane was visible by TEM. Therefore, multi-angle DLS and static light scattering (SLS) were employed to help define the actual morphology of the $P(PAIC)_{10}$-*b*-$P(MAIC)_{50}$ nanoparticles. A goniometer was used which allowed the measurement of DLS and SLS data at different angles. The DLS data gave the apparent hydrodynamic radius (R_h) of the particles while the SLS data yielded the gyration radius (R_g) and their ratio (R_g/R_h) provides information on the morphology of the analysed nano-objects. If the ratio is 0.78, the particles are full micelles with the mass homogeneously distributed while a value of 1 indicates a hollow sphere with all the mass in the outer shell (*i.e.* vesicle, polymersome).[92] The light scattering experiments were

conducted at 0.1, 0.3, 0.5, 0.75 and 1 mg·mL^{-1} in DMSO to account for concentration effects. For the multi-angle DLS, the mean translational diffusion coefficient (D) was calculated from the relaxation times at each angle, $\tau(\vartheta, c)$ determined from the autocorrelation functions at each angle (ϑ, c) by the REPES algorithm as described by Jakeš.[93] The Stokes-Einstein equation was used to determine the R_h of the particles (Equation 2.1). The calculated R_h was 290±26 nm which gave a diameter of 580 nm consistent with the size measured with the fixed angle DLS at 630 nm.

$$R_h = \frac{k_B T}{6\pi\eta D} \qquad 2.1$$

For the multi-angle SLS, following Andersson *et al.*[94], a Zimm plot was constructed using the Debye method (Equation 2.2 and Equation 2.3) to determine the R_g of the nanoparticles. To do this, the R_ϑ/Kc *versus* q^2 data were plotted and a third order polynomial model was used to extrapolate $q \to 0$. The fit's intercept provided the molecular weight according to light scattering (M_{LS}) while the slope at $q^2 = 0$ can be utilised to retrieve R_g at the different concentrations. A first order model was employed for the $c \to 0$ extrapolation (Figure 2.12) which yielded R_g and M_{LS}

$$\frac{R_\theta}{Kc} = -\frac{M{R_g}^2}{3}q^2 + M \qquad 2.2$$

$$\frac{\partial\, R_\theta/Kc}{\partial q^2} = -\frac{M{R_g}^2}{3} \qquad 2.3$$

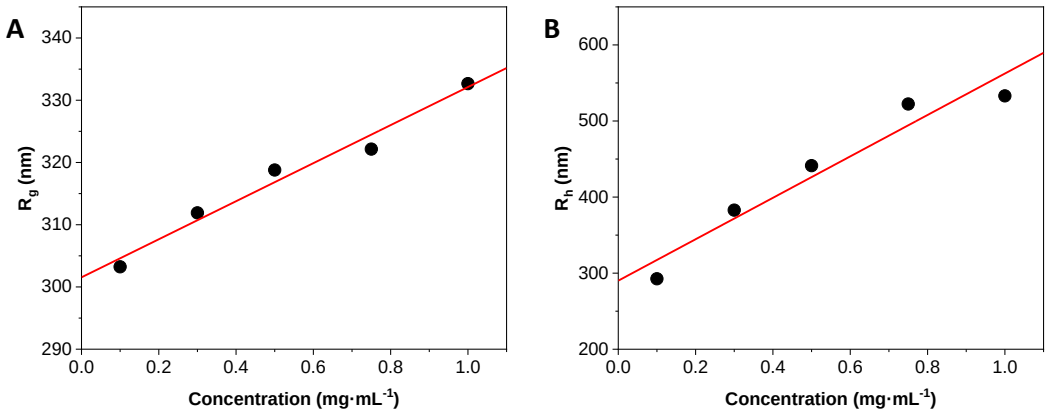

Figure 2.12. (A) Multi-angle SLS with R_g as a function of concentration and its linear regression where the intercept is R_g at $\rightarrow 0$. (B) Multi-angle DLS with R_h as a function of concentration and its linear regression where the intercept is R_h at $c \rightarrow 0$.

For SLS calculations, refractive index increment (dn/dc) was necessary and was measured using a differential refractometer which gave 2.14±0.35 × 10^{-4} L·g^{-1}. The P(PAIC)$_{10}$-*b*-P(MAIC)$_{50}$ nanoparticles had a R_g of 302±2 nm, which gave a R_g/R_h ratio of 1.04±0.1 and the aggregation number ($M_{w,\,theo}/M_{LS}$) with a M_{LS} of 2.10 ± 0.10 × 10^5 kDa was calculated to be 3.68±0.29 × 10^3 which was in line with a vesicle morphology which confirmed the hollow sphere nature of the P(PAIC)$_{10}$-*b*-P(MAIC)$_{50}$ nanoparticles.[92] The radius values from the multi-angle measurement were consistent with the previous R_{DLS} (315 nm) and R_{TEM} (245 nm) analysis.

2.5. Chiral induction of circular dichroism absorption

In order to use our polymeric system in a biologically relevant environment, the spherical micelle samples were transferred into water by dialysis. An increase of the micelle diameter from 25 to 60 nm was observed by DLS following the dialysis step; however, no major change in size over $>$ 4 weeks indicated the particles were colloidally stable (Figure 2.13). To verify the morphology of the nano-objects after the transfer in water, dry-state TEM images were taken. This confirmed the spherical nature of the nanostructures and presented aggregates of the micelles that could be the reason of the large size distribution measured by DLS. Indeed, the size calculated from the nano-objects in the TEM images was 21 nm, more in line with the sizes found for the micelles in DMSO. The capability to obtain stable, helix-containing micelles in aqueous media expanded the window of potential applications, which prompted us to explore the possibility of inducing chirality in small molecules *via* encapsulation within the nanoparticle cores.

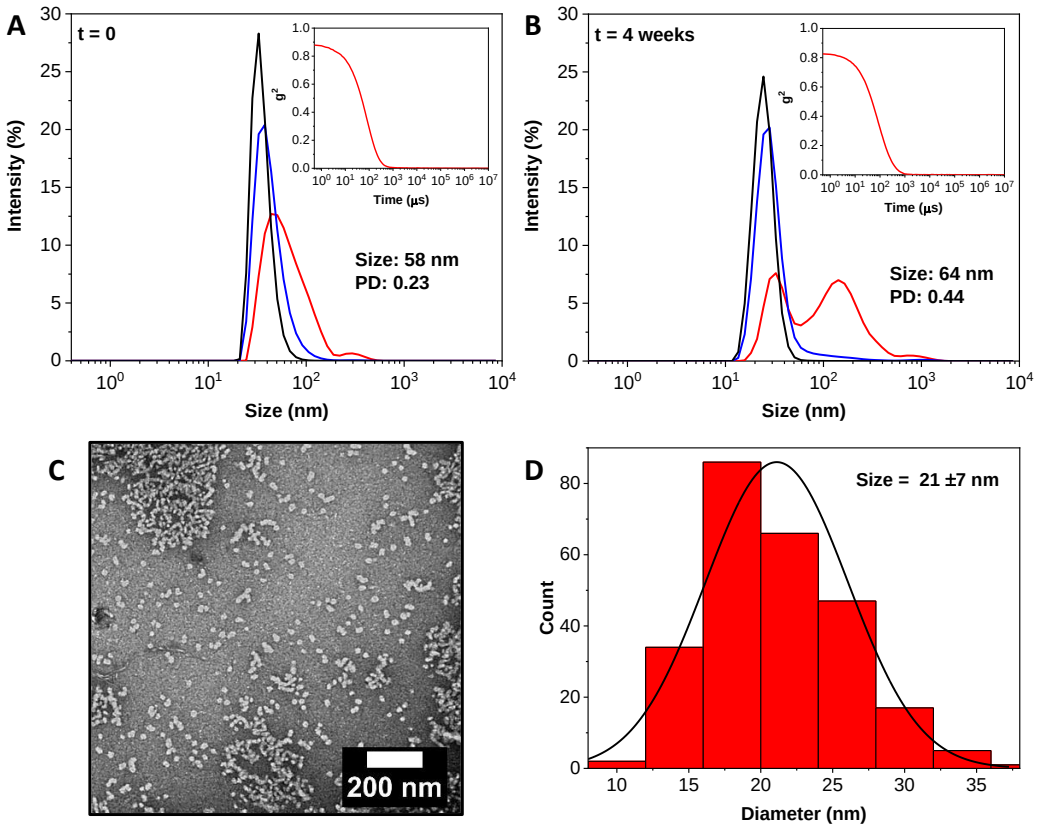

Figure 2.13. Intensity-weighted size distributions of P(PAIC)$_{20}$-*b*-P(MAIC)$_{30}$ in water obtained by DLS at (A) t = 0 and (B) after 4 weeks (right) that showed only little aggregation over time. *Inset:* DLS autocorrelation function. (C) Dry-state TEM images of sphere morphologies obtained from NiCCo-PISA of P(PAIC)$_{20}$-*b*-P(MAIC)$_{30}$ after transfer in water by dialysis which showed individual particles along with aggregates. (D) Histogram of spherical particles' size distribution measured from particle analysis of TEM images.

To assess the capability of the spherical micelles to encapsulate solvophobic species, NiCCo-PISA targeting P(PAIC)$_{20}$-*b*-P(MAIC)$_{30}$ was conducted in a solution that contained 1 wt % - relative to the polymer content - of the lipophilic dye Nile Red (NR). The dye was expected to be taken up into the solvophobic nanoparticle cores during the PISA process and the resulting dialysed solution to be fluorescent. After dialysis against water (4-6 kDa MWCO), the aqueous solution was centrifuged, and the supernatant was filtered to remove unencapsulated NR. The resulting solution retained fluorescence, and further analysis by spectrophotometry confirmed the presence of NR within the nanoparticles (Figure 2.14A). As a consequence of the dye's solvatochromic nature, a shift from the maximum emission of NR in water (λ

= 660 nm) to the encapsulated solution (λ = 635 nm) was observed, which proved the effective encapsulation of NR in the nanostructure cores, and the lack of a signal at λ = 660 nm confirmed the successful removal of unencapsulated NR (Figure 2.14B). Polarity of the solvents is known to be one of the parameters that dictates the shift in maximum emission in the solvatochromic effect. In order to employ NR as a kind of polarity probe, solutions of NR in solvents with different polarities were analysed by spectrophotometry (Figure 2.15A) which showed a visible shift in maximum emission from λ = 573 nm for toluene to λ = 662 nm for water, which indicated clearly the solvatochromic behaviour for NR: as the polarity increases, the maximum emission shifts to the longer wavelength. The maximum emission of the different solvents' solutions were compared to the solvent's relative polarity (Figure 2.15B) which demonstrated this shift of the maximum emission wavelength followed a linear law however, DMSO diverged from the trend. As was mentioned earlier, polarity is not the only parameter that plays a role in the solvatochromic effect. This comparison indicated that the interior of the NP was comparable to isopropyl alcohol (IPA).

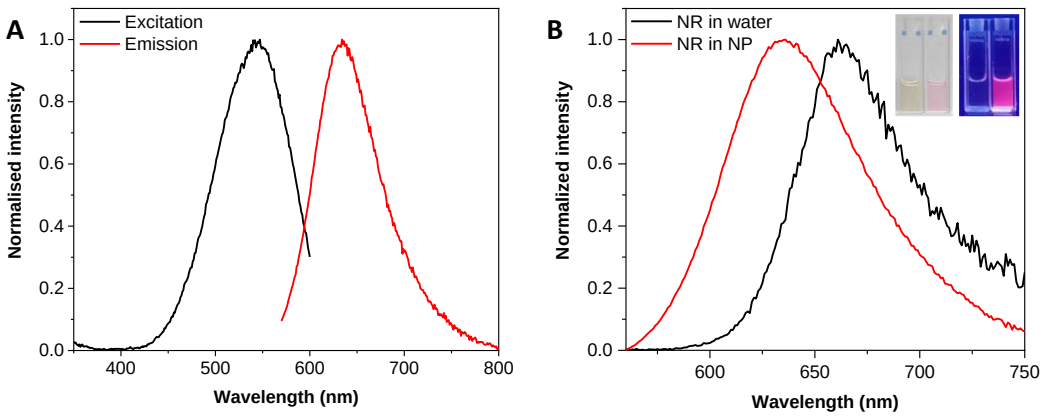

Figure 2.14. (A) Fluorescence spectra for the excitation (black line, λ_{ex} = 540 nm) and emission (red line, λ_{em} = 630 nm) of Nile Red in THF. (B) Fluorescence spectra (λ_{ex} = 540 nm) of Nile Red in water (black line) and encapsulated in NPs of P(PAIC)$_{20}$-*b*-P(MAIC)$_{30}$ (red line, 5 mg·mL^{-1}). *Inset:* aqueous solution of NPs (yellow solution) and NR encapsulated in NPs (purple solution) under ambient light (left) and UV light (right).

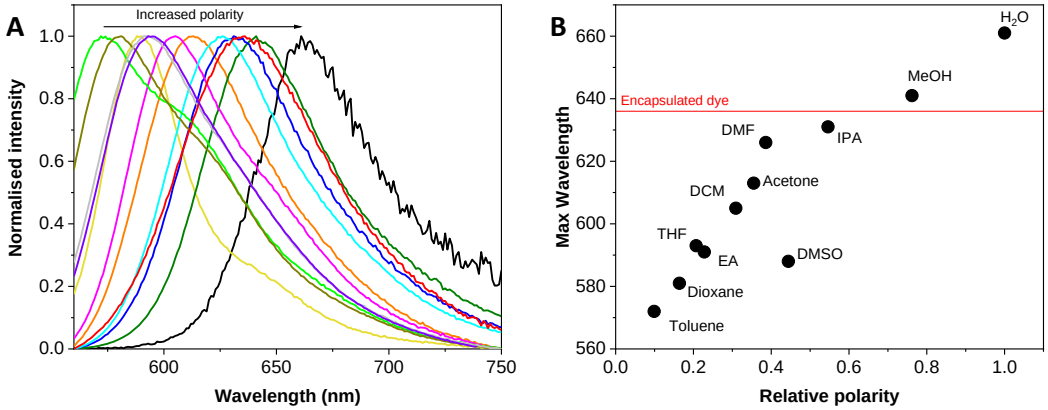

Figure 2.15. (A) Fluorescence spectra (λ_{ex} = 540 nm) of Nile Red in solvents with different polarity (from left to right): toluene, dioxane, DMSO, ethyl acetate, THF, DCM, Acetone, DMF, IPA, NPs in water MeOH and water. (B) Wavelength of the maximum emission *vs* the relative polarity of the solvents (water = 1).

This uptake experiment was repeated with different initial concentrations of NR (0.5, 2, 5, 10, and 15 wt %) to determine the maximum loading efficiency. Aliquots from each NiCCo-PISA were taken after purification and freeze-dried. The resulting residues were dissolved in THF and analysed by UV/Vis spectroscopy. To allow calculation of the quantity of each compound (copolymer and dye), calibration curves for Nile Red and P(PAIC)$_{20}$-*b*-P(MAIC)$_{30}$ diblock copolymer in solution were measured (Figure 2.16 and Figure 2.17) in THF. The UV/Vis spectra of the two species indicate that they each absorb at a different region (λ = 530 nm for Nile Red and λ = 360 nm for the diblock copolymer). The UV/Vis absorption (λ = 530 nm) for different concentrations of Nile red in THF (A_{530}), showed a linear relation (Equation 2.4) with the concentration of NR (c_{NR}) in accordance with the Beer-Lambert law. Therefore, the concentration of Nile Red can be deduced from the absorbance at λ = 530 nm:

$$c_{NR} = \frac{A_{530}}{120} \qquad 2.4$$

The same equation can be applied to the concentration of P(PAIC)$_{20}$-*b*-P(MAIC)$_{30}$ (c_P) and the absorption of the diblock copolymer at $\lambda = 360$ nm (A_{360}):

$$c_P = \frac{A_{360}}{4.07} \qquad 2.5$$

The content of NR and copolymer can be calculated from the UV/Vis spectrum of the NiCCo-PISA solution content and therefore, the concentration (wt%) of dye relative to the polymer and the encapsulation efficiency.

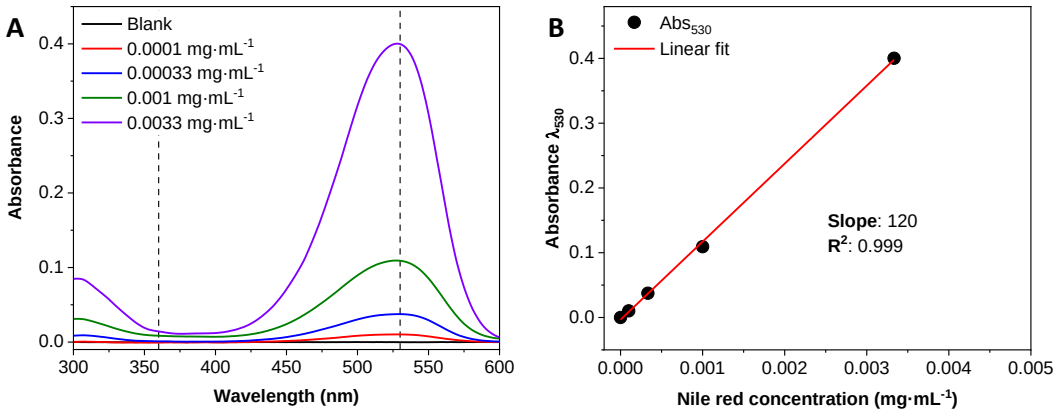

Figure 2.16. (A) UV/Vis spectra of different concentrations of Nile Red in THF. (B) Calibration curve for Nile Red in THF.

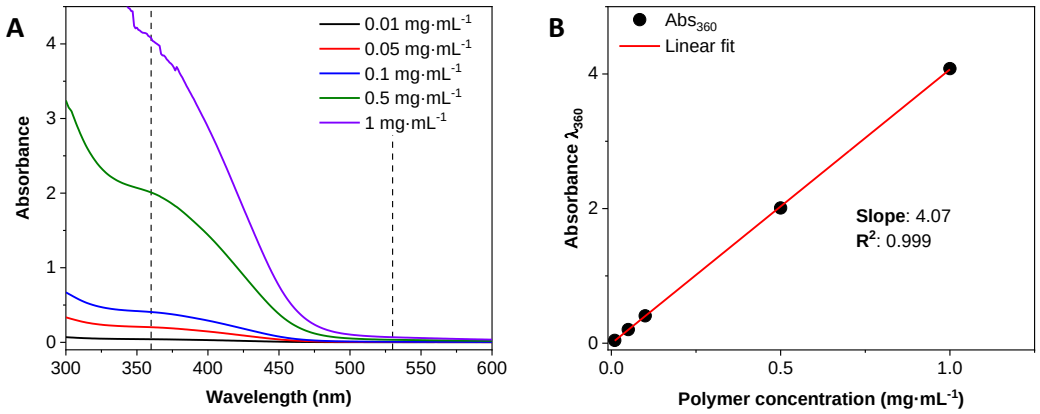

Figure 2.17. (A) UV/Vis spectra of different concentrations of P(PAIC)$_{20}$-*b*-P(MAIC)$_{30}$ in THF. (B) Calibration curve for P(PAIC)$_{20}$-*b*-P(MAIC)$_{30}$ in THF.

Using this formulation, the encapsulated NR and encapsulation efficiency were calculated for each initial concentration (Figure 2.18 and Table 2.5). When analysing the efficiency, this parameter decreased from 80% for 0.5 wt% of initial concentration to 8.5% for 15 wt% of initial NR. However, to calculate the actual quantity of NR encapsulated in the NPs, it was necessary to take into account both the initial concentration of NR and the encapsulation efficiency. The encapsulated dye increased from 0.46 wt% at 0.5 wt% of initial dye concentration until the dye quantity reached a maximum of 2.3 wt% encapsulated at 5 wt% of initial NR concentration which gave a maximum loading of 42%. After reaching this ceiling, the encapsulated NR decreased, which is normal behaviour for encapsulation at high concentration.

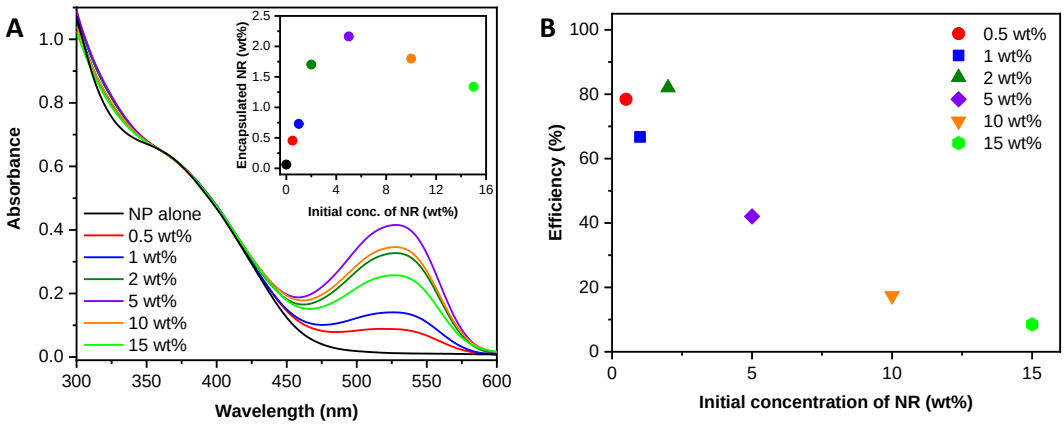

Figure 2.18. (A) UV/Vis (THF, 1 mg·mL^{-1}) spectra of the copolymer and encapsulated dye at different initial NR concentration; *Inset*: Concentration of encapsulated NR depending on the initial NR concentration. (B) Encapsulation efficiency of nile red into spherical nanoparticles of P(PAIC)$_{20}$-*b*-P(MAIC)$_{30}$.

Table 2.5. Encapsulation values and characterisation by CD spectroscopy of NR encapsulated in P(PAIC)$_{20}$-*b*-P(MAIC)$_{30}$ by NiCCo-PISA.

Initial conc. NR[a] (wt%)	Encapsulated NR (wt%)	Encapsulation efficiency (%)	CD_{360}	ΔCD_{360}
0	-	-	0.93	0
0.5	0.46	78	0.15	-0.78
1	0.73	67	-1.0	-2.0
2	1.7	82	-2.2	-3.1
5	2.2	42	-3.9	-4.8
10	2.0	17	-2.2	-3.1
15	1.3	8.5	-1.5	-2.4

[a]Solid content relative to the polymer content.

Achiral (*i.e.* CD-inactive) dyes confined within helical supramolecular assemblies have been shown to exhibit CD activity by chirality transfer from the helical environment.[85-88] The helical core of the P(PAIC)$_{20}$-*b*-P(MAIC)$_{30}$ spherical micelles was hypothesised to induce a similar effect on the encapsulated NR which would arise solely from its chiral-core environment without supramolecular helicity. To verify this hypothesis, the CD spectrum of the dye-loaded spherical micelles was measured and showed a signal between $\lambda = 450$ nm and $\lambda = 600$ nm with a maximum at $\lambda = 515$ nm which corresponded to NR (Figure 2.19A) and provided evidence that the chiral nanoparticle environment influenced the absorption of a dye that was otherwise CD-inactive. This chiral induction was shown to evolve linearly with the content of NR in the nano-objects, which demonstrated that the CD signal originated from the encapsulated dye (Figure 2.19B). The chiral-induction effect of the core's helical environment unveiled the potential of these nano-objects in applications such as chiral recognition and asymmetric catalysis.

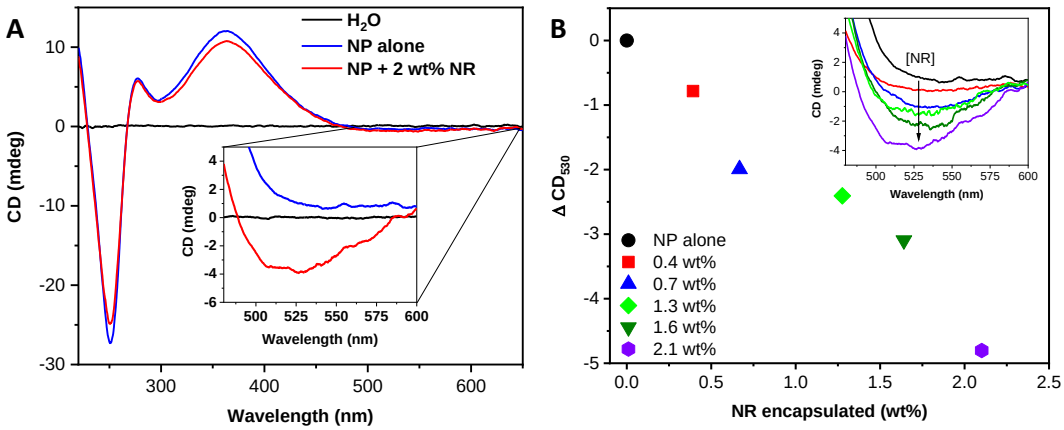

Figure 2.19. (A) CD (H_2O) absorption spectra of the nanoparticle (NP) (blue) and NR-loaded NP (red). Inset: Close-up on the NR absorption region at a higher concentration to allow detection of the signal. (B) Linear dependence of the CD response to the loading of NR in the NPs. Inset: CD (H_2O) absorption spectra of the NiCCo-PISA solutions with different NR loadings.

2.6. Conclusion

A new solvophilic aryl isocyanide monomer was developed: PAIC. Block copolymerisation of MAIC and PAIC was conducted successfully in DMSO that led to NiCCo-PISA which produced nanoparticles with helical blocks, and achieved nano-objects with common morphologies confirmed by TEM imaging – spheres, worm-like micelles and polymersomes– by varying the DP of the corona- or the core-forming blocks. This relation was presented as a phase diagram, which demonstrated that higher overall solvophobic content yielded higher-order morphologies. The size of the spherical morphologies was measured by DLS and the vesicle morphology was confirmed by multi angle SLS/DLS. Preservation of the helicity of the core polymer for all the morphologies during the self-assembly process was confirmed by CD. The P(PAIC)$_{20}$-*b*-P(MAIC)$_{30}$ spherical micelles were successfully transferred in water by dialysis and proved to aggregate during the purification step. However, the size distribution measured by DLS stayed stable over 4 weeks. Encapsulation of NR into the micelles was performed effectively with P(PAIC)$_{20}$-*b*-P(MAIC)$_{30}$ copolymer for a range of dye concentrations and after transfer into water the helical core was shown by CD spectroscopy to have a chiral-induction effect. Overall, the reported methodology and the resulting nano-objects could find applications in areas such as nanomedicine, chiral separation, and enantioselective catalysis.

2.7. Appendix

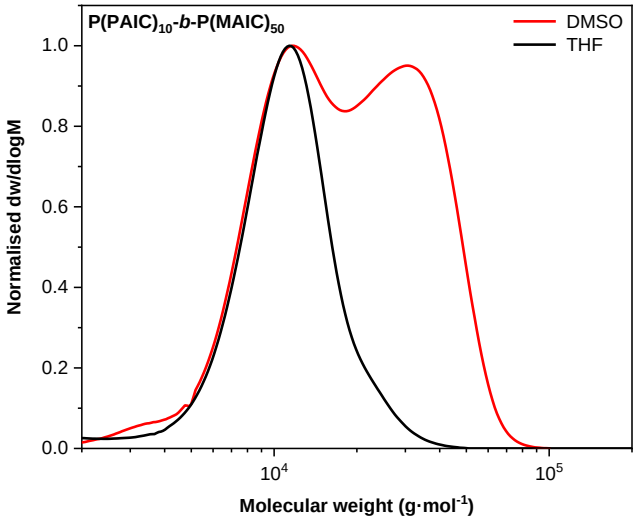

Figure A2.20. Normalised SEC RI molecular weight distributions (THF + 2% v/v NEt_3, 40 °C, PS standards) of $P(PAIC)_{10}$-*b*-$P(MAIC)_{50}$ synthesised in DMSO (red line) and THF (black line).

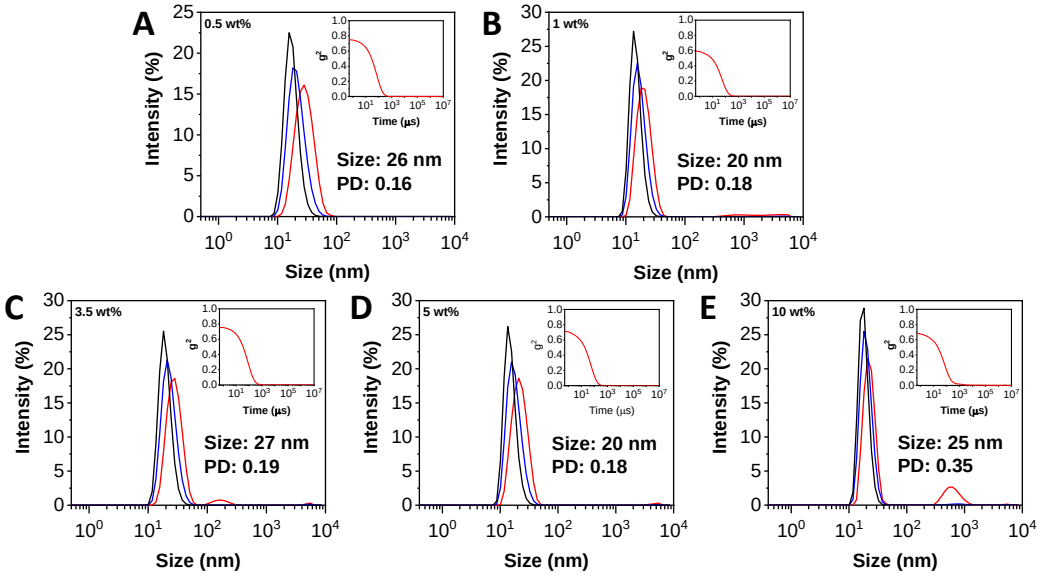

Figure A2.21. Intensity-weighted size distributions of NiCCo-PISA mixture of $P(PAIC)_{20}$-*b*-$P(MAIC)_{30}$ conducted solids weight content of (A) 0.5, (B) 1, (C) 3.5, (D) 5 and (E) 10 wt% in DMSO obtained by DLS. The intensity (red line), volume (blue line) and number (black line) distributions are displayed. The hydrodynamic diameters are given in nm along with the PD below.

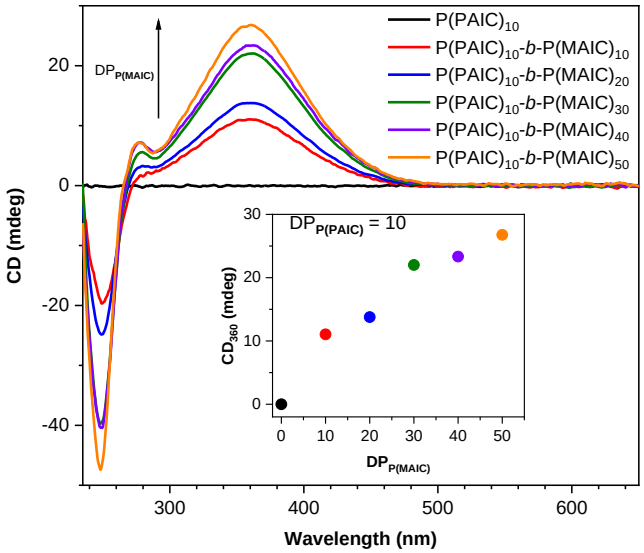

Figure A2.22. CD (THF, 0.5 mg·mL^{-1}) spectra of PAIC monomer and P(PAIC)$_{10}$-*b*-P(MAIC)$_x$ copolymers (x = 0, 10, 20, 30, 40, 50). *Inset*: CD signal at λ = 360 nm plotted *vs* DP$_{P(MAIC)}$.

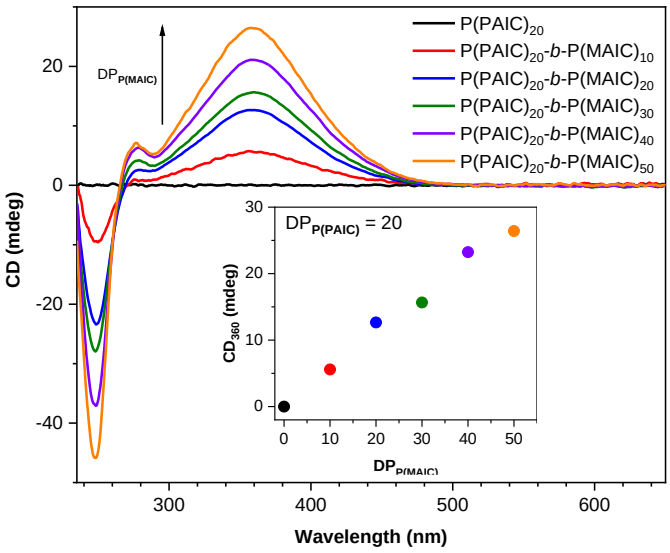

Figure A2.23. CD (THF, 0.5 mg·mL^{-1}) spectra of PAIC monomer and P(PAIC)$_{20}$-*b*-P(MAIC)$_x$ copolymers (x = 0, 10, 20, 30, 40, 50). *Inset*: CD signal at λ = 360 nm plotted *vs* DP$_{P(MAIC)}$.

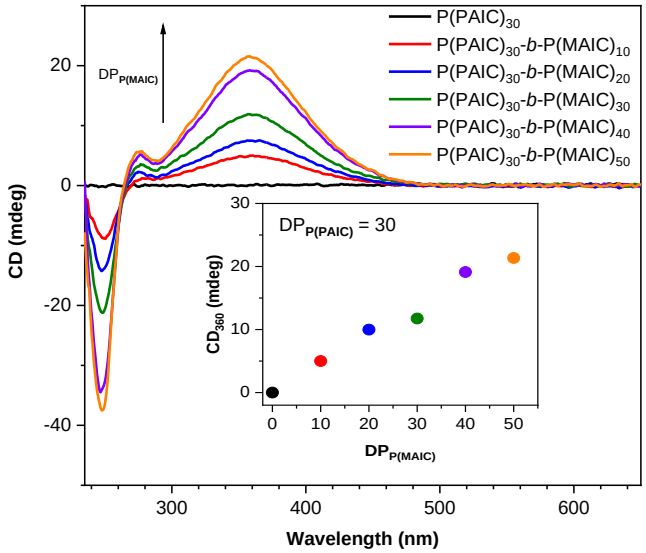

Figure A2.24. CD (THF, 0.5 mg·mL^{-1}) spectra of PAIC monomer and P(PAIC)$_{30}$-*b*-P(MAIC)$_x$ copolymers (x = 0, 10, 20, 30, 40, 50). *Inset*: CD signal at λ = 360 nm plotted *vs* DP$_{P(MAIC)}$.

2.7.1. TEM images of the NiCCo-PISA mixtures

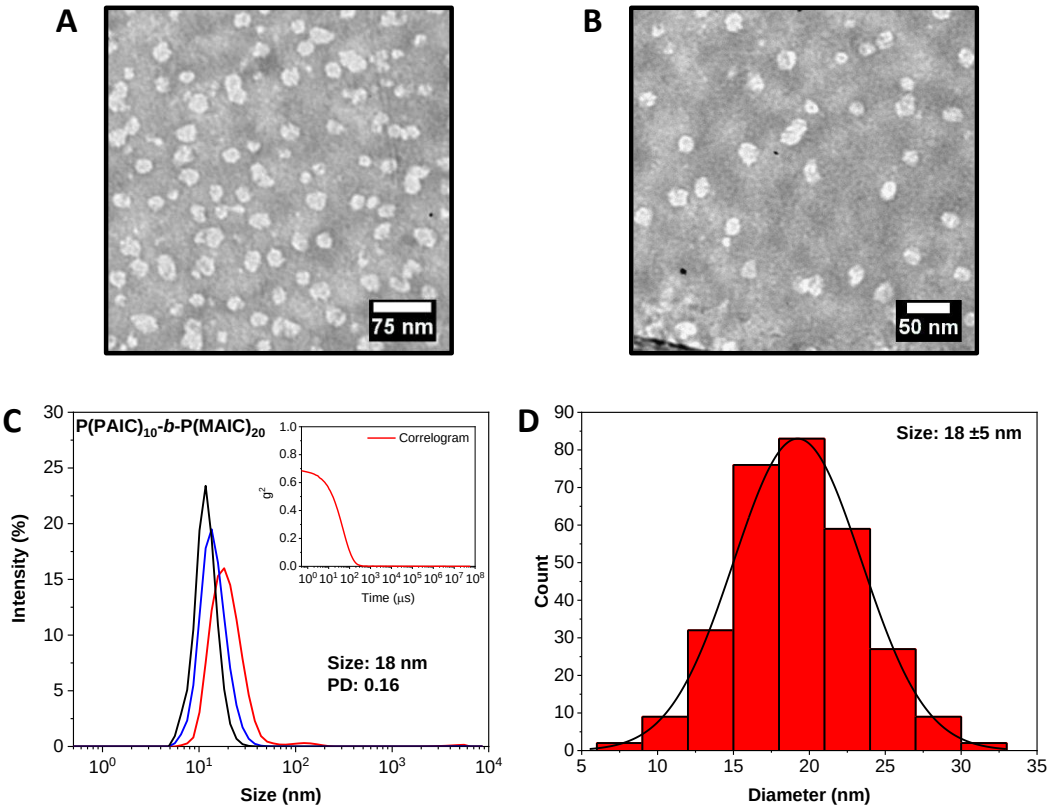

Figure A2.25. (A and B) Dry-state TEM images of the sphere morphology obtained from NiCCo-PISA of $P(PAIC)_{10}$-*b*-$P(MAIC)_{20}$. (C) Intensity-weighted size distributions of $P(PAIC)_{10}$-*b*-$P(MAIC)_{20}$ in DMSO obtained by DLS. *Inset:* DLS autocorrelation function. (D) Histogram of spherical particles' size distribution measured from particle analysis of TEM images.

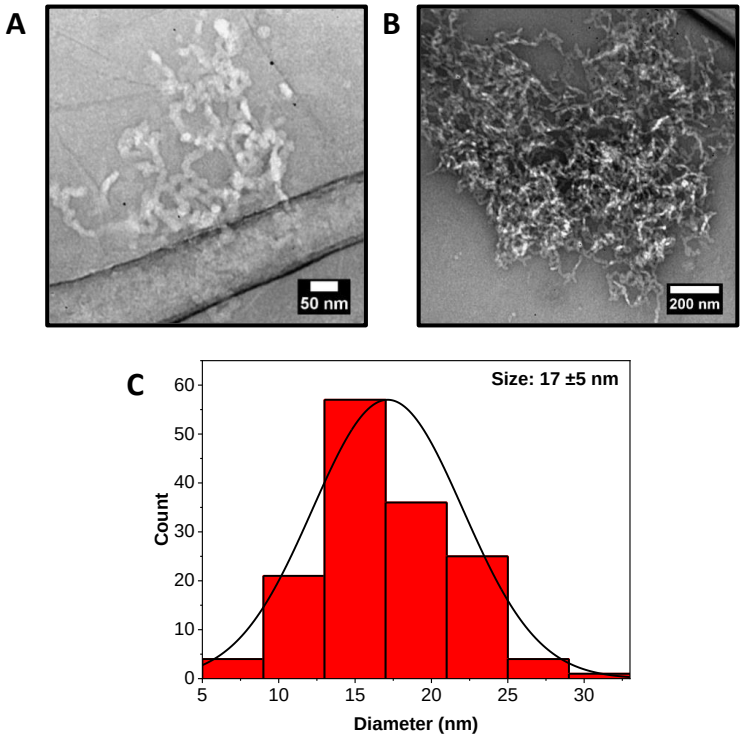

Figure A2.26. (A and B) Dry-state TEM images of the mixed sphere and worm morphologies obtained from NiCCo-PISA of P(PAIC)$_{10}$-*b*-P(MAIC)$_{30}$. (C) Histogram of spherical particles' size distribution measured from particle analysis of TEM images.

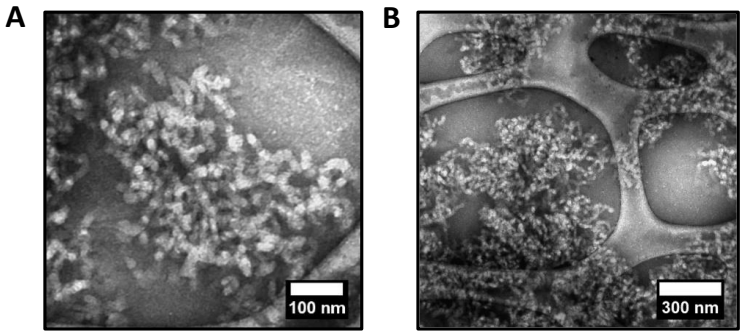

Figure A2.27. (A and B) Dry-state TEM images of the worm morphology obtained from NiCCo-PISA of P(PAIC)$_{10}$-*b*-P(MAIC)$_{40}$.

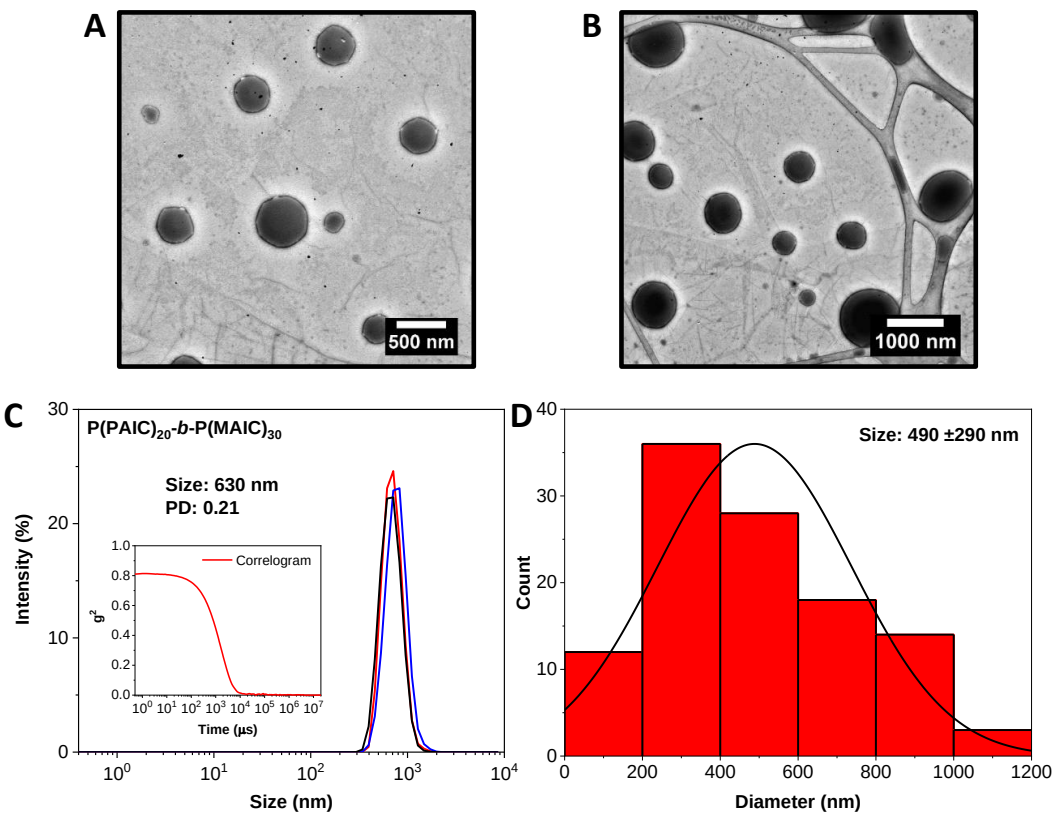

Figure A2.28. (A and B) Dry-state TEM images of the vesicle morphology obtained from NiCCo-PISA of P(PAIC)$_{10}$-*b*-P(MAIC)$_{50}$. (C) Intensity-weighted size distributions of P(PAIC)$_{10}$-*b*-P(MAIC)$_{50}$ in DMSO obtained by DLS. *Inset:* DLS autocorrelation function. (D) Histogram of spherical particles' size distribution measured from particle analysis of TEM images.

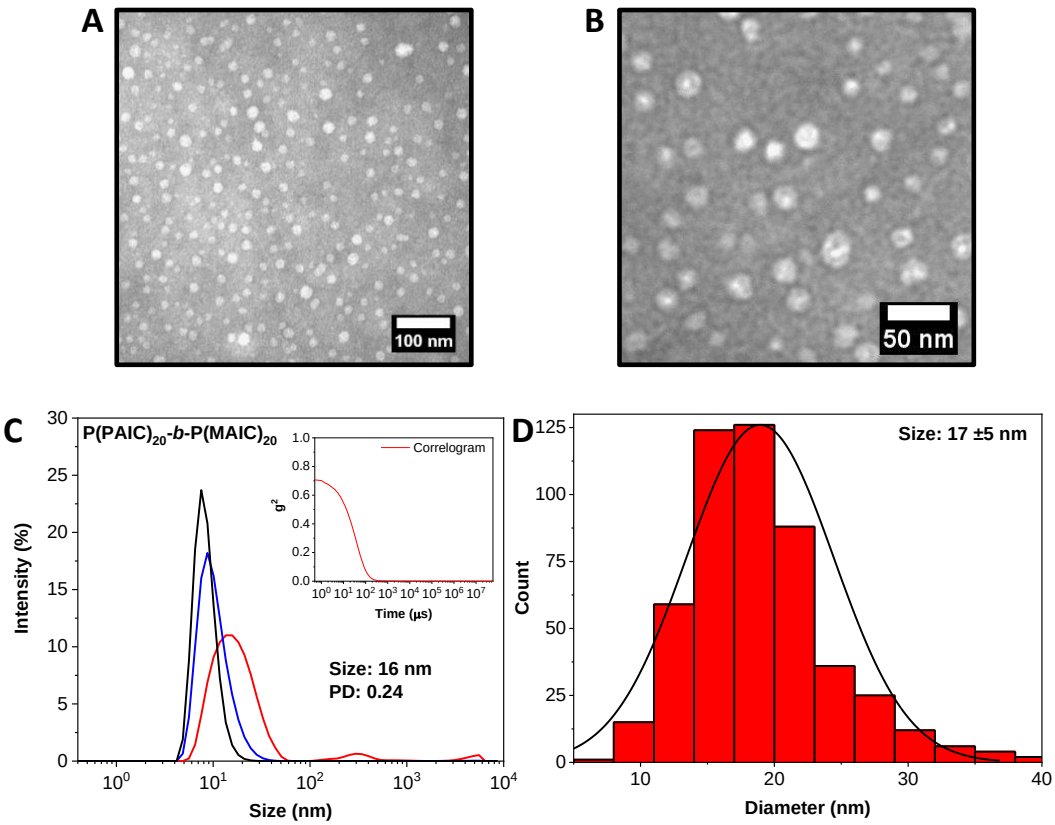

Figure A2.29. (A and B) Dry-state TEM images of the sphere morphology obtained from NiCCo-PISA of P(PAIC)$_{20}$-*b*-P(MAIC)$_{20}$. (C) Intensity-weighted size distributions of P(PAIC)$_{20}$-*b*-P(MAIC)$_{20}$ in DMSO obtained by DLS. *Inset:* DLS autocorrelation function. (D) Histogram of spherical particles' size distribution measured from particle analysis of TEM images.

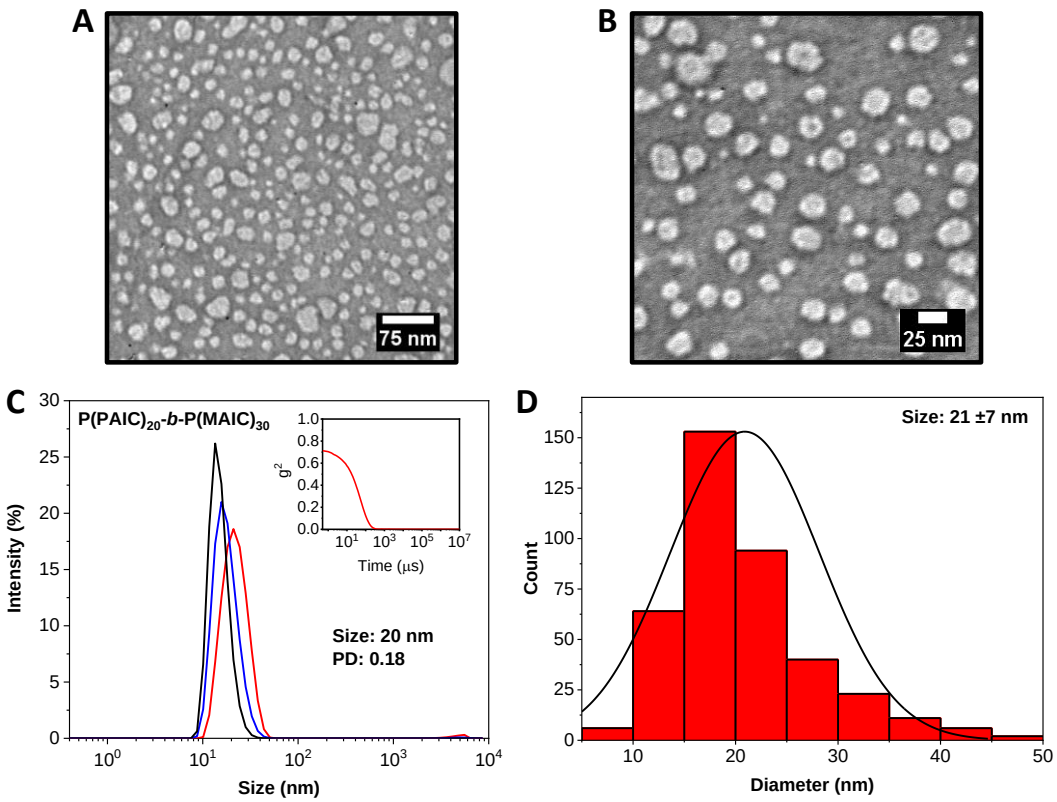

Figure A2.30. (A and B) Dry-state TEM images of the sphere morphology obtained from NiCCo-PISA of P(PAIC)$_{20}$-*b*-P(MAIC)$_{30}$. (C) Intensity-weighted size distributions of P(PAIC)$_{20}$-*b*-P(MAIC)$_{30}$ in DMSO obtained by DLS. *Inset:* DLS autocorrelation function. (D) Histogram of spherical particles' size distribution measured from particle analysis of TEM images.

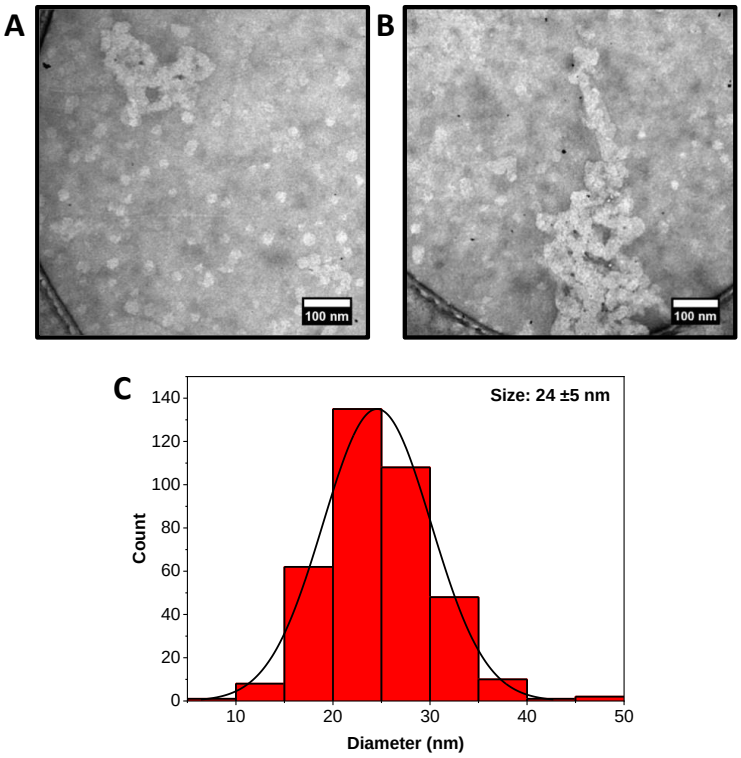

Figure A2.31. (A and B) Dry-state TEM images of the mixed sphere and worm morphologies obtained from NiCCo-PISA of P(PAIC)$_{20}$-*b*-P(MAIC)$_{40}$. (C) Histogram of spherical particles' size distribution measured from particle analysis of TEM images.

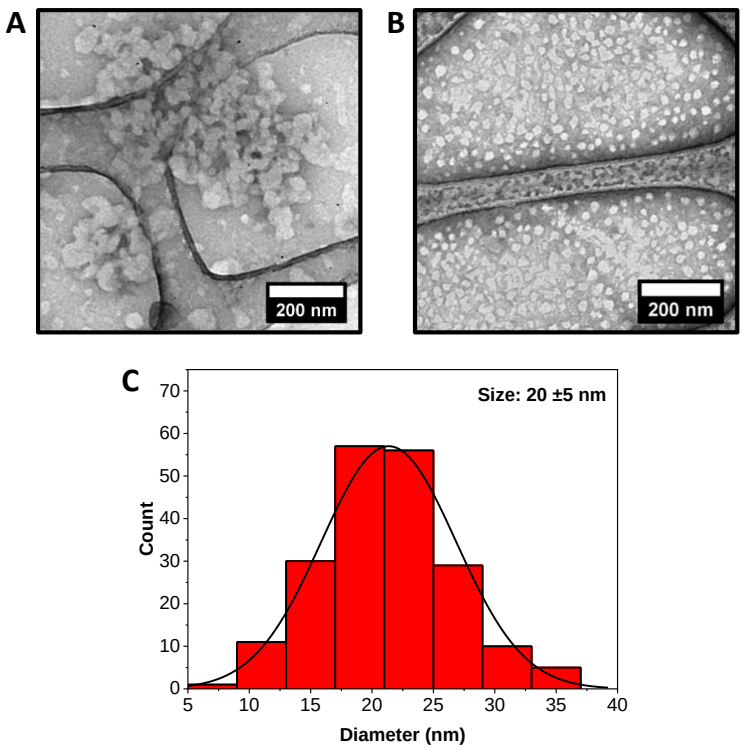

Figure A2.32. (A and B) Dry-state TEM images of the mixed sphere and worm morphologies obtained from NiCCo-PISA of P(PAIC)$_{20}$-*b*-P(MAIC)$_{50}$. (C) Histogram of spherical particles' size distribution measured from particle analysis of TEM images.

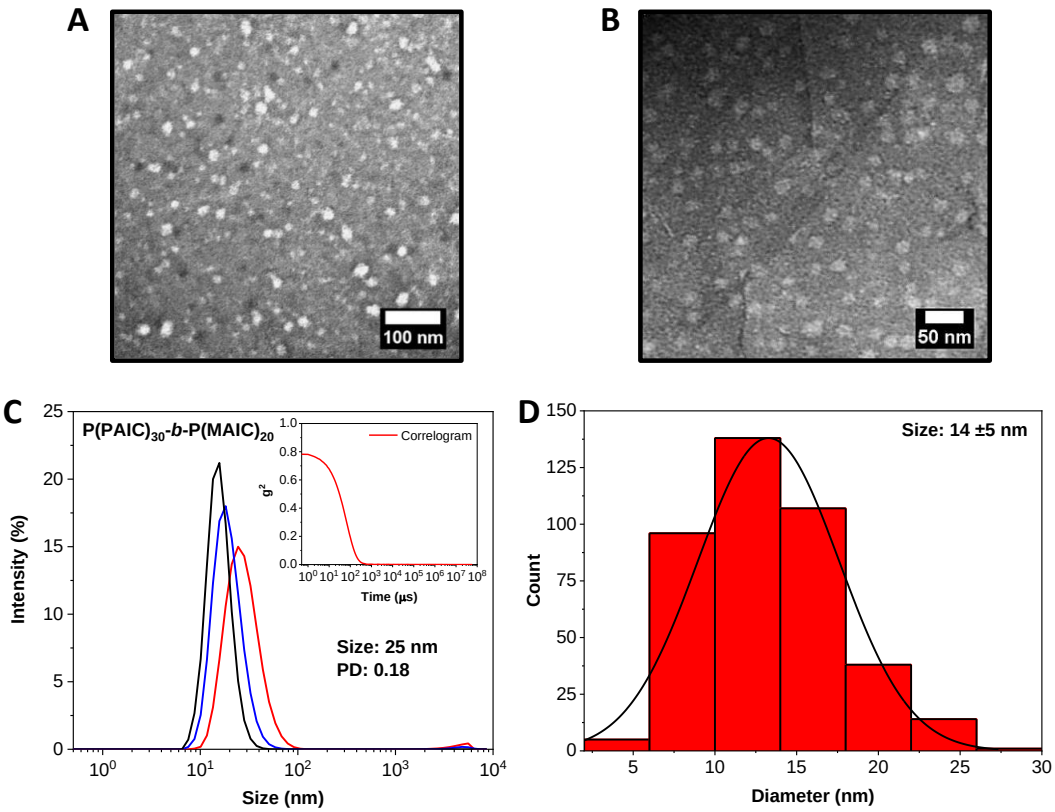

Figure A2.33. (A and B) Dry-state TEM images of the sphere morphology obtained from NiCCo-PISA of P(PAIC)$_{30}$-*b*-P(MAIC)$_{20}$. (C) Intensity-weighted size distributions of P(PAIC)$_{30}$-*b*-P(MAIC)$_{20}$ in DMSO obtained by DLS. *Inset:* DLS autocorrelation function. (D) Histogram of spherical particles' size distribution measured from particle analysis of TEM images.

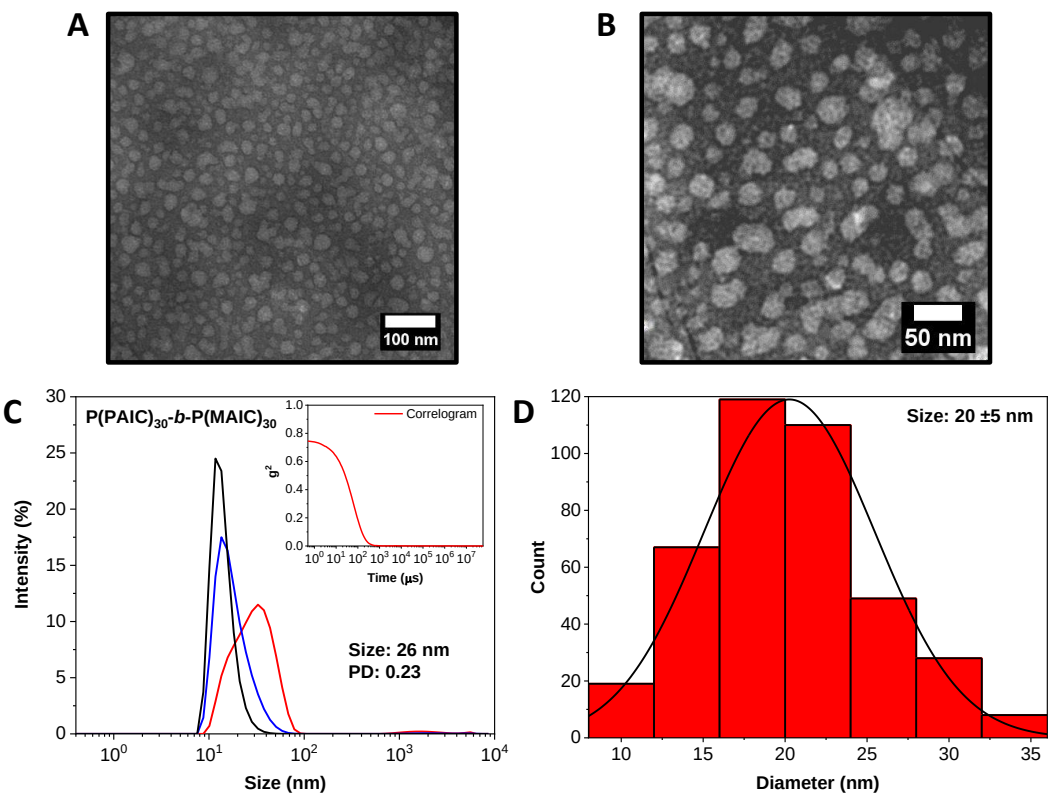

Figure A2.34. (A and B) Dry-state TEM images of the sphere morphology obtained from NiCCo-PISA of P(PAIC)$_{30}$-*b*-P(MAIC)$_{30}$. (C) Intensity-weighted size distributions of P(PAIC)$_{30}$-*b*-P(MAIC)$_{30}$ in DMSO obtained by DLS. *Inset:* DLS autocorrelation function. (D) Histogram of spherical particles' size distribution measured from particle analysis of TEM images.

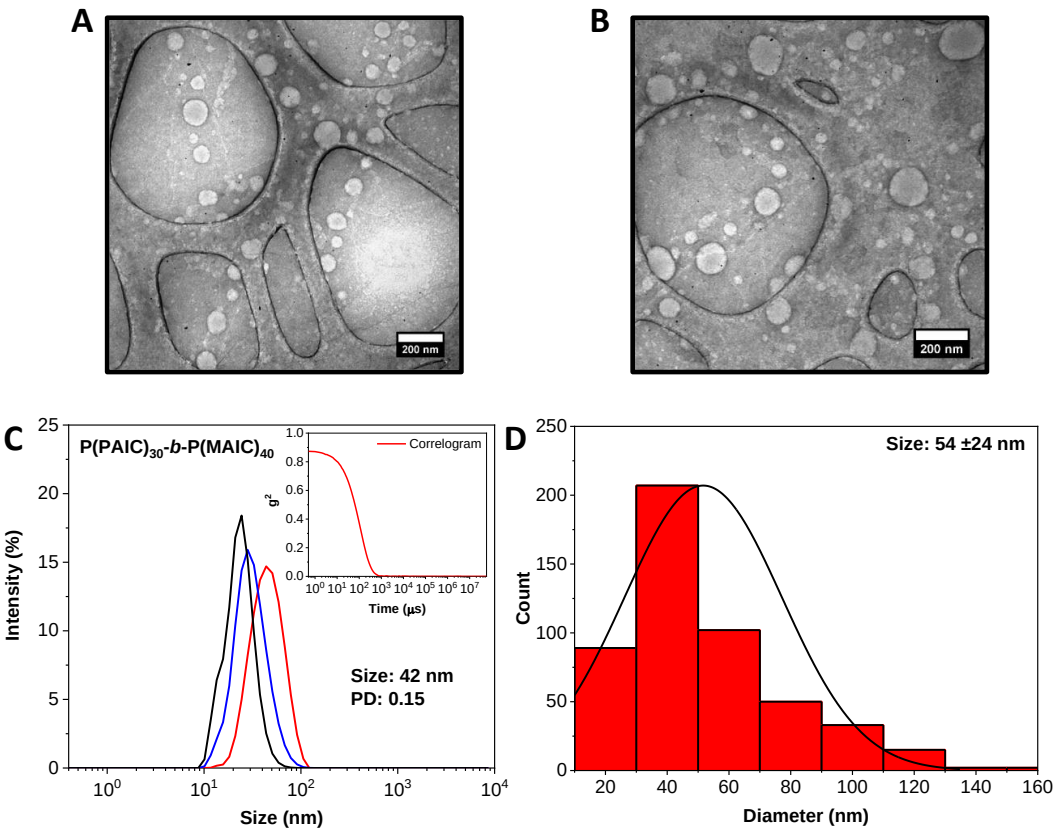

Figure A2.35. (A and B) Dry-state TEM images of the sphere morphology obtained from NiCCo-PISA of P(PAIC)$_{30}$-*b*-P(MAIC)$_{40}$. (C) Intensity-weighted size distributions of P(PAIC)$_{30}$-*b*-P(MAIC)$_{40}$ in DMSO obtained by DLS. *Inset:* DLS autocorrelation function. (D) Histogram of spherical particles' size distribution measured from particle analysis of TEM images.

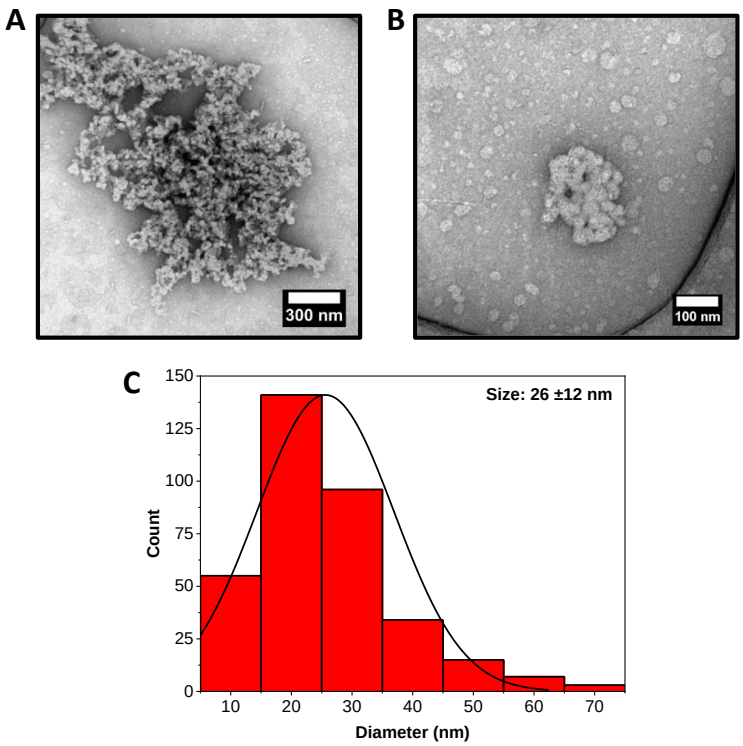

Figure A2.36. (A and B) Dry-state TEM images of the mixed sphere and worm morphologies obtained from NiCCo-PISA of P(PAIC)$_{30}$-*b*-P(MAIC)$_{50}$. (D) Histogram of spherical particles' size distribution measured from particle analysis of TEM images.

2.8. References

1. Pelley, J. W., 3 - Protein Structure and Function. In *Elsevier's Integrated Biochemistry*, Pelley, J. W., Ed. Mosby: Philadelphia, 2007; pp 19-28.
2. Pavletich, N. P.; Pabo, C. O., *Science,* 1991, 5007, 809-817.
3. Desjarlais, J. R.; Berg, J. M., *Proc. Natl. Acad. Sci. U.S.A.* 1992, 16, 7345-7349.
4. Gamsjaeger, R.; Liew, C. K.; Loughlin, F. E.; Crossley, M.; Mackay, J. P., *Trends Biochem. Sci.* 2007, 2, 63-70.
5. Agrawal, A. K.; Jenekhe, S. A., *Macromolecules* 1993, 5, 895-905.
6. Drenth, W.; Nolte, R. J. M., *Acc. Chem. Res.* 1979, 1, 30-35.
7. Goodwin, A.; Novak, B. M., *Macromolecules* 1994, 19, 5520-5522.
8. Jennings, B. R.; Brown, B. L., *Eur. Polym. J* 1971, 7, 805-826.
9. Cook, R., *Macromolecules* 1987, 8, 1961-1964.
10. Rich, A.; Crick, F. H. C., *J. Mol. Biol* 1961, 5, 483-IN484.
11. Sun, Y.-L.; Luo, Z.-P.; Fertala, A.; An, K.-N., *Biochemical and Biophysical Research Communications* 2002, 2, 382-386.
12. Bella, J.; Eaton, M.; Brodsky, B.; Berman, H. M., *Science,* 1994, 5182, 75-81.
13. Nakano, T.; Okamoto, Y., *Chem. Rev.* 2001, 12, 4013-4038.
14. Yashima, E.; Maeda, K.; Iida, H.; Furusho, Y.; Nagai, K., *Chem. Rev.* 2009, 11, 6102-6211.
15. Yashima, E.; Ousaka, N.; Taura, D.; Shimomura, K.; Ikai, T.; Maeda, K., *Chem. Rev.* 2016, 22, 13752-13990.
16. Kouwer, P. H. J.; Koepf, M.; Le Sage, V. A. A.; Jaspers, M.; van Buul, A. M.; Eksteen-Akeroyd, Z. H.; Woltinge, T.; Schwartz, E.; Kitto, H. J.; Hoogenboom, R.; Picken, S. J.; Nolte, R. J. M.; Mendes, E.; Rowan, A. E., *Nature* 2013, 7434, 651-655.
17. Jaspers, M.; Pape, A. C. H.; Voets, I. K.; Rowan, A. E.; Portale, G.; Kouwer, P. H. J., *Biomacromolecules* 2016, 8, 2642-2649.
18. Zimoch, J.; Padial, J. S.; Klar, A. S.; Vallmajo-Martin, Q.; Meuli, M.; Biedermann, T.; Wilson, C. J.; Rowan, A.; Reichmann, E., *Acta Biomater.* 2018, 129-139.
19. Miyabe, T.; Iida, H.; Ohnishi, A.; Yashima, E., *Chem. Sci.* 2012, 3, 863-867.
20. Numata, M.; Kinoshita, D.; Hirose, N.; Kozawa, T.; Tamiaki, H., *Chem. Lett.* 2013, 3, 266-268.
21. Liu, N.; Ma, C.-H.; Sun, R.-W.; Huang, J.; Li, C.; Wu, Z.-Q., *Polym. Chem.* 2017, 14, 2152-2163.
22. Wang, Q.; Chu, B.-F.; Chu, J.-H.; Liu, N.; Wu, Z.-Q., *ACS Macro Lett.* 2018, 2, 127-131.

23. Reggelin, M.; Doerr, S.; Klussmann, M.; Schultz, M.; Holbach, M., *Proc. Natl. Acad. Sci. U.S.A.* 2004, 15, 5461-5466.
24. Bécart, D.; Diemer, V.; Salaün, A.; Oiarbide, M.; Nelli, Y. R.; Kauffmann, B.; Fischer, L.; Palomo, C.; Guichard, G., *J. Am. Chem. Soc.* 2017, 36, 12524-12532.
25. Yamamoto, T.; Murakami, R.; Suginome, M., *J. Am. Chem. Soc.* 2017, 7, 2557-2560.
26. Zhao, B.; Deng, J. R.; Deng, J. P., *ACS Macro Lett.* 2017, 1, 6-10.
27. Zhou, L.; Chu, B.-F.; Xu, X.-Y.; Xu, L.; Liu, N.; Wu, Z.-Q., *ACS Macro Lett.* 2017, 824-829.
28. Tamura, K.; Miyabe, T.; Iida, H.; Yashima, E., *Polym. Chem.* 2011, 1, 91-98.
29. Yashima, E.; Iida, H.; Okamoto, Y., Enantiomeric Differentiation by Synthetic Helical Polymers. In *Differentiation of Enantiomers I*, Springer, Cham: 2013; pp 41-72.
30. Ohira, A.; Okoshi, K.; Fujiki, M.; Kunitake, M.; Naito, M.; Hagihara, T., *Adv. Mater.* 2004, 18, 1645-1650.
31. Mayer, S.; Zentel, R., *Macromol. Rapid Commun.* 2000, 13, 927-930.
32. Song, C.; Liu, X.; Liu, D.; Ren, C.; Yang, W.; Deng, J., *Macromol. Rapid Commun.* 2013, 18, 1426-1445.
33. Klok, H. A.; Langenwalter, J. F.; Lecommandoux, S., *Macromolecules* 2000, 21, 7819-7826.
34. Kim, K. T.; Park, C.; Kim, C.; Winnik, M. A.; Manners, I., *Chem. Commun.* 2006, 13, 1372-1374.
35. Ding, L.; Huang, Y. Y.; Zhang, Y. Y.; Deng, J. P.; Yang, W. T., *Macromolecules* 2011, 4, 736-743.
36. Kolli, H. B.; Frezza, E.; Cinacchi, G.; Ferrarini, A.; Giacometti, A.; Hudson, T. S.; De Michele, C.; Sciortino, F., *Soft Matter* 2014, 41, 8171-8187.
37. Shi, S.-Y.; He, Y.-G.; Chen, W.-W.; Liu, N.; Zhu, Y.-Y.; Ding, Y.-S.; Yin, J.; Wu, Z.-Q., *Macromol. Rapid Commun.* 2015, 16, 1511-1520.
38. Reuther, J. F.; Siriwardane, D. A.; Campos, R.; Novak, B. M., *Macromolecules* 2015, 19, 6890-6899.
39. Priftis, D.; Leon, L.; Song, Z.; Perry, S. L.; Margossian, K. O.; Tropnikova, A.; Cheng, J.; Tirrell, M., *Angew. Chem. In.t Ed.* 2015, 38, 11128-11132.
40. Mammoottil, N. R.; Reuther, J. F.; Siriwardane, D. A.; Kulikov, O. V.; Novak, B. M., *J. Polym. Sci. A Polym. Chem.* 2017, 18, 2915-2934.
41. Zhang, C.; Li, M.; Lu, H. Y.; Chen, C. F., *RSC Adv.* 2018, 2, 1014-1021.
42. Li, B. S.; Lam, J. W.; Yu, Z. Q.; Tang, B. Z., *Langmuir* 2012, 13, 5770-5774.

43. Fan, J.; Li, R.; He, X.; Seetho, K.; Zhang, F.; Zou, J.; Wooley, K. L., *Polym. Chem.* 2014, 13, 3977-3981.
44. Caillol, S.; Lecommandoux, S.; Mingotaud, A.-F.; Schappacher, M.; Soum, A.; Bryson, N.; Meyrueix, R., *Macromolecules* 2003, 4, 1118-1124.
45. Rodríguez-Hernández, J.; Lecommandoux, S., *J. Am. Chem. Soc.* 2005, 7, 2026-2027.
46. Schatz, C.; Louguet, S.; Le Meins, J.-F.; Lecommandoux, S., *Angew. Chem. Int. Ed.* 2009, 14, 2572-2575.
47. Babin, J.; Rodriguez-Hernandez, J.; Lecommandoux, S.; Klok, H.-A.; Achard, M.-F., *Faraday Discussions* 2005, 0, 179-192.
48. Chécot, F.; Lecommandoux, S.; Gnanou, Y.; Klok, H.-A., *Angew. Chem. Int. Ed.* 2002, 8, 1339-1343.
49. Chécot, F.; Brûlet, A.; Oberdisse, J.; Gnanou, Y.; Mondain-Monval, O.; Lecommandoux, S., *Langmuir* 2005, 10, 4308-4315.
50. Agut, W.; Brûlet, A.; Schatz, C.; Taton, D.; Lecommandoux, S., *Langmuir* 2010, 13, 10546-10554.
51. Agut, W.; Taton, D.; Brûlet, A.; Sandre, O.; Lecommandoux, S., *Soft Matter* 2011, 20, 9744-9750.
52. Hoog, H.-P. M. d.; Vriezema, D. M.; Nallani, M.; Kuiper, S.; Cornelissen, J. J. L. M.; Rowan, A. E.; Nolte, R. J. M., 2008, 5, 1003-1010.
53. Cornelissen, J. J. L. M.; Fischer, M.; Sommerdijk, N. A. J. M.; Nolte, R. J. M., *Science* 1998, 5368, 1427-1430.
54. Vriezema, D. M.; Hoogboom, J.; Velonia, K.; Takazawa, K.; Christianen, P. C. M.; Maan, J. C.; Rowan, A. E.; Nolte, R. J. M., *Angew. Chem. Int. Ed.* 2003, 7, 772-776.
55. Yamashita, H.; Misawa, T.; Oba, M.; Tanaka, M.; Naito, M.; Kurihara, M.; Demizu, Y., *Bioorg. Med. Chem* 2017, 6, 1846-1851.
56. Tang, H.; Yin, L.; Kim, K. H.; Cheng, J., *Chem. Sci.* 2013, 10, 3839-3844.
57. Chen, Y.; Zhang, Z.-H.; Han, X.; Yin, J.; Wu, Z.-Q., *Macromolecules* 2016, 20, 7718-7727.
58. Zhang, W.-M.; Zhang, J.; Qiao, Z.; Liu, H.-Y.; Wu, Z.-Q.; Yin, J., *Polym. Chem.* 2018, 31, 4233-4242
59. Penfold, N. J. W.; Yeow, J.; Boyer, C.; Armes, S. P., *ACS Macro Lett.* 2019, 8, 1029-1054.
60. Warren, N. J.; Armes, S. P., *J. Am. Chem. Soc.* 2014, 29, 10174-10185.
61. Cunningham, V. J.; Alswieleh, A. M.; Thompson, K. L.; Williams, M.; Leggett, G. J.; Armes, S. P.; Musa, O. M., *Macromolecules* 2014, 16, 5613-5623.
62. Derry, M. J.; Fielding, L. A.; Armes, S. P., *Polym. Chem.* 2015, 16, 3054-3062.

63. Foster, J. C.; Varlas, S.; Couturaud, B.; Jones, J. R.; Keogh, R.; Mathers, R. T.; O'Reilly, R. K., *Angew. Chem. Int. Ed.* 2018, 48, 15733-15737.
64. Lecommandoux, S.; Grazon, C.; Salas-Ambrosio, P.; Ibarboure, E.; Buol, A.; Garanger, E.; Grinstaff, M. W.; Bonduelle, C., *Angew. Chem. Int. Ed.* 2019, ja, doi:10.1002/anie.201912028.
65. D'Agosto, F.; Rieger, J.; Lansalot, M., *Angew. Chem. Int. Ed.* 2020, 22, 8368-8392.
66. Kapishon, V.; Whitney, R. A.; Champagne, P.; Cunningham, M. F.; Neufeld, R. J., *Biomacromolecules* 2015, 7, 2040-2048.
67. Okubo, M.; Sugihara, Y.; Kitayama, Y.; Kagawa, Y.; Minami, H., *Macromolecules* 2009, 6, 1979-1984.
68. Kitayama, Y.; Chaiyasat, A.; Minami, H.; Okubo, M., *Macromolecules* 2010, 18, 7465-7471.
69. Kitayama, Y.; Moribe, H.; Kishida, K.; Okubo, M., *Polym. Chem.* 2012, 6, 1555-1559.
70. Cordella, D.; Ouhib, F.; Aqil, A.; Defize, T.; Jérôme, C.; Serghei, A.; Drockenmuller, E.; Aissou, K.; Taton, D.; Detrembleur, C., *ACS Macro Lett.* 2017, 2, 121-126.
71. Ferguson, C. J.; Hughes, R. J.; Pham, B. T. T.; Hawkett, B. S.; Gilbert, R. G.; Serelis, A. K.; Such, C. H., *Macromolecules* 2002, 25, 9243-9245.
72. Johnson, J. A.; Lewis, D. R.; Díaz, D. D.; Finn, M. G.; Koberstein, J. T.; Turro, N. J., *J. Am. Chem. Soc.* 2006, 20, 6564-6565.
73. Wan, W.-M.; Pan, C.-Y., *Macromolecules* 2007, 25, 8897-8905.
74. Canning, S. L.; Smith, G. N.; Armes, S. P., *Macromolecules* 2016, 6, 1985-2001.
75. Kim, K. H.; Kim, J.; Jo, W. H., *Polymer* 2005, 9, 2836-2840.
76. Darabi, A.; Shirin-Abadi, A. R.; Jessop, P. G.; Cunningham, M. F., *Macromolecules* 2015, 1, 72-80.
77. Guégain, E.; Zhu, C.; Giovanardi, E.; Nicolas, J., *Macromolecules* 2019, 10, 3612-3624.
78. Zhang, L.; Song, C.; Yu, J.; Yang, D.; Xie, M., *J. Polym. Sci. A Polym. Chem.* 2010, 22, 5231-5238.
79. Wright, D. B.; Touve, M. A.; Adamiak, L.; Gianneschi, N. C., *ACS Macro Lett.* 2017, 9, 925-929.
80. Foster, J. C.; Varlas, S.; Blackman, L. D.; Arkinstall, L. A.; O'Reilly, R. K., *Angew. Chem. Int. Ed.* 2018, 33, 10672-10676.
81. Varlas, S.; Foster, J. C.; O'Reilly, R. K., *Chem. Commun.* 2019, 62, 9066-9071.
82. Wright, D. B.; Proetto, M. T.; Touve, M. A.; Gianneschi, N. C., *Polym. Chem.* 2019, 23, 2996-3000.
83. Duan, P.; Cao, H.; Zhang, L.; Liu, M., *Soft Matter* 2014, 30, 5428-5448.

84. Li, Y.; Wang, T.; Liu, M., *Soft Matter* 2007, 10, 1312-1317.
85. Okazaki, Y.; Goto, T.; Sakaguchi, R.; Kuwahara, Y.; Takafuji, M.; Oda, R.; Ihara, H., *Chem. Lett.* 2016, 4, 448-450.
86. Li, H.; Zheng, X.; Su, H.; Lam, J. W. Y.; Sing Wong, K.; Xue, S.; Huang, X.; Huang, X.; Li, B. S.; Tang, B. Z., *Sci. Rep.* 2016, 19277.
87. Han, J.; You, J.; Li, X.; Duan, P.; Liu, M., *Adv. Mater.* 2017, 19, 1606503.
88. Liu, M.; Zhang, L.; Wang, T., *Chem. Rev.* 2015, 15, 7304-7397.
89. Asaoka, S.; Joza, A.; Minagawa, S.; Song, L.; Suzuki, Y.; Iyoda, T., *ACS Macro Lett.* 2013, 10, 906-911.
90. Takei, F.; Yanai, K.; Onitsuka, K.; Takahashi, S., *Chem. Eur. J.* 2000, 6, 983-993.
91. Lee, J.; Shin, S.; Choi, T.-L., *Macromolecules* 2018, 19, 7800-7806.
92. Patterson, J. P.; Robin, M. P.; Chassenieux, C.; Colombani, O.; O'Reilly, R. K., *Chem. Soc. Rev.* 2014, 8, 2412-2425.
93. Jakeš, J., *Collection of Czechoslovak Chemical Communications* 1995, 11, 1781-1797.
94. Andersson, M.; Wittgren, B.; Wahlund, K.-G., *Anal. Chem.* 2003, 16, 4279-4291.

Chapter 3 Functional nanostructures by NiCCo-PISA of helical poly(aryl isocyanide)s copolymers

3.1. Declaration of authorship

Spectrophotometry was performed by Ms Yujie Xie at the University of Birmingham.

This work was published in *Polymer Chemistry*:

Functional nanostructures by NiCCo-PISA of helical poly(aryl isocyanide) copolymers, Sètuhn Jimaja, Yujie Xie, Jeffrey C. Foster, Daniel Taton, Andrew P. Dove and Rachel K. O'Reilly, *Polym. Chem* 2020, Advance Article

3.2. Introduction

Post-polymerisation modification (PPM) is a powerful and versatile approach that has been widely employed as a tool to introduce functional groups onto a polymer to broaden its range of properties.[1-4] For example, functionality in a micelle's core provides an easy and polyvalent way to introduce different moieties such as dyes for labelling applications[5, 6] in the nanomedical field, catalysts or covalent attachment of drugs.[7] It can also be employed as a method to modify the polarity of the micelle core, which leads to morphological transition.[8] In order to achieve the desired functionality, a variety of handles are employed in PPM: amides,[9-11] nitriles,[12] hydrazides,[13] thiazolidines,[14] epoxides,[15-17] cyanuric chlorides,[18] halogenated alkyls,[19, 20] azides,[21] alkynes,[22] alkenes,[23-25] β-ketoesters,[26] thiocarbamates,[27] and thioethers.[28] Similarly, various reactions are employed to achieve PPM: click chemistry,[29] transesterification,[30] nucleophilic aromatic substitution,[18] nitroxide radical coupling,[31] thiol-para-fluoro click reaction,[8, 32, 33] keto–enol tautomerisation,[34] dihydroxylation,[35] thiol-ene,[36] thiol–disulfide exchange,[37] and multi component reactions (MCRs) such as the Ugi and Passerini rections[38] and the Kabachnik-Fields MCR.[39] PPM is mainly aimed at side-chain chemistry however, end-chain modification has also been extensively studied.[23, 40-42]

The molecule of interest introduced during PPM can be either a nucleophile or an electrophile; therefore, one must carefully consider the type and functionality that is desired. However, active nucleophile pendant chains are more prone to disrupt the polymerisation and/or be incompatible with comonomers and, consequently, they must be protected during the polymerisation process, which requires additional steps. Therefore, an electrophilic pendant group is generally preferable as the active site for PPM approaches. The PPM approach also allows to bypass the potentially time-

consuming steps of synthesising novel functional monomers, where functionality could disrupt the polymerisation process and/or be incompatible with the monomer active site. The number of synthetic steps required for monomer synthesis is reduced overall as only the monomer that bears the active site is needed to achieve the different functionalities.

Practically, PPM has been employed in the modification of sequence-defined precursors for digital polymers as demonstrated by Lutz and co-workers. They have developed poly(phosphodiester)s decorated with alkyne functionality that they modified with the copper(I)-catalysed azide alkyne cycloaddition (CuAAC) click reaction with azides.[43] In the area of self-assembly, Wooley and co-workers have developed polyphosphoesters that contained alkyne[44] or alkene[25, 45] groups that could be functionalised easily by thiol nucleophiles through thiol-yne or thiol-ene click chemistry, respectively and that would modify their behaviour once self-assembled. In one instance, they demonstrated the PPM of a polyphosphoester that contained alkyne *via* click thiol-yne reaction with primary thiols attached to functional groups which exhibited various charges in water. The self-assembly of the resulting copolymers led to the formation of micelles with different surface charge: non-ionic, anionic, cationic and zwitterionic (Scheme 3.1). Finally, PPM is very useful to develop stimuli-responsive polymers[37, 46-48] and this area will be expanded in Chapter 4.

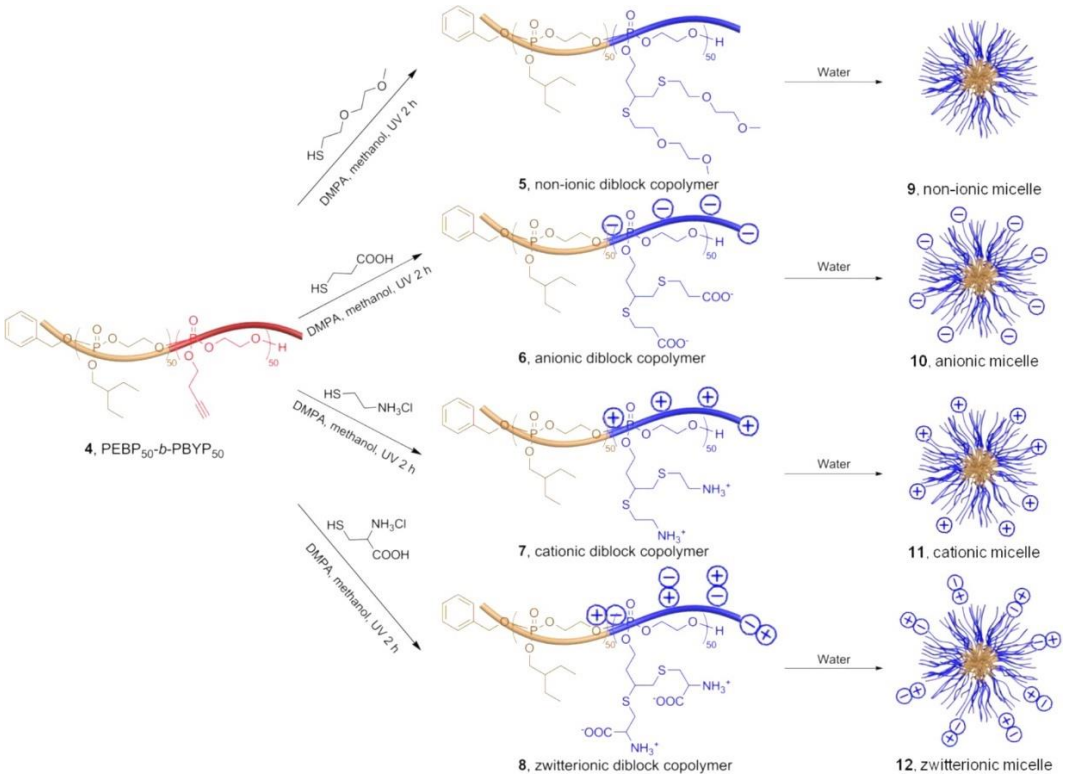

Scheme 3.1. Functionalisation of polyphosphoesters decorated with alkyne side-chains by a range of thiols self-assembled into micelles with different surface charges. Reproduced from the work of Wooley and co-workers published in ACS, Journal of the American Chemical Society. [44]

Pentafluorophenyl (PFP) esters are activated electrophiles reactive towards amines and alcohols when the right conditions are selected. PFP esters can be employed in PPM as active site bearing monomers when the desired functionality can be tied to a nucleophile. For RAFT, both pentafluorophenyl methacrylate (PFPMA) and pentafluorophenyl acrylate (PFPA) have been developed and studied to demonstrate their employment as effective monomers for the development of responsive functional polymers *via* PPM with primary amines.[30, 49-52] Meijer and co-workers have developed single-chain polymeric nanoparticles (SCPNPs) composed of polyacrylate copolymers that contained PFPA. This system was easily modified by reaction with different amines to provide the SCPNPs with precise functionality: ligand capable of binding copper for catalysis and Jeffamine for photosensitisation.[53] PFPMA has lately

been employed by Couturaud *et al.* to conduct RAFT PISA in DMSO and subsequently cross-link the core composed of activated esters to achieve redox-responsive nanoparticles.[54]

PFP-derived monomers have therefore already been proven to undergo PISA in DMSO and, considering that it is the solvent employed for NiCCo-PISA, it was hypothesised that a similar PFP aryl isocyanide monomer could be used for this self-assembly technique. Wu and co-workers have developed a PFP aryl isocyanide (FAIC, Figure 3.1) that could be employed as a comonomer to introduce an electrophile handle into helical polyisocanides (Scheme 3.2).[55-57] They have shown that the *in situ* substitution of the PFP ester by a chiral moiety could take place during the polymerisation and that helicity could be induced as a consequence of the disparity between the reaction rate of aminolysis (fast) and polymerisation (slow), which made this effectively a one-pot polymerisation of chiral monomers. They also demonstrated the FAIC monomer could readily polymerise under the same conditions as the menthyl-ester arylisocyanide (MAIC) employed in Chapter 2. If the solvophobicity of the FAIC and MAIC monomers towards DMSO are similar, their copolymerisation would represent an ideal system for the synthesis of functionalisable NiCCo-PISA micelles. The chiral menthyl pendant of the MAIC monomer induces screw-sense selective polymerisation as shown in Chapter 2 and it is hypothesised that a copolymer that contained FAIC and MAIC as comonomers would result in helical polymers.

In the field of circularly polarised luminescence (CPL), helical assemblies have been employed as scaffolds for inducing circularly polarised emission of embedded dyes. [58-63] Having a functionality that allows the grafted dye to be chosen in the final step of the synthesis would make for more reproducible CPL nanostructures.

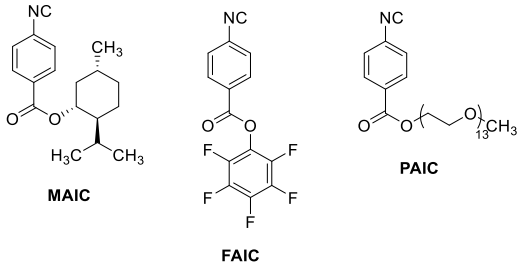

Figure 3.1. Menthyl-ester arylisocyanide (MAIC), pentalfuorophenol ester arylisocyanide (FAIC) and PEG-ester aryl isocyanide (PAIC) monomers used in this work.

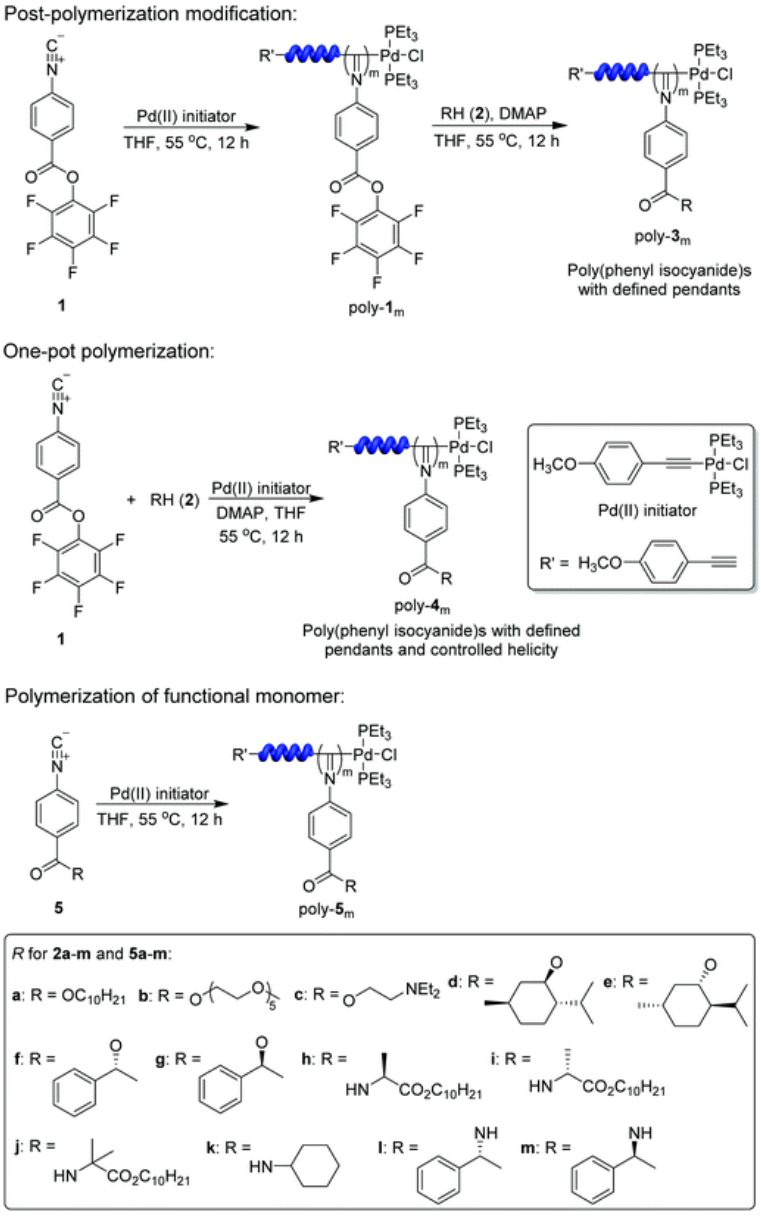

Scheme 3.2. Post-polymerisation modification approach with the FAIC monomer that illustrates the wide scope of nucleophiles that can be employed. Reproduced from the work of Yin *et al.* published in RSC, Polymer Chemitry.[55]

In this Chapter, the synthesis, helicity, and self-assembly behaviour of P(PAIC)-*b*-P(MAIC-*co*-FAIC) block copolymers synthesised by NiCCo-PISA as a possible platform to graft different nucleophiles into the helical core using complementary methods such as NMR spectroscopy, FT-IR spectroscopy and spectrophotometry was explored. Moreover, the efficiency of PPM of the resulting nano-objects using different primary amines and alcohols, and the effect of the new functionality on the nano-objects' stability and properties was investigated. The combination of the simplicity of the synthesis of helix-containing micelles conferred by NiCCo-PISA and the wide range of potential modifications possible by PPM would result in a versatile and facile synthesis of functional helix-containing micelles.

3.3. Functionalisable helical polymers

The FAIC monomer was synthesised following a different route than the MAIC and PAIC monomers (Scheme 3.3). A formamidobenzoic acid compound was first achieved by reaction of aminobenzoic acid with ethyl formate. The formamide was coupled with PFP and the successful coupling was validated by the presence of three signals in the ^{19}F NMR spectrum of the purified compound in addition to appearance of the PFP signal by ^{13}C NMR and shift of the aryl protons signal by ^{1}H NMR. As for the MAIC and PAIC syntheses, the formamide intermediates have two conformations - *cis* or *trans* – that are clearly observed by NMR spectroscopy. In this case, the *cis* conformation composed up to 25 % of the total material. Finally, the PFP ester formamide was dehydrated into the isocyanide by reacting with $POCl_3$ under basic conditions to yield FAIC. The product, like MAIC and PAIC, was kept at -25 °C under nitrogen atmosphere to slow down its decomposition.

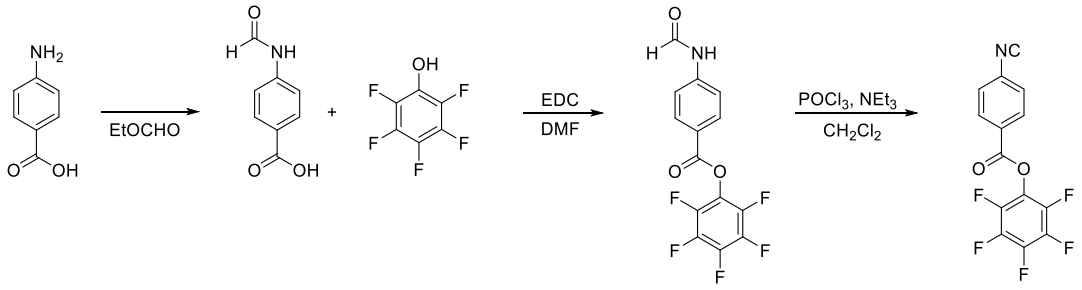

Scheme 3.3. Synthesis route for FAIC: formylation of the 4-aminobenzoic acid followed by the coupling with pentafluorophenol catalysed by EDC and the dehydration into the isocyanide monomer (FAIC).

To develop functionalised particles, it was necessary to introduce FAIC into the NiCCo-PISA micelles without disrupting the polymerisation or self-assembly processes. In order to investigate the former, MAIC and FAIC were copolymerised in THF aiming for a DP 30 (similar to the core of the micelles employed in the previous Chapter) with different comonomer ratios to achieve

statistical copolymers that contained 0-100 mol% of FAIC units. After purification by repeated precipitation in methanol, the analysis of the copolymers by SEC indicated that there was no major change in the profile between the different copolymers, with number average molecular weights (M_n) which ranged between 4.4-4.5 kDa and dispersity ($Đ_M$) between 1.13-1.21 (Figure 3.3 and Table 3.1) across the series. However, the P(FAIC)$_{30}$ homopolymer, when dissolved in THF, produced a slightly turbid solution, which indicated that a small portion of the polymer was insoluble in this solvent. After filtration using a 0.2 µm PTFE filter, the solution became clear, which indicated the successful removal of the insoluble fraction.

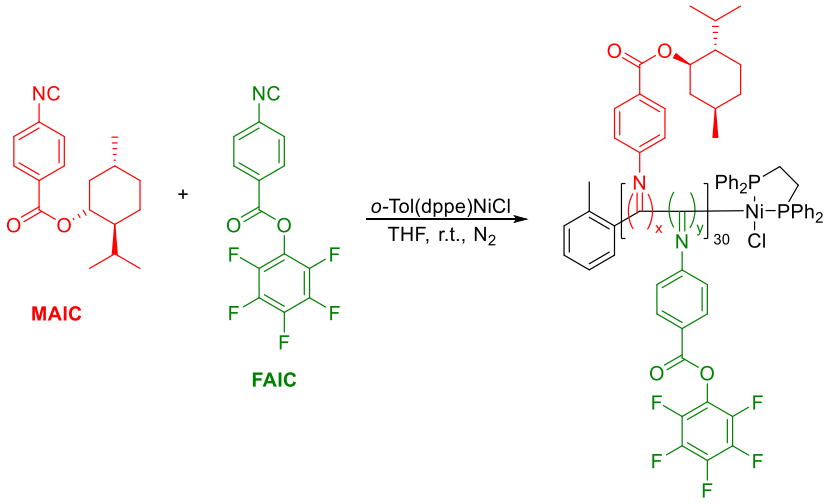

Scheme 3.4. Copolymerisation of MAIC and FAIC with DP = 30.

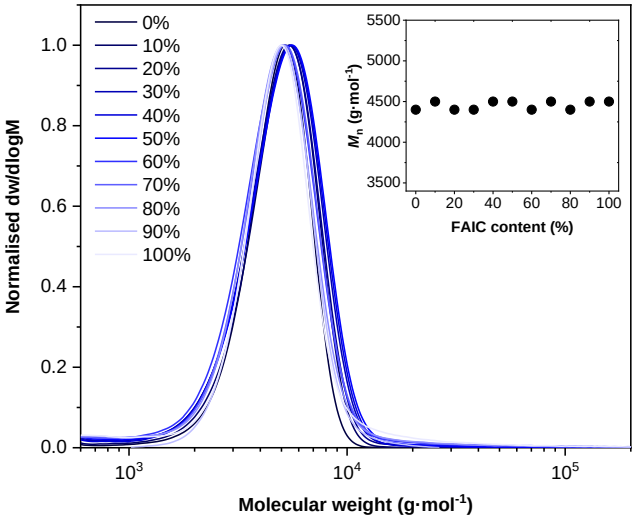

Figure 3.2. Normalised SEC RI molecular weight distributions (THF + 2% v/v NEt_3, 40 °C, PS standards) of P(MAIC)$_x$-*co*-P(FAIC)$_y$ DP 30 with content of FAIC which ranged between 0-100 mol%.

The helicity of the copolymers, quantified by the strength of the signal at $\lambda =$ 360 nm in the CD spectra, assigned to the n–π* transition of the C=N of the polyisocyanide backbone, was linearly dependent on the content of MAIC (chiral monomer), which decreased until no CD absorption was present at 100% of FAIC in the absence of chiral information (Figure 3.3 and Table 3.1). This linear dependence suggested an absence of the *sergeant-soldier* phenomenon observed in some dynamic helical polymers, where a small amount of chiral monomer is sufficient to induce a large helicity and leads to a non-linear helicity/molecular weight relationship.[64] This phenomenon has already been observed for a similar type of copolymer, where Takahashi and co-workers have copolymerised *L*- and *D*-MAIC with their achiral *p*-cyclohexyl counterpart and showed an induction of screw-sense for DP 100 random copolymers.[65] However, the small deviation from the linear decrease of the CD signal between 20% and 50% of FAIC content resemble, with a smaller amplitude, the trend of copolymers that effectively have *sergeant-soldier* effect and could be a consequence of such an effect. The phenomenon has been demonstrated with DP 100 copolymers and there might be a critical molecular

weight higher than DP 30 necessary to achieve the maximum *sergeant-soldier* effect. On the other hand, PIC copolymers with bulky substituent are known to be static and therefore generally do not exhibit *sergeant-soldier* effect which would explain the lack of screw-sense induction.

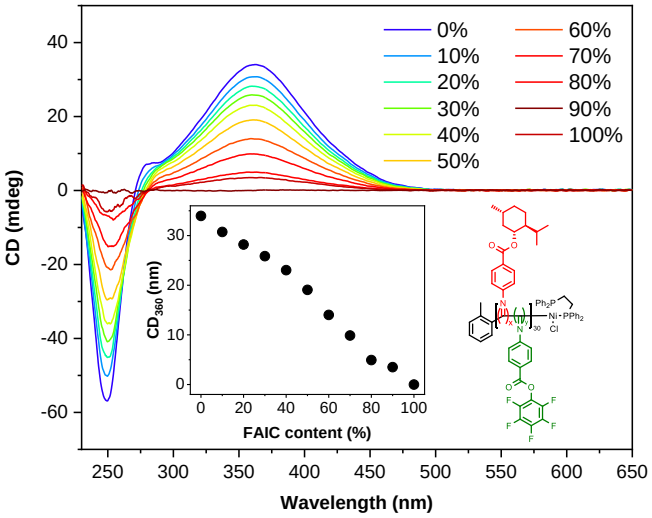

Figure 3.3. CD (THF, 0.5 mg·mL^{-1}) spectra of P(MAIC)$_x$-*co*-P(FAIC)$_y$ DP 30 with content of FAIC from 0% to 100%.

The successful integration of the PFP units into the copolymers was detected by ^{19}F NMR spectroscopy (Figure 3.4). The broad signals at δ = -153, -158 and -162 ppm corresponded to the incorporated PFP moieties from the FAIC monomer. The broadening of the signal was a consequence of the conformational mobility restriction by the polyisocyanide rigid helix. The line width at half height (LWHH) of the copolymer signal as calculated using the MestReNova software was found to be between 350 and 450 Hz while the molecular FAIC signals were comprised between 10 to 15 Hz. The intensity of the fluorine signals increased with the quantity of PFP present in the copolymer, which indicated the increase of FAIC comonomer inside the copolymer except for the polymer that contained 100% of PFP. The lower signal in ^{19}F NMR spectroscopy of the P(FAIC)$_{30}$ homopolymer was a consequence of its poor solubility in chloroform. The broadness of the PFP ^{19}F

NMR signal of the copolymers did not change, which indicated that the rigidity of the helices did not vary with the quantity of FAIC monomer inserted. Overall, this demonstrated that the copolymerisation of FAIC with MAIC did not have any major influence on the copolymer molecular weight or distribution. This was a good indicator that the copolymerisation of MAIC and FAIC should be applicable in NiCCo-PISA. On the other hand, the decrease of chiral information clearly impacted the helicity of the resulting copolymers, which meant that the quantity of the MAIC comonomer needed to be high enough to keep the core helical.

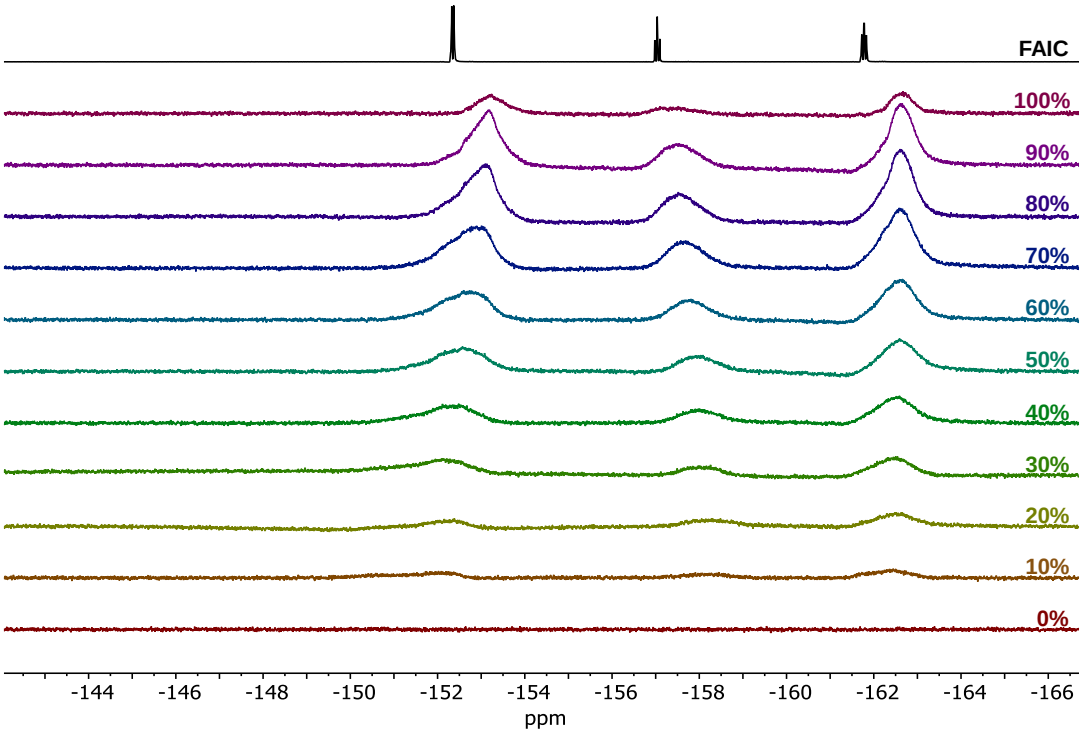

Figure 3.4. ^{19}F NMR spectrum of P(MAIC)$_x$-*co*-P(FAIC)$_y$ DP 30 with FAIC content from 0% to 100% compared to molecular FAIC in $CDCl_3$ (377 MHz, 298 K).

Table 3.1. Characterisation of synthesised P(MAIC)$_x$-*co*-P(FAIC)$_y$ copolymers.

Polymer	FAIC (%)	$M_{n,\,SEC}$ (kDa)[a]	$Đ_M$ [a]	CD$_{360}$ (mdeg)[b]
P(MAIC)$_{30}$	0	4.4	1.13	34
P(MAIC)$_{27}$-*co*-P(FAIC)$_3$	10	4.5	1.16	31
P(MAIC)$_{24}$-*co* -P(FAIC)$_6$	20	4.4	1.19	28
P(MAIC)$_{21}$-*co* -P(FAIC)$_9$	30	4.4	1.20	26
P(MAIC)$_{18}$-*co* -P(FAIC)$_{12}$	40	4.5	1.19	23
P(MAIC)$_{15}$-co-P(FAIC)$_{15}$	50	4.5	1.21	19
P(MAIC)$_{12}$-co-P(FAIC)$_{18}$	60	4.4	1.17	14
P(MAIC)$_9$-*co*-P(FAIC)$_{21}$	70	4.5	1.15	10
P(MAIC)$_6$-*co*-P(FAIC)$_{24}$	80	4.4	1.15	5
P(MAIC)$_3$-*co*-P(FAIC)$_{27}$	90	4.5	1.15	4
P(FAIC)$_{30}$	100	4.5	1.16	0

[a]Determined by SEC (THF + 2% v/v NEt_3) using polystyrene (PS) standards. [b]CD (THF, 0.5 mg·mL^{-1}) signal at λ = 360 nm.

3.4. Functionalised NiCCo-PISA micelles

In order to achieve core-functionalisable micelles and study the impact of the relatively more solvophobic FAIC monomer on the final self-assembled morphology, NiCCo-PISA was conducted in DMSO with $DP_{P(PAIC)}$ of 20 and $DP_{solvophobic}$ (*i.e.* $DP_{P(MAIC)} + DP_{P(FAIC)}$) of 30 aiming for micelles (Figure 3.5). Different FAIC loadings were targeted: 0%, 20%, 50% and 100 mol% of the core. The resulting $P(PAIC)_{20}$-*b*-$(P(MAIC)_y$-*co*-$P(FAIC)_z)_{30}$ diblock copolymers were named following their FAIC content in the solvophobic block: D0%, D20%, D50% and D100%. The unfunctionalisable D0% that contained no PFP moiety was chosen as a control to ensure the nucleophiles would not react with the MAIC and PAIC units. D20%, D50% and D100% were chosen to differentiate the impact on the nanoparticles of the different loading of nucleophiles.

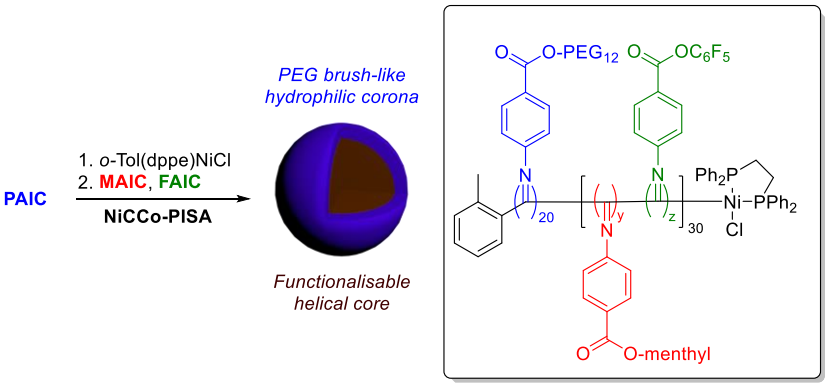

Figure 3.5. $P(PAIC)_{30}$-*b*-$(P(MAIC)_y$-*co*-$P(FAIC)_z)_{30}$ or DZ% copolymer achieved by NiCCo-PISA for core-functionalisable nano-objects.

DLS analysis of the copolymer assemblies was conducted to ensure that the particle distribution was not affected by the incorporation of FAIC into the copolymer. Indeed, no major change in size was detected for D20% and D50% compared to D0% (Figure 3.6). However, for D100%, the size distribution and correlogram indicated that aggregation occurred, which was likely caused by the higher solvophobicity of the FAIC monomer compared to the MAIC

monomer. This meant an increased solvophobicity of the nano-objects' core which altered the surface energy of the nanostructures and led to morphological evolution.

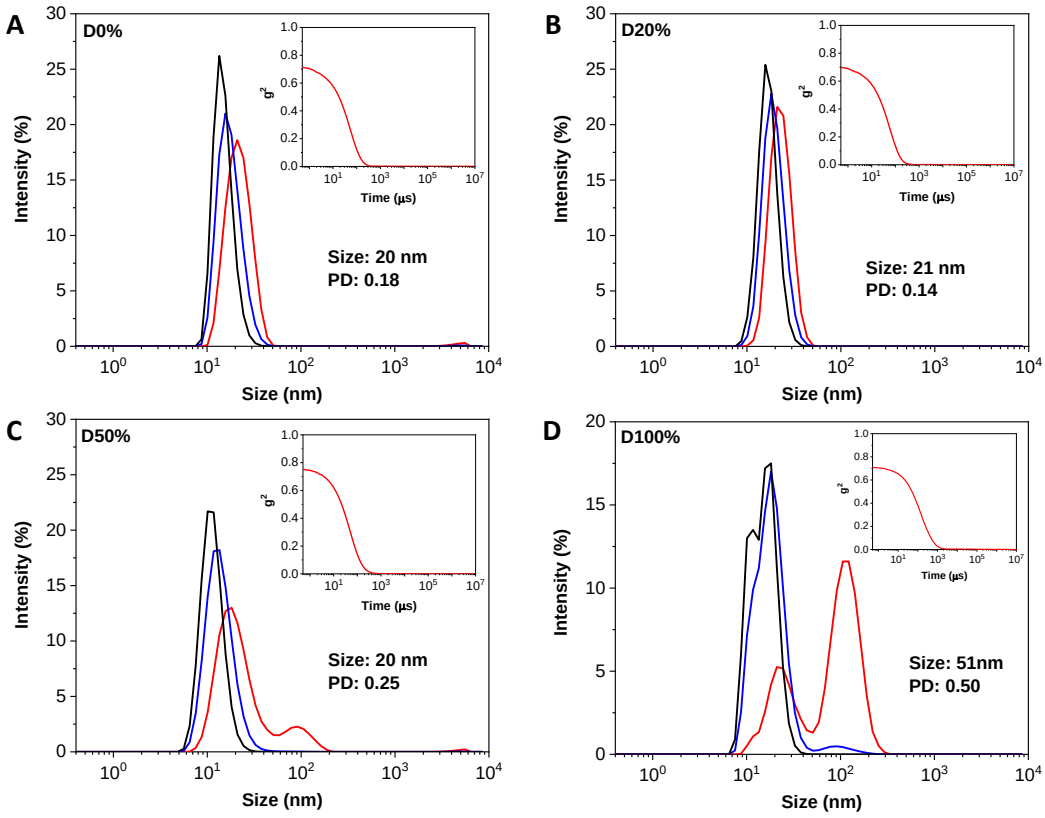

Figure 3.6. Size distributions of (A) D0%, (B) D20%, (C) D50% and (D) D100% in DMSO obtained by DLS. The intensity (red line), volume (blue line) and number (black line) distributions are displayed. The insets show the correlograms.

The different copolymers were analysed by CD spectroscopy and the results showed that the helicity was retained during the self-assembly process as was shown in the previous Chapter with the PISA of the P(PAIC)$_{20}$-*b*-P(MAIC)$_{30}$ copolymer without FAIC (Figure 3.7). However, a decrease in the CD signal was observed until 0 mdeg was reached for 100% of FAIC, concordant with the CD analysis conducted on the P(MAIC)$_x$-*co*-P(FAIC)$_y$ DP 30 copolymers.

SEC of the purified D0%, D20% and D50% diblock copolymers displayed no detectable change in molecular weight, which indicated that the polymerisation

process was not impacted by the incorporation of FAIC as demonstrated earlier for the P(MAIC)$_x$-*co*-P(FAIC)$_y$ DP 30 copolymers. In contrast, the D100% copolymer showed at least two different populations with a $Đ_M$ so large that the molecular weight distribution (MWD) extended outside of the calibration range which rendered calculations of M_w, M_n and $Đ_M$ inaccurate. This MWD hinted that the self-assembly had an impact on the growth of the polymer as seen in Chapter 2 when NiCCo-PISA was conducted with high DP_{MAIC} and the copolymers with the more solvophobic core led to bimodal molecular weight distributions.

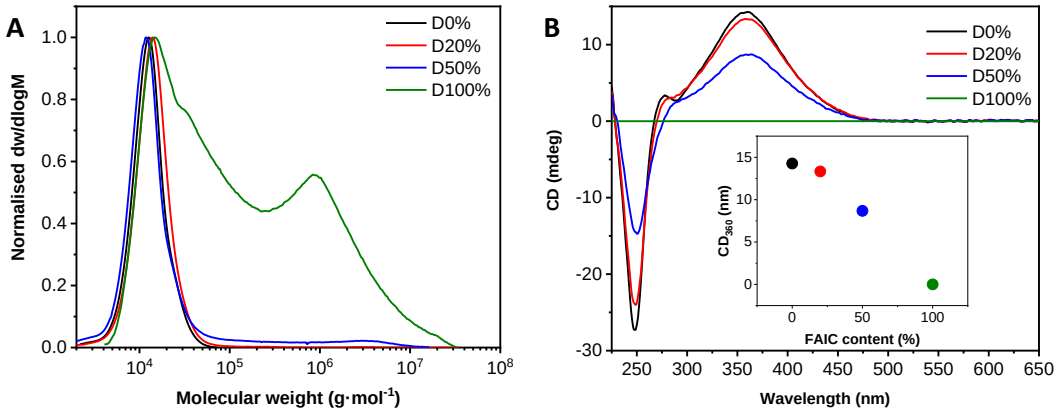

Figure 3.7. (A) CD (THF, 0.5 mg·mL^{-1}) spectra and (B) normalised SEC RI molecular weight distributions (THF + 2% v/v NEt$_3$, 40 °C, PS standards) of P(PAIC)$_{20}$-*b*-(P(MAIC)$_y$-*co*-P(FAIC)$_z$)$_{30}$ with 0%, 20%, 50% and 100% of FAIC.

The copolymerisation of D100% was repeated in THF (a better solvent for both blocks than DMSO) to assess the role of the polymer solubility in the bimodal distribution. The copolymerisation in THF also gave a broad, bimodal distribution - although with a smaller high molecular weight secondary population (Figure 3.8). This could indicate that the formation of self-assembled nanostructures was also occurring in THF as a consequence of the low solubility of the FAIC block in this solvent as illustrated earlier with the P(FAIC)$_{30}$ homopolymer. However, this secondary population might also arise from a disruption of the polymerisation process caused by the self-assembly of

the growing copolymer chains followed by bimolecular coupling which led to dead chains. Because the polymerisation for this diblock copolymer was not controlled, D100% was not used in the subsequent substitution reactions.

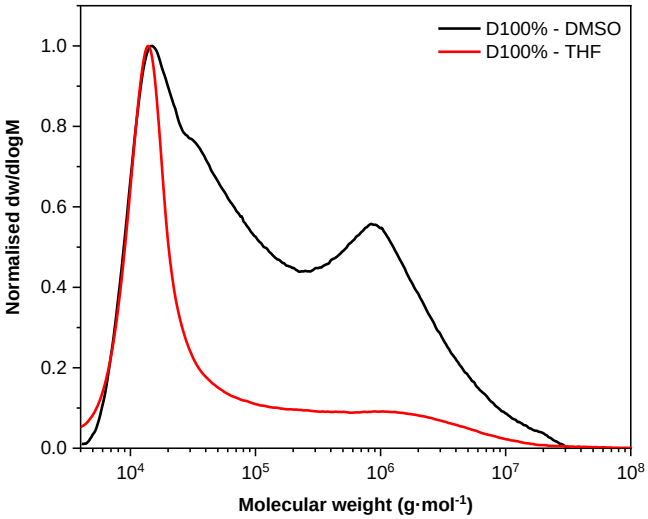

Figure 3.8. Normalised SEC RI molecular weight distributions (THF + 2% v/v NEt_3, 40 °C, PS standards) of D100% polymerised in THF (black) and DMSO (red).

Table 3.2. Characterisation of synthesised D0%, D20%, D50% and D100% copolymers.

Polymer	D_{DLS} (nm) [a]	$M_{n,\,SEC}$ (kDa) [b]	$Đ_M$ [b]	CD_{360} (mdeg) [c]
D0%	20 (0.18)	11.2	1.24	16
D20%	21 (0.14)	12.4	1.24	15
D50%	20 (0.25)	10.5	1.34	7
D100%	51 (0.50)	-[d]	-[d]	0

[a]Spherical particles size measured by DLS with PD in parenthesis. [b]Determined by SEC (THF + 2% v/v NEt_3) using PS standards. [c]CD (THF, 0.5 mg·mL^{-1}) signal at λ = 360 nm. [d]Molecular weight distribution is outside the calibration range.

In the following sections, the substitution reaction of the copolymers D0%, D20% and D50% by primary amine nucleophiles (Scheme 3.5) were tested and verified in order to assess the scope of polymer modification for the block copolymers. Nucleophiles were varied to assess the generality of the PPM

approach in the P(PAIC)$_x$-*b*-(P(MAIC)$_y$-*co*-P(FAIC)$_z$)$_n$ system confirmed with complementary techniques.

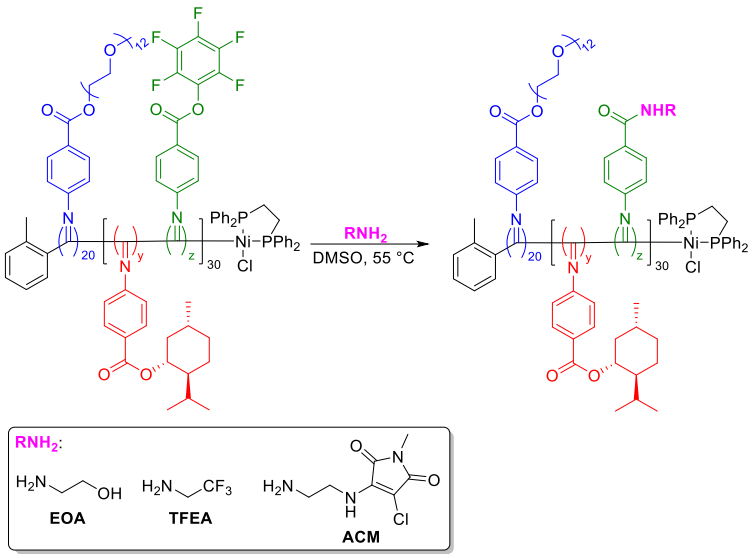

Scheme 3.5. Substitution of P(PAIC)$_x$-*b*-(P(MAIC)$_y$-*co*-P(FAIC)$_z$)$_n$ with three nucleophiles: ethanolamine (EOA), trifluoroethylamine (TFEA) and an aminochloromaleimide (ACM).

3.4.1. Functionalisation with ethanolamine

Firstly, ethanolamine (EOA) – a primary amine that contains an alcohol functionality – was reacted *in situ* after the NiCCo-PISA with D0%, D20% and D50% (Scheme 3.6). Aminolysis of PFP are usually conducted in basic conditions that accelerate the reaction rate however, these conditions also lead to hydrolysis of the PFP esters into carboxylic acids.[54] With aminolysis being faster than hydrolysis, the choice was made to conduct the reactions without base to diminish the hydrolysis at the cost of reaction speed. Moreover, the higher rate of reaction of the amine compared to the alcohol ensured that the aminolysis would be the dominant reaction leaving the free alcohol as the resulting functionality. It was hypothesised that the alcohol functionality, once integrated into the copolymer, would be easily detected by FT-IR spectroscopy

after removal of the excess reactant and drying to avoid unwanted signal from water.

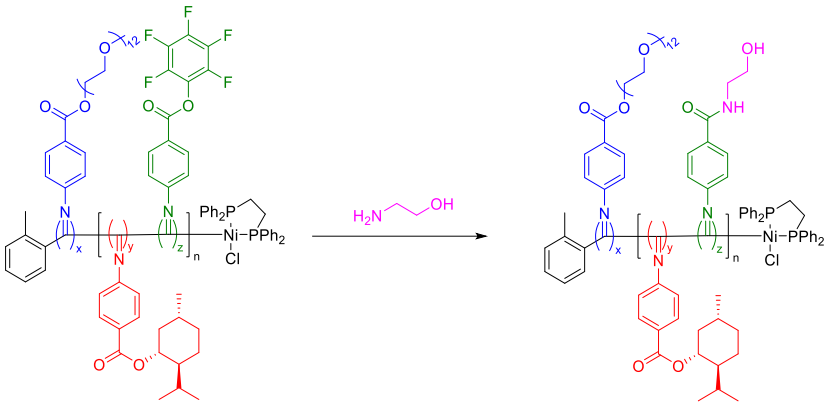

Scheme 3.6. Substitution of P(PAIC)$_x$-*b*-(P(MAIC)$_y$-*co*-P(FAIC)$_z$)$_n$ with ethanolamine (EOA).

An excess of the polar amine was employed to ensure the diffusion of the compound into the solvophobic core of the micelles and its reaction with the activated ester. The reaction was allowed to stir for 24 h before it was analysed by DLS (Figure 3.9 and Table 3.3) to verify the stability of the nanostructures to the change in polarity expected in the core from the substitution of the PFP units for alcohol functionalities. The size of the assemblies did not change for D0%+EOA at 20 nm, which indicated a good stability of the non-reactive nanostructure to the reaction conditions. The diameter of D20%+EOA slightly increased from 19 to 21 nm, which is within error. However, there was a clear indication of the modification of the nanostructure morphology for D50%+EOA, where the initial size was 20 nm with a PD of 0.25 and the diameter after substitution increased to 34 nm with a PD of 1 which indicated an extremely broad distribution of sizes. This can be explained by the increase in polarity and therefore solubility of the core that clearly impacted the assembly of the copolymer. This overall higher solvophilicity led to the partial disassembly of the nano-objects which led to a mixture of unimers and nanostructures represented by the broad DLS size

distribution. Moreover, the decrease in the correlation function maximum – from 0.8 to 0.7 - was further evidence of disassembly.

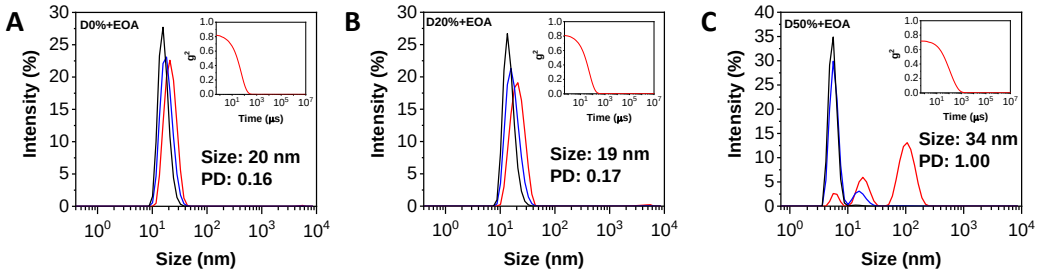

Figure 3.9. Size distributions of (A) D0%+EOA, (B) D20%+EOA, and (C) D50%+EOA in DMSO obtained by DLS. The intensity (red line), volume (blue line) and number (black line) distributions are displayed. The insets show the correlograms.

After this first study, the reaction mixtures were dialysed against water for 3 days resulting in macroscopic precipitation for all of them, which indicated aggregation of the nanostructures. The suspensions were freeze-dried to allow solid-state analysis and redissolution in good solvents in order to avoid light-scattering effect during spectroscopic measurements. Before analysis by FT-IR spectroscopy, the copolymers were freeze-dried over 48 h to avoid any trace of water in the samples that could conceal the EOA O-H stretch signal. FT-IR spectroscopy (Figure 3.10 and Table 3.3) informed on the substitution reaction *via* several bands. A broad band at 3350 cm^{-1} (O-H and N-H, stretch) indicated the presence of alcohol and amide groups and therefore the successful insertion of EOA into the copolymer. The signal strength is directly related to the quantity of the associated functionality and this is well indicated by the stronger signal for D50%+EOA compared to D20%+EOA. The absence of amide and alcohol signals for D0%+EOA demonstrated the stability of the MAIC and PAIC pendant groups to the reaction conditions, which ensured that no reaction took place in the corona or substitution of the chiral units. In addition, four bands in particular indicated that the substitution of PFP units was successful: 1761 cm^{-1} (C=O, stretch) and 1246 cm^{-1} (C-O, stretch) for the

ester function; 1516 cm^{-1} (C=C, stretch) for the PFP aromatic unit and 1037 cm^{-1} (C-F, stretch) for the fluorine. Their disappearance suggested the aminolysis reaction reached completion (>95%) and no PFP unit was detectable.

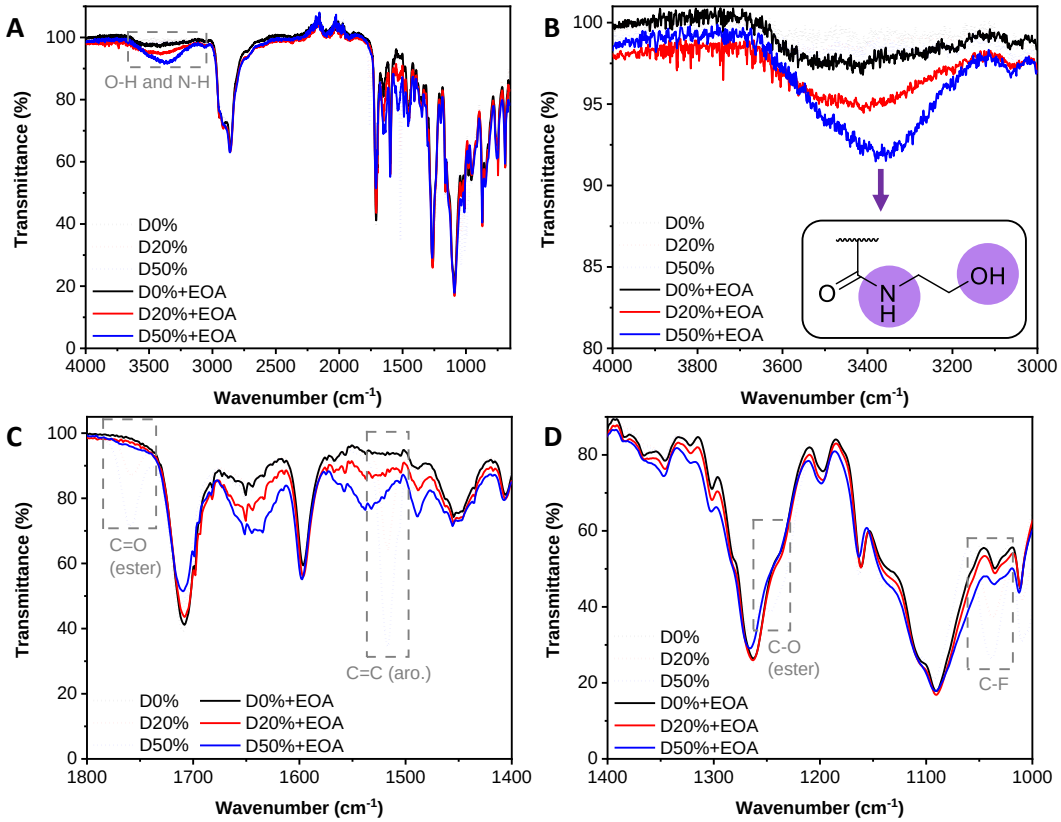

Figure 3.10. FT-IR spectra of the D0% (black), D20% (red) and D50% (blue) copolymers unreacted (dotted line) and reacted with EOA (solid line). (A) Full spectrum. (B) Zoom in the 4000-3000 cm^{-1} region. (C) Zoom in the 1800-1400 cm^{-1} region. (D) Zoom in the 1400-1000 cm^{-1} region.

To further verify the absence of PFP units, ^{19}F NMR spectroscopy of D20% and D50% before and after reaction was conducted (Figure 3.11). The presence of the three broad signals at δ = -153, -158 and -162 ppm which corresponded to the incorporated PFP units in the unreacted copolymers and indicated that the PFP moiety was resistant to the reaction conditions in the absence of amine as well as the dialysis. Moreover, the LWHH for the fluorine signals were similar to that calculated earlier for the P(MAIC)$_x$-*co*-P(FAIC)$_y$ DP 30 copolymer: 350 to 450 Hz. The complete disappearance of these signals

in the presence of amine suggested the complete reaction of the activated esters after aminolysis. The absence of molecular PFP signal also demonstrated that the reaction by-product, pentafluorophenol, was successfully removed during the purification step. By ^{1}H NMR spectroscopy, a new broad signal appeared after the aminolysis at δ = 2.30 ppm, in concordance with the EOA CH_2 protons at δ = 2.65 ppm (Figure 3.12). The broadness of the signal indicated that the moiety was inside the rigid helix which confirmed that the signal was not produced by molecular EOA.

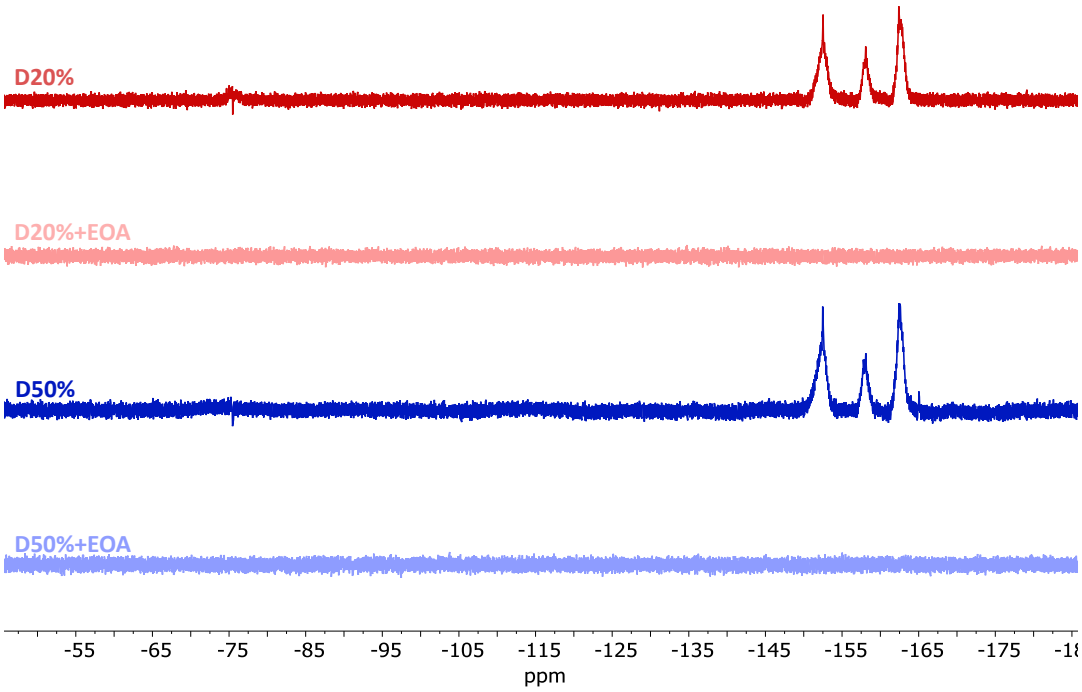

Figure 3.11. ^{19}F NMR of D20%, D20%+EOA, D50% and D50%+EOA in $CDCl_3$ (377 MHz, 298 K).

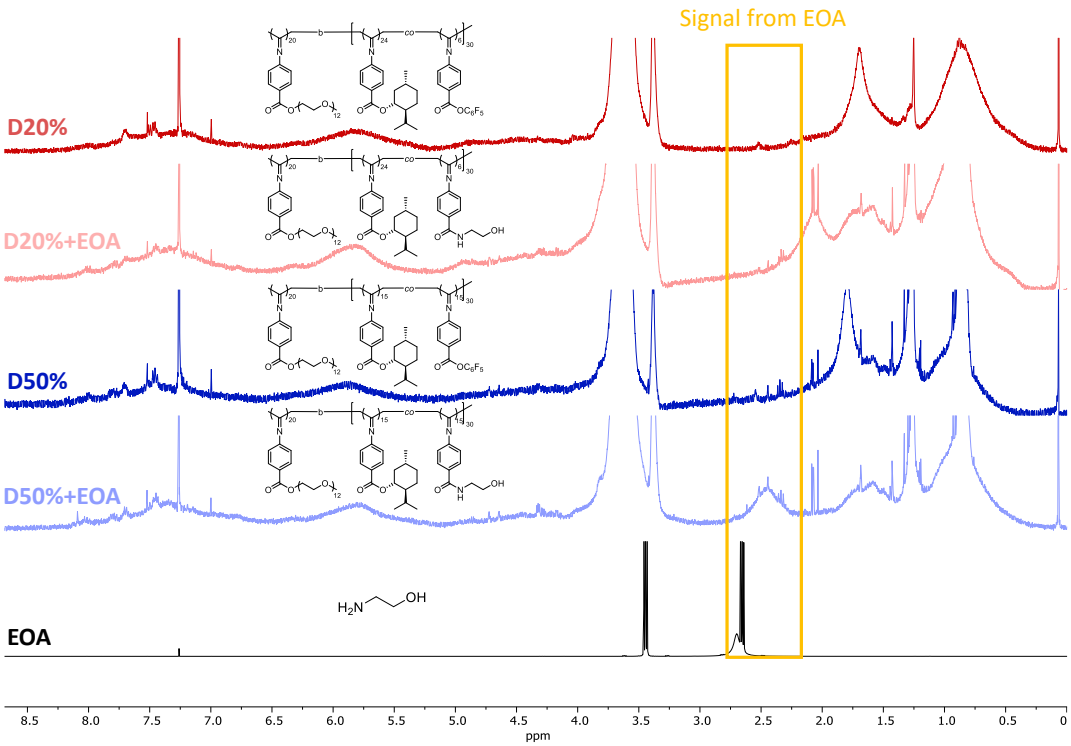

Figure 3.12. ^{1}H NMR of D20%, D20%+EOA, D50%, D50%+EOA and EOA in $CDCl_3$ (400 MHz, 298 K).

The SEC analysis of the copolymers before and after substitution showed no significant change in the molecular weight distribution of the D20%+EOA except a slight high molecular weight tailing. On the other hand, D50%+EOA displayed a broad MWD which indicated the alcohol functionalities interacted with the SEC column and artificially broadened the distribution. The SEC measurement was repeated in $CHCl_3$ and the broadening persisted which indicated this effect was not caused by the solvent or the solvent-specific column employed. Some of the tailing might also be caused by the possible hydrolysis of the PFP groups into carboxylic groups. Similar to the D100% homopolymer presented earlier, the D50%+EOA MWD was too broad to calculate M_w, M_n, and $Đ_M$. CD spectroscopy was employed to determine the change in helicity after the aminolysis (Figure 3.13). Both copolymers showed no significant change in helicity after substitution. The signal at $\lambda = 360$ nm stayed constant while the signal at 250 nm decreased

slightly. This latter absorption band was derived from the aromatic rings in the copolymer and therefore was expected to decrease after substitution. These data confirmed the stability of the helical backbone to the reaction conditions and their resilience to the substitution of 20% to 50% of the core units by a more polar moiety. Moreover, PICs are sterically locked however, modification with a less sterically hindered achiral group did not lead to decrease in the overall screw-sense selectivity for this copolymer which showed the robustness of its helicity.

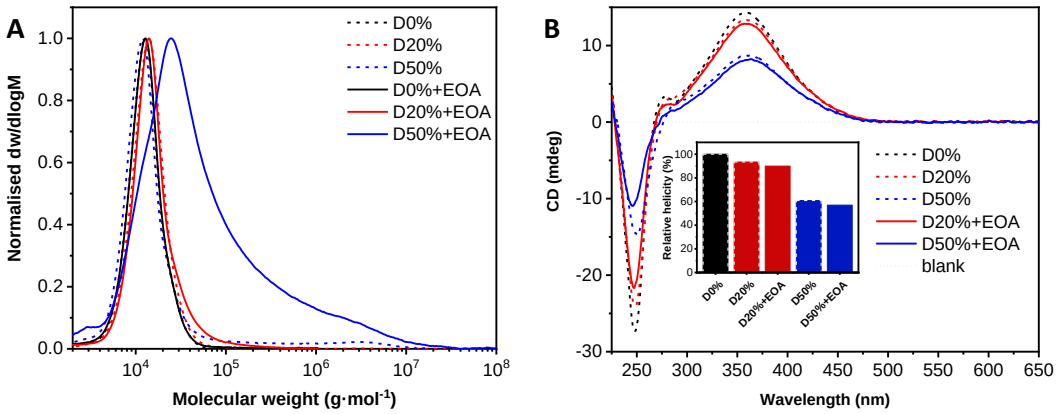

Figure 3.13. (A) Normalised SEC RI molecular weight distributions (THF + 2% v/v NEt_3, 40 °C, PS standards) and (B) CD (THF, 0.5 mg·mL^{-1}) spectra of D0%, D20%, D20%+EOA, D50% and D50%+EOA. The inset shows the helicity (CD at $\lambda = 360$ nm) of the copolymers compared to D0%.

Table 3.3. Characterisation of D0%, D20% and D50% reacted with EOA.

Polymer	D_{DLS} (nm)[a]	$M_{n,\,SEC}$ (kDa)[b]	$Đ_M$ [b]	CD_{360} (mdeg)[c]
D0%	20 (0.18)	11.2	1.24	14
D0%+EAO	20 (0.16)	11.4	1.22	-[e]
D20%	21 (0.14)	12.4	1.24	13
D20%+EOA	19 (0.17)	13.5	1.38	13
D50%	20 (0.25)	10.5	1.34	9
D50%+EOA	34 (1.00)	-[d]	-[d]	8

[a]Spherical particles size measured by DLS with PD in parenthesis. [b]Determined by SEC (THF + 2% v/v NEt_3) using PS standards. [c]CD (THF, 0.5 mg·mL^{-1}) signal at λ = 360 nm. [d]Molecular weight distribution is outside the calibration range. [e]Not measured.

3.4.2. Functionalisation with trifluoroethylamine

Trifluoroethylamine (TFEA) – a primary amine that contained fluorine – was reacted *in situ* after the NiCCo-PISA with D0%, D20% and D50% (Scheme 3.7). It was hypothesised that the fluorine functionality, once integrated into the copolymer, could be easily detected by ^{19}F NMR spectroscopy, where the signal for PFP is expected to be different than that of TFEA, after removal of the excess reactant. The fluorinated amine was reacted in the same way as EOA and the resulting solutions were analysed by DLS (Figure 3.14) to assess the impact of the new fluorinated core on the stability of the nanostructures. Similar to the EOA substitution, both D0%+TFEA and D20%+TFEA exhibited little to no change in diameter after the reaction. In contrast, the size distribution of D50%+TFEA was slightly altered, with diameter that increased from 20 nm to 23 nm and the PD from 0.25 to 0.32. In this instance, however, the result was not as substantial as it was for EOA. This less dramatic change in size distribution was likely a consequence of the similar solvophobicity of TFEA compared to PFP. Moreover, the correlation function's

maximum was quite low (0.6) and might have been a consequence of the change in refractive index that would become closer to that of DMSO after substitution.

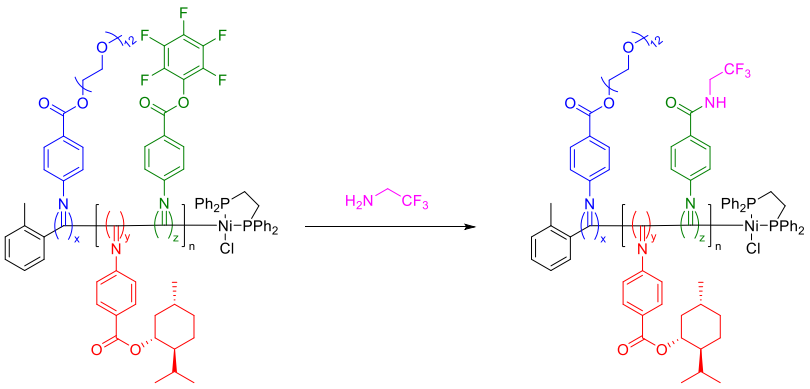

Scheme 3.7. Substitution of P(PAIC)$_x$-*b*-(P(MAIC)$_y$-*co*-P(FAIC)$_z$)$_n$ with trifluoroethylamine (TFEA).

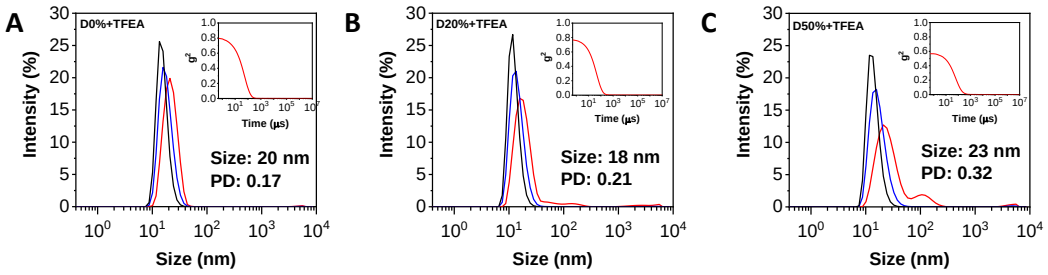

Figure 3.14. Size distributions of (A) D0%+TFEA, (B) D20%+TFEA, and (C) D50%+TEFA in DMSO obtained by DLS. The intensity (red line), volume (blue line) and number (black line) distributions are displayed. The insets show the correlograms.

By FT-IR spectroscopy, the analysis was similar to that of EOA. In particular, a new signal at 3300 cm^{-1} indicated the presence of the new amide functionality (Figure 3.15). The same signal as for the EOA reaction disappeared, which showed the completion of the reaction (>95%) except for D20%+TFEA. The excess used for the substitution reactions was proportional to the FAIC quantity in the diblock copolymers; therefore, the lower excess employed for the substitution of D20%+TFEA explains the non-completion of the reaction. The area of the signal for the unreacted PFP at 1705 cm^{-1} which

relates to the C=O ester group was calculated to correspond to a reaction completion of 70% *via* relative integration to the signal at 1597 cm^{-1} of C=N band that did not change during the reaction.

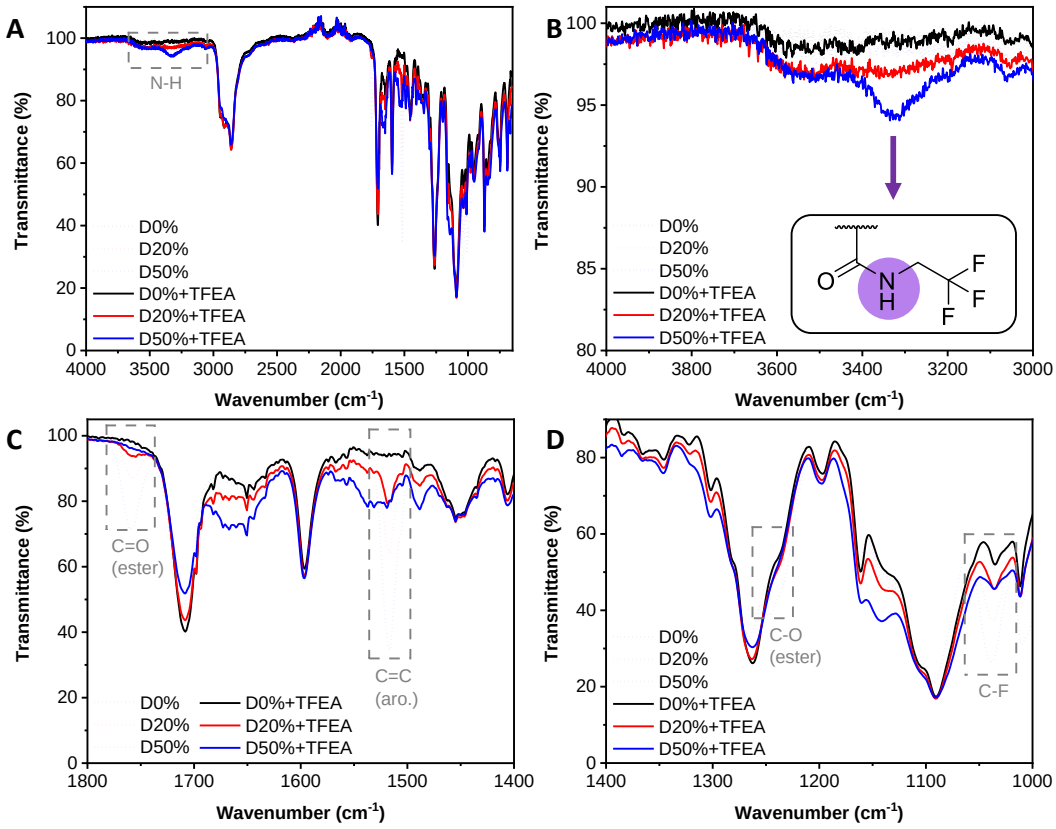

Figure 3.15. FT-IR spectra of the D0% (black), D20% (red) and D50% (blue) copolymers unreacted (dotted line) and reacted with TFEA (solid line). (A) Full spectrum. (B) Zoom in the 4000-3000 cm^{-1} region. (C) Zoom in the 1800-1400 cm^{-1} region. (D) Zoom in the 1400-1000 cm^{-1} region.

^{19}F NMR spectroscopy clearly indicated the change from the unreacted copolymers D20% and D50% to the TFEA substituted copolymers, D20%+TFEA and D50%+TFEA (Figure 3.16). The three signals for the PFP units disappeared and were replaced by a new broad signal at δ = -72 ppm, which showed that there was no PFP signal to be detected. The broadness of the signal also implied that the new fluorine moiety was part of the rigid helix. The absence of a sharp signal at δ = -73 ppm confirmed the complete incorporation of TFEA and the successful removal of unreacted TFEA by the purification steps. No new signal was detected by ^{1}H NMR

spectroscopy due to an overlap of the TFEA proton signal with the PAIC signal at δ = 3.75-3.25 ppm (Figure A3.24).

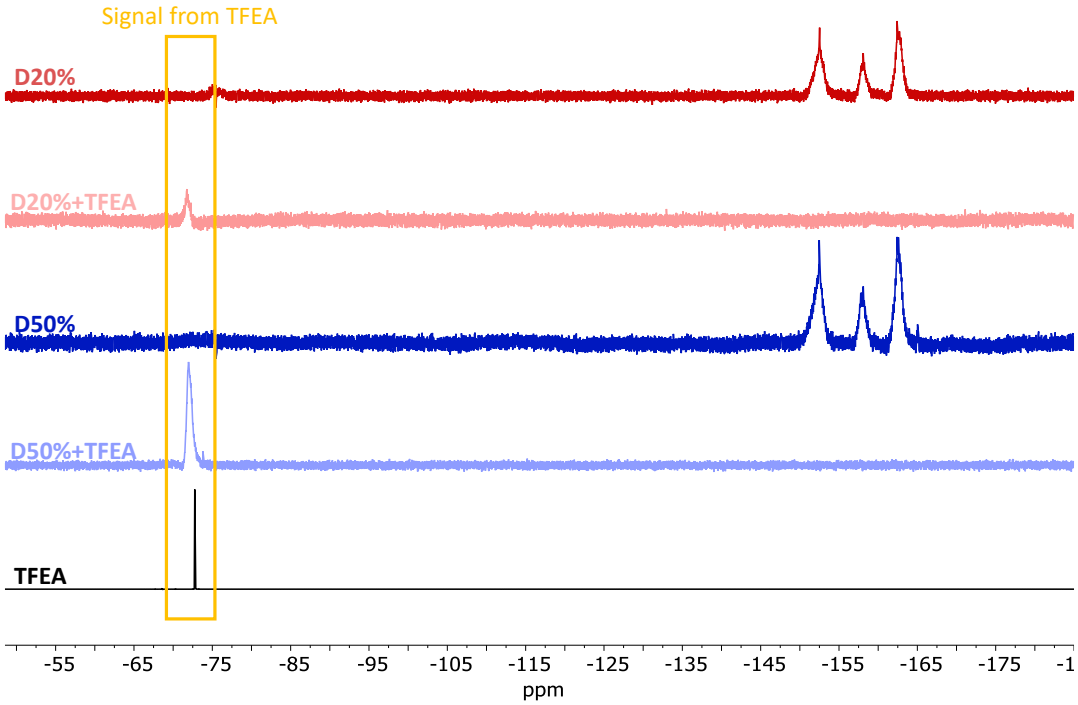

Figure 3.16. ^{19}F NMR of D20%, D20%+TFEA, D50%, D50%+TFEA and TFEA in $CDCl_3$ (377 MHz, 298 K).

The impact of the substitution of the copolymers by TFEA was noticeable by SEC (Figure 3.17A) but less so than for EOA. Only D50%+TFEA showed a clear tailing in the high molecular weight region, which indicated interaction of the copolymer with the SEC column. The TFEA unit chemistry diverges only slightly from the PFP, therefore the tailing was unlikely to arise from their interaction with the SEC column. However, it was likely to arise from the carboxylic acid pendant groups which came from the portion of PFP moieties that underwent hydrolysis. The tailing effect is much smaller than for D50%+EOA, which possibly indicated a small number of hydrolysed moieties. The CD spectra of the TFEA substituted polymers were similar to the spectra of the EOA substituted copolymers (Figure 3.17B). The helicity of the TFEA substituted copolymers decreased slightly; however, there was no

change detected that would indicate a complete loss of helicity or replacement of the menthyl chiral units with TFEA chiral moiety. The decrease was also more pronounced at $\lambda = 250$ nm than 360 nm for the reasons presented earlier for the EOA substitution – *i.e.* the signal at $\lambda = 250$ nm is derived from the aromatic rings in the copolymer and therefore is expected to decrease after substitution.

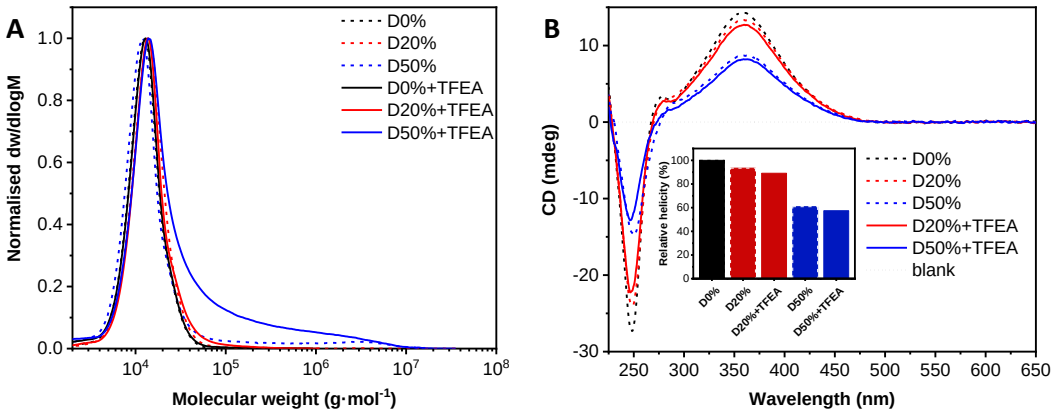

Figure 3.17. (A) Normalised SEC RI molecular weight distributions (THF + 2% v/v NEt_3, 40 °C, PS standards) of D0%, D0%+TFEA D20%, D20%+TFEA, D50% and D50%+TFEA. (B) CD (THF, 0.5 mg·mL^{-1}) spectra of D0%, D20%, D20%+TFEA, D50% and D50%+TFEA. The inset shows the helicity (CD at $\lambda = 360$ nm) of the copolymers compared to D0%.

Table 3.4. Characterisation of D0%, D20% and D50% reacted with TFEA.

Polymer	D_{DLS} (nm) [a]	$M_{n,SEC}$ (kDa) [b]	$Đ_M$ [b]	CD_{360} (mdeg) [c]
D0%	20 (0.18)	11.2	1.24	14
D0%+TFEA	20 (0.17)	11.4	1.25	-[e]
D20%	21 (0.14)	12.4	1.24	13
D20%+TFEA	18 (0.21)	13.0	1.20	13
D50%	20 (0.25)	10.5	1.34	9
D50%+TFEA	23 (0.32)	-[d]	-[d]	8

[a]Spherical particles size measured by DLS with PD in parenthesis. [b]Determined by SEC (THF + 2% v/v NEt_3) using PS standards. [c]CD (THF, 0.5 mg·mL^{-1}) signal at λ = 360 nm. [d]Molecular weight distribution is outside the calibration range. [e]Not measured.

3.4.3. Functionalisation with maleimide dye

To further analyse the copolymer's nanostructures and composition, a fluorescent aminochloromaleimide (ACM) was synthesised[66] for introduction into the nano-object cores (Scheme 3.8). The NiCCo-PISA mixtures were reacted for 24 h with five equivalents of ACM respective to the FAIC content in DMSO at 55 °C. By DLS, while the D20%+ACM copolymer still formed micelles of similar size to the unmodified diblock copolymer, the D50%+ACM copolymer's nano-object distribution indicated a possible disassembly of the nanostructures (Figure 3.18). The higher solvophilicity of the dye compared with the PFP units likely increased the solvability of the core which induced the solvation of the micelle unimer constituents.

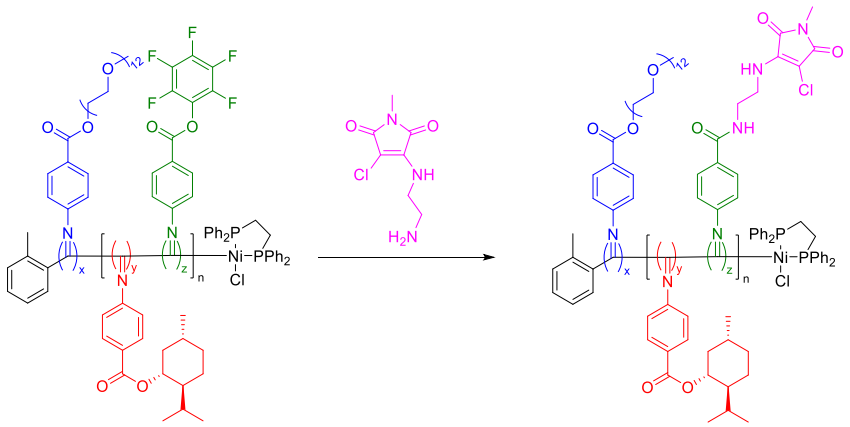

Scheme 3.8. Substitution of P(PAIC)$_x$-*b*-(P(MAIC)$_y$-*co*-P(FAIC)$_z$)$_n$ with a aminochloromaleimide (ACM).

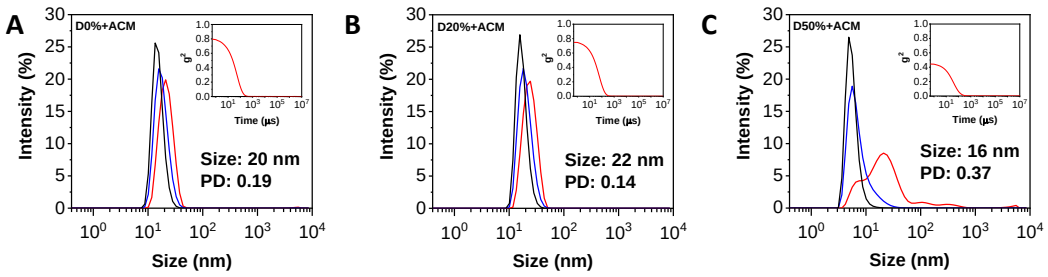

Figure 3.18. Size distributions of (A) D0%+AMC, (B) D20%+ACM, and (C) D50%+ACM in DMSO obtained by DLS. The intensity (red line), volume (blue line) and number (black line) distributions are displayed. The insets show the correlograms.

By FT-IR spectroscopy, decrease in the FAIC signals was detectable for both reactions but neither reached completion (Figure 3.19). The dye being hydrophilic, it was possible that its diffusion into the core might have been impeded by the hydrophobic nature of the core. Integration of the signal at 1760 cm^{-1} gave an apparent conversion of 50% and 70% for D20%+ACM and D50%+ACM, respectively. However, the dye-substituted copolymers' signal at 1760 cm $^{-1}$ showed a broader signal than the unreacted copolymers. The signal likely overlapped with the new amide signal which diminished artificially the conversion. This low conversion and therefore lower increase in core solvophilicity explain the better structural integrity of the dye-substituted copolymer micelles compared to the previous functionalised nanostructures (*i.e.*

D50%+EOA and D50%+TFEA). However, the following spectroscopic analyses are more qualitative than quantitative and are simply used to confirm the presence or absence of ACM.

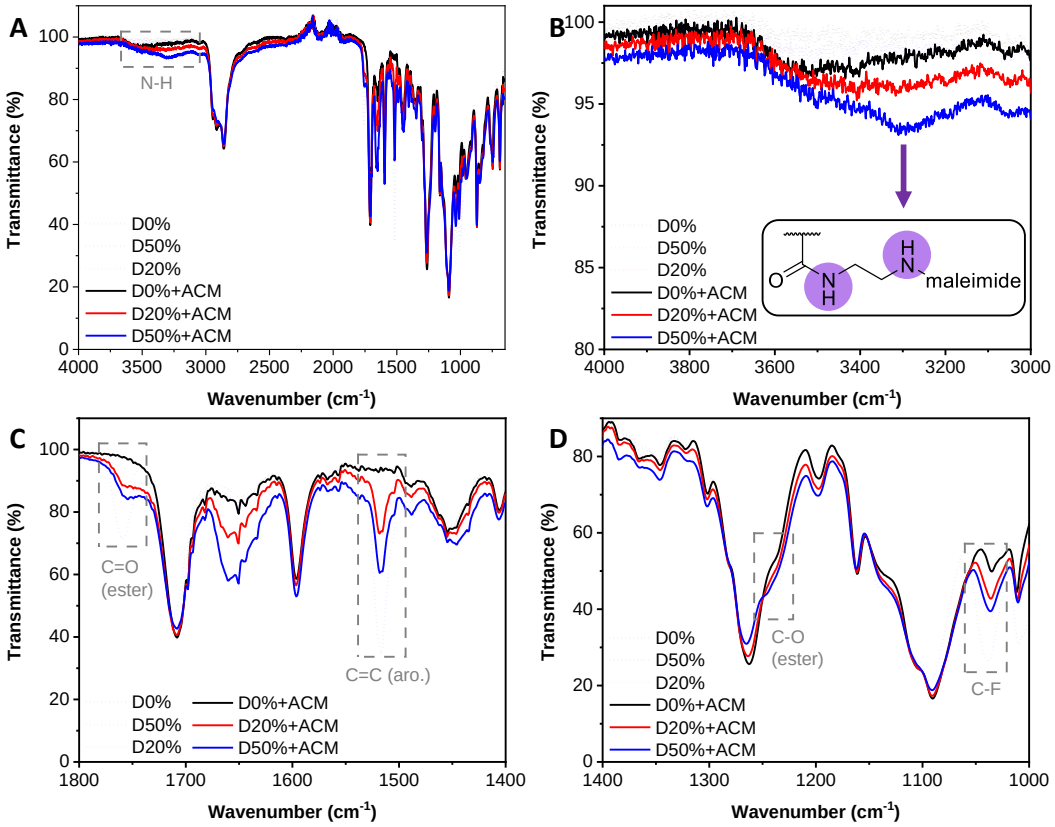

Figure 3.19. FT-IR spectra of the D0% (black), D20% (red) and D50% (blue) copolymers unreacted (dotted line) and reacted with ACM (solid line). (A) Full spectrum. (B) Zoom in the 4000-3000 cm^{-1} region. (C) Zoom in the 1800-1400 cm^{-1} region. (D) Zoom in the 1400-1000 cm^{-1} region.

SEC analysis of the dye-substituted copolymer showed no change in the molecular weight distribution for D0%+ACM which is consistent with no reaction of the maleimide with the PEG or menthyl units. The D20%+ACM copolymer showed a slight tailing in the high molecular weight region, while the D50%+ACM copolymer exhibited clear tailing in this region which indicated a large interaction of the dye-substituted copolymer with the SEC column (Figure 3.20A). As seen previously, the interaction arises from the functionalised moiety and can be augmented by the hydrolysed PFP pendant

groups. In the case of the dye-substituted copolymers, the secondary amine was likely to interact with the SEC column in the same way the alcohol functionalities did for the D50%+EOA copolymer. CD spectroscopy showed an increase of the CD signals at λ = 250 nm and 360 nm for both dye-substituted copolymers (Figure 3.20B). ACM is active in these regions as evidenced by its UV/Vis spectrum. CD spectroscopy measures the absorbance of the helical species and as a consequence of the ACM similar absorption to the copolymer, the CD signal was stronger. This further corroborates the successful introduction of the dye into the copolymer and demonstrates that the polymer does not completely obfuscates the grafted ACM. This would be important for circularly polarised light applications, where the dye's emission and its detection are essential.

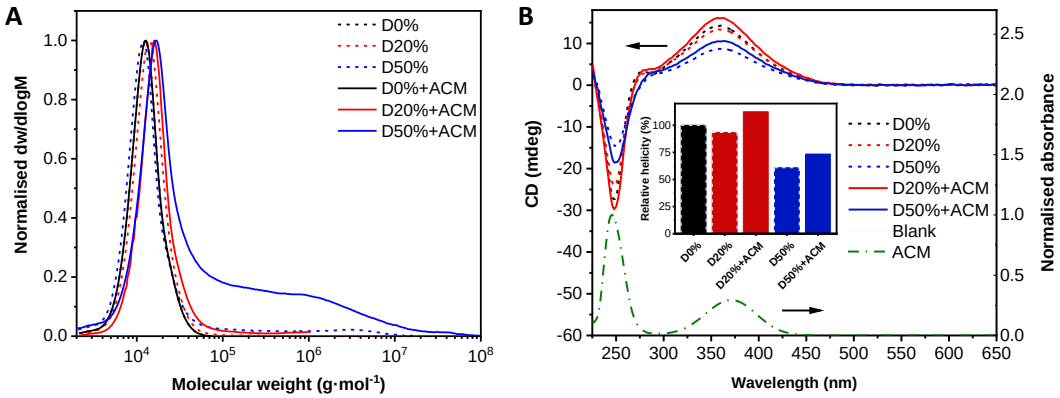

Figure 3.20. (A)Normalised SEC RI molecular weight distributions (THF + 2% v/v NEt_3, 40 °C, PS standards) and B) CD (THF, 0.5 mg·mL^{-1}) spectra of D0%, D0%+ACM D20%, D20%+ACM, D50% and D50%+ACM. The inset shows the helicity (CD at λ = 360 nm) of the copolymers compared to D0%.

The incorporation of the maleimide dye was also detected by UV/Vis spectroscopy, with an increase of the signal at λ = 360 nm the ACM signal which overlapped with the copolymer signal (Figure 3.21). In addition, the UV/Vis spectra of the copolymers in water were dramatically different between the different copolymers (Figure 3.21A); however, this might be a

consequence of light scattering by the nano-objects. Measurements made in THF (*i.e.* without assembly) show a difference in absorption in the 360 nm region that coincides with the absorption of the dye and the polymer (Figure 3.21B). This absorption increased coincident with higher ACM loading.

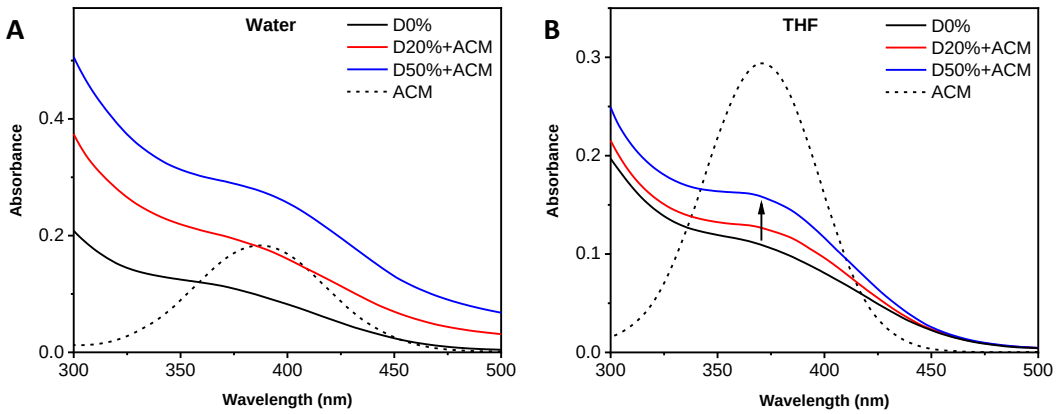

Figure 3.21. UV/Vis in (A) water, (B) THF spectra of the copolymers D0% (black line), D20%+ACM (red line) and D50%+ACM (blue line) compared to the spectrum of the free ACM (black dash).

By fluorescence spectrophotometry, while the original polymer D0% was not fluorescent in the absence of ACM substitution, an emission band was detected at 488 nm for the dye-substituted polymers in THF, in line with the fluorescence emission of the free dye (Figure 3.22A). Moreover, a solution of the copolymer D0% and the free ACM displayed a signal at the same wavelength which proved that the copolymer itself did not interfere with the wavelength maximum emission (λ_{em}). After transfer of the species in water, the λ_{em} for the dye-substituted nanostructures shifts to 510 nm with a wavelength maximum emission difference (Δ_λ) of 22 nm while for the free ACM the change is larger with the new λ_{em} at 577 nm and $\Delta_\lambda = 89$ nm (Figure 3.22B). The maleimide dye is a solvatochromic fluorophore, therefore, the λ_{em} is dependent on its environment and particularly on the environment polarity. The changes in λ_{em} for the different solvents indicated that the dye was located in environments with different polarity. Therefore, the shifts in λ_{em} from the free

dye in water to the free ACM in THF indicated the passage from a highly polar solvent to a less polar solvent. The λ_{em} of the nanostructures that contained the dye suggests that the micelle core is less polar than water but more than THF. The high signal-to-noise ratio for ACM emission in water was a consequence of the poor emission of the dye in water because of quenching by water molecules. Maleimide dyes are effectively quenched in protic solvents as a result of electron driven proton transfer from the hydrogen bonding between water and the fluorophore.[67] The sharp signals present in the emission spectra of the D50%+ACM micelles in water are a consequence of the scattering of light by the nano-objects.

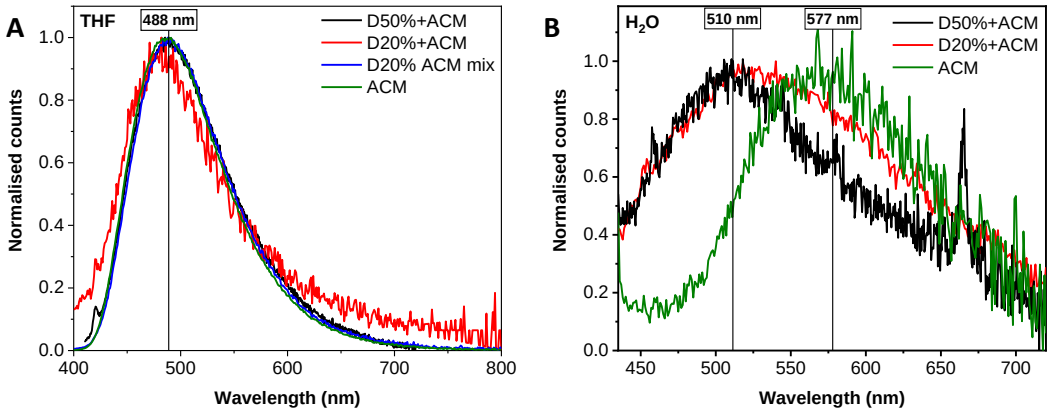

Figure 3.22. Fluorescence spectra for the different copolymer substituted by ACM along with the free ACM in (A) THF and (B) water.

The lifetime measurements of the dye displayed vast discrepancies between the different copolymers (Figure 3.23A, Table 3.5). Indeed, the less ACM was present, the shorter the measured lifetime of the dye in the copolymer which indicated quenching, possibly by the polymer itself, occurred. To investigate the influence of the spatial location of the dye, solutions of the D20% and D50% copolymer with the relevant quantity of the free ACM were measured in THF. No shift in lifetime was observed, which reinforced the idea that the decrease of lifetime was a consequence of the dye being in close proximity to the polymer (Figure 3.23B). The lifetime measurements in water indicated

that ACM was readily quenched which is expected for a maleimide dye since they are effectively quenched by small amount of water (Figure 3.23C). Even within the hydrophobic core of the NiCCo-PISA micelles, the presence of water is impossible to avoid and is sufficient to quench ACM.

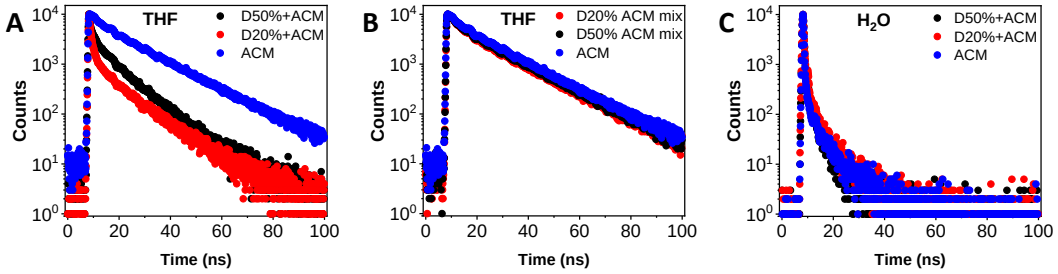

Figure 3.23. Lifetime measurement spectra. (A) Comparison between D20%+ACM, D50%+ACM and the free ACM in THF. (B) Copolymers mix with ACM and free ACM in THF. (C) Copolymers mix with ACM and free ACM in water.

Table 3.5. Lifetime measurements of the different assembled copolymers and free ACM in water and THF.

Sample	$\tau_{Av,a}$ (ns)	$\tau_{Av,I}$ (ns)
D20%+ACM (THF)[a]	6.5 ± 0.2	11.1 ± 0.3
D20%+ACM (water)[b]	1.1 ± 0.1	4.2 ± 0.1
D20% ACM (mix, THF)[c]	13.8 ± 0.1	15.4 ± 0.1
D50%+ACM (THF)[a]	7.7 ± 0.2	9.9 ± 0.3
D50%+ACM (water)[b]	0.7 ± 0.1	3.2 ± 0.1
D50% ACM (mix, THF)[c]	14.2 ± 0.1	15.5 ± 0.1
ACM (THF)	14.8 ± 0.1	15.7 ± 0.1
ACM (water)	0.8 ± 0.1	5.1 ± 0.2

[a]Functionalised copolymer after solution in THF (disassembled) [b]Functionalised copolymer in water (assembled) [c]Mixture of non-functionalised copolymer and ACM in THF (disassembled)

Table 3.6. Characterisation of D0%, D20% and D50% reacted with ACM.

Polymer	D_{DLS} (nm)[a]	$M_{n,\,SEC}$ (kDa)[b]	$Đ_M$[b]	CD_{360} (mdeg)[c]
D0%	20 (0.18)	11.2	1.24	14
D0%+ACM	20 (0.19)	11.2	1.24	-[e]
D20%	21 (0.14)	12.4	1.24	13
D20%+ACM	22 (0.14)	14.5	1.28	16
D50%	20 (0.25)	10.5	1.34	9
D50%+ACM	16 (0.37)	-[d]	-[d]	10

[a]Spherical particles size measured by DLS with PD in parenthesis. [b]Determined by SEC (THF + 2% v/v NEt_3) using PS standards. [c]CD (THF, 0.5 mg·mL^{-1}) signal at λ = 360 nm. [d]Molecular weight distribution is outside the calibration range. [e]Not measured.

3.5. Conclusion

Helical-core micelles that could easily be functionalised by different primary amine nucleophiles were synthesised by NiCCo-PISA and analysed by different analytical methods (NMR, FT-IR, fluorescence, and CD spectroscopy, and SEC) which showed the effective introduction of a range of functionalities that included alcohols, fluorinated units, fluorescent dyes, and catalytic moieties (Table 3.7). ^{19}F NMR and FT-IR spectroscopies were employed to evaluate the reaction completion. High conversions were observed (≥70%) for most reactions. The PFP units inside the hydrophobic core were shown to be resistant to hydrolysis under the reaction conditions and against dialysis, which indicated that these micelles could be employed for applications in aqueous conditions. When hydrophilic amines were employed (*i.e.* EOA and ACM) disassembly of the micelles was observed for the D50% substituted copolymer while the D20% copolymer nanostructures stayed stable after substitution which demonstrated the effect of the modification of the core's polarity on the nano-objects structural integrity. Possible hydrolysis of the copolymers was detected by SEC with the appearance of a high molecular weight tail for D50% substituted copolymers however, the effect was marginal. The introduction of a maleimide dye inside of the micelle cores indicated, by the presence of a solvatochromic effect, a difference in hydrophobicity of the nanostructures' core with the aqueous milieu. Lifetime measurements indicated the presence of water in the core that readily quenched the grafted ACM.

Table 3.7. Overview of the characterisation of the copolymer nanoparticles synthesised in this Chapter.

Polymer	FAIC (%)	Nucleophile	D_{DLS} (nm)[a]	$M_{n,\,SEC}$ (kDa)[b]	$Đ_M$[b]	CD_{360} (mdeg)[c]
D0%	0	-[d]	20 (0.18)	11.2	1.24	14
D0%+EAO	0	EOA	20 (0.16)	11.4	1.22	-[f]
D0%+TFEA	0	TFEA	20 (0.17)	11.4	1.25	-[f]
D0%+ACM	0	ACM	20 (0.19)	11.2	1.24	-[f]
D20%	20	-[d]	21 (0.14)	12.4	1.24	13
D20%+EOA	20	EOA	19 (0.17)	13.5	1.38	13
D20%+TFEA	20	TFEA	18 (0.21)	13.0	1.20	13
D20%+ACM	20	ACM	22 (0.14)	14.5	1.28	16
D50%	50	-[d]	20 (0.25)	10.5	1.34	9
D50%+EOA	50	EOA	34 (1.00)	-[e]	-[e]	8
D50%+TFEA	50	TFEA	23 (0.32)	-[e]	-[e]	8
D50%+ACM	50	ACM	16 (0.37)	-[e]	-[e]	10

[a]Spherical particles size measured by DLS with PD in parenthesis. [b]Determined by SEC (THF + 2% v/v NEt_3) using PS standards. [c]CD (THF, 0.5 mg·mL^{-1}) signal at $\lambda = 360$ nm. [d]Unreacted copolymer [e]Molecular weight distribution is outside the calibration range. [f]Not measured

3.6. Appendix

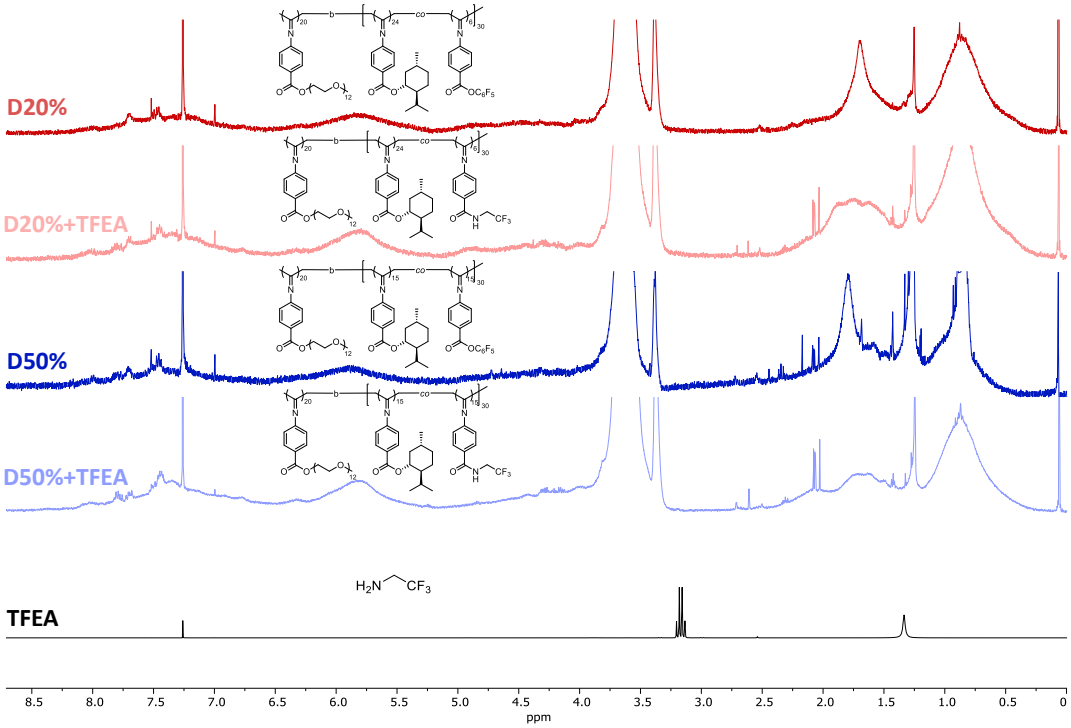

Figure A3.24. ^{1}H NMR of D20%, D20%+TFEA, D50%, D50%+TFEA and TFEA in $CDCl_3$ (400 MHz, 298 K).

3.7. References

1. Lutz, J.-F.; Sumerlin, B. S., The Role of Click Chemistry in Polymer Synthesis. In *Click Chemistry for Biotechnology and Materials Science*, J. Lahann ed.; John Wiley & Sons, Ltd 2009; pp 69-88.
2. Boaen, N. K.; Hillmyer, M. A., *Chem. Soc. Rev.* 2005, 3, 267-275.
3. Gauthier, M. A.; Gibson, M. I.; Klok, H.-A., *Angew. Chem. Int. Ed.* 2009, 1, 48-58.
4. Günay, K. A.; Theato, P.; Klok, H.-A., *J. Polym. Sci. A Polym. Chem.* 2013, 1, 1-28.
5. Battistella, C.; Yang, Y.; Chen, J.; Klok, H.-A., *ACS Omega* 2018, 8, 9710-9721.
6. Das, A.; Theato, P., *Macromolecules* 2015, 24, 8695-8707.
7. Zhong, Y.; Zeberl, B. J.; Wang, X.; Luo, J., *Acta Biomater.* 2018, 21-37.
8. Busatto, N.; Keddie, J. L.; Roth, P. J., *Polym. Chem.* 2020, 3, 704-711.
9. Ren, J.; Liu, H.; Zhang, X.; Hu, Y.; Zhou, G.; Masuda, T., *Polym. Chem.* 2020, 20, 3427-3433.
10. Larsen, M. B.; Herzog, S. E.; Quilter, H. C.; Hillmyer, M. A., *ACS Macro Lett.* 2018, 1, 122-126.
11. Larsen, M. B.; Wang, S.-J.; Hillmyer, M. A., *J. Am. Chem. Soc.* 2018, 38, 11911-11915.
12. Sruthi, P. R.; Anas, S., *J. Polym. Sci.* 2020, 8, 1039-1061.
13. Crisan, D. N.; Creese, O.; Ball, R.; Brioso, J. L.; Martyn, B.; Montenegro, J.; Fernandez-Trillo, F., *Polym. Chem.* 2017, 31, 4576-4584.
14. Kubo, T.; Swartz, J. L.; Scheutz, G. M.; Sumerlin, B. S., *Macromol. Rapid Commun.* 2019, 1, 1800590.
15. Atkins, C. J.; Patias, G.; Town, J. S.; Wemyss, A. M.; Eissa, A. M.; Shegiwal, A.; Haddleton, D. M., *Polym. Chem.* 2019, 5, 646-655.
16. Krappitz, T.; Feibusch, P.; Aroonsirichock, C.; Hoven, V. P.; Theato, P., *Macromolecules* 2017, 4, 1415-1421.
17. Kuroishi, P. K.; Bennison, M. J.; Dove, A. P., *Polym. Chem.* 2016, 46, 7108-7115.
18. Kubo, T.; Figg, C. A.; Swartz, J. L.; Brooks, W. L. A.; Sumerlin, B. S., *Macromolecules* 2016, 6, 2077-2084.
19. Barlow, T. R.; Brendel, J. C.; Perrier, S., *Macromolecules* 2016, 17, 6203-6212.
20. Ono, R. J.; Liu, S. Q.; Venkataraman, S.; Chin, W.; Yang, Y. Y.; Hedrick, J. L., *Macromolecules* 2014, 22, 7725-7731.
21. Lee, J.; Han, S.; Kim, M.; Kim, B.-S., *Macromolecules* 2020, 1, 355-366.

22. Chen, Y.; Wilson, J. A.; Petersen, S. R.; Luong, D.; Sallam, S.; Mao, J.; Wesdemiotis, C.; Becker, M. L., *Angew. Chem. Int. Ed.* 2018, 39, 12759-12764.
23. Mocny, P.; Menétrey, M.; Klok, H.-A., *Macromolecules* 2019, 21, 8394-8403.
24. Sinclair, F.; Chen, L.; Greenland, B. W.; Shaver, M. P., *Macromolecules* 2016, 18, 6826-6834.
25. Lim, Y. H.; Heo, G. S.; Rezenom, Y. H.; Pollack, S.; Raymond, J. E.; Elsabahy, M.; Wooley, K. L., *Macromolecules* 2014, 14, 4634-4644.
26. Sims, M. B.; Lessard, J. J.; Bai, L.; Sumerlin, B. S., *Macromolecules* 2018, 16, 6380-6386.
27. Wu, Y.-C. M.; Swager, T. M., *J. Am. Chem. Soc.* 2019, 32, 12498-12501.
28. Park, N. H.; Fevre, M.; Voo, Z. X.; Ono, R. J.; Yang, Y. Y.; Hedrick, J. L., *ACS Macro Lett.* 2016, 11, 1247-1252.
29. Dai, Y.; Zhang, X.; Xia, F., *Macromol. Rapid Commun.* 2017, 19, n/a-n/a.
30. Gibson, M. I.; Fröhlich, E.; Klok, H.-A., *J. Polym. Sci. A Polym. Chem.* 2009, 17, 4332-4345.
31. Coiai, S.; Passaglia, E.; Cicogna, F., *Polym. Int* 2019, 1, 27-63.
32. Agar, S.; Baysak, E.; Hizal, G.; Tunca, U.; Durmaz, H., *J. Polym. Sci. A Polym. Chem.* 2018, 12, 1181-1198.
33. Noy, J.-M.; Friedrich, A.-K.; Batten, K.; Bhebhe, M. N.; Busatto, N.; Batchelor, R. R.; Kristanti, A.; Pei, Y.; Roth, P. J., *Macromolecules* 2017, 18, 7028-7040.
34. Easterling, C. P.; Coste, G.; Sanchez, J. E.; Fanucci, G. E.; Sumerlin, B. S., *Polym. Chem.* 2020, 17, 2955-2958.
35. Alkattan, M.; Prunet, J.; Shaver, M. P., *Angew. Chem. Int. Ed.* 2018, 39, 12835-12839.
36. Yuen, A. Y.; Bossion, A.; Veloso, A.; Mecerreyes, D.; Hedrick, J. L.; Dove, A. P.; Sardon, H., *Polym. Chem.* 2018, 18, 2458-2467.
37. Liu, X.; Hu, D.; Jiang, Z.; Zhuang, J.; Xu, Y.; Guo, X.; Thayumanavan, S., *Macromolecules* 2016, 17, 6186-6192.
38. Sehlinger, A.; Verbraeken, B.; Meier, M. A. R.; Hoogenboom, R., *Polym. Chem.* 2015, 20, 3828-3836.
39. Kakuchi, R.; Theato, P., *ACS Macro Lett.* 2014, 4, 329-332.
40. Alizadeh, M.; Kilbinger, A. F. M., *Macromolecules* 2018, 11, 4363-4369.
41. Gody, G.; Roberts, D. A.; Maschmeyer, T.; Perrier, S., *J. Am. Chem. Soc.* 2016, 12, 4061-4068.
42. Bell, C. A.; Hedir, G. G.; O'Reilly, R. K.; Dove, A. P., *Polym. Chem.* 2015, 42, 7447-7454.

43. König, N. F.; Al Ouahabi, A.; Poyer, S.; Charles, L.; Lutz, J.-F., *Angew. Chem. Int. Ed.* 2017, 25, 7297-7301.
44. Zhang, S.; Zou, J.; Zhang, F.; Elsabahy, M.; Felder, S. E.; Zhu, J.; Pochan, D. J.; Wooley, K. L., *J. Am. Chem. Soc.* 2012, 44, 18467-18474.
45. Cho, S.; Heo, G. S.; Khan, S.; Huang, J.; Hunstad, D. A.; Elsabahy, M.; Wooley, K. L., *Macromolecules* 2018, 9, 3233-3242.
46. Sirianni, Q. E. A.; Rabiee Kenaree, A.; Gillies, E. R., *Macromolecules* 2019, 1, 262-270.
47. Zhu, Y.; Batchelor, R.; Lowe, A. B.; Roth, P. J., *Macromolecules* 2016, 2, 672-680.
48. Foster, J. C.; Matson, J. B., *Macromolecules* 2014, 15, 5089-5095.
49. Jochum, F. D.; Theato, P., *Macromolecules* 2009, 16, 5941-5945.
50. Zhang, Q.; Schattling, P.; Theato, P.; Hoogenboom, R., *Eur. Polym. J.* 2015, 435-441.
51. Gaballa, H.; Lin, S.; Shang, J.; Meier, S.; Theato, P., *Polym. Chem.* 2018, 24, 3355-3358.
52. Lin, S.; Das, A.; Theato, P., *Polym. Chem.* 2017, 7, 1206-1216.
53. Liu, Y.; Pauloehrl, T.; Presolski, S. I.; Albertazzi, L.; Palmans, A. R. A.; Meijer, E. W., *J. Am. Chem. Soc.* 2015, 40, 13096-13105.
54. Couturaud, B.; Georgiou, P. G.; Varlas, S.; Jones, J. R.; Arno, M. C.; Foster, J. C.; O'Reilly, R. K., *Macromol. Rapid Commun.* 2019, 2, 1800460.
55. Yin, J.; Xu, L.; Han, X.; Zhou, L.; Li, C.; Wu, Z.-Q., *Polym. Chem.* 2017, 3, 545-556.
56. Xu, L.; Xu, X.-H.; Liu, N.; Zou, H.; Wu, Z.-Q., *Macromolecules* 2018, 19, 7546-7555.
57. Su, M.; Liu, N.; Wang, Q.; Wang, H.; Yin, J.; Wu, Z.-Q., *Macromolecules* 2016, 1, 110-119.
58. Duan, P.; Cao, H.; Zhang, L.; Liu, M., *Soft Matter* 2014, 30, 5428-5448.
59. Li, Y.; Wang, T.; Liu, M., *Soft Matter* 2007, 10, 1312-1317.
60. Okazaki, Y.; Goto, T.; Sakaguchi, R.; Kuwahara, Y.; Takafuji, M.; Oda, R.; Ihara, H., *Chem. Lett.* 2016, 4, 448-450.
61. Li, H.; Zheng, X.; Su, H.; Lam, J. W. Y.; Sing Wong, K.; Xue, S.; Huang, X.; Huang, X.; Li, B. S.; Tang, B. Z., *Sci. Rep.* 2016, 19277.
62. Liu, M.; Zhang, L.; Wang, T., *Chem. Rev.* 2015, 15, 7304-7397.
63. Han, J.; You, J.; Li, X.; Duan, P.; Liu, M., *Adv. Mater.* 2017, 19, 1606503.
64. Green, M. M.; Reidy, M. P.; Johnson, R. D.; Darling, G.; O'Leary, D. J.; Willson, G., *J. Am. Chem. Soc.* 1989, 16, 6452-6454.
65. Takei, F.; Onitsuka, K.; Takahashi, S., *Polym. J.* 2000, 6, 524-526.
66. Xie, Y.; Husband, J. T.; Torrent-Sucarrat, M.; Yang, H.; Liu, W.; O'Reilly, R. K., *Chem. Commun.* 2018, 27, 3339-3342.

67. Staniforth, M.; Quan, W.-D.; Karsili, T. N. V.; Baker, L. A.; O'Reilly, R. K.; Stavros, V. G., *J. Phys. Chem. A* 2017, 34, 6357-6365.

Chapter 4 Cross-linked and stimulus-responsive NiCCo-PISA micelles

4.1. Declaration of authorship

Transmission electron microscopy was conducted by Mr Spyridon Varlas and the synthesis of 4,2-[1-(2-amino-ethoxy)-1-methyl-ethoxy]-ethylamine was performed by Dr Maria Chiara Arno at the University of Birmingham.

4.2. Introduction

Smart nanomaterials that undergo alteration when subjected to a particular stimulus have received plenty of attention[1-4] and the design and development of these stimuli-responsive materials are of interest for applications such as drug-delivery[5-8], biological imaging[7, 9, 10] chiroptical materials[11] and sensing[12-14]. A wide variety of different triggers has been developed: pH[12, 15-20], temperature[19, 21-25], light[26-31], magnetic field[32-34], CO_2,[35] glucose,[36-38] β-cyclodextrin,[39] ions,[14, 40, 41] electric potential,[42] and redox potential,[16, 43-46] which allows to generate systems with a range of different responses such as changes in size,[19, 24, 31] morphologies,[47-49] light emission,[11, 13] and permeability[27, 28, 50, 51] that are a result of an alteration in the solubility of the NPs. Complex systems were elaborated to allow multi-stimuli responsive structures.[33, 50, 52-57] Stimuli-responsive polymer nano-objects are achieved by using responsive polymers for the corona and/or the core of the NPs. Additionally, reactive cross-linkers can be employed to impart responsivity to a system. Cross-linked nano-objects are of interest for the stability they confer to the nano-objects which allows the conservation of their morphology under changes to their solvation state (*i.e.* different solvent or drying).

An interesting application of stimuli-responsive NPs is the triggered disassembly of self-assembled nanostructures usually intended for drug delivery systems that need to release their cargo in a specific environment such as the particularly acidic or reductive conditions found in tumours. The introduction of a cross-linker that is cleaved under specific conditions allows the controlled stimuli-responsive disassembly which depends on the cross-linker that is employed such as disulfide bonds reactive towards thiols and reductive compounds,[43, 45, 58, 59] or acetals reactive towards acidic conditions.[16, 60, 61] Thus,

different stimuli can be leveraged to trigger disassembly of nanostructures under specific conditions.

Helical polymers such as polyisocyanides have successfully been employed in stimuli-responsive systems and in a noteworthy report, Wu and co-workers developed a dual-responsive nanomaterial able to release its cargo in a cell environment (Figure 4.1). They synthesised an amphiphilic triblock copolymer poly(*L*-lactic acid)(-IR780)-*b*-hydrophobic poly(phenyl isocyanide)-*b*-hydrophilic poly(phenyl isocyanide) (PLLA(-IR780)-HBPPI-HPPPI) through sequential living copolymerisation in one-pot where IR780 is a NIR absorptive dye. The copolymer self-assembled into nanostructures and, in addition to exhibiting a rapid cellular intake (10-12 min) in part as a result of its helical structure that mimics that of cell penetrating proteins,[62, 63] it combined two triggers that increased the solubility of the core in water. Firstly, the HBPPI block contained phenylboronic pinacol ester that was oxidation responsive and hydrolysed in the presence of H_2O_2 to boronic acid. Secondly, the PLLA core was pH-responsive and hydrolysed under acidic conditions. When these two triggers were combined, the micelles disassembled which released their cargo.[52]

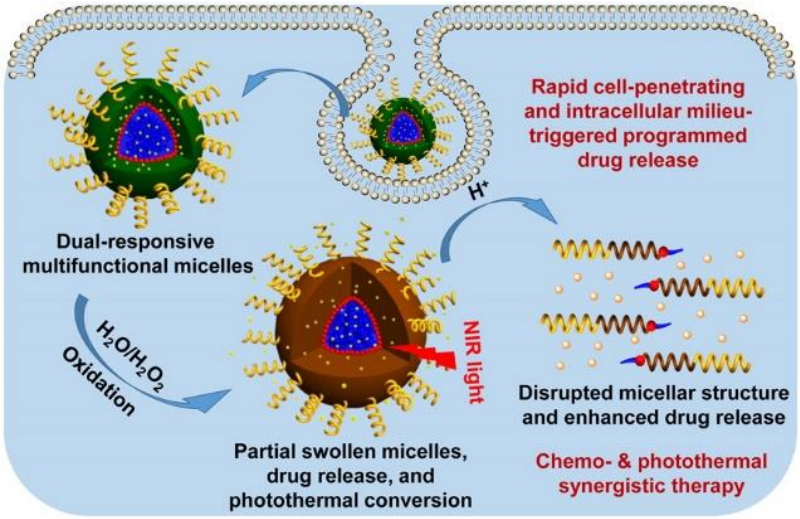

Figure 4.1. Cellular intake and stimuli-responsive behaviour of self-assembled PIC micelles. Reproduced from the work of Zong-Quan and co-workers published in ACS, Macromolecules.[52]

In this Chapter, the inherent thermoresponsivity of the NiCCo-PISA NPs which resulted from the PEG corona was studied. Moreover, the utility of P(PAIC)-*b*-P(MAIC-*co*-FAIC) nanostructures synthesised by NiCCo-PISA followed by PPM as presented in Chapter 3 was explored using different primary amines and alcohols as a platform to achieve core cross-linked micelles which provided stability to the nanostructures. Then, the PPM with reactive cross-linkers to achieve stimulus-responsive micelles that could be affected by pH or a reducing environment was investigated.

4.3. Thermoresponsive NiCCo-PISA micelles

Thermoresponsive nanostructures can be employed to release their cargo at a certain temperature or, if they are used as nanoreactors, this behaviour can be leveraged to allow facile recovery of the nanomaterial. The corona of the NiCCo-PISA micelles is composed of brush polymers decorated with PEG which is a known thermoresponsive polymer that exhibits lower critical solution temperature (LCST) behaviour in water.[64] This responsive corona was hypothesised to lead to an increase in hydrophobicity when heated above its cloud point, which induced the thermally-triggered precipitation of the NPs.[65] The thermoresponsivity of the NPs was measured *via* turbidimetry using a UV/Vis spectrometer by monitoring the change in transmitted light at $\lambda = 600$ nm (a wavelength at which the polymer does not absorb) over a range of temperatures. Turbidimetry was measured at different concentrations of D0% in water (0.5, 2 and 5 mg·mL^{-1}) in order to assess the effect of NP concentration on the thermoresponsive behaviour (Figure 4.2). The solution that contained 5 mg·mL^{-1} of NPs exhibited a strong attenuation of transmitted light with an onset at 52 °C and reached complete attenuation (*i.e.* 0% transmittance) at 75 °C, which demonstrated the thermally-triggered aggregation of the NPs (pictures in Figure 4.2). The 2 mg·mL^{-1} solution displayed a higher temperature onset at 61 °C followed by a sharp decrease in transmitted light from 100% to 15% at 75 °C. This first decrease was followed by a second slow drop in transmitted light until 5% transmittance was reached at 95 °C. This loss of intensity in two stages was explained by a first aggregation at 60 °C as a result of the increase of hydrophobicity of the NPs, followed by a slower aggregation into bigger objects of the first precipitated aggregates. The solution of 0.5 mg mL^{-1} NPs exhibited the highest onset at 67 °C and the weakest light attenuation reached a plateau of 71% at 85 °C before a sharp loss of intensity

at 95 °C which decreased to 63%. For all concentrations, the thermally-triggered aggregation was irreversible which was hypothesised to be a result of the entanglement of the brush-like corona between the aggregated micelles.[66] The different trigger temperature between the experiments demonstrated a concentration effect on the thermoresponsivity of the NPs where NP concentration had an inversely proportional influence on the temperature at which the particles start aggregating.

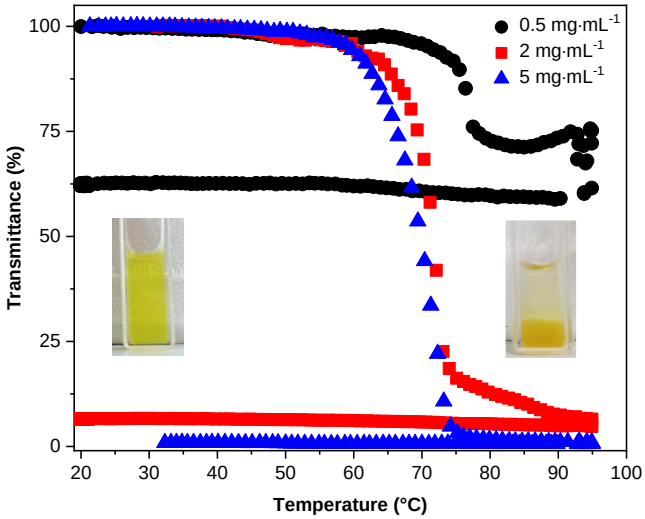

Figure 4.2. UV/Vis (λ = 600 nm) turbidimetry of D0% at 0.5 mg·mL^{-1} (blue triangles), 2 mg·mL^{-1} (red squares) and 5 mg·mL^{-1} (black circles). Pictures of the 5 mg·mL^{-1} solution before (left) and after (right) thermally-triggered aggregation.

The evolution of the thermoresponsivity of the NPs was also followed by DLS which allowed the monitoring of the nano-objects size. Two concentrations, 0.5 and 5 mg·mL^{-1}, were studied. The evolution of the size measured by DLS in solution was a rough indicator of the aggregation of the NPs by thermally-triggered precipitation. For the 0.5 mg·mL^{-1} solution, the nano-objects size stayed stable around 72 nm until the solution reached 80 °C after which the size increased rapidly along with the count rate to achieve 2450 nm at 95 °C. The trigger temperature found by DLS (80 °C) was higher than the one measured by UV/Vis (67 °C) which was first hypothesised to be a result of the difference in the technique employed - light scattering *vs* light absorption –

however, the size distribution (PD) and derived count rate (DCR) analysis were more in line with the UV/Vis turbidometry results. The PD change was more sensitive with a trigger temperature at 65 °C where the PD decreased from 0.23 to 0.08 at 80 °C before it increased again to 0.65 at 95 °C. This behaviour indicated a possible separation of the aggregates present in the initial solution between 65 °C and 80 °C before aggregation occurs again after 80 °C. The value of the DCR provides information on the presence or absence of NPs in the suspension where an increase in DCR indicates aggregation and a decrease indicates a sedimentation or dissolution of the particles. For both concentrations, the DCR, after a first phase of stagnation, increased exponentially until it reached a maximum then decreased to, or below, the initial value. This behaviour was explained by the aggregation of the NPs that would increase the DCR then, the precipitation out of solution and deposition at the bottom of the cuvette would lead to a decrease in DCR value as there are fewer objects in suspension to measure. The onset and maximum values were found at 65 °C and 85 °C respectively which corresponded to the values found by UV/Vis turbidimetry. This demonstrated the similarity of the behaviour observed by UV/Vis turbidimetry (transmittance) and DLS turbidimetry (PD and DCR). The results for the 5 $mg \cdot mL^{-1}$ solutions indicated a similar behaviour which corresponded to the UV/Vis turbidimetry (Figure 4.3).

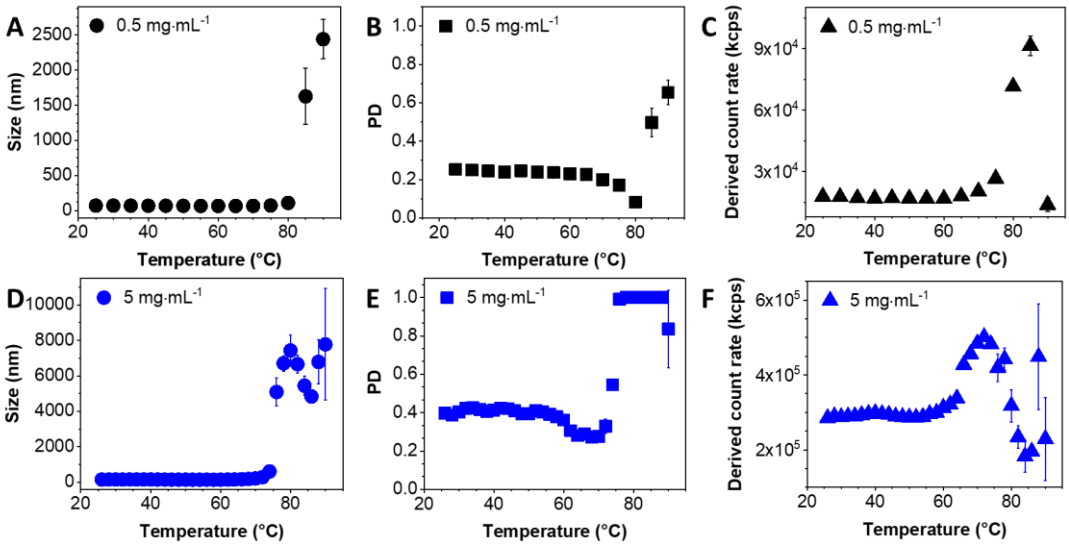

Figure 4.3. DLS monitoring of thermoresponsive behaviour of D0% at different concentration. In black, 0.5 mg·mL^{-1} measurement of the (A) size, (B) PD and (C) derived count rate in function of the temperature, and in blue, 5 mg·mL^{-1} measurement of the (D) size, (E) PD and (F) derived count rate in function of the temperature.

4.4. Cross-linking of NiCCo-PISA micelles with stable aliphatic diamine cross-linkers

Building on the functionalisation of the NiCCo-PISA micelles demonstrated in Chapter 3, cross-linking was attempted to impart stability to the nanostructures with aliphatic diamine cross-linkers: 1,2-ethanediamine (EDA), 1,4-butanediamine (BDA) and 1,6-hexanediamine (HDA) (Scheme 4.1). The three selected cross-linkers have different alkyl chain length and therefore variable hydrophobicity and size that could influence their diffusion inside of the core of the nano-objects. The change in the spacer length was hypothesised to influence the size of the micelles after transfer into a non-selective solvent where the longer chains would lead to larger size of the solvated nanoparticles. The amount of cross-linker employed must be carefully evaluated to avoid free amines that would increase the hydrophilicity of the micelles' core and could lead to disassembly of the nanostructures as evidenced in Chapter 3 with the EOA substituted micelles.

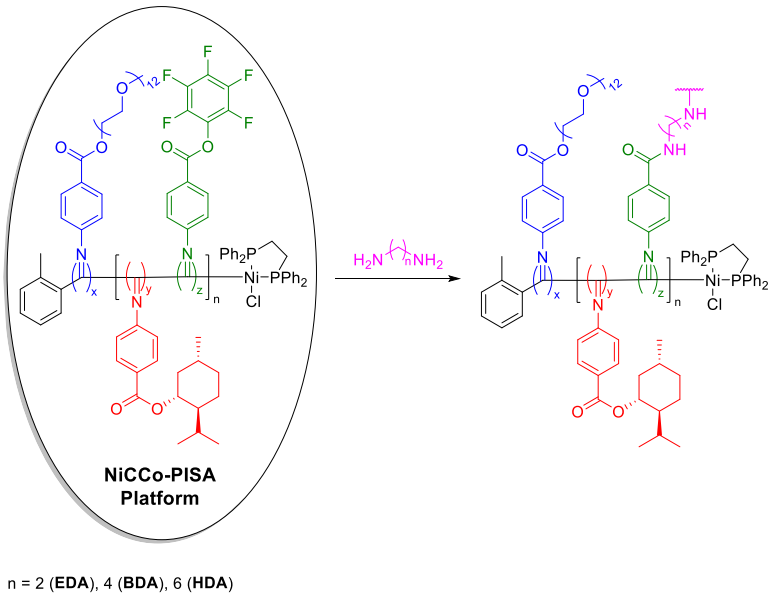

Scheme 4.1. Overview of the NiCCo-PISA block copolymer as a platform for alkyl diamine cross-linked nanomaterials.

The NiCCo-PISA suspensions of D20% and D50% were first reacted with 0.5 equivalent of cross-linker - relative to the quantity of FAIC - in DMSO at 55 °C for 24 h. Similar to what was described in Chapter 3, no base was employed in order to reduce the hydrolysis of the pentafluorophenyl esters (PFP) during the reaction. To assess the completion of the reaction, an aliquot of each reaction mixture was dialysed and freeze-dried before analysis by FT-IR spectroscopy. By observing the signals from the PFP C=O ester at 1755 cm^{-1} and C=C aromatic at 1520 cm^{-1} it was possible to monitor the reaction. These signals revealed the presence of PFP in both the D20% and D50% cross-linked copolymers which indicated that the reactions were incomplete. The cross-linking was repeated with 0.6 equivalent of cross-linker and the reaction was continued for three days. These new conditions pushed the substitution to completion (Figure 4.4, for D20% results see Figure A4.17). Moreover, the presence of the PFP unit after the incomplete reactions and dialysis, proved the stability of this functionality in aqueous milieu under the reaction conditions selected. Therefore, the core of the non-substituted D20% and D50% nanostructures was proven to be stable in water. As explained above, the freeze-dried copolymers were analysed by FT-IR spectroscopy to investigate the change in functional groups after the cross-linking where the PFP signals are expected to disappear and be replaced by new amide signals. For all the amine cross-linkers, the signal from the C=O ester at 1755 cm^{-1} was replaced by a weaker and broader signal at 1750 cm^{-1} which originated from the new amide bond (C=O stretching). In Chapter 3, the signal at 1755 cm^{-1} was used to monitor the completion of the reaction, however the presence of the new amide signal made it unsuitable to determine the reaction yield. Hence, the signal for the C=C aromatic signal from the PFP unit at 1520 cm^{-1} was employed to monitor the presence of PFP in the copolymers. Two other signals indicated the presence or absence of PFP: 1240 cm^{-1} for the C-O ester bond

and 1030 cm^{-1} for the C-F bond. However, D20% did not contain enough PFP units to allow detection of a C-O ester bond. A new broad signal appeared at 3300 cm^{-1} for all the cross-linked micelles which indicated that the new amide N-H bond.

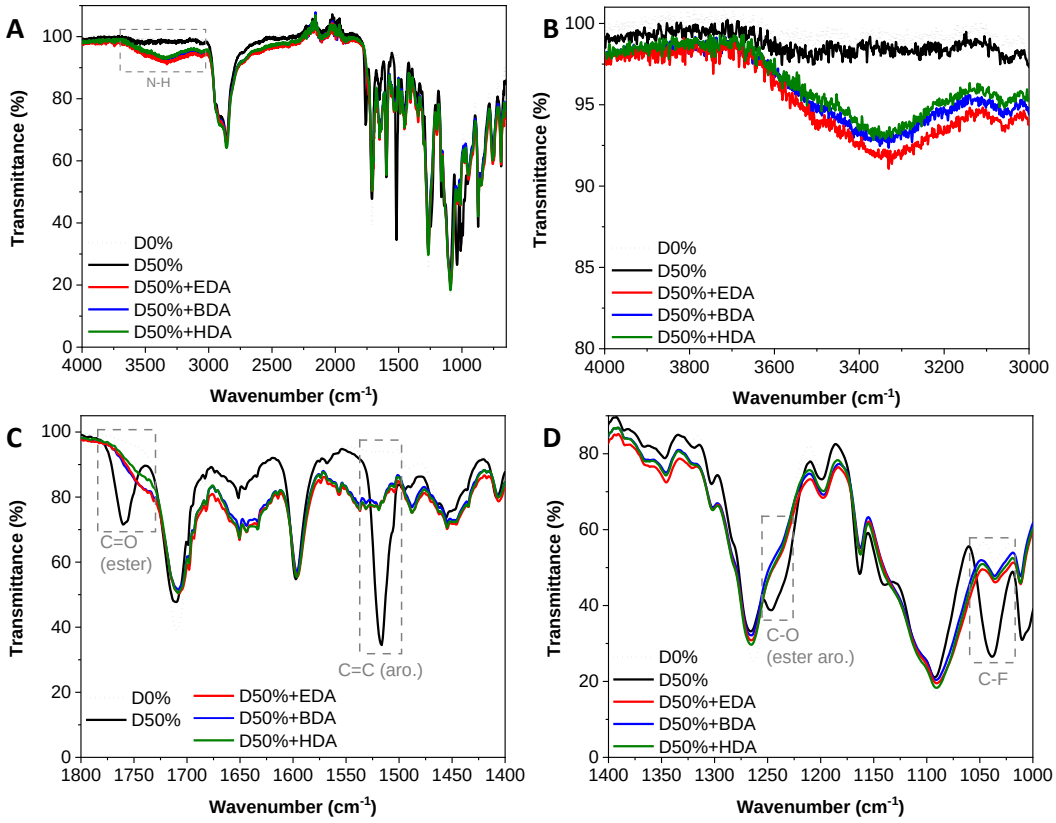

Figure 4.4. FT-IR spectra of the D50% copolymer (black line) cross-linked with EDA (red line), BDA (blue line) and HDA (green line).(A) Full spectrum. (B) Zoom in the 4000-3000 cm^{-1} region. (C) Zoom in the 1800-1400 cm^{-1} region. (D) Zoom in the 1400-1000 cm^{-1} region.

The analysis of the crude reaction mixtures by DLS indicated sizes of 18, 22 and 20 nm, and PDs of 0.11, 0.22 and 0.14 for D50%+EDA, D50%+BDA and D50%+HDA respectively (Figure A4.18 and Figure A4.19), in line with the previous results observed in Chapter 2. The cross-linking on both D20% and D50% did not have any visible effect on the nanostructures' stability. The DMSO suspensions of cross-linked nanostructures were transferred into water by dialysis over three days. The first observation was the transition from a transparent solution for the DMSO mixtures to opaque

suspensions after the transfer in water. This visual cue was validated by the DLS measurements where the measured size of the particles increased from approximatively 20 nm in DMSO to 80-200 nm in water with PDs which ranged from 0.19 to 0.24, which indicated a larger range of sizes. These larger apparent sizes could have been a consequence of the swelling of the NPs in water, their aggregation or a combination of these two effects. One way to rapidly verify if nanoparticles are stabilised by cross-linking is to transfer them into a non-selective solvent for both blocks. Non-cross-linked nano-objects will disassemble (*i.e.* dissolve) and this loss of integrity is indicated by a low correlogram function and very small size by DLS. On the other hand, effectively cross-linked NPs produce a significant size distribution and correlogram by DLS. To assess this, the dialysed micelles were freeze-dried and re-solvated in THF. Analysis of these solutions by DLS indicated that the presence of nano-objects of similar dimensions to the NPs suspended in DMSO (Figure 4.5A-C) while the non-crosslinked nano-objects displayed no self-assembly (Figure 4.5D), which suggested that the cross-linked NPs were stable in a non-selective solvent, which demonstrated an efficient cross-linking and the successful stabilising effect of the cross-linked core. When the different cross-linkers were compared, the sizes and PDs of the NPs in DMSO, no significant change was detected while in THF the sizes and PDs decreased with the increase of the cross-linker chain length. This effect was especially noticeable for the D50% series. D50%+EDA – the shortest chain with two carbons – displayed a size of 40 nm in THF while D50%+BDA – four carbons – and D50%+HDA – six carbons – exhibited 32 nm and 28 nm respectively. Unlike what was hypothesised, the shorter the chain, the larger the size. Given the rigidity of the copolymer backbone it is possible that the shorter cross-linkers when reacted once were less capable of reaching another reactive PFP pendant group - because of their length and/or lack of flexibility - to complete the cross-linking

which left unreacted amines in the core. The presence of free amine in the core would lead to an increase in the core's hydrophilicity and larger sizes when the nano-objects are fully solvated.

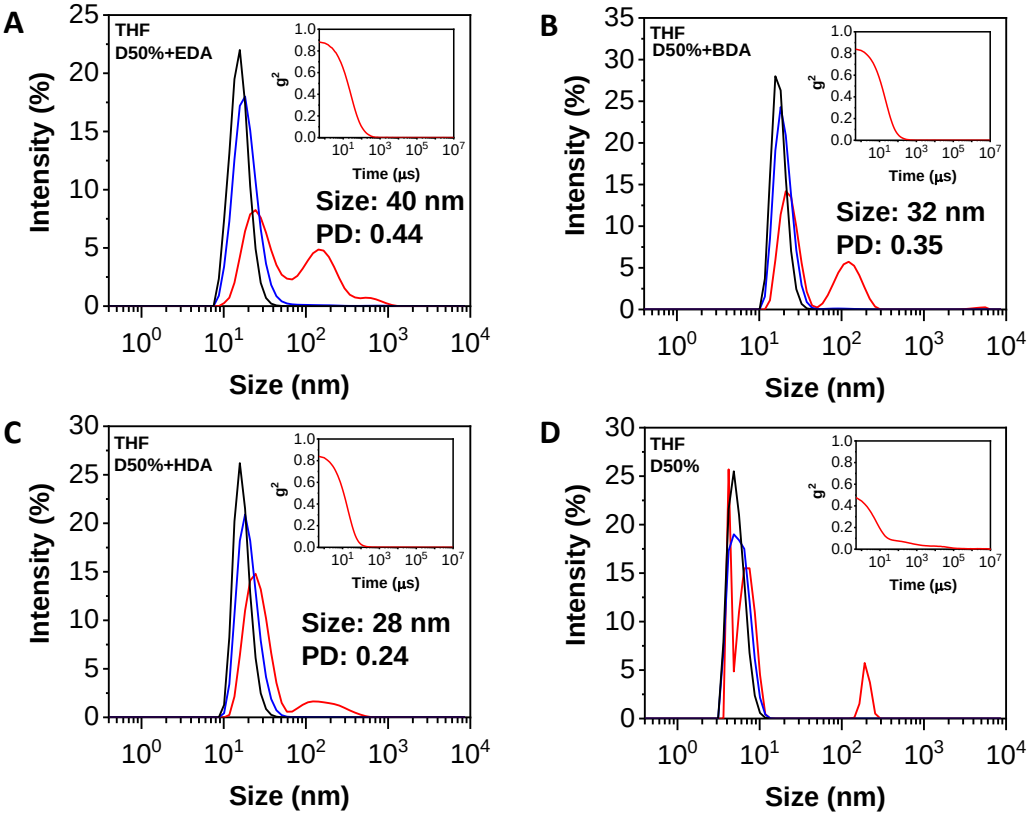

Figure 4.5. Size distributions of (A) D50%+EDA, (B) D50%+BDA, (C) D50%+HDA and (D) D50% in THF obtained by DLS. The intensity (red line), volume (blue line) and number (black line) distributions are displayed. The insets show the correlograms.

In light scattering, the signal that originates from aggregates of the measured NPs can artificially broaden the correlogram and increase the measured size. Analysis by multi-angle DLS (MADLS) allows the partial differentiation between the diffusion modes (*i.e.* the signal that comes from the individual nano-objects) and the spurious modes not caused by Brownian motion but by small amount of large scattering species such as dust, bubbles or aggregates. D0%, D50%+EDA, D50%+BDA and D50%+HDA suspensions of 0.1 mg·mL^{-1} in water were analysed after filtration on a 0.22 µm Nylon filter to remove bigger particles such as dust. The decay rate (Γ) was calculated from

the correlation function measured at angles 40° to 150° and a Γ *vs* q^2 plot (Equation 4.1) was constructed for each copolymer solution (Figure A4.20):

$$\Gamma = q^2 D \qquad 4.1$$

Where q is the wave vector (a function of the measurement angle) and D is the apparent diffusion coefficient. The slope of the linear regression represents the diffusion coefficient (D) in the Einstein-Stokes equation (Equation 4.1):

$$R_h = \frac{k_B T}{6\pi\eta D} \qquad 4.2$$

Where k_B is the Boltzmann constant, T is the absolute temperature and η is the solvent's viscosity. When executed for our systems, the linear regressions showed a $R^2 \geq 0.99$ which indicated a good statistical concordance. When the hydrodynamic radii (R_h) for the copolymer nanoparticles in suspension were calculated, this technique yielded smaller size than DLS which ranged from 70 to 90 nm with smaller discrepancies between the values but still quite far from what would be expected from 20 nm cross-linked particles transferred into water (Table A4.3). However, aggregation caused increase of the measured sizes were still possible.

To verify the potential aggregation of the nano-objects, zeta-potential of the different suspension of micelles in water were measured. The zeta-potential is a measure of the potential difference between the colloidal dispersions medium and the stationary layer of fluid attached to the dispersed particle. If the zeta-potential of a nanoparticles dispersion is comprised between ±30 mV, the repulsive electrostatic forces are too low to avoid the attractive forces between the nanoparticles that led to their contact and entanglement visualised as their aggregation and precipitation out of solution (*i.e.* flocculation).[67] The zeta potential of the solution of micelles varied between 7 and -27 mV (Table 4.1)

therefore, the surface charges of the NPs are too low to avoid aggregation which justified the large sizes measured by DLS in water.

To observe the actual morphology of the cross-linked nano-objects after the transfer into water, TEM images were taken of the D50%+HDA suspension. Spherical micelles with similar sizes to the ones observed in DMSO were visible, which reinforced the hypothesis that the large sizes measured by DLS and MADLS came from flocculation (Figure 4.6). On the TEM images, aggregates of individual micelles were observed which confirmed the flocculation effect and showed that the morphology of the spherical nanoparticles did not change. Flocculation happened when the particles were transferred from DMSO into water and was a consequence of the change in polarity of the solvent. During dialysis, the environment slowly became more polar which leads to a greater attraction between the amphiphilic stabilised micelles. The aggregation of the NPs was certainly aggravated by the brush nature of the corona block. Indeed, the corona was a densely grafted brush polymer $P(PAIC)_{30}$ and the neutral PEG side chains were therefore more likely to entangle and favour aggregation of the NPs. The average size of the NPs in the dry state TEM images was calculated by measuring 250 NPs and gave 15 ±3 nm (average ±standard deviation), smaller than the size measured by DLS in DMSO. This can be explained by shrinkage of the micelles caused upon drying for TEM preparation. Moreover, the fact that the individual micelles could be distinguished from the aggregates led to smaller sizes than the ones measured by DLS and MADLS in water.

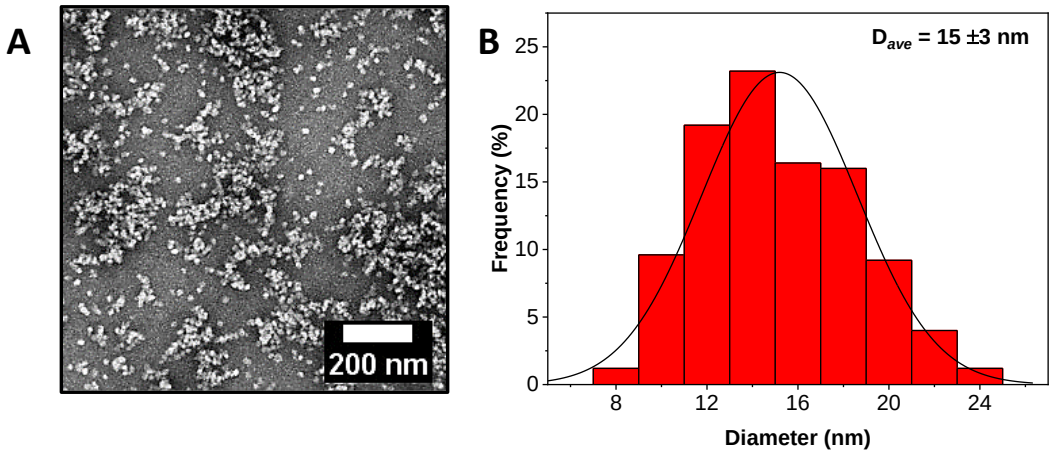

Figure 4.6. (A) Dry-state TEM image of D50%+HDA after dialysis. (B) Histogram of spherical particles' size distribution measured from particle analysis of TEM images of 250 particles.

Table 4.1. Characterisation of the NiCCo-PISA copolymers before and after cross-linking.

Polymer	D_{DLS} DMSO[a] (nm)	D_{DLS} THF[a] (nm)	D_{DLS} H_2O[a] (nm)	D_{TEM}[b] (nm)	Zeta pot. (mV)
D0%	20 (0.18)	-[c]	100 (0.20)	21 ±7	-15 ±5
D20%	21 (0.14)	-[c]	46 (0.25)	-[d]	-17 ±4
D20%+EDA	21 (0.12)	36 (0.30)	190 (0.27)	-[d]	-17 ±3
D20%+BDA	21 (0.13)	33 (0.28)	180 (0.19)	-[d]	-2 ±3
D20%+HDA	21 (0.12)	34 (0.37)	200 (0.19)	-[d]	3 ±3
D50%	22 (0.16)	-[c]	140 (0.15)	-[d]	7 ±7
D50%+EDA	18 (0.11)	40 (0.44)	170 (0.24)	-[d]	5 ±5
D50%+BDA	22 (0.22)	32 (0.35)	80 (0.19)	-[d]	0 ±4
D50%+HDA	20 (0.14)	28 (0.24)	100 (0.20)	15 ±3	-1 ±3

[a]Hydrodynamic radius measured by DLS at a 173° angle. PD is in parenthesis. [b]Dried state TEM from water suspension of NPs. [c]No assemblies. [d]Not measured

Measurement of the helicity of the micelle core was conducted by CD spectroscopy of the cross-linked micelles in THF to ensure solvation of both blocks at 0.5 mg·mL^{-1}. This analysis revealed that for all systems the core was

still helical after the cross-linking reactions. A measurable decrease of the CD signal at $\lambda = 360$ nm (CD_{360}) was detected for D50% reacted with EDA, BDA and HAD, from 9 mdeg for the unreacted copolymer to 6 mdeg for the cross-linked micelles (Figure 4.7 and Table A). The decrease was smaller for the D20% cross-linked micelles. While D20%+EDA was at a similar level than the unsubstituted D20% copolymer at 13 mdeg, D20%+BDA and D20%+HAD decreased to 11 mdeg and 12 mdeg, respectively. The D50% original helix contained more "defects" (*i.e.* achiral moieties) and had a lower CD_{360} than D20%. Thus, a small decrease in the overall helicity caused by the cross-linking reaction had a larger impact on the final helicity. However, the drop was not complete, and the helicity was mainly retained (>60%) after the cross-linking reaction for both D20% and D50%-based micelles. This was encouraging for applications that would leverage the helical core of the nano-objects and proved the stability of the core's helices to the reaction conditions employed.

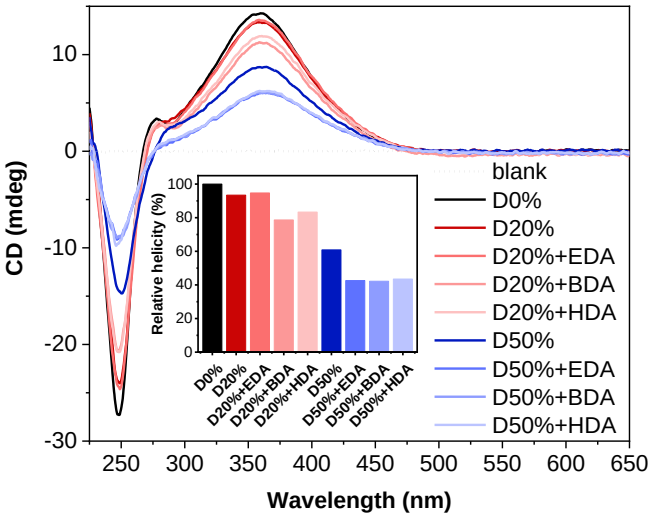

Figure 4.7. CD (THF, 0.5 mg·mL^{-1}) spectra of (A) the unsubstituted D20% and its cross-linked counterparts, and (B) the unsubstituted D50, and its cross-linked counterparts. D0% and a blank are added as reference. The inset shows the helicity (CD at $\lambda = 360$ nm) of the copolymers compared to D0%

4.5. Cross-linking of NiCCo-PISA micelles with responsive cross-linkers

After cross-linking with aliphatic diamines, the introduction of reactive cross-linkers that offer a response to a stimulus or take part in a reaction as catalyst was explored. Two primary amine cross-linkers were investigated as the responsive cross-linkers: cystamine (CA) that contained a redox sensitive disulfide bridge and 2-[1-(2-amino-ethoxy)-1-methyl-ethoxy]-ethylamine (AEE) that had a pH sensitive acetal linker (Scheme 4.2).

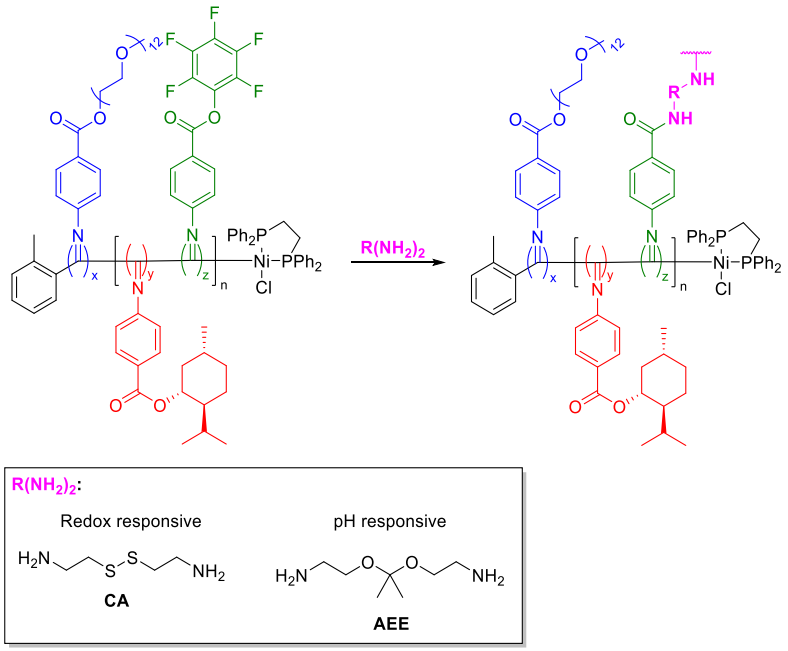

Scheme 4.2. Overview of the NiCCo-PISA block copolymer as a platform for cross-linked nanomaterials with responsive cross-linker.

The same reaction conditions as the previous cross-linking experiments were employed and FT-IR spectroscopy analysis showed completion of the reactions for both CA and AEE cross-linking (Figure 4.8, for D20% results see Appendix). The new signal for the amide N-H bond at 3400 cm^{-1} was present for the CA and AEE cross-linked copolymers. This area is also where the O-H bond signal for carboxylic acid is present and the lack of signal for D0% indicated the absence of hydrolysis.

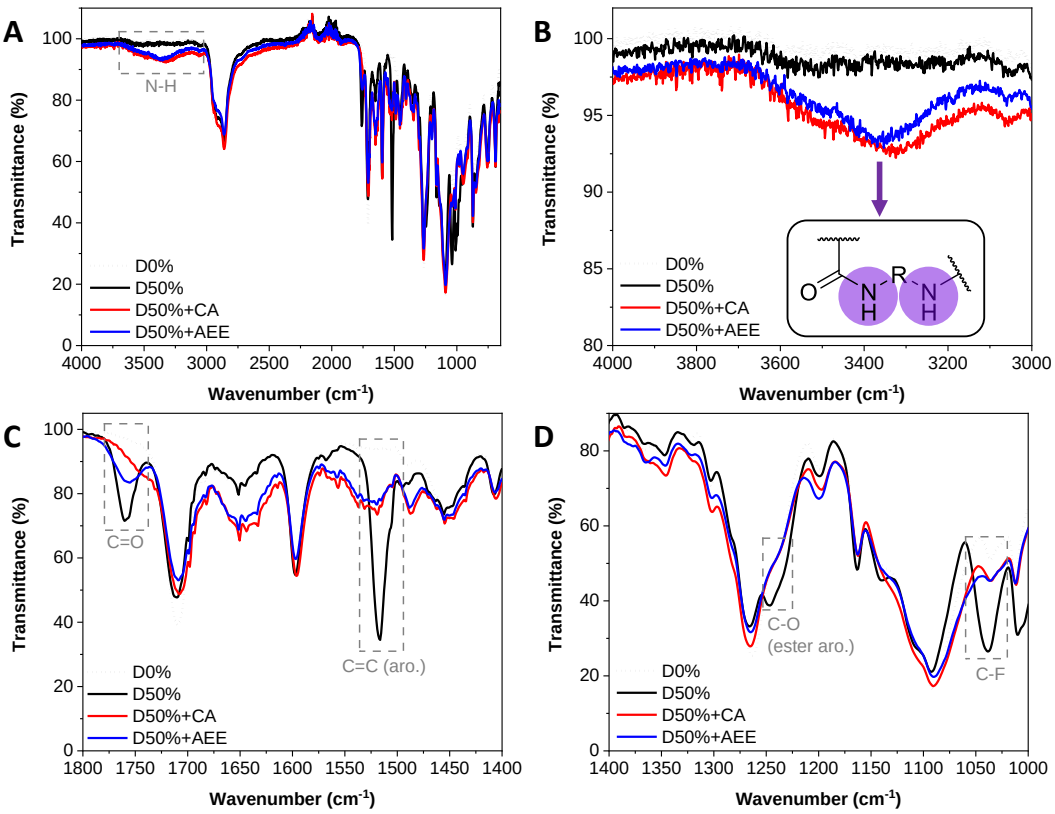

Figure 4.8. FT-IR spectra of the D50% copolymer (black line) cross-linked with CA (red line) and AEE (blue line). (A) Full spectrum. (B) Zoom in the 4000-3000 cm^{-1} region. (C) Zoom in the 1800-1400 cm^{-1} region. (D) Zoom in the 1400-1000 cm^{-1} region.

DLS analysis of the nano-objects' after cross-linking indicated no major change in the NP size distribution with sizes around 20 nm and PD in line with the non-cross-linked micelles (Figure 4.9, Table 4.2 and the Appendix). The NPs were transferred to water by dialysis over three days. Macroscopic precipitation was observed for the CA cross-linked nano-objects translated into large sizes measured by DLS between 140 and 200 nm and PDs which ranged from 0.29 to 0.46 which indicated broad sizes distributions. On the other hand, the D20%+AEE and D50%+AEE exhibited sizes of 64 nm and 55 nm, and PDs of 0.27 and 0.18, respectively, which indicated sizes closer to the individual micelles in DMSO. The NPs were freeze-dried, re-solvated in THF and the resulting solutions were analysed by DLS to assess the stabilisation effect of the cross-linking. Assemblies were detected which indicated that the micelles were still in suspension and no sign of aggregation of the NPs was visible by

DLS after transfer in THF. The sizes and PD values in THF were similar to the HDA cross-linked micelles which was expected as CA and AEE and cross-linkers are eight and nine atoms long respectively (Figure 4.9). A similar trend as before with EDA, BDA and HDA in THF was observed. The longer the cross-linker chain, the closer the NP size distribution in THF were to the NPs in DMSO and the narrower their distribution. Moreover, this effect was improved with the increasing density of cross-linking site. D20%+CA and D20%+AEE had both sizes of 35 nm with PDs of 0.33 and 0.25 respectively similar to the "stable" D20% cross-linked micelles. D50%+CA and D50%+AEE $_2$ both had a size of 26 nm with a PD of 0.20 and 0.16 respectively. The sizes and PDs were similar to D50%+HAD which indicated an efficient cross-linking.

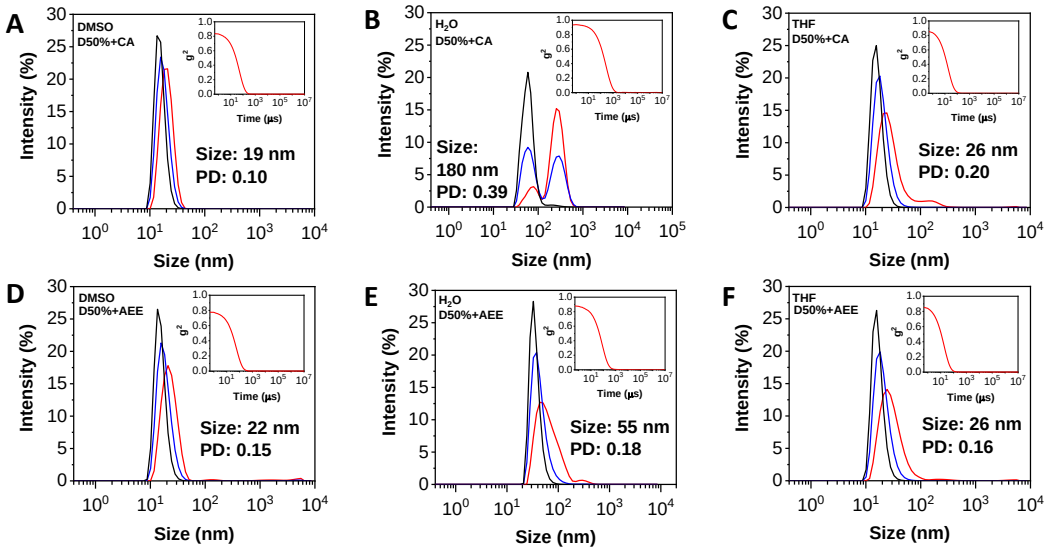

Figure 4.9. Size distributions of D50%+CA in (A) DMSO, (B) H_2O and (C) THF, and D50%+AEE in (D) DMSO, (E) H_2O and (F) THF obtained by DLS. The intensity (red line), volume (blue line) and number (black line) distributions are displayed. The insets show the correlograms.

TEM imaging of D50%+CA (Figure 4.10) and D50%+AEE (Figure 4.11) was conducted to assess the morphology of the cross-liked nano-objects. Reminiscent of the D50%+HAD and D0% in water, the dry-state TEM

images of the stimuli-responsive micelles exhibited spherical morphologies and aggregates of the NPs that could explain their large sizes by DLS. The size measured on the images (from 300 particles each) were 16 ±3 nm for D50%+CA and 15 ±3 nm for D50%+AEE closer to the sizes measured in DMSO before dialysis (20 nm) and with a narrow distribution.

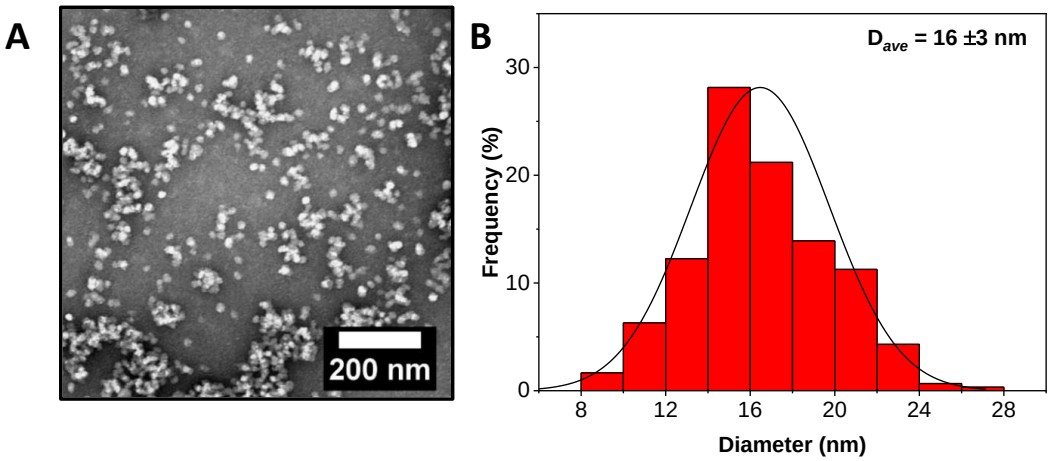

Figure 4.10. (A) Dry-state TEM image of D50%+CA after dialysis. (B) Histogram of spherical particles' size distribution measured from particle analysis of TEM images of 300 particles.

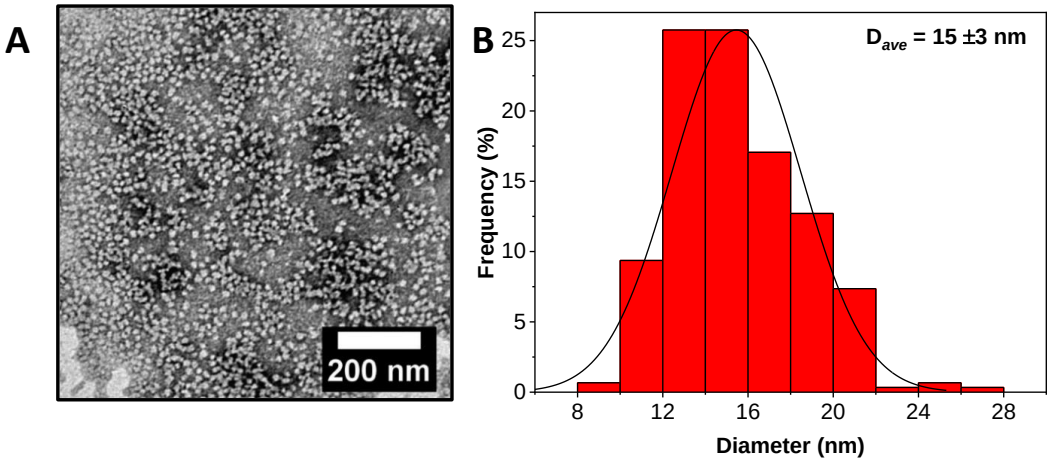

Figure 4.11. (A) Dry-state TEM image of D50%+AEE after dialysis. (B) Histogram of spherical particles' size distribution measured from particle analysis of TEM images of 300 particles.

Table 4.2. Characterisation of the NiCCo-PISA copolymers before and after cross-linking.

Polymer	D_{DLS} DMSO[a] (nm)	D_{DLS} THF[a] (nm)	D_{DLS} H_2O[a] (nm)	D_{TEM}[b] (nm)	Zeta pot. (mV)
D0%	20 (0.18)	-[c]	100 (0.20)	21 ±7	-15 ±5
D20%	21 (0.14)	-[c]	46 (0.25)	-[d]	-17 ±4
D20%+CA	21 (0.11)	35 (0.33)	180 (0.32)	-[d]	-12 ±3
D20%+AEE	22 (0.15)	35 (0.25)	64 (0.27)	-[d]	-17 ±3
D50%	22 (0.16)	-[c]	140 (0.15)	-[d]	7 ±7
D50%+CA	19 (0.10)	26 (0.20)	180 (0.29)	16 ±3	-13 ±3
D50%+AEE	22 (0.15)	26 (0.16)	55 (0.18)	15 ±3	-9 ±9

[a]Hydrodynamic radius measured by DLS at a 173° angle. PD is in parenthesis. [b]Dried state TEM from water suspension of NPs. [c]No assembly. [d]Not measured.

CD spectroscopy of the CA cross-linked micelles exhibited a lower CD_{360} than the unsubstituted D20% or D50% (Figure 4.12 and Table A4.5). On the other hand, D20%+AEE and D50%+AEE micelles displayed higher CD_{360} with 14 mdeg and 8.9 mdeg respectively. These variations were lower than a 10% increase from the original D20% and D50% copolymers which was within measurement error. The overall results indicate that the helicity was retained after the cross-linking reaction which proved the effective synthesis of potentially stimuli-responsive cross-linked NPs that contained a chiral core.

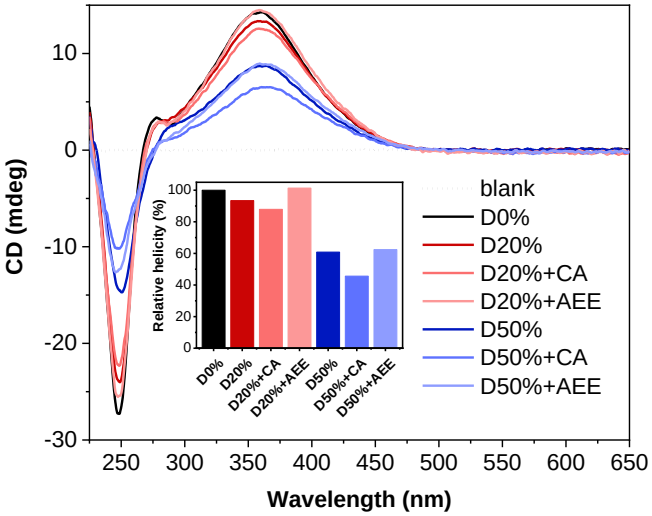

Figure 4.12. CD (THF, 0.5 mg·mL^{-1}) spectra of the unsubstituted D20% and its cross-linked counterparts, and the unsubstituted D50, and its cross-linked counterparts. D0% and a blank are added as reference. The inset shows the helicity (CD at $\lambda = 360$ nm) of the copolymers compared to D0%.

4.5.1. Redox responsive NPs

CA cross-linked NPs (D20%+CA and D50%+CA) in water at a concentration of 0.2 mg·mL^{-1} were subjected to *L*-glutathione (GSH) reducing agent at a concentration of 10 mM. The disulfide bond was expected to cleave and result in more solvophilic thiol functionalities (Scheme 4.3) inside the core, which would drive the nano-objects towards disassembly. As demonstrated by the EOA substituted micelles in Chapter 3, the introduction of hydrophilic functionalities in the core can lead to disassembly of the nano-objects.

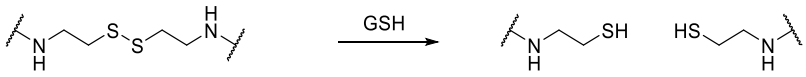

Scheme 4.3. Scheme of the redox-triggered cleavage of the cystamine disulfide linkers.

The size distribution of the NPs was monitored by DLS over a period of 4 weeks (Figure 4.13). The degradation of the responsive NPs was still ongoing after several days which was slow compared to previously reported systems.[43,

[45] The longer reaction time can be linked to two factors. First, the high hydrophobicity of the NPs core – that contained *L*-menthyl side-chains - prevented a fast entry of the hydrophilic thiol. Secondly, the aggregation behaviour of the NPs might have delayed the complete disassembly of the systems into the unimers and could explain the continuous increase in size. The switch from the stabilising disulfide bridges to thiol functionalities increased the unimers' exchange rate and favoured micelle aggregation which led to the size increase observed for D20%+CA from 190 nm to 585 nm, a three-fold growth. In the case of D50%+CA only a slight slope was noticeable over the whole reaction time and the size increased from 155 nm to 220 nm which is not expected with a higher density cross-linked NP. An increase of cleavable groups typically leads to a greater response to the stimulus. In the case of the disulfide bond, cleavage by GSH is a reversible reaction and the closer proximity of the functionalities in the core in D50% than D20% could have led to more restoration of the cross-linking bonds which exhibited seemingly more stable NPs. D0% treated with GSH showed no sign of swelling, aggregation or disassembly with a size that did not evolve over the reaction time which stayed around 125 nm. This indicated that the CA cross-linked micelles are effectively triggered by the presence of a redox agent to start a change in the NPs size distribution especially noticeable for D20%+CA.

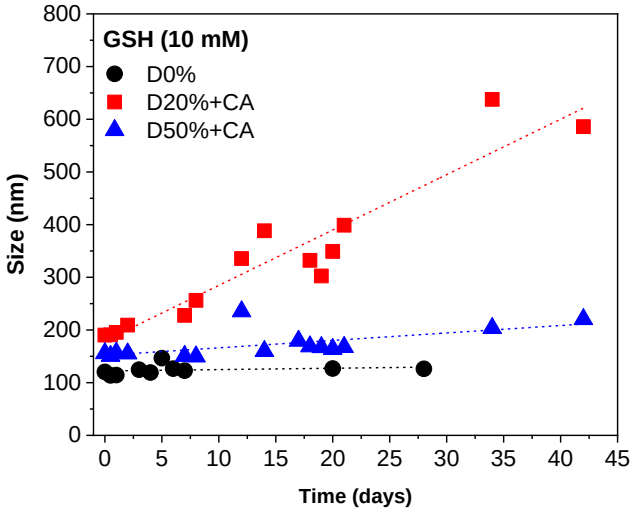

Figure 4.13. Evolution of the of the CA-substituted copolymer's size while reacted with GSH monitored by DLS

4.5.2. pH responsive NPs

AEE cross-linked NPs (D20%+AEE and D50%+AEE) were subjected to acidic pH to assess their pH-responsiveness. The acetal linkers are cleaved into alcohols under acidic conditions (Scheme 4.4) which led to an increase of the core solvophilicity and potential disassembly of the NPs. The resulting functionality is identical to the EOA substituted micelles in Chapter 3. The size evolution of the AEE crosslinked micelles was monitored by DLS over a period of 4 weeks.

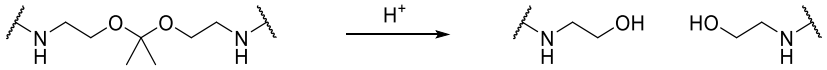

Scheme 4.4. Scheme of the acid-triggered cleavage of the acetal linkers.

The NPs were incubated at pH 2 for 4 weeks, D20%+AEE showed a little increase in size 30 nm (from 215 nm to 245 nm) over 4 weeks. The starting size of the D20%+AEE was larger than the previously measured DLS size (64 nm) as a consequence of the ongoing aggregation of the neutral NPs in solution. The change in size for the unreactive, non-cross-linked NPs D0% from 100 nm

to 110 nm that corresponded to a negligible increase of 10 nm which suggested that they kept the same size during their time under these low pH conditions. On the other hand, the D50%+AEE micelles exhibited a steady increase of their size from 55 nm at t_0 to 205 nm after 4 weeks which indicated a clear response towards the acid stimuli which was expected for the higher density cross-linked NPs. The fact that the D50%+AEE micelles were from the beginning less aggregated than their D20% counterpart speaks also in favour of the aggregation-induced slow disassembly hypothesis.

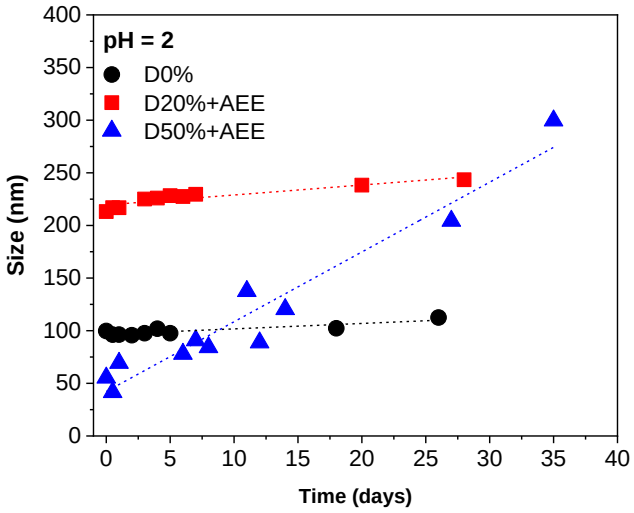

Figure 4.14. Evolution of the of the AEE-substituted copolymer's size at pH 2 monitored by DLS

In order to circumvent the very slow rate of the disassembly reactions in water, the acid-triggered cleavage was analysed in THF where the disassembly was hypothesised to be much faster as a consequence of the better solubility of the core in THF compared to water. First, D20%+AEE and D50%+AEE were reacted with HCl in THF at 10 mM and the disassembly time frame, monitored every 10 minutes by DLS, was shorter than the time between the measurement points (Figure 4.16). In the long term (24 days), both assemblies, after a first dramatic increase in size, started to disassemble. The D50%+AEE however, had a slower decrease from 300 nm to 120 nm in 4 weeks while D20%+AEE had a drop in size as dramatic as the initial increase over the first three days

and the size stayed constant around 75 nm afterwards. This hinted at a possible lower stability of D20%+AEE and/or a faster cleavage of the AEE links compared to D50%+AEE which could be a consequence of the difference in linkage density. The overall monitoring proved that both systems were pH sensitive and disassembled under acidic trigger.

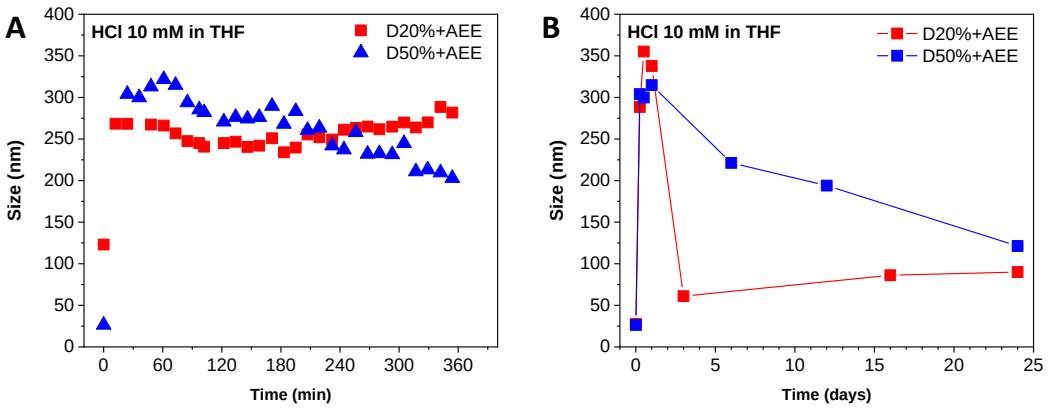

Figure 4.15. Evolution of the of the AEE-substituted copolymer's size at HCl 10mM in THF monitored by DLS over (A) 5 h and (B) 24 days.

The reaction with 10 mM of HCl in THF was too quick to observe the gradual evolution of the size distribution. To slow down the disassembly process, a concentration of HCl 100 times lower was employed (100 µM) and the results were as expected that the disassembly was happening slower than in the HCl 10 mM case. The size increased following an exponential trend before it reached a plateau at 120 nm (Figure 4.16). In 3 h, the size monitored by DLS increased from 20 nm to 120 nm as a result of the swelling of the micelles for both D20%+AEE and D50%+AEE. The points for the D20%+AEE system were more scattered than its D50% counterpart which hinted to a stability issue of the former. The higher hydrophilicity of the cleaved D50%+AEE would lead to a higher dynamic of the unimers and a more uniform distribution of the sizes in the sample. On a longer period of 24 days, the D50%+AEE size stagnates at between 150 and 120 nm while D20%+AEE size decreases right after it reached plateau until a size of around

50 nm after 4 weeks. This confirms the behaviour observed for the higher concentration of HCl where the D20%+AEE system disassembled faster than the D50%+AEE.

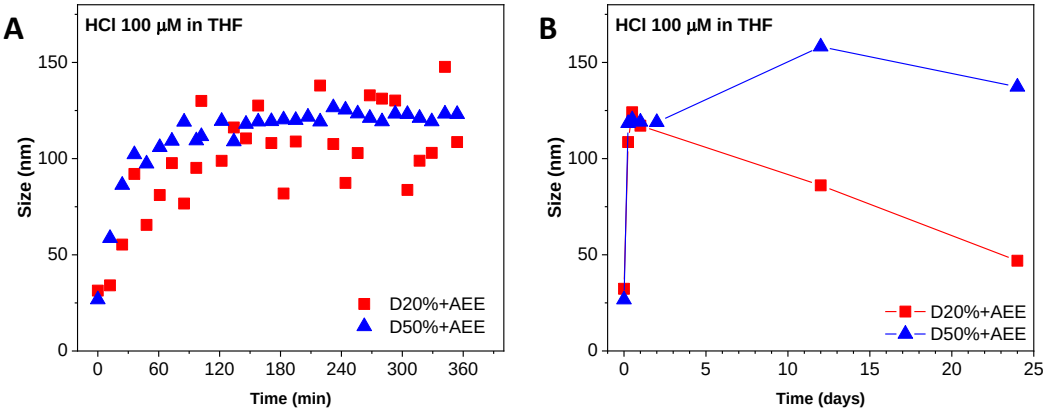

Figure 4.16. Evolution of the of the AEE-substituted copolymer's size at HCl 100 µM in THF monitored by DLS over (A) 5 h and (B) 24 days.

4.6. Conclusions

Nano-objects with a cross-linked helical core were achieved after modification of the PPM methodology developed in Chapter 3 to employ a range of cross-linkers (Scheme 4.5). Moreover, the thermoresponsivity of the NPs was confirmed by UV/Vis and DLS turbidometry. The stability of the cross-linked micelles was confirmed by DLS measurements in THF while the preservation of the helicity was confirmed by CD spectroscopy. Micelles cross-linked by cystamine exhibited redox-triggered disassembly behaviour monitored by DLS in water while NPs crosslinked with AEE exhibited a response to low pH in water and THF monitored by DLS. This study augmented the investigation on the use of NiCCo-PISA as scaffold for possible applications in smart materials or nanoreactors where the chiral core could be leveraged for enantioselectivity as will be investigated in Chapter 5.

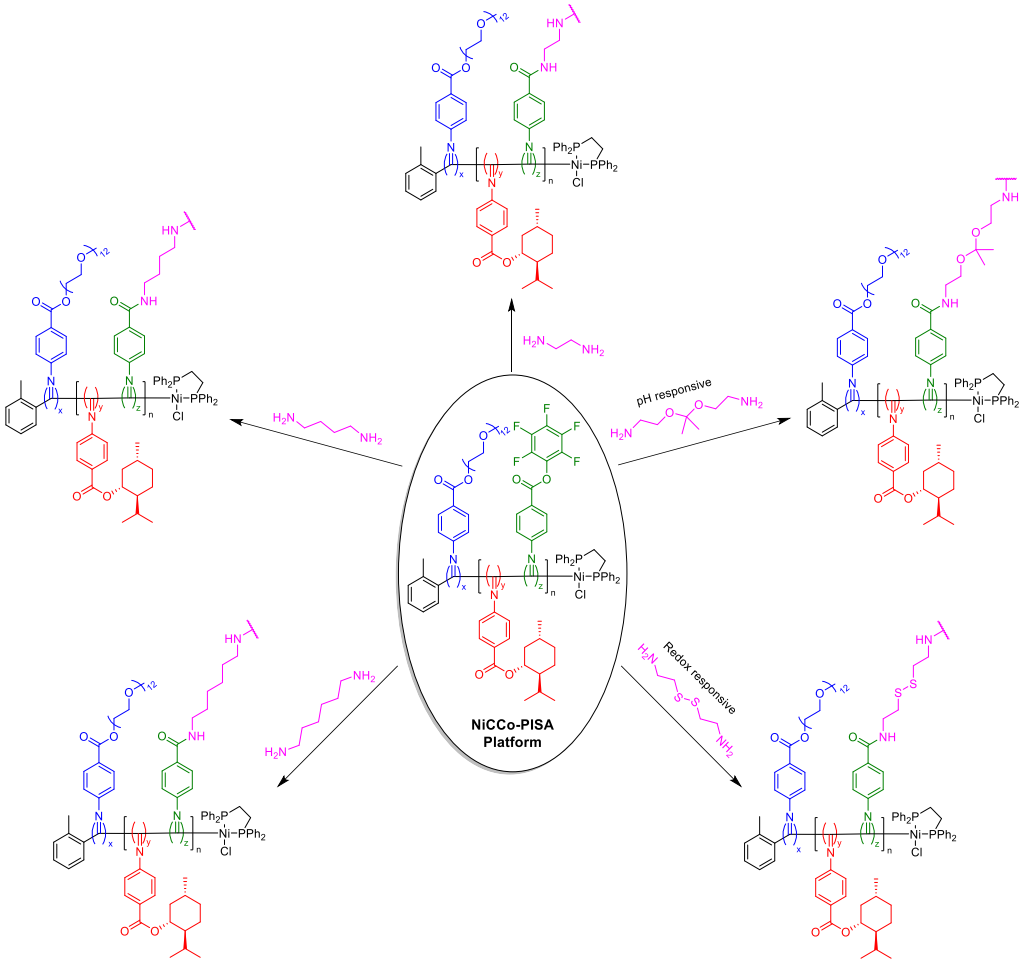

Scheme 4.5. Overview of the NiCCo-PISA block copolymer as a platform for cross-linked nanomaterials.

4.7. Appendix

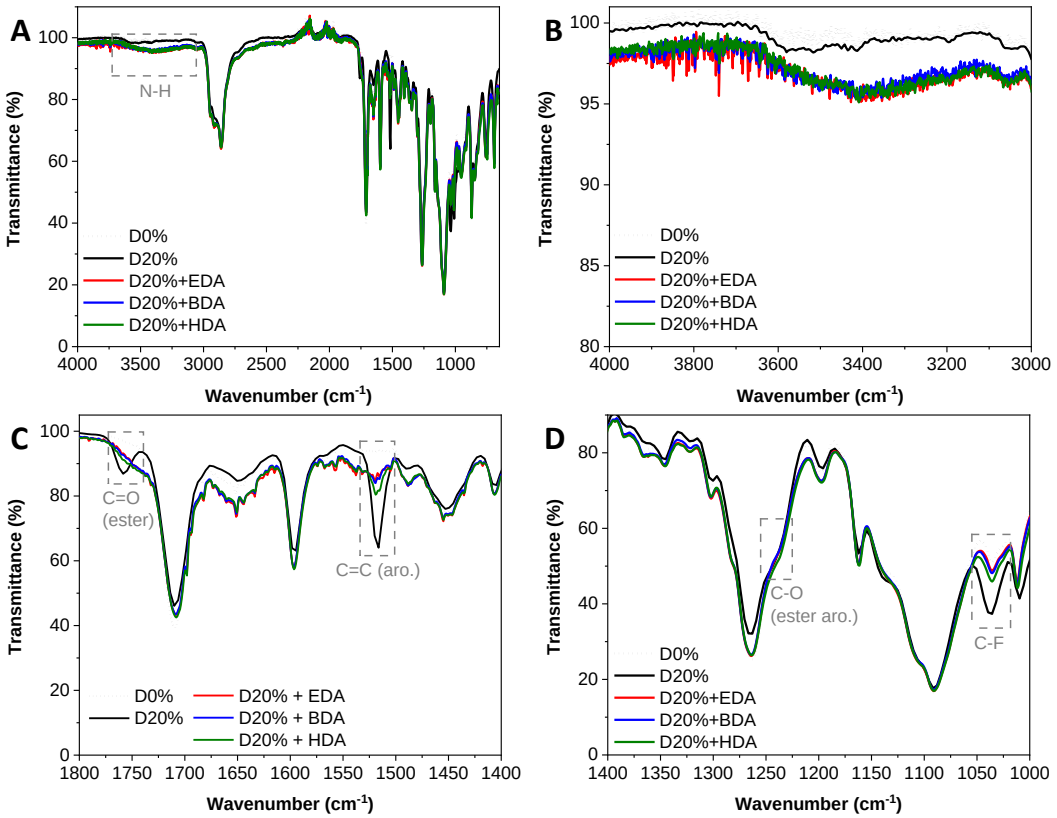

Figure A4.17. FT-IR spectra of the D20% copolymer (black line) cross-linked with EDA (red line), BDA (blue line) and HDA (green line). (A) Full spectrum. (B) Zoom in the 4000-3000 cm^{-1} region. (C) Zoom in the 1800-1400 cm^{-1} region. (D) Zoom in the 1400-1000 cm^{-1} region.

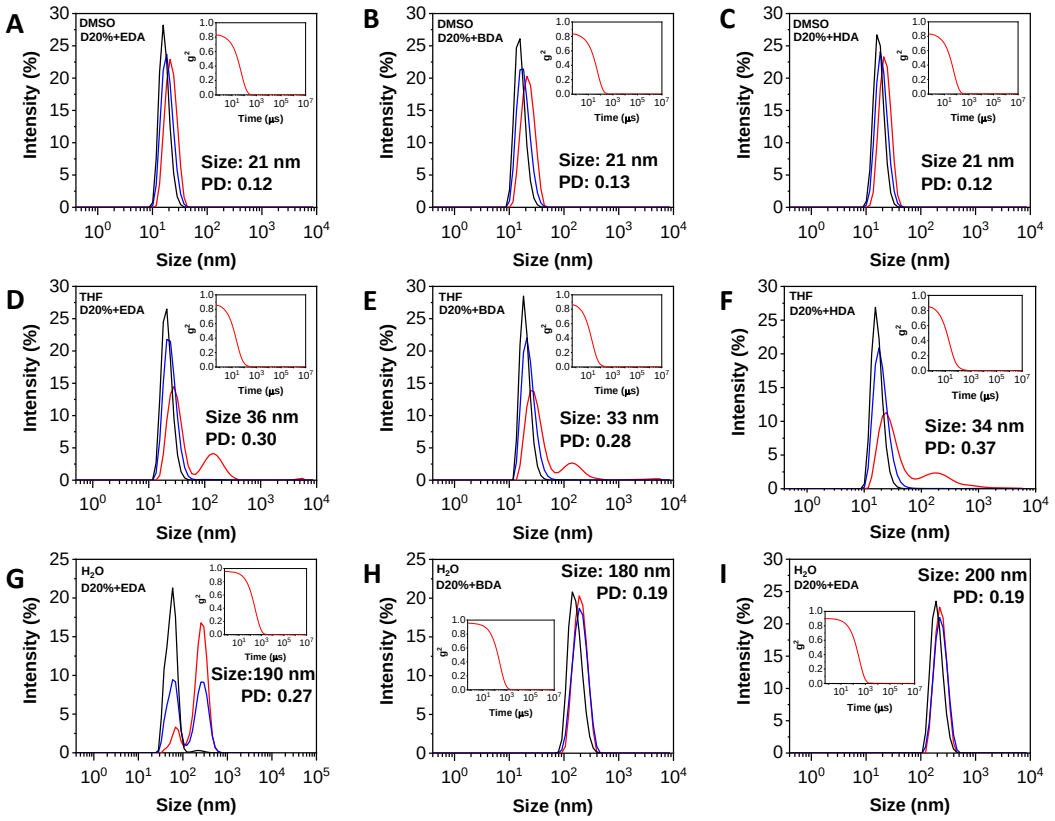

Figure A4.18. Size distributions of cross-linked D20%+EDA, D20%+BDA and D20%+HDA in (A-C) DMSO, (D-F) H_2O and (G-I) THF obtained by DLS. The intensity (red line), volume (blue line) and number (black line) distributions are displayed. The insets show the correlograms.

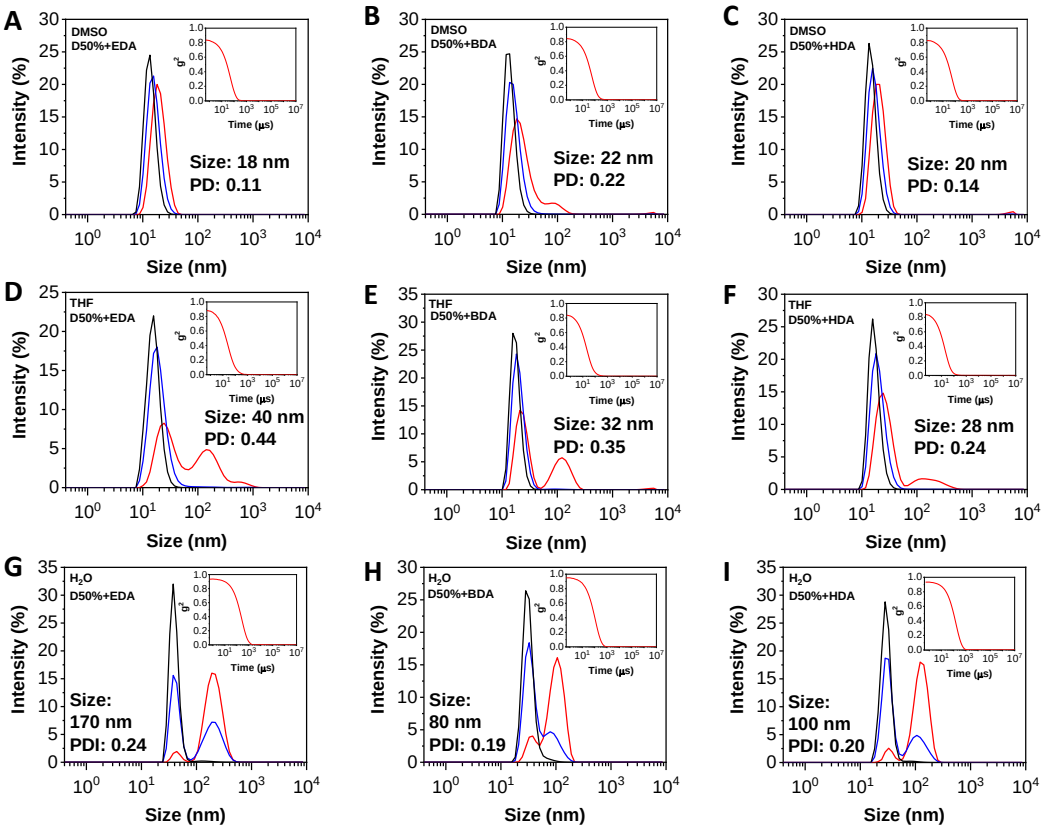

Figure A4.19. Size distributions of cross-linked D50%+EDA, D50%+BDA and D50%+HDA in (A-C) DMSO, (C-F) H_2O and (G-I) THF obtained by DLS. The intensity (red line), volume (blue line) and number (black line) distributions are displayed. The insets show the correlograms.

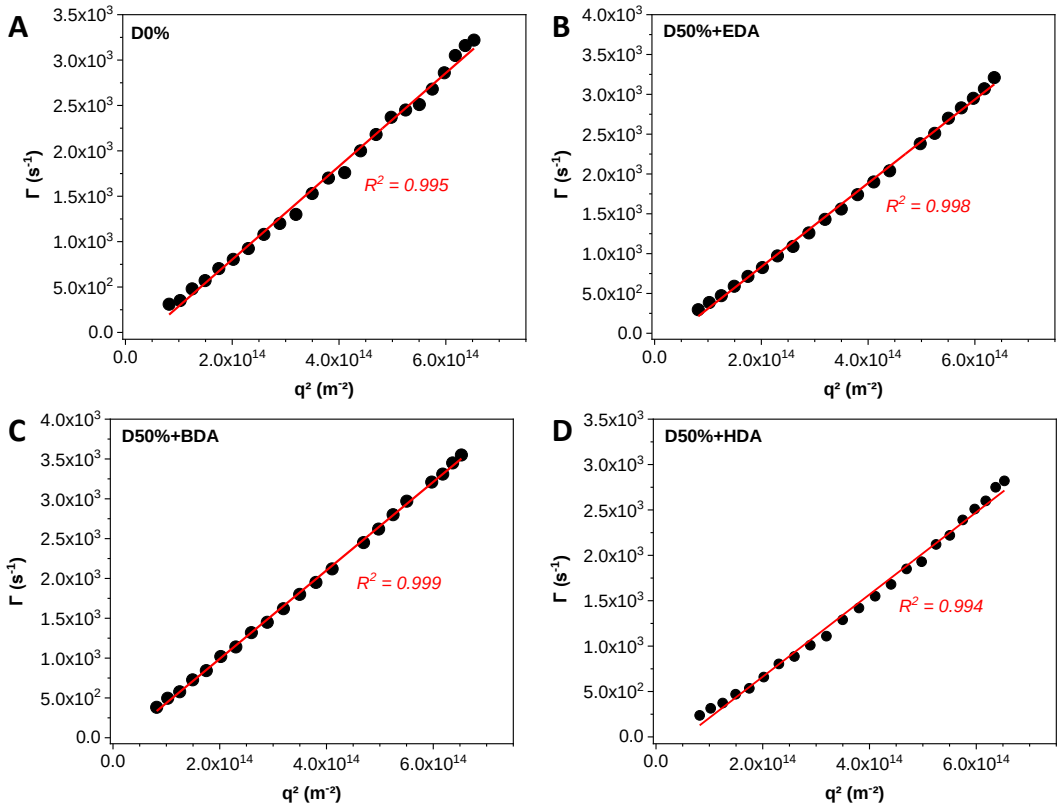

Figure A4.20. Multiple angle dynamic light scattering analysis of (A) D0% and cross-linked (B) D50%+EDA, (C) D50%+BDA and (D) D50%+HDA at 0.1 mg·mL^{-1} in water.

Table A4.3. Results from MADLS compared to the mono angle DLS at 173°.

Polymer	$D_{\mathrm{DLS,\ 173°}}$ H_2O (nm)[a]	D_{MADLS} H_2O (nm)[b]
D0%	100 (0.20)	84 ±1.3
D50%+EDA	170 (0.24)	82 ±1.2
D50%+BDA	80 (0.19)	76 ±0.5
D50%+HDA	100 (0.20)	95 ±1.6

[a]Hydrodynamic radius measured by DLS at a 173° angle. PD is in parenthesis. [b]D_h values calculated from multiple angle DLS analysis using the Stokes-Einstein equation (mean ± 10%)

Table A4.4. CD spectroscopy of the NiCCo-PISA copolymers before and after cross-linking

Polymer	CD_{360} (mdeg)[a]
D0%	14
D20%	13
D20%+EDA	13
D20%+BDA	11
D20%+HDA	12
D50%	8.7
D50%+EDA	6.0
D50%+BDA	6.0
D50%+HDA	6.2

[a]CD signal at $\lambda = 360$ nm in THF.

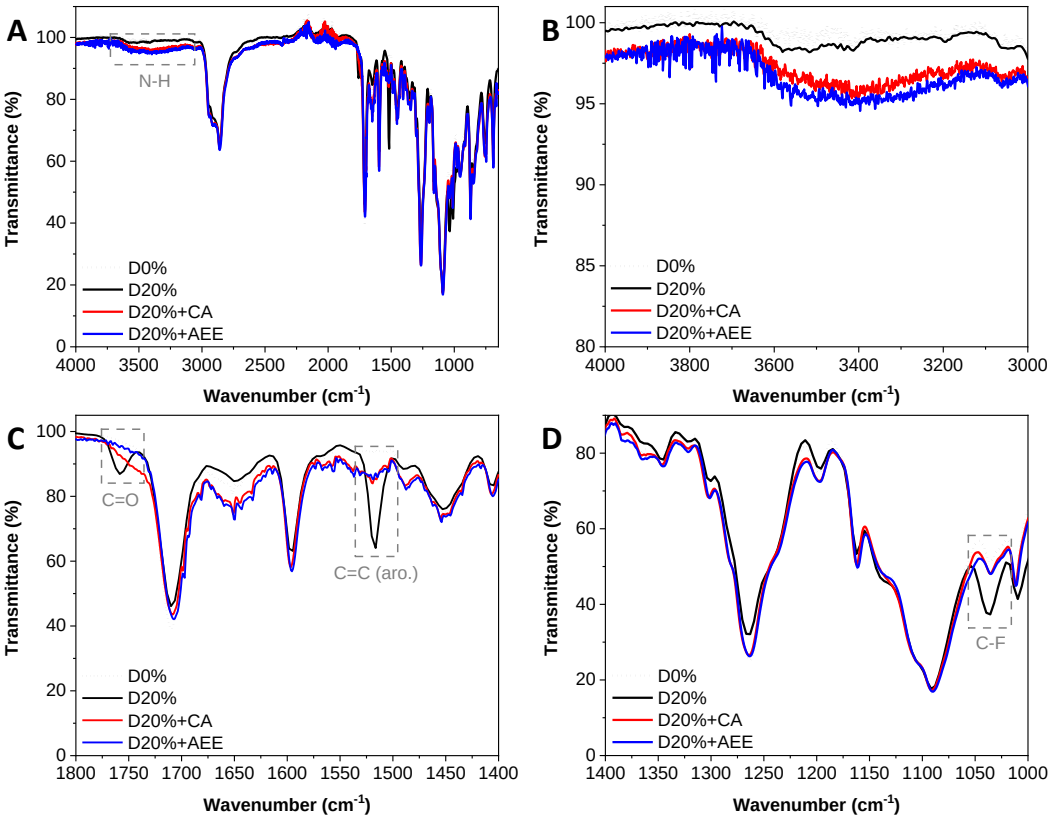

Figure A4.21. FT-IR spectra of the D20% copolymer (black line) cross-linked with CA (red line) and AEE (blue line). (A) Full spectrum. (B) Zoom in the 4000-3000 cm^{-1} region. (C) Zoom in the 1800-1400 cm^{-1} region. (D) Zoom in the 1400-1000 cm^{-1} region.

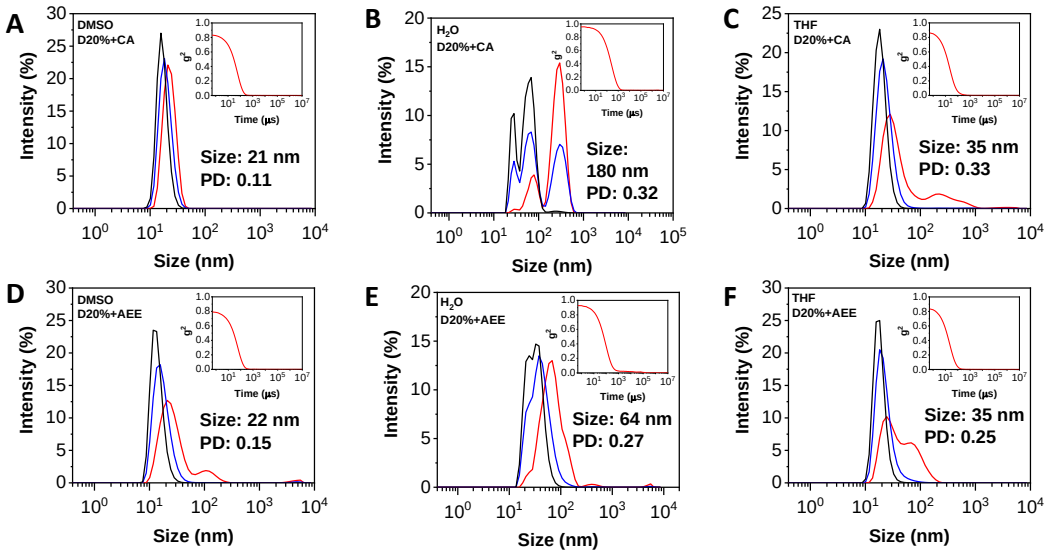

Figure A4.22. Size distributions of cross-linked D20%+CA in (A) DMSO, (B) H_2O and (C) THF, and D50%+AEE in (D) DMSO, (E) H_2O and (F) THF obtained by DLS. The intensity (red line), volume (blue line) and number (black line) distributions are displayed. The insets show the correlograms.

Table A4.5. CD spectroscopy of the NiCCo-PISA copolymers before and after cross-linking

Polymer	CD_{360} (mdeg)[a]
D0%	14
D20%	13
D20%+CA	13
D20%+AEE	14
D50%	8.7
D50%+CA	6.5
D50%+AEE	8.9

[a]CD signal at $\lambda = 360$ nm in THF.

4.8. References

1. Yoshida, M.; Lahann, J., *ACS Nano* 2008, 6, 1101-1107.
2. Stuart, M. A. C.; Huck, W. T. S.; Genzer, J.; Müller, M.; Ober, C.; Stamm, M.; Sukhorukov, G. B.; Szleifer, I.; Tsukruk, V. V.; Urban, M.; Winnik, F.; Zauscher, S.; Luzinov, I.; Minko, S., *Nat Mater* 2010, 2, 101-113.
3. Motornov, M.; Roiter, Y.; Tokarev, I.; Minko, S., *Progress in Polymer Science* 2010, 1, 174-211.
4. Liu, X.; Yang, Y.; Urban, M. W., *Macromol. Rapid Commun.* 2017, 13, 1700030.
5. Sur, S.; Rathore, A.; Dave, V.; Reddy, K. R.; Chouhan, R. S.; Sadhu, V., *Nano-Struct. Nano-Objects* 2019, 100397.
6. Mura, S.; Nicolas, J.; Couvreur, P., *Nat Mater* 2013, 11, 991-1003.
7. Salata, O. V., *J. Nanobiotechnol.* 2004, 1, 3.
8. Colson, Y. L.; Grinstaff, M. W., *Adv. Mater.* 2012, 28, 3878-3886.
9. Wan, Q.; Wang, K.; He, C.; Liu, M.; Zeng, G.; Huang, H.; Deng, F.; Zhang, X.; Wei, Y., *Polym. Chem.* 2015, 47, 8214-8221.
10. Elsabahy, M.; Heo, G. S.; Lim, S.-M.; Sun, G.; Wooley, K. L., *Chem. Rev.* 2015, 19, 10967-11011.
11. Li, H.; Li, H.; Wang, W.; Tao, Y.; Wang, S.; Yang, Q.; Jiang, Y.; Zheng, C.; Huang, W.; Chen, R., *Angew. Chem. Int. Ed.* 2020, 12, 4756-4762.
12. Maji, S.; Cesur, B.; Zhang, Z.; De Geest, B. G.; Hoogenboom, R., *Polym. Chem.* 2016, 9, 1705-1710.
13. Yan, Q.; Yuan, J.; Yuan, W.; Zhou, M.; Yin, Y.; Pan, C., *Chem. Commun.* 2008, 46, 6188-6190.
14. Feng, D.-Q.; Zhu, W.; Liu, G.; Wang, W., *RSC Adv.* 2016, 99, 96729-96734.
15. Rodríguez-Hernández, J.; Lecommandoux, S., *J. Am. Chem. Soc.* 2005, 7, 2026-2027.
16. Arno, M. C.; Williams, R. J.; Bexis, P.; Pitto-Barry, A.; Kirby, N.; Dove, A. P.; O'Reilly, R. K., *Biomaterials* 2018, 184-192.
17. Lu, C.; Urban, M., *ACS Nano* 2015, 3, 3119-3124.
18. Motornov, M.; Zhou, J.; Pita, M.; Gopishetty, V.; Tokarev, I.; Katz, E.; Minko, S., *Nano Letters* 2008, 9, 2993-2997.
19. Agut, W.; Brûlet, A.; Schatz, C.; Taton, D.; Lecommandoux, S., *Langmuir* 2010, 13, 10546-10554.
20. Deirram, N.; Zhang, C.; Kermaniyan, S. S.; Johnston, A. P. R.; Such, G. K., *Macromol. Rapid Commun.* 2019, 10, 1800917.
21. Bergbreiter, D. E.; Case, B. L.; Liu, Y.-S.; Caraway, J. W., *Macromolecules* 1998, 18, 6053-6062.

22. Kanaoka, S.; Yagi, N.; Fukuyama, Y.; Aoshima, S.; Tsunoyama, H.; Tsukuda, T.; Sakurai, H., *J. Am. Chem. Soc.* 2007, 40, 12060-12061.
23. Zayas, H. A.; Lu, A.; Valade, D.; Amir, F.; Jia, Z.; O'Reilly, R. K.; Monteiro, M. J., *ACS Macro Lett.* 2013, 4, 327-331.
24. Lee, S. M.; Bae, Y. C., *Macromolecules* 2014, 23, 8394-8403.
25. Keogh, R.; Blackman, L. D.; Foster, J. C.; Varlas, S.; O'Reilly, R. K., *Macromol. Rapid Commun.* 2020, 6, 1900599.
26. Kundu, P. K.; Samanta, D.; Leizrowice, R.; Margulis, B.; Zhao, H.; Börner, M.; Udayabhaskararao, T.; Manna, D.; Klajn, R., *Nat Chem* 2015, 8, 646-652.
27. Yan, T.; Li, F.; Qi, S.; Tian, J.; Tian, R.; Hou, J.; Luo, Q.; Dong, Z.; Xu, J.; Liu, J., *Chem. Commun.* 2020, 1, 149-152.
28. Rifaie-Graham, O.; Ulrich, S.; Galensowske, N. F. B.; Balog, S.; Chami, M.; Rentsch, D.; Hemmer, J. R.; Read de Alaniz, J.; Boesel, L. F.; Bruns, N., *J. Am. Chem. Soc.* 2018, 25, 8027-8036.
29. Tsoi, S.; Zhou, J.; Spillmann, C.; Naciri, J.; Ikeda, T.; Ratna, B., *Macromol. Chem. Phys.* 2013, 6, 734-741.
30. Kumar, K.; Knie, C.; Bléger, D.; Peletier, M. A.; Friedrich, H.; Hecht, S.; Broer, D. J.; Debije, M. G.; Schenning, A. P. H. J., *Nat. Commun.* 2016, 1, 11975.
31. Zhao, T.; Wang, P.; Li, Q.; Al-Khalaf, A. A.; Hozzein, W. N.; Zhang, F.; Li, X.; Zhao, D., *Angew. Chem. Int. Ed.* 2018, 10, 2611-2615.
32. Agut, W.; Taton, D.; Brûlet, A.; Sandre, O.; Lecommandoux, S., *Soft Matter* 2011, 20, 9744-9750.
33. Majewski, A. P.; Schallon, A.; Jérôme, V.; Freitag, R.; Müller, A. H. E.; Schmalz, H., *Biomacromolecules* 2012, 3, 857-866.
34. Thévenot, J.; Oliveira, H.; Sandre, O.; Lecommandoux, S., *Chem. Soc. Rev.* 2013, 17, 7099-7116.
35. Yu, L.; Zhang, Y.; Dai, X.; Xu, Q.; Zhang, L.; Tan, J., *Chem. Commun.* 2019, 79, 11920-11923.
36. Zhang, J.; Ma, N.; Tang, F.; Cui, Q.; He, F.; Li, L., *ACS Appl. Mater. Interfaces* 2012, 3, 1747-1751.
37. Wang, D.; Liu, T.; Yin, J.; Liu, S., *Macromolecules* 2011, 7, 2282-2290.
38. Zhang, J.; Tanaka, J.; Gurnani, P.; Wilson, P.; Hartlieb, M.; Perrier, S., *Polym. Chem.* 2017, 28, 4079-4087.
39. Deng, W.; Chen, J.; Kulkarni, A.; Thompson, D. H., *Soft Matter* 2012, 21, 5843-5846.
40. Chen, L.-J.; Zhao, G.-Z.; Jiang, B.; Sun, B.; Wang, M.; Xu, L.; He, J.; Abliz, Z.; Tan, H.; Li, X.; Yang, H.-B., *J. Am. Chem. Soc.* 2014, 16, 5993-6001.

41. Bergman, M. J.; Pedersen, J. S.; Schurtenberger, P.; Boon, N., *Soft Matter* 2020, 11, 2786-2794.
42. Kim, S. H.; Kim, J. H.; Choi, H. J.; Park, J., *RSC Adv.* 2015, 88, 72387-72393.
43. Couturaud, B.; Georgiou, P. G.; Varlas, S.; Jones, J. R.; Arno, M. C.; Foster, J. C.; O'Reilly, R. K., *Macromol. Rapid Commun.* 2019, 2, 1800460.
44. Tanaka, J.; Moriceau, G.; Cook, A.; Kerr, A.; Zhang, J.; Peltier, R.; Perrier, S.; Davis, T. P.; Wilson, P., *Macromolecules* 2019, 3, 992-1003.
45. Maiti, C.; Parida, S.; Kayal, S.; Maiti, S.; Mandal, M.; Dhara, D., *ACS Appl. Mater. Interfaces* 2018, 6, 5318-5330.
46. Gao, Y.; Dong, C.-M., *Polym. Chem.* 2017, 7, 1223-1232.
47. Wang, Y.; Xing, P.; Li, S.; Ma, M.; Yang, M.; Zhang, Y.; Wang, B.; Hao, A., *Langmuir* 2016, 41, 10705-10711.
48. Deng, R.; Ning, Y.; Jones, E. R.; Cunningham, V. J.; Penfold, N. J. W.; Armes, S. P., *Polym. Chem.* 2017, 35, 5374-5380.
49. North, S. M.; Armes, S. P., *Polym. Chem.* 2020, 12, 2147-2156.
50. Thomi, L.; Schaefer, P.; Landfester, K.; Wurm, F. R., *Macromolecules* 2016, 1, 105-109.
51. Han, X.; Zhang, J.; Qiao, C.-Y.; Zhang, W.-M.; Yin, J.; Wu, Z.-Q., *Macromolecules* 2017, 11, 4114-4125.
52. Chen, Y.; Zhang, Z.-H.; Han, X.; Yin, J.; Wu, Z.-Q., *Macromolecules* 2016, 20, 7718-7727.
53. Wu, H.; Dong, J.; Zhan, X.; Yang, H.; Zhao, Y.; Zhu, S.; Wang, G., *RSC Adv.* 2014, 67, 35757-35761.
54. Cheng, R.; Meng, F.; Deng, C.; Klok, H.-A.; Zhong, Z., *Biomaterials* 2013, 14, 3647-3657.
55. Su, M.; Shi, S.-Y.; Wang, Q.; Liu, N.; Yin, J.; Liu, C.; Ding, Y.; Wu, Z.-Q., *Polym. Chem.* 2015, 36, 6519-6528.
56. Liu, C.-W.; Su, M.; Li, X.-L.; Xue, T.; Liu, N.; Yin, J.; Zhu, Y.-Y.; Wu, Z.-Q., *Soft Matter* 2015, 28, 5727-5737.
57. An, X.; Zhu, A.; Luo, H.; Ke, H.; Chen, H.; Zhao, Y., *ACS Nano* 2016, 6, 5947-5958.
58. Koo, A. N.; Lee, H. J.; Kim, S. E.; Chang, J. H.; Park, C.; Kim, C.; Park, J. H.; Lee, S. C., *Chem. Commun.* 2008, 48, 6570-6572.
59. Li, Y.; Xiao, K.; Luo, J.; Xiao, W.; Lee, J. S.; Gonik, A. M.; Kato, J.; Dong, T. A.; Lam, K. S., *Biomaterials* 2011, 27, 6633-6645.
60. He, H.; Bai, Y.; Wang, J.; Deng, Q.; Zhu, L.; Meng, F.; Zhong, Z.; Yin, L., *Biomacromolecules* 2015, 4, 1390-1400.
61. Paramonov, S. E.; Bachelder, E. M.; Beaudette, T. T.; Standley, S. M.; Lee, C. C.; Dashe, J.; Fréchet, J. M. J., *Bioconjugate Chem.* 2008, 4, 911-919.

62. Yamashita, H.; Misawa, T.; Oba, M.; Tanaka, M.; Naito, M.; Kurihara, M.; Demizu, Y., *Bioorg. Med. Chem* 2017, 6, 1846-1851.
63. Zhang, W.-M.; Zhang, J.; Qiao, Z.; Liu, H.-Y.; Wu, Z.-Q.; Yin, J., *Polym. Chem.* 2018, 31, 4233-4242
64. Gibson, M. I.; O'Reilly, R. K., *Chem. Soc. Rev.* 2013, 17, 7204-7213.
65. Grzelczak, M.; Liz-Marzán, L. M.; Klajn, R., *Chem. Soc. Rev.* 2019, 5, 1342-1361.
66. Blackman, L. D.; Gibson, M. I.; O'Reilly, R. K., *Polym. Chem.* 2017, 1, 233-244.
67. Kumar, A.; Dixit, C. K., 3 - Methods for characterization of nanoparticles. In *Advances in Nanomedicine for the Delivery of Therapeutic Nucleic Acids*, Nimesh, S.; Chandra, R.; Gupta, N., Eds. Woodhead Publishing: 2017; pp 43-58.

Chapter 5 Helical poly(aryl isocyanide)s for catalysis of acylation reactions

5.1. Declaration of authorship

Transmission electron microscopy was conducted by Mr Spyridon Varlas at the University of Birmingham.

5.2. Introduction

Enantioselective reactions and catalysis are of major importance in pharmaceutical and biomedical fields. The methods employed generally leverage chiral species to impart the enantioselectivity and since helices are chiral objects, an enriched right- or left-handed polymer helix can be used to induce enantioselectivity in either chiral resolution or asymmetric catalysis. The chiral nature of the helix has been employed in chiral separation with various types of polymer helices such as polymethacrylates,[1-3] polyacetylenes[4, 5] and polyisocyanides.[6-9] A noteworthy example is the enantioselective enrichment of a racemic mixture by poly(aryl isocyanide) helix-containing micelles that has been showed by Wang *et al.*[9] They developed thermoresponsive amphiphilic star block copolymers decorated with left-handed helices and demonstrated that when these thermoresponsive nanoparticles (NPs) were precipitated in the presence of racemic methyl benzyl alcohol, the *S*-enantiomer was selectively adsorbed and removed from the racemic solution (Figure 5.1). The enantioselective absorption and release of one enantiomer in the micelles core led to enantioselective enrichment.

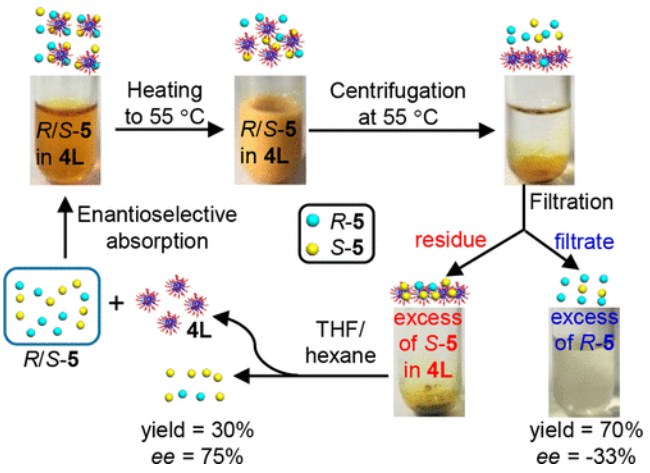

Figure 5.1. Diagram that explains the coprecipitation enantioselective enrichment of a racemic mixture of methyl benzyl alcohol (*R*- and *S*-5) with micelles 4L in water. Reproduced from the work of Wang *et al.* published in ACS Macro Letters.[9]

Pioneering the field of helical polymers for asymmetric catalysis, Reggelin *et al.* have studied polymethacrylates for enantioselective reactions primarily by employing them as chiral ligands.[10-13] The pros and cons of organocatalysis will not be discussed (see Chapter 1) and the focus will be on the organocatalytic area of helical polymer catalysts; however, it is noteworthy that helical polymers have also been used as chiral ligands for asymmetric metal catalysis.[10, 11, 14-17] In the area of organocatalysis, synthetic polymer helices have been employed as scaffolds for enantioselective catalysis either as a means to increase the selectivity of an already chiral catalyst[18-27] or to induce enantioselectivity to an achiral catalyst.[12, 28-30] In a notable instance, Guichard and co-workers have leveraged the helicity of chiral (thio)urea oligomer foldamers to achieve enantioselective Michael reactions with enantiomeric excess (ee%) up to >99%.[31] Shorter oligomers that do not fold yielded lower ee% which demonstrated the necessity for the oligomers to be in a helical conformation to achieve high enantioselectivity. Suginome and co-workers have developed helical poly(quinoxaline-2,3-diyl) copolymers grafted with achiral pyridyl pendant groups that exhibited enantioselective catalysis of the Steglich rearrangement.[30] The static helical copolymer was composed of 95% of chiral comonomer blended with 5% of the achiral catalyst comonomer (Scheme 5.1). The resulting helical catalyst was employed in several Steglich rearrangements that achieved up to 95% ee and demonstrated the effect of the helicity in these catalysts with pendant achiral active sites. The use of achiral catalytic moieties opens the path for helical functional copolymers similar to those developed in Chapter 3 that can be adapted by post-polymerisation modification (PPM) to include various achiral catalytic side-chains and easily achieve enantioselective helical catalysts from a unique polymeric scaffold without the need to develop a new catalytic system for every situation.

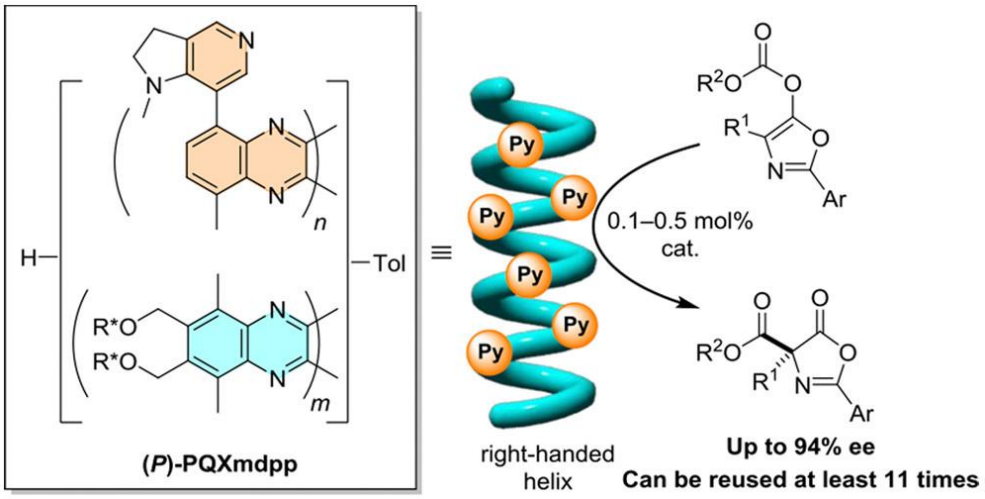

Scheme 5.1. Right-handed helical poly(quinoxaline-2,3-diyl)s copolymer decorated with achiral pyridyl pendant groups used in the enantioselective catalysis of Steglich rearrangement. Reproduced from the work of Yamamoto *et al.* published in ACS, Journal of the American Chemistry Society.[30]

One of the downsides of the catalytic systems presented above is that they are mostly run in toxic organic solvents. The development of nanoparticles that contain the helical catalysts stabilised by hydrophilic coronae in water (*i.e.* nanoreactors) are an alternative to the use of organic solvents. Moreover, these systems would improve on the molecular catalysts when the "concentrator effect" is considered - discovered by Helms *et al.* [32, 33]- which showed that catalytic reactions performed in confined environments display faster kinetics and sometimes better overall efficiencies. Polymeric nanoreactors have been shown to use a range of different active sites such as metals,[34-37] organic species,[38, 39] enzymes[40-44] or a combination[45] with various polymer structures such as single-chain nanoparticles,[46-48] tubes,[49, 50] micelles,[51-57] and polymersomes[58-66]. Finally, the phase separation between the distinct nanoreactor parts - corona, core or membrane – allows for the passive molecular recognition of species that diffuse inside the nano-object based on their hydrophobicity.[67-70]

Building upon the field of helical polymer enantioselective catalysis and nanoreactors, one can envision helical-core micelles that contain catalysts that would achieve chiral recognition while their hydrophobic core would allow them to speed up reaction rates in a green solvent such as water while also being recyclable. Moreover, the use of PPMs to insert the catalytic functionalities would allow these structures to be highly modular which enable the attachment of the desired catalyst to the preformed polymer helix. Poly(aryl isocyanides) copolymers that carry DMAP moieties for use as helical molecular catalysts have been developed. Diblock amphiphilic copolymers were synthesised to allow self-assembly into nanoreactors with a helical core. Finally, NiCCo-PISA functionalisable nano-objects developed in Chapters 3 and 4 were modified by PPM to achieve nanoreactors and employed in acylation reactions to assess their possible enantioselectivity.

5.3. Molecular helix catalysis of DMAP for acylation reactions

5.3.1. Molecular poly(aryl isocyanide) helices

Inspired by previous reports of helical catalysts, the first intention was to develop molecular polyisocyanide catalysts that contain pendant DMAP moieties. A first attempt at the synthesis of a monomer that contained the DMAP moiety directly attached to it was successful however, the monomer led to very broad MWD which indicated a negative interaction of the DMAP with the catalyst. After this ineffective attempt, the FAIC and PPM route was preferred.

Synthesis of helical statistical copolymers composed of 80 mol% of chiral menthyl aryl isocyanide (MAIC) and 20 mol% of pentafluoro phenol ester aryl isocyanide (FAIC) monomers with a degree of polymerisation (DP) of 150 was conducted in THF which led to polymer helices that could be easily functionalised by PPM (Scheme 5.2A). Unlike the copolymers synthesised in the previous Chapters, the copolymers in this section were synthesised with a palladium catalyst[71] (see Chapter 7) as a consequence of their synthesis that took place prior to the development of the nickel catalyst employed later. To introduce the DMAP functionality, a DMAP modified moiety primary alcohol (DMAP-OH) was synthesised through a known methodology.[72] DMAP-OH was reacted with the FAIC/MAIC copolymer under the same conditions as the previous primary amine nucleophiles *i.e.* DMSO at 55 °C with 5 equivalents of nucleophile respective to the FAIC content (Figure 5.2A). The DMAP unit was hypothesised to accelerate the alcohol reaction through an activation of the PFP ester followed by an intramolecular nucleophile substitution (Scheme 5.2B). The reactions were run without a base to lower the hydrolysis rate

which made the last deprotonation step entirely dependent on the free pentafluorophenolate in solution. Therefore, it was expected that protonated DMAP units would be present in the final product. In the case that this system should be employed in catalysis as a nanoreactor, basic conditions should be employed in order ensure that all the DMAP units are free to achieve maximum efficiency of the nanoreactor. PPM with DMAP-OH appeared to occur more slowly than the previous reactions, with a reaction time of three days instead of one required to achieve completion of the substitution. This lower reaction rate was likely to be a consequence of the weaker nucleophilicity of the alcohol compared to the amines even with DMAP activation.

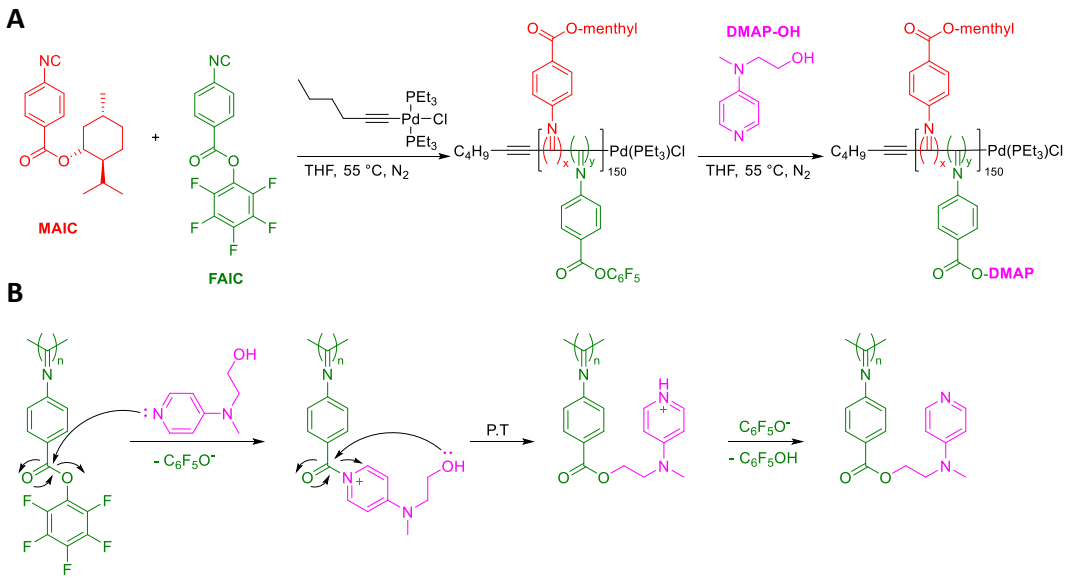

Scheme 5.2. (A) Scheme of the FAIC copolymer synthesis with the subsequent PPM with DMAP-OH to yield the DMAP copolymer. (B) PFP ester activation of the FAIC moiety by DMAP-OH followed by the intramolecular substitution reaction.

Analysis by SEC was conducted to assess the impact of the copolymerisation and PPM on the polymer molecular weight distributions (MWD). The FAIC/MAIC copolymer had a number average molecular weight (M_n) of 19.0 kDa which was close to the 25.0 kDa from the MAIC homopolymer (Figure 5.2A). The larger variance between the homopolymer and the copolymer compared to that exhibited in the previous Chapters was a result of the absence

of a large solvophilic block (*i.e.* P(PAIC)) attached to the MAIC/FAIC block which made the modification in comonomer composition more impactful on the resulting copolymer M_n. The dispersity ($Đ_M$) for both MWDs were similar at 1.20 and 1.24 for the homopolymer and copolymer respectively. The introduction of the DMAP moiety was conducted in a similar fashion to Chapter 3, which yielded a copolymer with a M_n lower than both the MAIC homopolymer and FAIC/MAIC copolymer at 14.4 kDa. Moreover, an increase of $Đ_M$ was found with a value of 1.44. These differences were a consequence of the DMAP moiety which interacted with the SEC columns which led to a shifted and artificially broadened MWD that indicated the successful reaction of the pentafluorophenyl (PFP) ester units.

Analysis of the various polymers by CD spectroscopy was employed to evaluate and compare their helicity. The CD signal at $\lambda = 360$ nm (CD_{360}) was taken as the comparison point. The values were larger than for the previously reported copolymers in previous Chapters as a result of the absence of a large solvophilic achiral block. The CD_{360} for the MAIC homopolymer, the FAIC/MAIC copolymer and the DMAP-functionalised copolymer were 48, 49, and 49 mdeg, respectively, which indicated that the helicity of the macromolecules was maintained before and after introduction of chiral FAIC and PPM with DMAP-OH (Figure 5.2B).

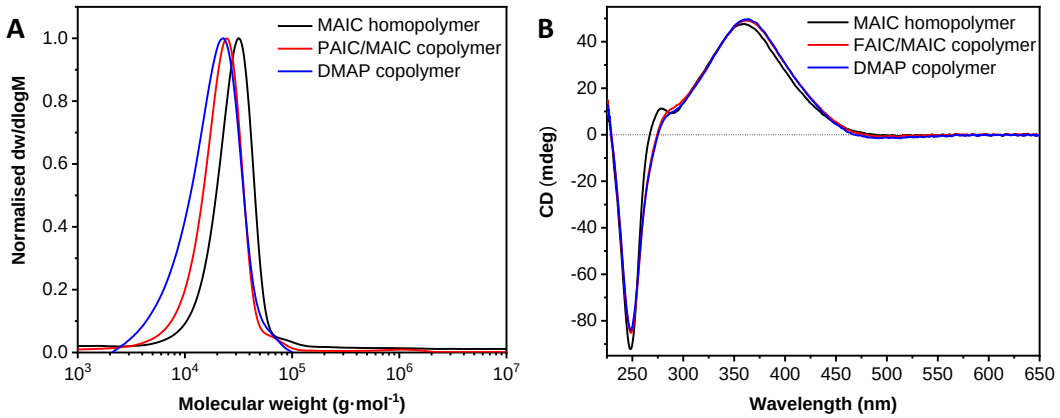

Figure 5.2. (A) Normalised SEC RI molecular weight distributions (THF + 2% v/v NEt_3, 40 °C, PS standards) of the MAIC homopolymer, FAIC copolymer and DMAP copolymer. (B) CD (THF, 0.5 $mg \cdot mL^{-1}$) spectra of the MAIC homopolymer, FAIC copolymer and DMAP copolymer.

Both the FAIC/MAIC and DMAP copolymers were analysed by NMR spectroscopy to detect the introduction of the DMAP moiety. ^{19}F NMR spectroscopy informed on the presence or absence of PFP moieties in the copolymer and clearly showed broad signals at δ = 152, 158, and 162 ppm which corresponded to the PFP units in the FAIC/MAIC copolymer similar to the monomeric FAIC shifts (Figure 5.3). The broadened signal indicated that the PFP units were in a rigid environment *i.e.* the helical copolymer. The introduction of the DMAP moiety was verified by the disappearance of the PFP signals which indicated that the reaction of these units and their replacement. By ^{1}H NMR spectroscopy, the FAIC/MAIC copolymer exhibited three distinct broad signals at δ = 7.8-6.8, 6.2-5.2 and 5.0-4.2 ppm which corresponded to two aryls and one menthol proton (Figure 5.4). The introduction of the DMAP moiety was clearly visible with the emergence of three new broad signals related to the two aryl protons of the DMAP units at δ = 8.3-7.9 and 6.8-6.4 ppm, and the methyl group found at δ = 3.3-2.8 ppm. The broadness of the signal further confirmed the successful introduction of the moiety into the rigid helix. The combination of ^{1}H and ^{19}F NMR spectroscopy demonstrated the successful reaction of the PFP units and their replacement by the DMAP moieties.

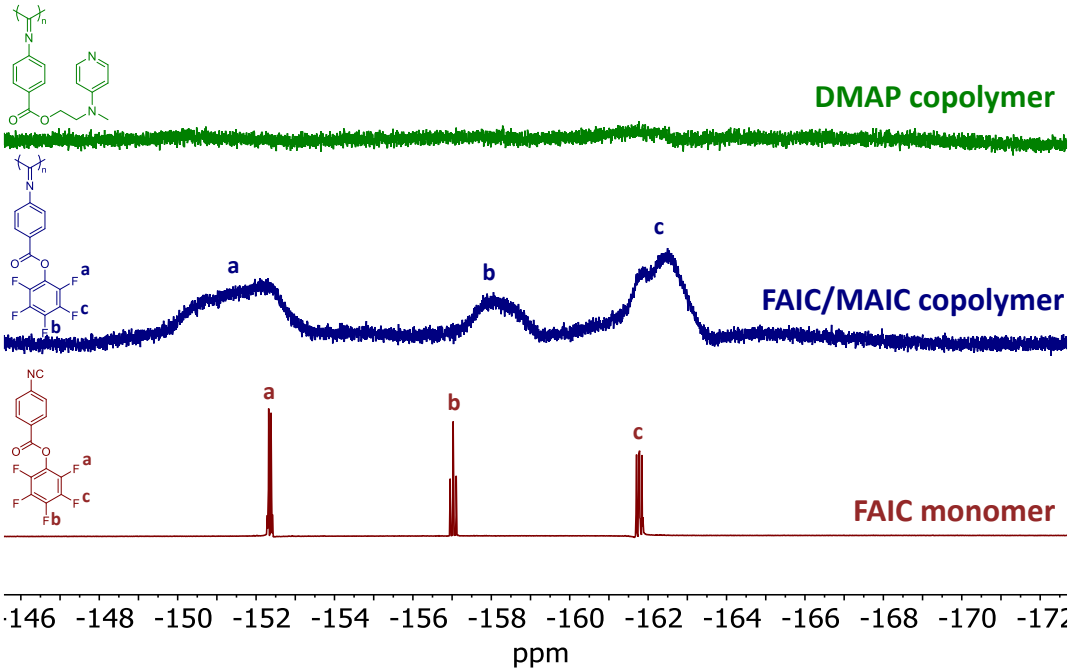

Figure 5.3. ^{19}F NMR of FAIC monomer, FAIC/MAIC copolymer and DMAP copolymer in $CDCl_3$ (377 MHz, 298 K).

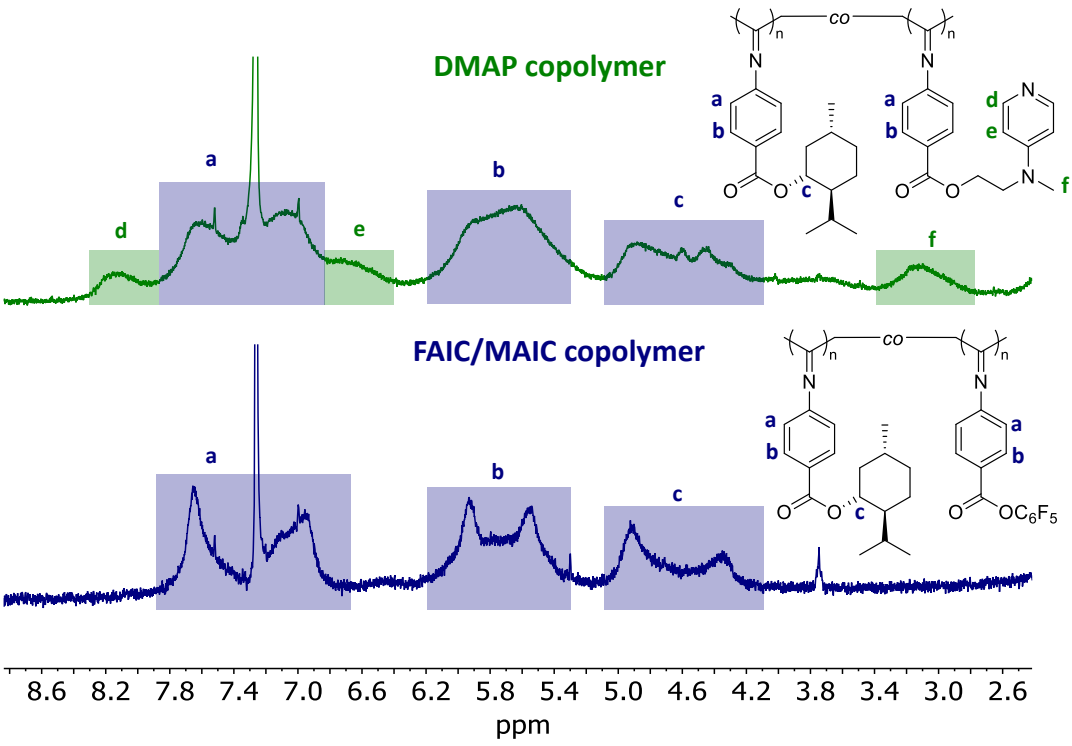

Figure 5.4. ^{1}H NMR of FAIC monomer, FAIC/MAIC copolymer and DMAP copolymer in $CDCl_3$ (400 MHz, 298 K).

To verify the stability of the MAIC units towards the reaction conditions, the MAIC homopolymer was subjected to PPM conditions with DMAP-OH for 3 days. Analysis by SEC showed no difference in the MWD which proved the resilience of the MAIC's ester to the nucleophilic substitution of DMAP-OH (see Appendix: Figure A5.21A). The FAIC copolymer was heated at 55 °C in THF (reaction conditions without nucleophile) and the resulting copolymer was similar in MWD which demonstrated the resistance of the FAIC copolymer's activated esters to the hydrolysis from the water traces present in THF (Figure A5.21B)

The DMAP copolymer was employed as a helical catalyst that contained 20% of DMAP (hDMAP-20%) in the acylation reaction of 1-phenyl-1-propanol with butyric anhydride (Figure 5.5A). The reactions were conducted in THF at 0.02 M of alcohol (1 equiv.) with butyric anhydride (3 equiv.) under basic conditions (*i*-Pr_2NEt, 1.5 equiv.) and a catalyst loading of 1 mol%. Mesitylene was added to the reaction mixture as an internal standard. To monitor the reaction progress and enantioselectivity, chiral GC-MS was employed, to separate the different reagents and products along with their enantiomers (Figure 5.5B). To this end, aliquots (0.1 mL) were taken from the reaction mixtures at different time points and diluted in THF (1.5 mL) before filtration through silica to remove the catalyst. The filtrate was further filtered through a 0.22 µm filter before analysis by GC-MS.

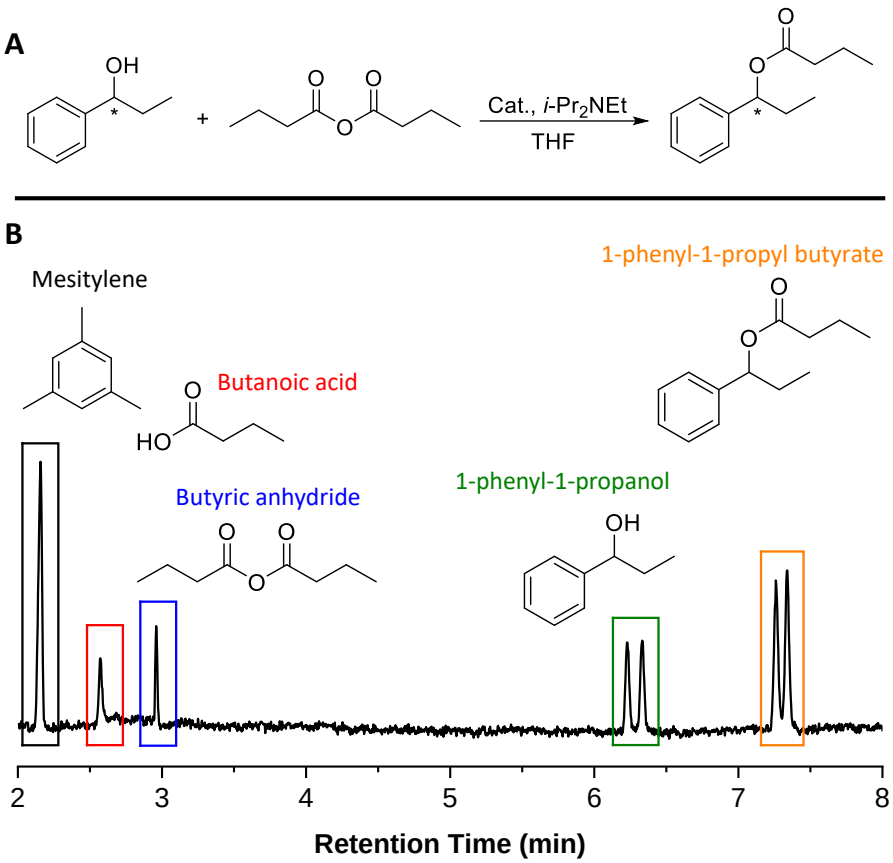

Figure 5.5. (A) Scheme of the acylation reaction in THF of 1-phenyl-1-propanol by butyric anhydride catalysed with hDMAP under basic conditions. (B) An example of a GC-MS chromatogram of the reaction mixture that indicates the different reagents and products.

The reaction catalysed by either molecular DMAP or hDMAP-20% was conducted and showed a higher activity for the molecular DMAP after 24 h of reaction with a quantitative conversion compared to a 49% conversion for hDMAP-20% (Figure 5.6). This difference was explained by possible hydrolysis of the PFP units during PPM that would have led to a lower loading of active site for the helical copolymer than expected. Unfortunately, no enantioselectivity was detected for the hDMAP-20% catalysed reaction. The density of DMAP moieties was suspected to be too high to allow proper enantioselectivity induction from the pendant menthol groups therefore, a hDMAP-1% was synthesised. As expected the lower loading of FAIC units led to almost identical MWD between the MAIC homopolymer, the FAIC copolymer (1%) and the DMAP copolymer (1%) *i.e.* hDMAP-1% (Figure

A5.22B). Catalysis of the acylation reaction was conducted with 0.1 mol% of catalyst instead of 1 mol% for reasons of quantities available of the hDMAP-1% copolymer. As expected, the catalysed reaction proved slower than the hDMAP-20% and reached 49% conversion after 96 h similarly to hDMAP-20%. No enantiomeric excess was detected.

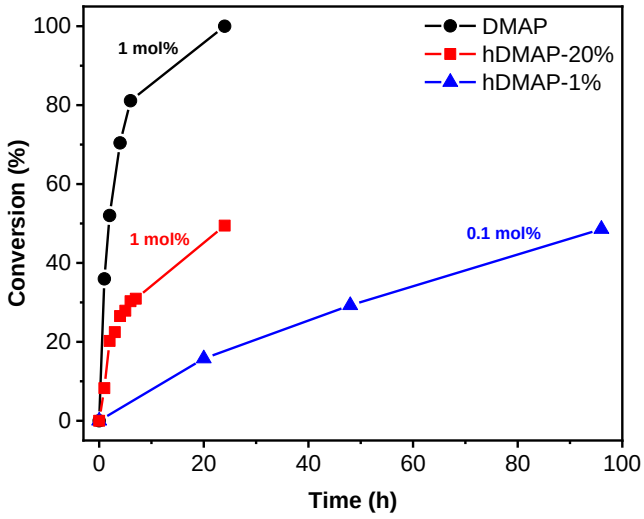

Figure 5.6. Alcohol conversion over time measured by GC-MS of the acylation reaction catalysed by DMAP (black spheres), hDMAP-20% (red squares) or hDMAP-1% (blue triangles). The catalyst loading is indicated in mol%. 0.02 M [OH]

5.3.2. Solvent exchange self-assembled diblock amphiphile poly(aryl isocyanide)s

It was hypothesised that the tightly packed environment of a micelle could lead to an asymmetric reaction *via* enantioseparation of a racemic reagent over the diffusion into the chiral core. Amphiphilic block copolymers that could be self-assembled by solvent-exchange (SE) were synthesised with PEG aryl isocyanide (PAIC) as their corona-forming monomer in THF before PPM by DMAP-OH (Scheme 5.3). The DP of both the hydrophilic and hydrophobic blocks were chosen as 50 that produced a final DP of 100. To assess the effect of the location of the DMAP unit, two types of blocks were prepared, diblock

copolymers with a mixed core of MAIC and FAIC *i.e.* P(PAIC)-*b*-(P(MAIC)-*co*-(P(FAIC)) and triblock copolymers with a layer of MAIC followed by a core of FAIC *i.e.* P(PAIC)-*b*-P(MAIC)-*b*-P(FAIC). The triblock was achieved by sequential addition of the MAIC and FAIC comonomer *in-situ* during the polymerisation process without purification between additions. Moreover, both structures were synthesised with either 10 mol% or 20 mol% of FAIC (compared to the MAIC monomer).

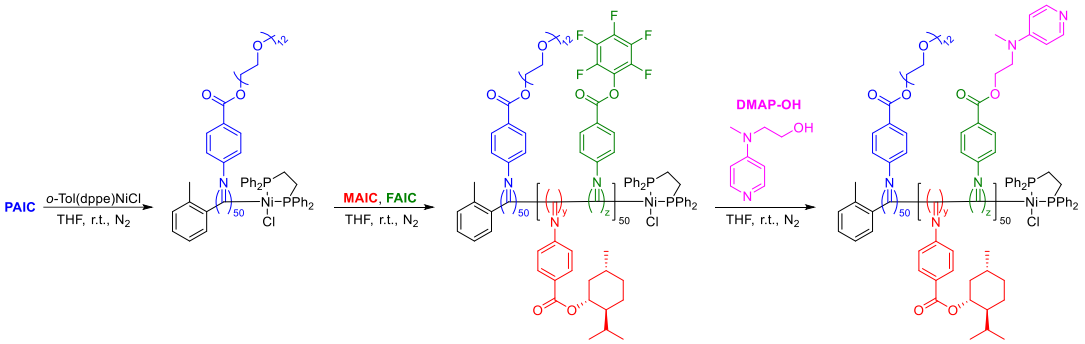

Scheme 5.3. Homopolymerisation of PAIC $DP_{PAIC} = 20$ followed by the chain extension with a mixture of FAIC and MAIC $DP_{FAIC+MAIC} = 30$ which yielded an amphiphilic diblock copolymer. PPM of the copolymer with DMAP-OH produces DMAP helical copolymers.

The copolymers were analysed by SEC with the 10 mol% diblock (SED10%) and triblock (SET10%) copolymers which exhibited M_n of 17.0 and 17.5 kDa, respectively, were observed while the 20 mol% diblock (SED20%) and triblock (SET20%) copolymers had M_n of 13.2 and 13.5 kDa, respectively (Figure 5.7A-B and Table 5.1). The difference in M_n between the 10 mol% and 20 mol% copolymers can be explained by the larger $Đ_M$ of the latter with values of 1.14 and 1.12 for SED10% and SET10%, respectively, while the $Đ_M$ of SED20% was 1.30 and SET20% was 1.32. After PPM with DMAP-OH, the MWD of all the copolymers shifted to lower M_n while the $Đ_M$ stayed constant for the 10 mol% copolymers and increased for the 20 mol% copolymers as a consequence of the higher density of DMAP moiety in the latter that could

interact with the SEC columns (Figure 5.7A-B and Table 5.1). Even though the M_n of the unsubstituted block copolymers were similar to the previously analysed FAIC copolymers (19.0 kDa), the effect of PPM with DMAP-OH on the MWD was lower as expected for block copolymers that contained fewer functionalisation points.

CD spectroscopy was employed to determine the helicity of the copolymers and its resilience to the PPM conditions. The unsubstituted copolymers exhibited values of CD_{360} around 3 mdeg, the low value consistent with a helical core of MAIC/FAIC attached to a large achiral corona of PAIC (Figure 5.7C-D and Table 5.1). After PPM with DMAP-OH, the presence of the CD signal demonstrated the stability of the helical core however, the CD_{360} decreased to values around 2 mdeg, which indicated a negative effect of the substitution on the helicity.

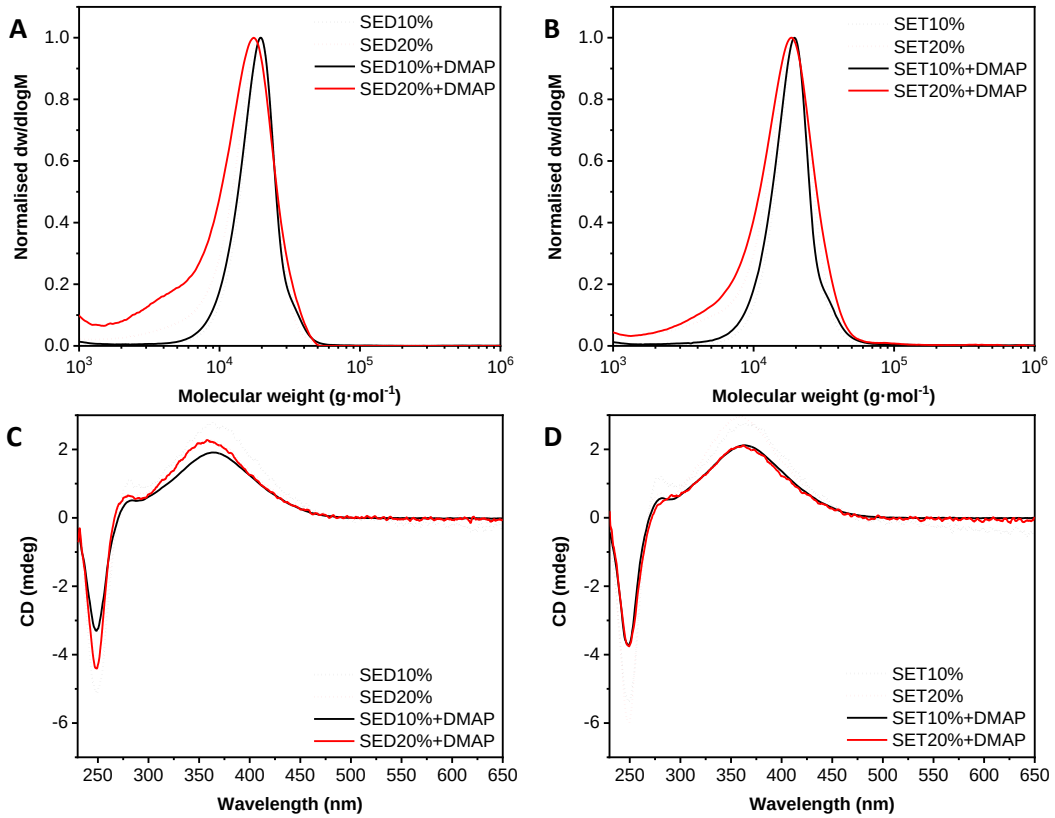

Figure 5.7. Normalised SEC RI molecular weight distributions (THF + 2% v/v NEt_3, 40 °C, PS standards) of the (A) diblock and (B) triblock copolymers before (dotted line) and after (solid line) PPM with DMAP-OH. CD (THF, 0.5 mg·mL^{-1}) spectra of the (C) diblock and (D) triblock copolymers before (dotted line) and after (solid line) PPM with DMAP-OH.

The self-assembly of the amphiphilic copolymer was conducted by solvent exchange (SE). The copolymers were dissolved in a non-selective solvent (*i.e.* THF) before water was added slowly (0.6 mL·h^{-1}) under strong stirring to achieve a suspension of nanostructures that was purified by dialysis in water for 3 days to remove unreacted reagents such as DMAP-OH. The resulting suspensions were analysed by DLS to measure the size of the nano-objects. The FAIC copolymers that contained 10 mol% of FAIC exhibited similar sizes of 29 nm and 25 nm for the solvent-exchange self-assembled SED10% and SET10%, respectively (Figure 5.8 and Table 5.1). The size distribution (PD) were low with 0.15 and 0.27 for SED10% and SET10%, respectively. Both the 20 mol% substituted copolymers exhibited similar sizes but proved

larger than their 10 mol% counterpart at 54 nm and 49 nm for SED20% and SET20%, respectively. This might be a result of their aggregation because, as explained in Chapter 3, this type of micelles with dense brush-like corona, were shown to be prone to aggregation that led to an increase of the measured size by DLS. Their PD was also low at 0.16 and 0.12 for SED20% and SET20% respectively.

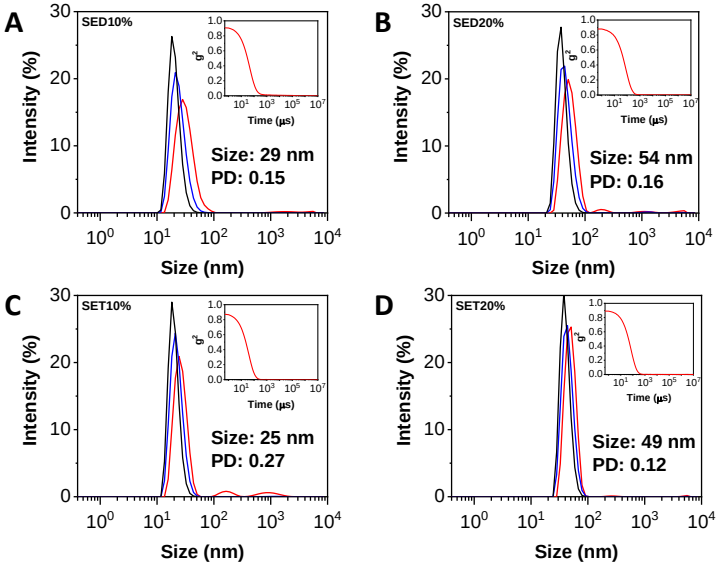

Figure 5.8. Size distributions of (A) SED10, (B) SED20%, (C) SET10% and (D) SET20% in DMSO obtained by DLS. The intensity (red line), volume (blue line) and number (black line) distributions are displayed. The insets show the correlograms.

DLS measurements were taken after the PPM by DMAP and purification by dialysis of the FAIC-containing copolymers. SED10%+DMAP exhibited an increase in size from 29 nm to 40 nm while SET10%+DMAP showed no change at 25 nm. Their PD stayed low at 0.24 and 0.12 for SED10%+DMAP and SET10%+DMAP respectively (Figure 5.9 and Table 5.1). Both the 20 mol% substituted copolymers displayed increase in size from around 50 nm for the unsubstituted copolymers to 100 nm and 78 nm. These increases might be a result of their swelling because of the higher polarity of their core along with possible aggregation.

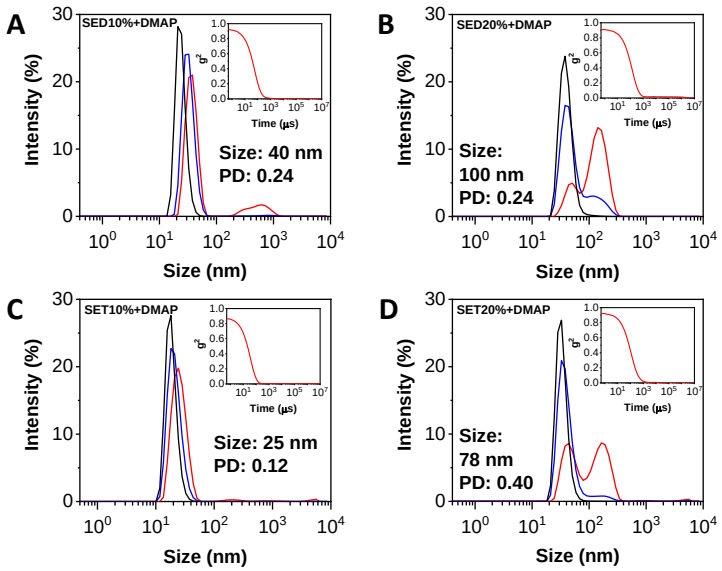

Figure 5.9. Size distributions of (A) SED10%+DMAP, (B) SED20%+DMAP, (C) SET10%+DMAP and (D) SET20%+DMAP in DMSO obtained by DLS. The intensity (red line), volume (blue line) and number (black line) distributions are displayed. The insets show the correlograms.

Table 5.1. Characterisation by SEC, CD and DLS of the nanostructures obtained by SE self-assembly of P(PAIC)$_{50}$-*b*-(P(MAIC)$_y$-*co*-P(FAIC)$_z$)$_{50}$ block copolymers.

Polymer	M_n (kDa)[a]	$Đ_M$[a]	CD$_{360}$ (mdeg)[b]	D_h (nm)[c]
SED10%	17.0	1.14	2.7	29 (0.15)
SET10%	17.5	1.12	2.7	25 (0.27)
SED20%	13.2	1.30	2.3	54 (0.16)
SET20%	13.5	1.32	3.0	49 (0.12)
SED10%+DMAP	16.6	1.14	1.9	40 (0.24)
SET10%+DMAP	16.4	1.18	2.1	25 (0.12)
SED20%+DMAP	9.4	1.63	2.2	100 (0.24)
SET20%+DMAP	11.2	1.53	2.1	78 (0.40)

[a]Determined by SEC (THF + 2% v/v NEt$_3$, 40 °C, PS standards). [b]CD signal at λ = 360 nm. [c]Spherical particles size measured by DLS with PD in parenthesis.

To verify the morphology of the SE self-assembled nano-objects, dry-state TEM of P(PAIC)$_{50}$-*b*-P(MAIC)$_{50}$ was conducted, which demonstrated the

spherical nature of the nanoparticles (Figure 5.10A). Measurement of the nanostructures' size on the TEM images yielded an average size of 18 ±3 nm close to what was found in Chapter 3 and 4 for the NiCCo-PISA nano-objects (Figure 5.10B). It was interesting to find that copolymers with such different DPs and MWDs achieved nanostructures of comparable sizes and morphologies.

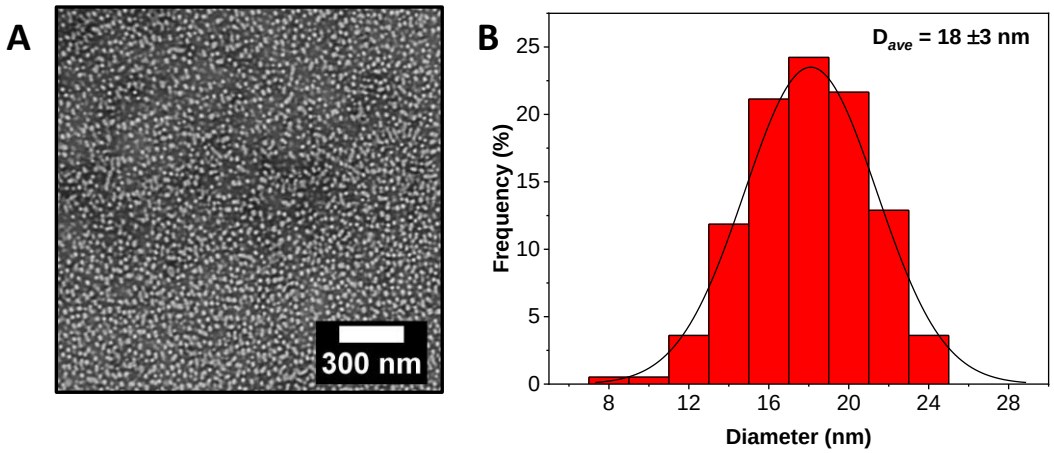

Figure 5.10. (A) Dry-state TEM images of the sphere morphology obtained from SE self-assembly of P(PAIC)$_{50}$-*b*-P(MAIC)$_{50}$. (B) Histogram of spherical particles' size distribution measured from particle analysis of TEM images.

The 20 mol% nanoreactors (SED20%+DMAP and SET20%+DMAP) were used in the subsequent acylation reaction. The nanoreactors effectively catalysed the reaction with conversions of 51% and 43% for SED20%+DMAP and SET20%+DMAP, respectively (Figure 5.11). The difference in final conversion might be a consequence of the location of the active sites where for SET20%+DMAP the reagents have to diffuse through the MAIC layer before they reach the core containing the DMAP moieties while the active sites are directly accessible in the mixed MAIC/DMAP core of SED20%+DMAP. Molecular DMAP, on the other hand, yielded no product after 2.5 h of reaction. The effect of the solvent on the activity of molecular DMAP has already been reported by Cotanda *et al.*,[73] which showed

that in water and under similar conditions this reaction only reached 8% after 24 h. Ishihara and co-workers explained that polar solvents caused the formation of ammonium salts and led to a decrease in reactivity, while less polar solvents facilitated the regeneration of the DMAP catalyst which resulted in higher reactivities.[74] The fact that the nanoreactors were able to catalyse the reaction while molecular DMAP was not demonstrated the "concentrator effect", where the hydrophobic core accelerates the diffusion of the hydrophobic substrate into the catalytic core which led to a high concentration of reagents close to the catalytic moieties thereby increasing the reaction rate. Finally, butyric anhydride is prone to deleterious hydrolysis even without DMAP, and while the anhydride was employed in excess (3 equiv.), the reaction eventually stopped before completion as a result of the complete consumption of anhydride.

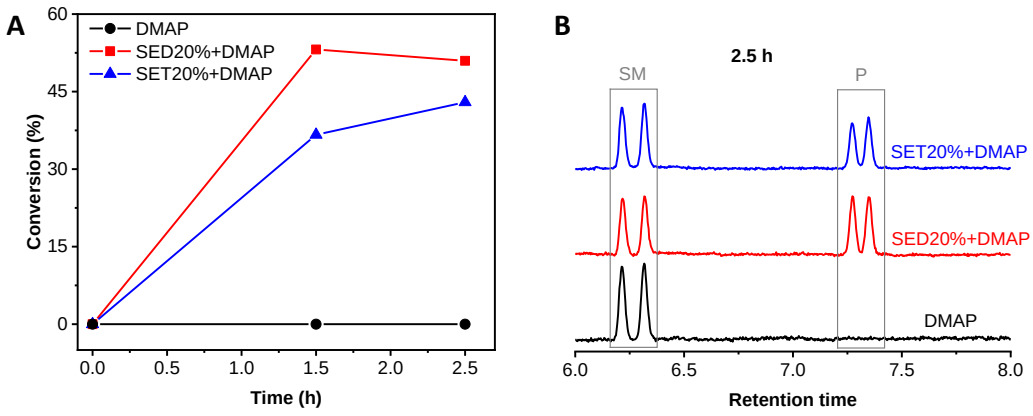

Figure 5.11. (A) Alcohol conversion over time measured by GC-MS of the acylation reaction catalysed by DMAP (black spheres), SED20%+DMAP (red squares) or SET20%+DMAP (blue triangles). (B) The final GC chromatogram after 2.5 h of reaction catalysed by DMAP, SED20%+DMAP or SET20%+DMAP that shows the starting material (SM) 1-phenyl-1-propanol and the product (P) 1-phenylpropyl butyrate signals. 1 mol% catalyst and 0.02 M [OH]

5.4. NiCCo-PISA nanoreactors for catalysis

5.4.1. DMAP-OH functionalised NiCCo-PISA nanoreactors

5.4.1.1. PPM of NiCCo-PISA nanoparticles with DMAP-OH

Using the functionalisable NiCCO-PISA micelles developed in Chapter 3, nanoreactors that contained DMAP catalytic moieties were synthesised with 20% and 50% of active site in the core block. DMAP-OH was reacted with the NiCCo-PISA nanostructures under the same conditions as the primary amine nucleophiles in the previous Chapters *i.e.* DMSO at 55 °C with 5 equivalents of nucleophiles respective to the FAIC content (Scheme 5.4).

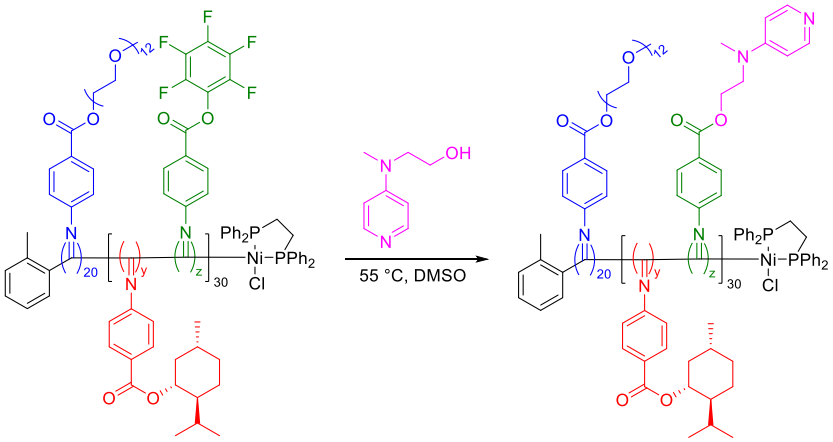

Scheme 5.4. Post-polymerisation modification of $P(PAIC)_{20}$-*b*-$(P(MAIC)_y$-*co*-$P(FAIC)_z)_{30}$ copolymer with DMAP-OH.

The reaction completeness was verified by FT-IR spectroscopy and this time, the signal at 1516 cm^{-1} which relates to the C=C benzene group was employed to integrate the unreacted PFP instead of the 1705 cm^{-1} band because the region was devoid of noise from the product. Moreover, the initial PFP signals at 1516 cm^{-1} were larger than the initial PFP signals at 1705 cm^{-1} which led to more accurate results. The quantity of unreacted PFP was calculated as previously *via* relative integration to the signal at 1597 cm^{-1} of the C=N band that does not change over the course of the reaction. The integration showed that D50%+DMAP copolymer was deprived of PFP units which suggested

a reaction conversion of >95% while the PFP signals that remained for D20%+DMAP indicated a reaction conversion of 75 %.

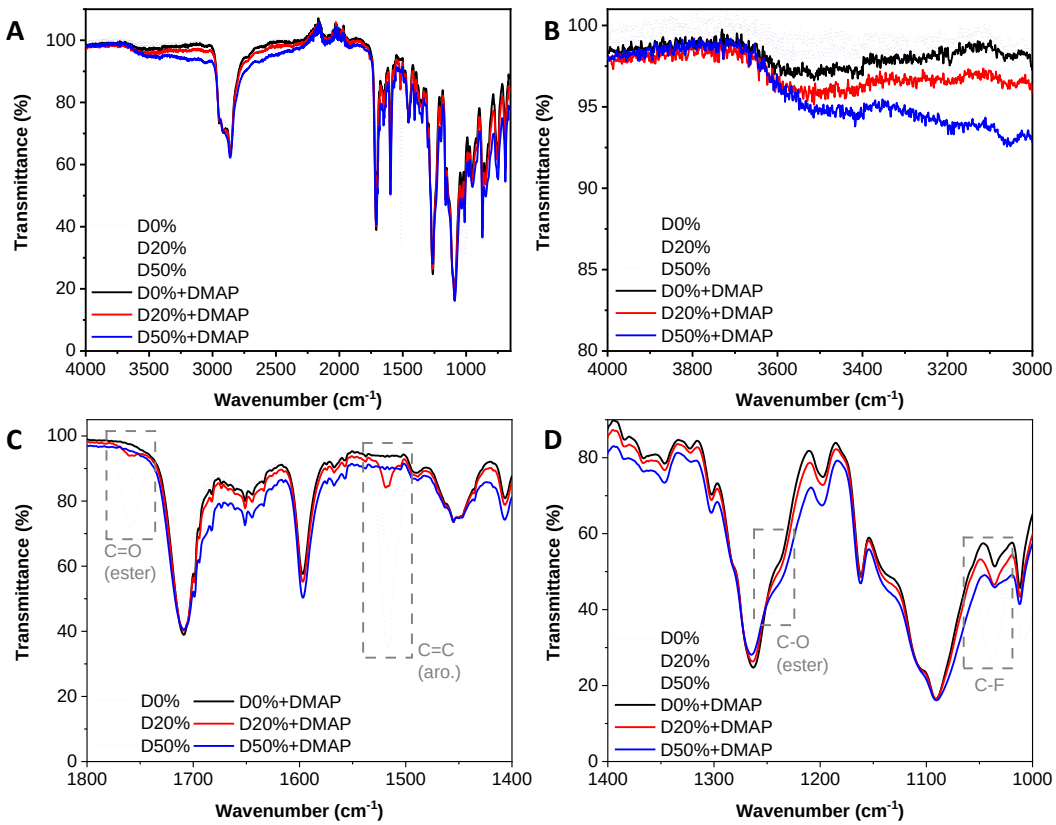

Figure 5.12. FT-IR spectra of the D0% (black), D20% (red) and D50% (blue) copolymers unreacted (dotted line) and reacted with DMAP-OH (solid line). (A) Full spectrum. (B) Zoom in the 4000-3000 cm^{-1} region. (C) Zoom in the 1800-1400 cm^{-1} region. (D) Zoom in the 1400-1000 cm^{-1} region.

By DLS, D0%+DMAP exhibited a larger size than the unreacted micelles D0% (20 nm compared to 33 nm) as a consequence of aggregation of the micelles over the course of the reaction (Figure 5.13). The diameter of the D20%+DMAP nanostructures was similar to the unreacted D20% with a very narrow size distribution PD = 0.08. This narrower size distribution can be explained if the DMAP-OH moiety influences the surface potential of the micelles. The normal PEG corona is neutral therefore, there is no interaction to prevent the aggregation of particles. With DMAP units that diffused from the core to the corona, the outer shell of the micelle becomes charged and

electrostatic repulsive interactions keep the particles apart from their neighbour which diminished the aggregation and led to narrower detected size distribution. The D50%+DMAP nanostructures' size decreased from 20 nm to 18 nm combined with a decrease of the correlogram function maximum, which indicated that the micelles disassembled as a consequence of the higher solubility of the core.

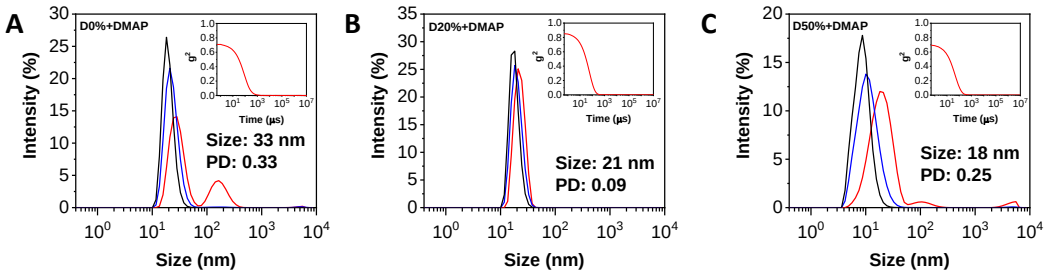

Figure 5.13. Size distributions of (A) D0%+DMAP, (B) D20%+ DMAP, and (C) D50%+ DMAP in DMSO obtained by DLS. The intensity (red line), volume (blue line) and number (black line) distributions are displayed. The insets show the correlograms.

While the DLS analysis could not clearly rule out a possible reaction of the nucleophile for D0%+DMAP, the SEC of the copolymer indicated no change in the MWD. This was not the case for D20%+DMAP and D50%+DMAP. Both possessed a high M_n tail or population, respectively, which indicated that the interaction of the DMAP pendant groups with the column material broadened the MWD. CD spectroscopy of the copolymers displayed a larger CD_{360} for the DMAP-OH copolymers compared with the un-functionalised D20% and D50% which can be explained by the possible absorption of the DMAP pendant groups in this region.

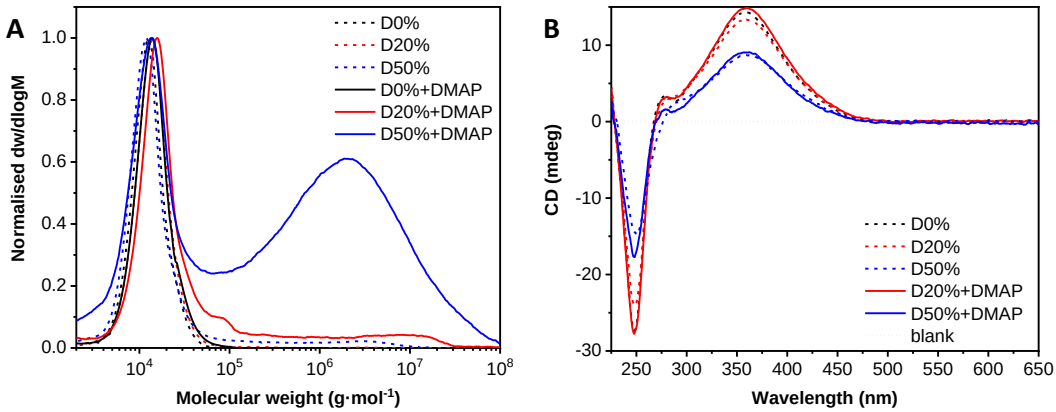

Figure 5.14. (A) Normalised SEC RI molecular weight distributions (THF + 2% v/v NEt_3, 40 °C, PS standards) of D0%, D0%+DMAP, D20%, D20%+DMAP, D50% and D50%+DMAP. (B) CD (THF, 0.5 mg·mL^{-1}) spectra of D0%, D20%, D20%+DMAP, D50% and D50%+DMAP.

Table 5.2. Characterisation of D0%, D20% and D50% before and after PPM with DMAP-OH.

Polymer	D_{DLS} (nm)[a]	$M_{n,\,SEC}$ (kDa)[b]	$Đ_M$[b]	CD_{360} (mdeg)[c]
D0%	20 (0.18)	11.2	1.24	14
D0%+DMAP	33 (0.33)	12.5	1.25	-
D20%	21 (0.14)	12.4	1.24	13
D20%+DMAP	21 (0.09)	14.9	1.41	15
D50%	20 (0.25)	10.5	1.34	9
D50%+DMAP	18 (0.25)	-[d]	-[d]	9

[a] Spherical particles size measured by DLS with PD in parenthesis. [b] Determined by SEC (THF + 2% v/v NEt_3) using PS standards. [c] CD (THF, 0.5 mg·mL^{-1}) signal at λ = 360 nm. [d] Molecular weight distribution is outside the calibration range.

The block copolymer with 50 mol% content of DMAP was discarded as nanoreactor because of the bimodal MWD displayed in SEC which caused the determination of the actual structure of the copolymer to be unsure. In order to be able to compare these new systems with the SE self-assembled nanoreactors, diblock and triblock NiCCo-PISA copolymers that contained 10

mol% of DMAP-OH were also synthesised and characterised as before, and the results were similar to those of the previous copolymers. (Figure A5.23-5). It is significant however to note that the T10%+DMAP reaction achieved completion while the D10%+DMAP achieved only 61 % conversion. This will surely impact the activity of the resulting nanoreactors.

5.4.1.2. Catalysis of acylation reactions with DMAP-OH functionalised NiCCo-PISA nanoparticles

The NiCCo-PISA 10 mol% diblock (D10%+DMAP) and triblock (T10%+DMAP) nanoreactors were compared to the SET10%+DMAP from the previous section and free DMAP in an acylation reaction conducted in water. As was previously found, free DMAP achieved a null conversion after 20 h while SET10%+DMAP and D10%+DMAP reached comparable alcohol conversions of 9% and 11%, respectively (Figure 5.15A). Interestingly, for T10%+DMAP and D10%+DMAP, the results were opposite to what was found for the SE self-assembled nanoreactors: the triblock copolymer nanoreactor proved faster and yielded higher conversions than the diblock system. However, as shown by FT-IR, the T10%+DMAP nanoreactors contained more active sites than the D10%+DMAP ones which explained the difference in activity. There was no enantiomeric excess for either D10%+DMAP nor T10%+DMAP (Figure 5.15B).

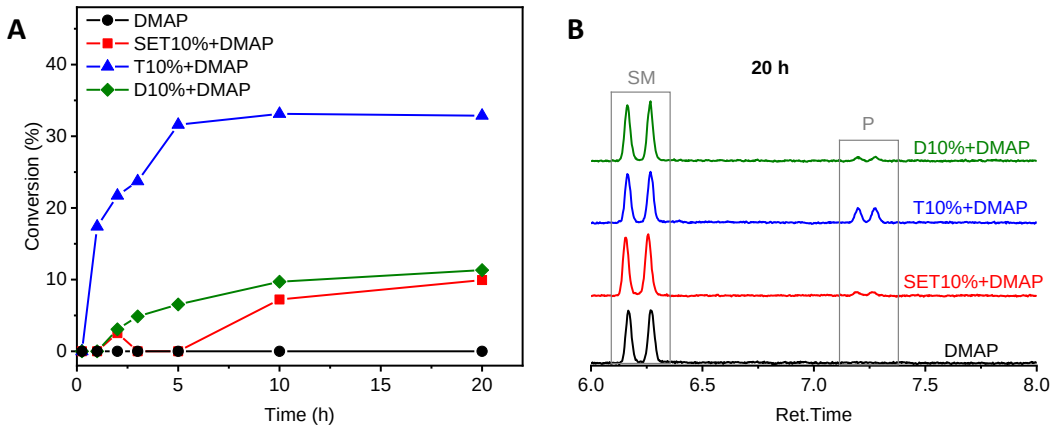

Figure 5.15. (A) Alcohol conversion over time measured by GC-MS of the acylation reaction catalysed by DMAP (black spheres), SET10%+DMAP (red squares), T10%+DMAP (blue triangles) or D10%+DMAP (green triangles). (B) The final GC chromatogram after 20 h of reaction catalysed by DMAP, SET10%+DMAP, T10%+DMAP or D10%+DMAP that shows the starting material (SM) 1-phenyl-1-propanol and the product (P) 1-phenylpropyl butyrate signals. 0.5 mol% catalyst and 0.02 M [OH]

It was hypothesised that a high rate of diffusion of the starting material into the nanoreactor core would prevent the chiral core from effectively differentiating between enantiomers which might have a negative effect on the enantioseparation. A more hydrophilic alcohol was chosen to determine the effect of hydrophilicity on the reaction rate and enantioselectivity. The more hydrophilic alcohol should diffuse more slowly into the core, which would lower the reaction rate and final conversion but would allow the chiral menthol side-chains to affect the diffusion rate of both enantiomers and achieve enantioselectivity. Toward this end, 1-phenyl-1-ethanol and 1-phenyl-1-propanol were reacted in a similar manner with butyric anhydride under basic conditions and catalysed by D10%+DMAP and D20%+DMAP in water. The nanoreactors with the highest DMAP content proved to be more active as a result of the higher density of active moieties at the NP's surface (Figure 5.16A). Moreover, as expected, the more hydrophilic alcohol (1-phenyl-1-ethanol) reacted slower and achieved lower conversions of 69% and 54% for D20%+DMAP and D10%+DMAP respectively as a consequence of its

lower diffusion rate through the micelle core compared to the more hydrophobic 1-phenyl-1-propanol that exhibited conversions of 88% and 79% for D20%+DMAP and D10%+DMAP respectively. Unfortunately, no significant enantiomeric excess was observed over the course of the reactions for all of the assessed systems (Figure 5.16B).

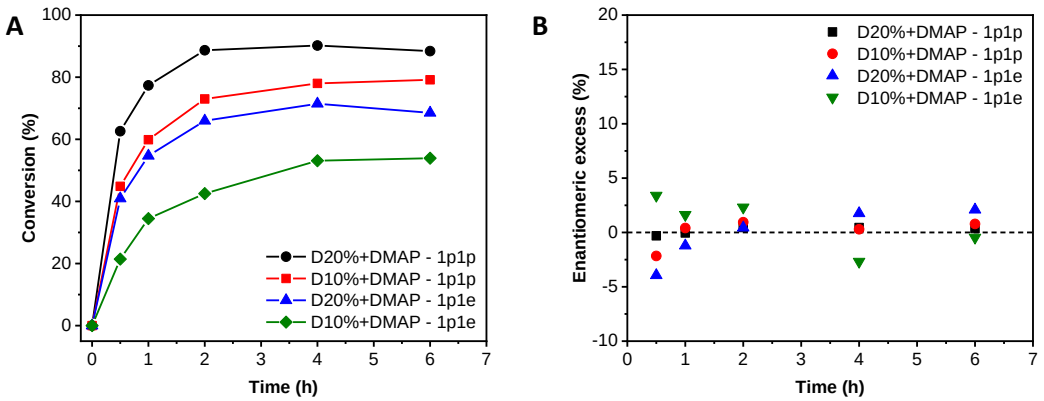

Figure 5.16. (A) Alcohol conversion and (B) enantiomeric excess over time measured by GC-MS of the acylation of 1-phenyl-1-propanol (1p1p) or 1-phenyl-1-ethanol (1p1e) reacted with butyric anhydride (3 equiv.) catalysed by D20%+DMAP (black spheres), D10%+DMAP (red squares), T20%+DMAP (blue triangles) or T10%+DMAP (green triangles). 0.5 mol% catalyst, 1.5 equiv. *i*-Pr$_2$NEt and 0.02 M [OH].

In order to verify the effects of the alcohol diffusion into the core and the basic conditions, two more parameters were tested. Firstly, the alcohol starting material was allowed to diffuse inside the chiral core over 5 h in the reaction mixtures without butyric anhydride to allow the system to reach equilibrium before the start of the reaction. The reaction rate and final conversions were comparable to the previous reaction and no enantiomeric excess was observed (Figure A5.26A-B). Then, reaction without basic conditions was conducted to assess the effect of *i*-Pr$_2$NEt on the reaction rate, final conversion, and enantiomeric excess. The reaction rates were slower with similar final conversions except for the acylation of 1-phenyl-1-ethanol catalysed with D10%+DMAP where the final conversion dropped from 54% to 35% which demonstrated the impact of the basic conditions on the reaction rate and final

conversion (Figure A5.27A-B). These differences were likely a consequence of the formation of DMAP salt over the course of the reaction that lowered the DMAP moieties activity.

All the experiments yielded no enantioselectivity and this could be explained by a couple of reasons. Firstly, the DMAP-OH units are linked through an ethyl linker to the helical backbone which make them distant enough from the menthyl pendant groups that they could be unaffected by their chirality. Secondly, in the case of the triblock copolymers, the hydrophilic block could be able to diffuse to the surface of the core which would render the chiral second layer inefficient. A way to counter the diffusion of the hydrophilic DMAP block would be to crosslink the core with a species that contained DMAP unit.

5.4.2. DMAP(OH)$_2$ cross-linked nanoreactors

5.4.2.1. PPM of NiCCo-PISA nano-objects with DMAP(OH)$_2$

Building on the cross-linked micelles developed in Chapter 4, nanoreactors stabilised with a cross-linker that comprised a DMAP unit were synthesised with 10 mol% and 25 mol% of DMAP active sites. To introduce the DMAP functionality with a cross-linker, a DMAP-modified moiety primary diol (DMAP(OH)$_2$) was synthesised through a modified literature methodology.[75] DMAP(OH)$_2$ was reacted with the FAIC/MAIC copolymer under the same conditions as the previous primary amine nucleophiles *i.e.* DMSO at 55 °C with 0.6 equivalents of nucleophiles respective to the FAIC which yielded quantities of DMAP half that of the FAIC content (Scheme 5.5).

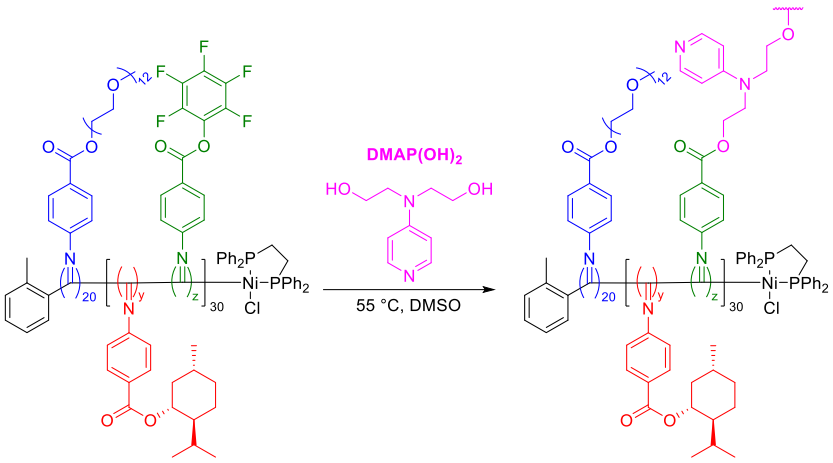

Scheme 5.5. Post-polymerisation modification of P(PAIC)$_{20}$-*b*-(P(MAIC)$_y$-*co*-P(FAIC)$_z$)$_{30}$ copolymer with DMAP(OH)$_2$.

Analysis by FT-IR spectroscopy indicated that the reactions were complete at 45% and 60% for D20%+DMAP(OH)$_2$ and D50%+DMAP(OH)$_2$ respectively (Figure 5.17). This was not a surprise as the diols would be less reactive than their diamine counterparts even with the intramolecular DMAP catalysis. However, no signal was detected in the 3600-3000 cm^{-1} region which indicated that no free O-H was present which suggested that all the reacted DMAP(OH)$_2$ succeeded to react twice an generate a cross-link. It also indicated the absence of hydrolysis.

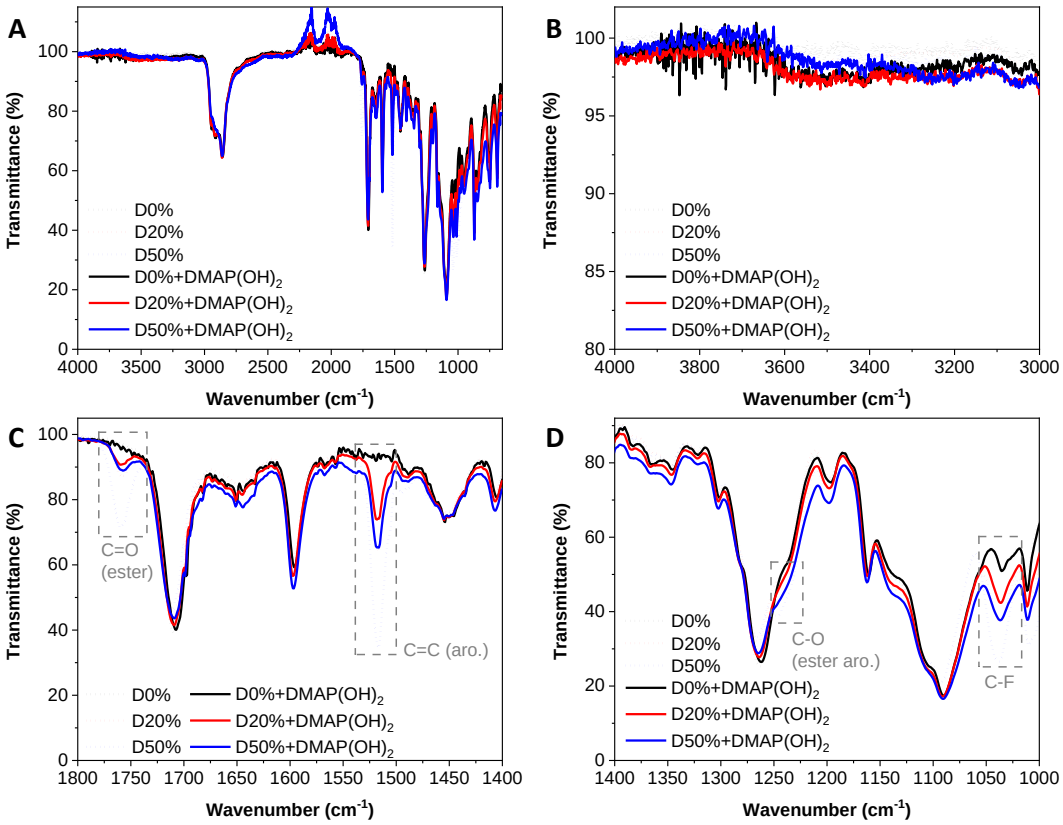

Figure 5.17. FT-IR spectra of the D0% (black), D20% (red) and D50% (blue) copolymers unreacted (dotted line) and reacted with $DMAP(OH)_2$ (solid line). (A) Full spectrum. (B) Zoom in the 4000-3000 cm^{-1} region. (C) Zoom in the 1800-1400 cm^{-1} region. (D) Zoom in the 1400-1000 cm^{-1} region.

DLS analysis of the nanoparticles after cross-linking indicated no major change in the size distribution with sizes around 20 nm and PD consistent with the non-cross-linked micelles (Figure 5.18A and Figure 5.18D). After dialysis for 3 d, macroscopic precipitation was observed for both D20%+$DMAP(OH)_2$ and D50%+$DMAP(OH)_2$ as a consequence of NPs aggregation which was indicated by larger sizes measured by DLS with an increase up to 200 nm for D20%+$DMAP(OH)_2$ and larger PDs with values of 0.46 and 0.39 for D20%+$DMAP(OH)_2$ and D50%+$DMAP(OH)_2$ respectively (Figure 5.18B and Figure 5.18E). The NPs were freeze-dried before solvation in THF and the resulting solutions were analysed by DLS to assess the stability of the cross-linked nano-object. Assemblies with sizes similar

to the micelles in DMSO were detected which demonstrated the stabilisation effect of the DMAP(OH)$_2$ cross-linker (Figure 5.18C and Figure 5.18F)

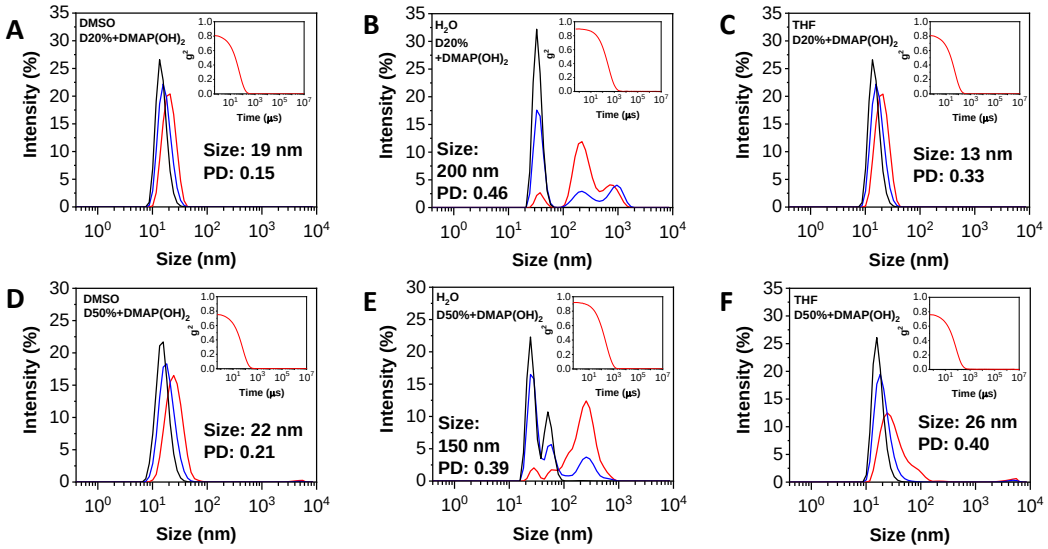

Figure 5.18. Size distributions of D20%+DMAP(OH)$_2$ in (A) DMSO, (B) H_2O and (C) THF, and D50%+ DMAP in (D) DMSO, (E) H_2O and (F) THF obtained by DLS. The intensity (red line), volume (blue line) and number (black line) distributions are displayed. The insets show the correlograms.

As a consequence of their large size, the cross-linked assemblies were not analysed by SEC to avoid obstruction of the columns. CD spectroscopy analysis of the copolymers indicated a drop in the helicity signal. D20%+DMAP(OH)$_2$ decreased from 13 mdeg for D20% to 12 mdeg while D50%+DMAP(OH)$_2$ decreased from 8.7 mdeg for D50% to 6.0 mdeg. The overall results indicated a retention of the helicity after the cross-linking reaction that confirmed the effective synthesis of cross-linked NPs that contained a chiral core.

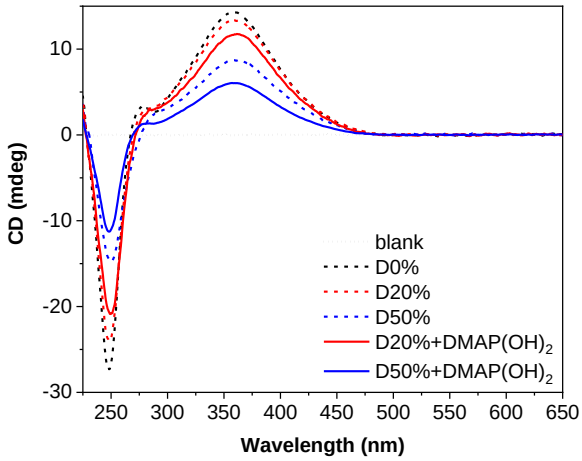

Figure 5.19. CD (THF, 0.5 mg·mL^{-1}) spectra of D0%, D20%, D20%+DMAP(OH)$_2$, D50% and D50%+DMAP(OH)$_2$.

The proof-of-concept for the cross-linking of NiCCo-PISA micelles with DMAP(OH)$_2$ was a success and as discussed at the end of the previous section, in order to assess the effect of a core cross-linked nanoreactors, triblock copolymers that contained 20 mol% of FAIC were self-assembled through NiCCo-PISA. PPM with DMAP(OH)$_2$ was conducted with 1, 0.7, 0.5 and 0.3 equivalents of nucleophile compared to the PFP sites to evaluate the effect of catalytic site density on the nanoreactors activity and enantioselectivity.

5.4.2.2. Catalysis of acylation reactions with DMAP(OH)$_2$ cross-linked NiCCo-PISA nanoparticles

The nanoreactors that contained different densities of catalytic sites were employed in the acylation reaction of 1-phenyl-1-propanol and displayed a difference in reaction rate dependent to the amount of active sites in the nanoreactors' core (Figure 5.20A). As expected, the nanoreactor modified with 1 equivalent of DMAP(OH)$_2$ displayed a final alcohol conversion of 89% while the nanoreactors modified with 0.7, 0.5 and 0.3 equivalents exhibited final alcohol conversions of 44%, 34% and 15% respectively. This demonstrated that the reaction rate of the nanoreactors could be tuned by changing the amount of nucleophile employed. Moreover, free PFP units are expected to be

left and further modification should be possible. As before, no significant enantioselectivity was detected over the course of the reactions time (Figure 5.20B). This absence of enantioselectivity could be a consequence of the fast diffusion of the alcohol into the core compared to the possible difference in diffusion rate between the two enantiomers. Moreover, the DMAP unit might protrude outside of the helix which would cancel the chiral hindrance caused by the menthyl pendant groups. Enantioselectivity could be achieved with more hydrophilic alcohols to slow down its diffusion into the core or with larger chiral groups that would increase the chiral hinderance and increase the diffusion rate difference between the two enantiomers. Another strategy would be to study a reaction that uses a prochiral starting material to induce the chirality instead of chiral separation between two enantiomeric starting material.

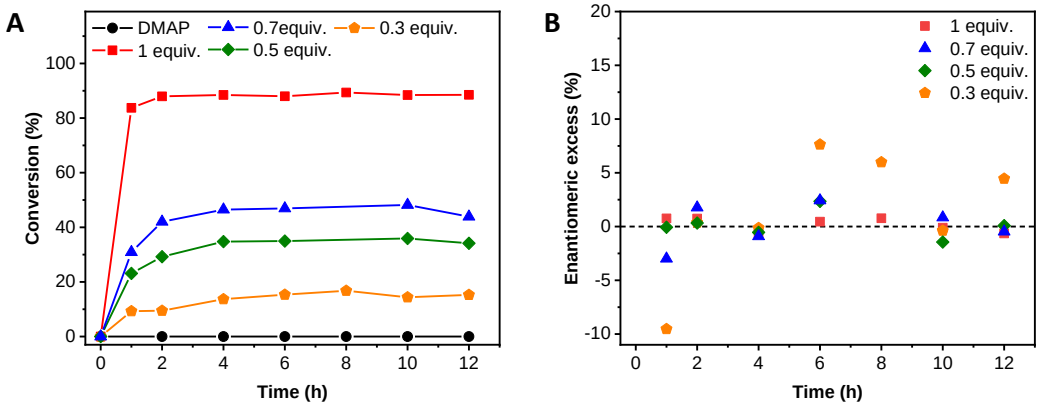

Figure 5.20. (A) Alcohol conversion and (B) enantiomeric excess over time measured by GC-MS of the acylation of 1-phenyl-1-propanol reacted with butyric anhydride (3 equiv.) catalysed by DMAP (black spheres) or T20%-DMAP(OH)$_2$ reacted with 1 (red squares), 0.7 (blue triangles), 0.5 (green triangles) or 0.3 (orange pentagons) equivalent of cross-linker. 0.5 mol% catalyst, 1.5 equiv. *i*-Pr$_2$NEt and 0.02 M [OH]

5.5. Conclusion

A range of menthol-bearing helical catalysts were produced in both molecular and self-assembled structures. The catalytic activity of the molecular helical catalyst was lower than DMAP in THF however, the nanostructures that contained DMAP moieties displayed catalysis activity in water while molecular DMAP did not. This illustrated the benefit of the encapsulation of an active moiety in a hydrophobic pocket surrounded by an aqueous media that led to higher activity overall. Various parameters were tested such as catalyst density and location, basic conditions and diffusion time however, while they all displayed different effects on the reaction rate and final conversions, no enantioselectivity was observed for any of these systems.

5.6. Appendix

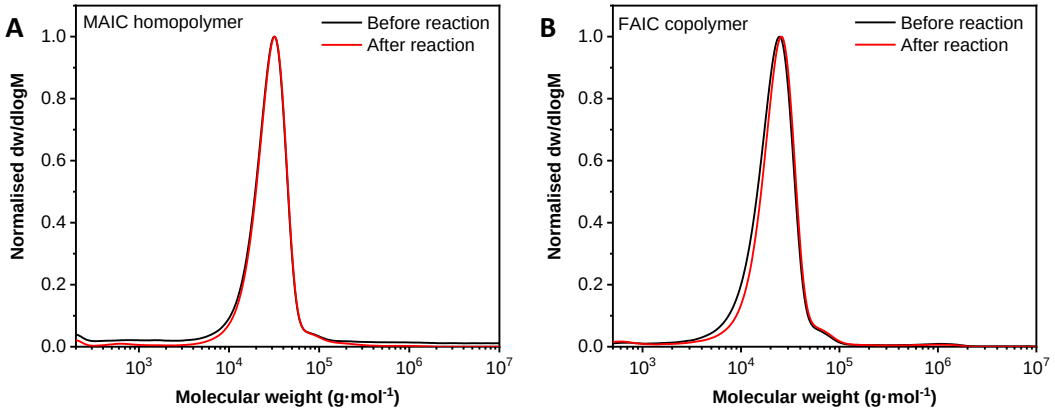

Figure A5.21. Normalised SEC RI molecular weight distributions (THF + 2% v/v NEt_3, 40 °C, PS standards) of (A) the MAIC homopolymer before (black) and after (red) reaction with DMAP-OH in THF at 55 °C, and (B) the FAIC copolymer before (black) and after (red) heating at 55 °C in THF.

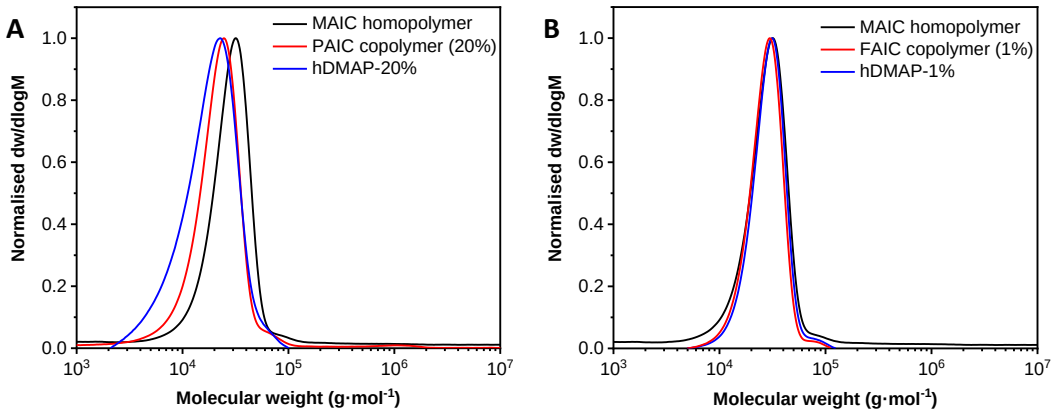

Figure A5.22. Normalised SEC RI molecular weight distributions (THF + 2% v/v NEt_3, 40 °C, PS standards) of (A) the MAIC homopolymer, FAIC copolymer and DMAP copolymer with 20 mol% FAIC units, and (B) the MAIC homopolymer, FAIC copolymer and DMAP copolymer with 1 mol% FAIC units.

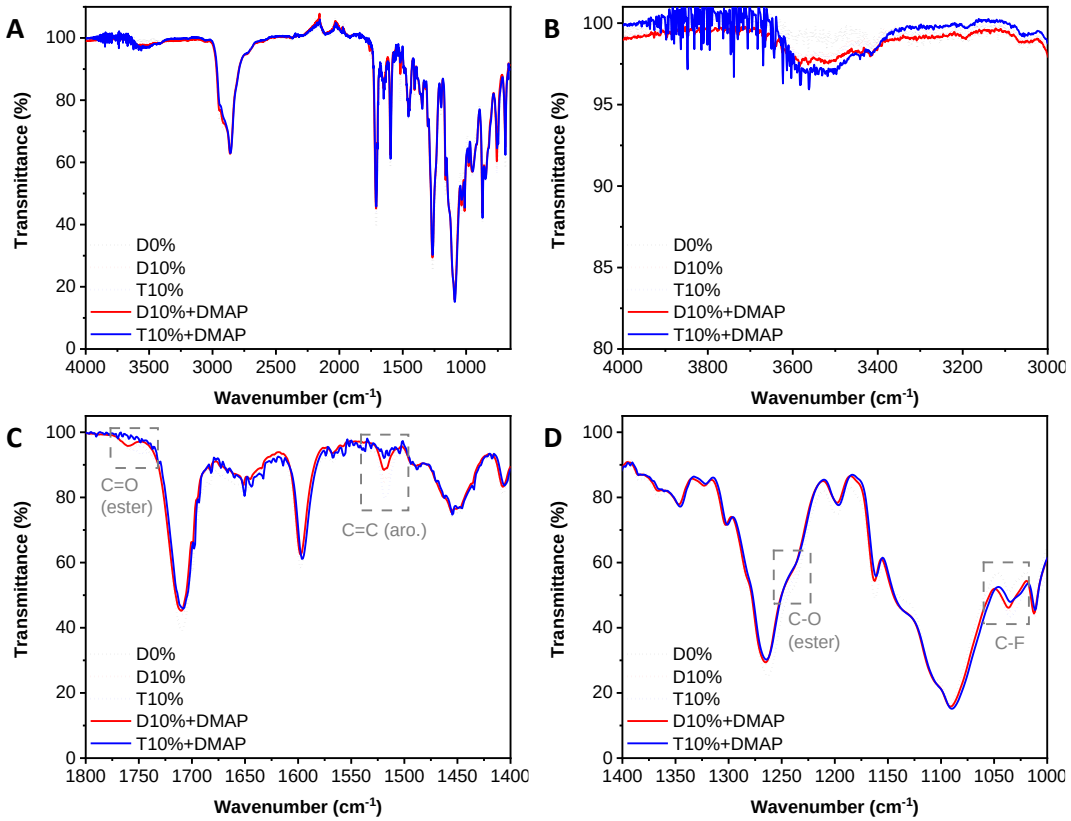

Figure A5.23. FT-IR spectra of the D0% (black), D10% (red) and T10% (blue) copolymers unreacted (dotted line) and reacted with DMAP-OH (solid line). (A) Full spectrum. (B) Zoom in the 4000-3000 cm^{-1} region. (C) Zoom in the 1800-1400 cm^{-1} region. (D) Zoom in the 1400-1000 cm^{-1} region.

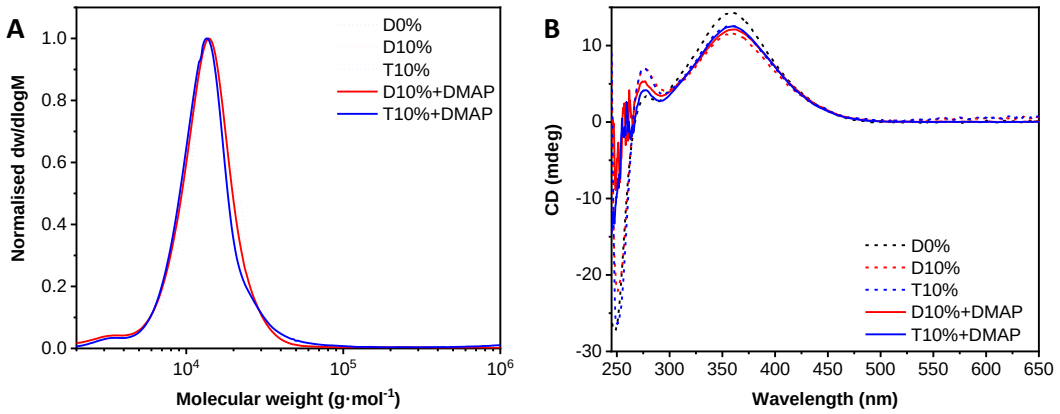

Figure A5.24. (A) Normalised SEC RI molecular weight distributions (THF + 2% v/v NEt_3, 40 °C, PS standards) and (B) CD (THF, 0.5 $mg{\cdot}mL^{-1}$) spectra of D0%, D10%, T10%, D10%+DMAP and T10%+DMAP.

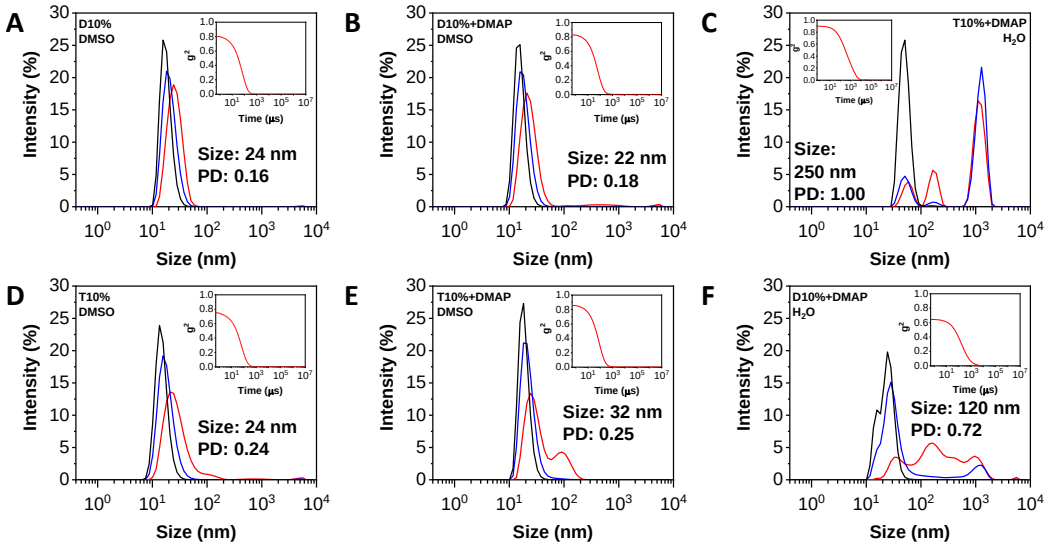

Figure A5.25. Size distributions of D10% (A) before and (B) after PPM with DMAP-OH in DMSO and (C) D10%+DMAP in H_2O, and T10% (A) before and (B) after PPM with DMAP-OH in DMSO and (C) T10%+DMAP in H_2O obtained by DLS. The intensity (red line), volume (blue line) and number (black line) distributions are displayed. The insets show the correlograms.

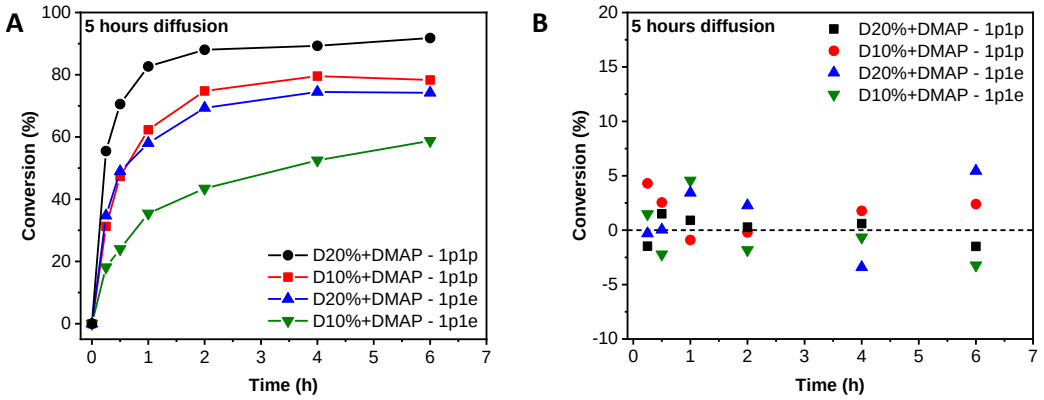

Figure A5.26. (A) Alcohol conversion and (B) enantiomeric excess over time measured by GC-MS of the acylation of 1-phenyl-1-propanol (1p1p) or 1-phenyl-1-ethanol (1p1e) reacted after 5 h of diffusion with butyric anhydride (3 equiv.) catalysed by D20%+DMAP (black spheres), D10%+DMAP (red squares), T20%+DMAP (blue triangles) or T10%+DMAP (green triangles). 0.5 mol% catalyst, 1.5 equiv. *i*-Pr_2NEt and 0.02 M [OH]

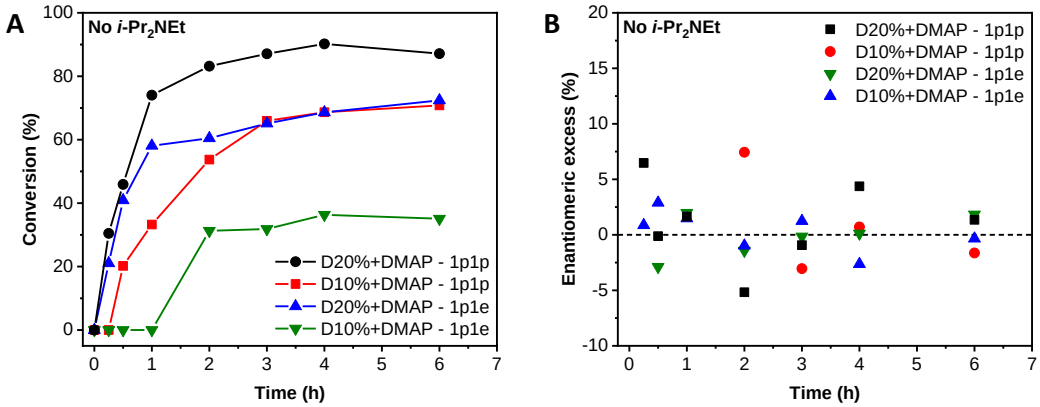

Figure A5.27. (A) Alcohol conversion and (B) enantiomeric excess over time measured by GC-MS of the acylation of 1-phenyl-1-propanol (1p1p) or 1-phenyl-1-ethanol (1p1e) reacted with butyric anhydride catalysed by D20%+DMAP (black spheres), D10%+DMAP (red squares), T20%+DMAP (blue triangles) or T10% (green triangles). 0.5 mol% catalyst, and 0.02 M [OH]

5.7. References

1. Yuki, H.; Okamoto, Y.; Okamoto, I., *J. Am. Chem. Soc.* 1980, 20, 6356-6358.
2. Okamoto, Y.; Honda, S.; Okamoto, I.; Yuki, H.; Murata, S.; Noyori, R.; Takaya, H., *J. Am. Chem. Soc.* 1981, 23, 6971-6973.
3. Nakano, T.; Satoh, Y.; Okamoto, Y., *Macromolecules* 2001, 8, 2405-2407.
4. Liu, L.; Zang, Y.; Hadano, S.; Aoki, T.; Teraguchi, M.; Kaneko, T.; Namikoshi, T., *Macromolecules* 2010, 22, 9268-9276.
5. Song, C.; Zhang, C.; Wang, F.; Yang, W.; Deng, J., *Polym. Chem.* 2013, 3, 645-652.
6. Miyabe, T.; Iida, H.; Banno, M.; Yamaguchi, T.; Yashima, E., *Macromolecules* 2011, 21, 8687-8692.
7. Miyabe, T.; Iida, H.; Ohnishi, A.; Yashima, E., *Chem. Sci.* 2012, 3, 863-867.
8. Liu, N.; Ma, C.-H.; Sun, R.-W.; Huang, J.; Li, C.; Wu, Z.-Q., *Polym. Chem.* 2017, 14, 2152-2163.
9. Wang, Q.; Chu, B.-F.; Chu, J.-H.; Liu, N.; Wu, Z.-Q., *ACS Macro Lett.* 2018, 2, 127-131.
10. Reggelin, M.; Schultz, M.; Holbach, M., *Angew. Chem. Int. Ed.* 2002, 9, 1614-1617.
11. Reggelin, M.; Doerr, S.; Klussmann, M.; Schultz, M.; Holbach, M., *Proc. Natl. Acad. Sci. U.S.A.* 2004, 15, 5461-5466.
12. Müller, C. A.; Hoffart, T.; Holbach, M.; Reggelin, M., *Macromolecules* 2005, 13, 5375-5380.
13. Reggelin, M.; Scholz, J.; Hamburger, M., *J. Polym. Sci. A Polym. Chem.* 2009, 18, 4830-4839.
14. Sanda, F.; Araki, H.; Masuda, T., *Chem. Lett.* 2005, 12, 1642-1643.
15. Yamamoto, T.; Suginome, M., *Angew. Chem. Int. Ed.* 2009, 3, 539-542.
16. Yamamoto, T.; Murakami, R.; Komatsu, S.; Suginome, M., *J. Am. Chem. Soc.* 2018.
17. Yoshinaga, Y.; Yamamoto, T.; Suginome, M., *ACS Macro Lett.* 2017, 705-710.
18. Zhou, L.; Chu, B.-F.; Xu, X.-Y.; Xu, L.; Liu, N.; Wu, Z.-Q., *ACS Macro Lett.* 2017, 824-829.
19. Zhou, L.; Shen, L.; Huang, J.; Liu, N.; Zhu, Y.-Y.; Wu, Z.-Q., *Chin J Polym Sci* 2018, 2, 163-170.
20. Maeda, K.; Tanaka, K.; Morino, K.; Yashima, E., *Macromolecules* 2007, 19, 6783-6785.
21. Iida, H.; Tang, Z.; Yashima, E., *J. Polym. Sci. A Polym. Chem.* 2013, 13, 2869-2879.

22. Zhang, D.; Zhang, H.; Song, C.; Yang, W.; Deng, J., *Synth. Met* 2012, 21–22, 1858-1863.
23. Zhang, D.; Ren, C.; Yang, W.; Deng, J., *Macromol. Rapid Commun.* 2012, 8, 652-657.
24. Tang, Z.; Iida, H.; Hu, H.-Y.; Yashima, E., *ACS Macro Lett.* 2012, 2, 261-265.
25. Miyake, G. M.; Iida, H.; Hu, H.-Y.; Tang, Z.; Chen, E. Y. X.; Yashima, E., *J. Polym. Sci. A Polym. Chem.* 2011, 24, 5192-5198.
26. Terada, K.; Masuda, T.; Sanda, F., *J. Polym. Sci. A Polym. Chem.* 2009, 19, 4971-4981.
27. Zhang, H.; Yang, W.; Deng, J., *J. Polym. Sci. A Polym. Chem.* 2015, 15, 1816-1823.
28. Miyabe, T.; Hase, Y.; Iida, H.; Maeda, K.; Yashima, E., *Chirality* 2009, 1, 44-50.
29. Takata, L. M. S.; Iida, H.; Shimomura, K.; Hayashi, K.; dos Santos, A. A.; Yashima, E., *Macromol. Rapid Commun.* 2015, 23, 2047-2054.
30. Yamamoto, T.; Murakami, R.; Suginome, M., *J. Am. Chem. Soc.* 2017, 7, 2557-2560.
31. Bécart, D.; Diemer, V.; Salaün, A.; Oiarbide, M.; Nelli, Y. R.; Kauffmann, B.; Fischer, L.; Palomo, C.; Guichard, G., *J. Am. Chem. Soc.* 2017, 36, 12524-12532.
32. Helms, B.; Guillaudeu, S. J.; Xie, Y.; McMurdo, M.; Hawker, C. J.; Fréchet, J. M. J., *Angew. Chem. Int. Ed.* 2005, 39, 6384-6387.
33. Helms, B.; Liang, C. O.; Hawker, C. J.; Fréchet, J. M. J., *Macromolecules* 2005, 13, 5411-5415.
34. Lestini, E.; Blackman, L. D.; Zammit, C. M.; Chen, T.; Williams, R. J.; Inam, M.; Couturaud, B.; O'Reilly, R. K., *Polym. Chem.* 2018.
35. Dergunov, S. A.; Khabiyev, A. T.; Shmakov, S. N.; Kim, M. D.; Ehterami, N.; Weiss, M. C.; Birman, V. B.; Pinkhassik, E., *ACS Nano* 2016.
36. Chen, S.; Cardozo, A. F.; Julcour, C.; Blanco, J.-F.; Barthe, L.; Gayet, F.; Lansalot, M.; D'Agosto, F.; Delmas, H.; Manoury, E.; Poli, R., *Polymer* 2015, 327-335.
37. Zhao, B.; Deng, J. R.; Deng, J. P., *ACS Macro Lett.* 2017, 1, 6-10.
38. Zayas, H. A.; Lu, A.; Valade, D.; Amir, F.; Jia, Z.; O'Reilly, R. K.; Monteiro, M. J., *ACS Macro Lett.* 2013, 4, 327-331.
39. Zhang, B.; Wang, F.; Zhou, H.; Gao, D.; Yuan, Z.; Wu, C.; Zhang, X., *Angew. Chem. Int. Ed.* 2019, 9, 2744-2748.
40. Meeuwissen, S. A.; Rioz-Martínez, A.; de Gonzalo, G.; Fraaije, M. W.; Gotor, V.; van Hest, J. C. M., *J. Mater. Chem* 2011, 47, 18923-18926.
41. Spulber, M.; Baumann, P.; Saxer, S. S.; Pieles, U.; Meier, W.; Bruns, N., *Biomacromolecules* 2014, 4, 1469-1475.

42. Peters, R. J. R. W.; Marguet, M.; Marais, S.; Fraaije, M. W.; van Hest, J. C. M.; Lecommandoux, S., *Angew. Chem. Int. Ed.* 2014, 1, 146-150.
43. Rifaie-Graham, O.; Ulrich, S.; Galensowske, N. F. B.; Balog, S.; Chami, M.; Rentsch, D.; Hemmer, J. R.; Read de Alaniz, J.; Boesel, L. F.; Bruns, N., *J. Am. Chem. Soc.* 2018, 25, 8027-8036.
44. Chuanoi, S.; Anraku, Y.; Hori, M.; Kishimura, A.; Kataoka, K., *Biomacromolecules* 2014, 7, 2389-2397.
45. Qu, P.; Kuepfert, M.; Jockusch, S.; Weck, M., *ACS Catal.* 2019, 4, 2701-2706.
46. Rothfuss, H.; Knöfel, N. D.; Roesky, P. W.; Barner-Kowollik, C., *J. Am. Chem. Soc.* 2018, 18, 5875-5881.
47. Garmendia, S.; Lawrenson, S. B.; Arno, M. C.; O'Reilly, R. K.; Taton, D.; Dove, A. P., *Macromol. Rapid Commun.* 2019, 15, 1900071.
48. Garmendia, S.; Dove, A. P.; Taton, D.; O'Reilly, R. K., *Polym. Chem.* 2018, 43, 5286-5294.
49. Tokura, Y.; Harvey, S.; Xu, X.; Chen, C.; Morsbach, S.; Wunderlich, K.; Fytas, G.; Wu, Y.; Ng, D. Y. W.; Weil, T., *Chem. Commun.* 2018, 22, 2808-2811.
50. Patterson, J. P.; Cotanda, P.; Kelley, E. G.; Moughton, A. O.; Lu, A.; Epps III, T. H.; O'Reilly, R. K., *Polym. Chem.* 2013, 6, 2033-2039.
51. Bouilhac, C.; Cloutet, E.; Taton, D.; Deffieux, A.; Borsali, R.; Cramail, H., *J. Polym. Sci. A Polym. Chem.* 2009, 1, 197-209.
52. Zhang, H. Y.; Ding, L.; Chen, Y.; Yang, W. T.; Deng, J. P., *Journal of Polymer Science Part a-Polymer Chemistry* 2012, 21, 4415-4422.
53. Lu, A.; Moatsou, D.; Hands-Portman, I.; Longbottom, D. A.; O'Reilly, R. K., *ACS Macro Lett.* 2014, 12, 1235-1239.
54. Lu, J.; Dimroth, J.; Weck, M., *J. Am. Chem. Soc.* 2015, 40, 12984-12989.
55. Lee, L.-C.; Lu, J.; Weck, M.; Jones, C. W., *ACS Catal.* 2016, 2, 784-787.
56. Thiele, M. J.; Davari, M. D.; Hofmann, I.; König, M.; Lopez, C. G.; Vojcic, L.; Richtering, W.; Schwaneberg, U.; Tsarkova, L. A., *Angew. Chem. Int. Ed.* 2018, 30, 9402-9407.
57. Le, D.; Dilger, M.; Pertici, V.; Diabaté, S.; Gigmes, D.; Weiss, C.; Delaittre, G., *Angew. Chem. Int. Ed.* 2019, 14, 4725-4731.
58. Zhu, Y.; Wang, F.; Zhang, C.; Du, J., *ACS Nano* 2014, 7, 6644-6654.
59. Einfalt, T.; Goers, R.; Dinu, I. A.; Najer, A.; Spulber, M.; Onaca-Fischer, O.; Palivan, C. G., *Nano Letters* 2015, 11, 7596-7603.
60. Dinu, M. V.; Spulber, M.; Renggli, K.; Wu, D.; Monnier, C. A.; Petri-Fink, A.; Bruns, N., *Macromol. Rapid Commun.* 2015, 6, 507-514.
61. Gaitzsch, J.; Huang, X.; Voit, B., *Chem. Rev.* 2016, 3, 1053-1093.
62. Li, J.; Li, Y.; Wang, Y.; Ke, W.; Chen, W.; Wang, W.; Ge, Z., *Nano Letters* 2017, 11, 6983-6990.

63. Liu, X.; Formanek, P.; Voit, B.; Appelhans, D., *Angew. Chem. Int. Ed.* 2017, 51, 16233-16238.
64. Varlas, S.; Blackman, L. D.; Findlay, H. E.; Reading, E.; Booth, P. J.; Gibson, M. I.; O'Reilly, R. K., *Macromolecules* 2018, 16, 6190-6201.
65. Womble, C. T.; Kuepfert, M.; Weck, M., *Macromol. Rapid Commun.* 2019, 1, 1800580.
66. Nishimura, T.; Hirose, S.; Sasaki, Y.; Akiyoshi, K., *J. Am. Chem. Soc.* 2020, 1, 154-161.
67. Liu, Y.; Wang, Y.; Wang, Y.; Lu, J.; Piñón, V.; Weck, M., *J. Am. Chem. Soc.* 2011, 36, 14260-14263.
68. Spulber, M.; Najer, A.; Winkelbach, K.; Glaied, O.; Waser, M.; Pieles, U.; Meier, W.; Bruns, N., *J. Am. Chem. Soc.* 2013, 24, 9204-9212.
69. Varlas, S.; Foster, J. C.; Georgiou, P. G.; Keogh, R.; Husband, J. T.; Williams, D. S.; O'Reilly, R. K., *Nanoscale* 2019, 26, 12643-12654.
70. Cotanda, P.; O'Reilly, R. K., *Chem. Commun.* 2012, 83, 10280-10282.
71. Chen, J.-L.; Su, M.; Jiang, Z.-Q.; Liu, N.; Yin, J.; Zhu, Y.-Y.; Wu, Z.-Q., *Polym. Chem.* 2015, 26, 4784-4793.
72. Huber, F.; Kirsch, S. F., *Chem. Eur. J.* 2016, 17, 5914-5918.
73. Cotanda, P.; Lu, A.; Patterson, J. P.; Petzetakis, N.; O'Reilly, R. K., *Macromolecules* 2012, 5, 2377-2384.
74. Sakakura, A.; Kawajiri, K.; Ohkubo, T.; Kosugi, Y.; Ishihara, K., *J. Am. Chem. Soc.* 2007, 47, 14775-14779.
75. Copp, F. C.; Timmis, G. M., *J. Chem. Soc.* 1955, 0, 2021-2027.

Chapter 6 Conclusion and future work

6.1. Conclusions

The objective of the research carried out for this thesis was to develop water-based nanoreactors for the asymmetric catalysis of transesterification reactions to mimic enzymes. To achieve this ambition, chiral core micelles with active pendant groups were envisioned as plausible nanoreactors that would differentiate between different enantiomers. To synthesise such nanostructures, a new type of polymerisation-induced self-assembly (PISA) based on the nickel-catalysed coordination polymerisation of helical aryl isocyanide copolymers (NiCCo-PISA) was developed. Synthesis of amphiphilic block copolymers composed of solvophilic achiral mPEGyl 4-isocyanobenzoate (PAIC) and solvophobic chiral menthyl 4-isocyanobenzoate (MAIC) was conducted in DMSO leading to the formation of a range of nano-object morphologies *i.e.* spherical micelles, worm-like micelles and polymersomes with helical cores. The helical nature of the P(PAIC)-*b*-P(MAIC) block copolymer assemblies' core was investigated by conducting the NiCCo-PISA process in the presence of an achiral dye. Induction of a CD signal was observed in the region of the CD-silent dye which showed the effect of the chiral core on encapsulated compounds. This study demonstrated the easy synthesis of helices-containing nanostructures and the positive effect the helical core could have.

Next, to allow the introduction of active pendant groups, integration of a perfluorophenyl 4-isocyanobenzoate (FAIC) monomer that could be easily substituted by nucleophiles was conducted by copolymerisation of FAIC and MAIC as the core forming comonomers in NiCCo-PISA. Synthesis of block copolymer P(PAIC)-*b*-(P(MAIC)-*co*-P(FAIC)) spherical micelles with different quantities of FAIC units was achieved, which provided functionalisable nano-objects with helical cores. The helicity of the resulting nanostructures was retained after the NiCCo-PISA process and post-

polymerisation modifications (PPMs) of the nano-objects with primary amines tethered to easily detectable alcohol (ethanolamine), fluorinated (trifluoroethylamine) and fluorescent (aminochloridemaleimide) pendant groups were conducted. Introduction of the different units was confirmed, and the helicity of the resulting nanostructures' core was retained after the substitution reactions. Interestingly, PPM of the nano-objects that contained a high quantity of FAIC units with polar side chains (*i.e.* ethanolamine or aminochloridemaleimide) led to the disassembly of the nanostructures in DMSO. To address this stability issue and possibly introduce stimulus-responsiveness to the system later, PPM of the nanostructures with primary diamines 1,2-ethanediamine, 1,4-butanediamine and 1,6-hexanediamine was conducted. The resulting nano-objects showed limited change in their size, morphology and helicity; moreover, they exhibited stability in both selective (*i.e.* DMSO and water) and non-selective solvents (*i.e.* THF) that would result in possible applications in a larger range of environments.

The study of the NiCCo-PISA nanostructures' core and corona responsiveness was conducted with different stimuli. Thermoresponsiveness of the nanostructure's corona was expected because of the PEG pendant groups that are known for exhibiting LCST behaviour. The nano-objects precipitated out of solution when heated in water which demonstrated a possible way to recover the nanoreactors when the reaction was complete. However, the comb-like nature of the corona combined with the grafting density made the thermally-triggered precipitation irreversible. Building on the cross-linked micelles system, responsiveness of the core was made possible by PPM of the nanostructures with stimulus-responsive cross-linkers. Cystamine cross-linked nanoparticles exhibited a reduction-triggered response, where the size of the assemblies changed over time when they were subjected to a L-glutathione (GSH) environment. 2-[1-(2-amino-ethoxy)-1-methyl-ethoxy]-ethylamine

(AEE) cross-link nanostructure were shown to be pH-responsive in both DMSO and THF with a faster reaction time in the latter case. Stimuli-responsiveness is interesting for controlled release of cargo and the chiral core could be leveraged for enantiomeric segregation. Moreover, both stimuli are part of what differentiate cancerous cells from healthy cells and could be employed for the targeted release of drug cargo into tumours.

Finally, catalysis was conducted with the acetylation of butyric anhydride with 1-phenyl-1-propanol and 1-phenyl-1-ethanol chosen as model reactions. The reactions were first done with polyisocyanide (PIC) helices P(PAIC)-*b*-(P(MAIC)-*co*-P(FAIC)) substituted with a DMAP primary alcohol dispersed in THF. This helical catalyst showed no enantioselectivity, maybe as a consequence of the distance between the DMAP active site and the helical backbone. A second system employed was the self-assembly of nanoreactors by solvent exchange of a P(PAIC)-*b*-(P(MAIC)-*co*-P(DMAP)) diblock copolymer on the same model as the catalytic helical PIC. While this system also did not exhibit enantioselectivity, the nanoreactors showed a faster reaction rate than molecular DMAP as a consequence of the "concentrator effect", which demonstrated an advantage of encapsulated catalysts over the free ones. Building on the previous Chapters, a new generation of nanoreactors were synthesised by PPM of the NiCCo-PISA P(PAIC)-*b*-(P(MAIC)-*co/b*-P(FAIC)) di- or tri-block copolymer micelles with a modified DMAP that contained either one or two primary alcohols with the latter that led to crosslinked nanoreactors. While both systems catalysed the reaction well in water and exhibited the "concentrator effect", no enantioselectivity was detected either.

In conclusion, this thesis reports on a methodology for the preparation of functionalisable helical-core nanostructures that were employed as

nanoreactors in acetylation reactions. While the nanoreactors designed in this thesis did not reach the goal of asymmetric synthesis that was set, the path to their synthesis unveiled a versatile system that could be employed in several other areas than catalysis such as circularly polarised luminescence, chiral smart nanomaterials and drug-delivery that would require more investigation to fully explore and understand.

6.2. Future work

As stated previously, the system developed in NiCCo-PISA is very versatile starting with the monomers employed. The synthesis of the monomers is fairly simple with a maximum of four steps and allows one to choose what side chain is attached. Moreover, if the functionality of the chosen side chain is incompatible with the synthesis or the polymerisation methodology, the functionalisable FAIC monomer can be used for PPM. Other chiral pendant groups can replace the menthyl: amino acids, DNA, sugars, terpenoids, *etc.* Amino acids would arrange in an array of hydrogen bonds to form a more stable helix as presented by Nolte and co-workers.[1] Moreover, the H-bonds could orient the reaction as presented by Yashima and co-workers and help enhance enantioselectivity.[2, 3]

In recent work, Seferos and co-workers demonstrated that the chain end for the *o*-Tol(dppe)NiCl catalyst is stable and could be isolated and purified before chain extension.[4] This could allow the transfer of the macroinitiator into other solvent before the NiCCo-PISA process to assess the effect of solvent on the final morphology and make available solvents of different polarities. Moreover, the macroinitiator could be characterised before chain-extension which would give more control on the resulting NiCCo-PISA copolymers.

Circularly polarised luminescence (CPL) is the phenomenon of circularly polarised light and material exhibiting such emission are valuable for applications such as chiroptical material, sensors and photoelectric devices.[5-8] The grafting or embedding of dyes into nano-objects' could induce CPL as has been demonstrated before for helical polymers or nanostructures. [9-12] The resulting nanoparticles can be tested to assess the effect of the different morphologies on the light emission while a range of dyes can easily be analysed thanks to the ease of synthesis of the NiCCo-PISA nanoparticles.

Building on the nanoreactor Chapter, different catalytic core such as 1,8-diazabicyclo(5.4.0)undec-7-ene (DBU), 1,5,7-triazabicyclo[4.4.0]dec-5-ene (TBD) or 1,1,3,3-tetramethylguanidine (TMG) can by synthesised or modified to bear one or several nucleophilic handle that would allow their introduction into the chiral core. This would give access to a range of different type of reactions while allowing the tuning of the catalytic core activity. Along with the active unit, alcohols and anhydrides with a range of hydrophobicity can be screened to vary the diffusion into the active core and study further the effect of the reagents' hydrophobicity on the reaction enantioselectivity.

The different morphologies (*i.e.* spherical micelles, worm-like micelles and polymersomes) could be tested for the applications listed above and study the effect of the morphology. For example, the polymersomes could be charged with a non-specific enzyme or a hydrophilic catalyst to discover if the chiral membrane can discriminate between enantiomers and allow one over the other to reach the encapsulated catalyst. Cross-linked nano-objects with different morphology could be subjected to the same stimulus to observe how their morphology impact their response to the stimulus.

6.3. References

1. Cornelissen, J. J. L. M.; Donners, J. J. J. M.; Gelder, R. d.; Graswinckel, W. S.; Metselaar, G. A.; Rowan, A. E.; Sommerdijk, N. A. J. M.; Nolte, R. J. M., *Science* 2001, 5530, 676-680.

2. Iida, H.; Tang, Z.; Yashima, E., *J. Polym. Sci. A Polym. Chem.* 2013, 13, 2869-2879.

3. Tang, Z.; Iida, H.; Hu, H.-Y.; Yashima, E., *ACS Macro Lett.* 2012, 2, 261-265.

4. Ye, S.; Cheng, S.; Pollit, A. A.; Forbes, M. W.; Seferos, D. S., *J Am Chem Soc* 2020, 25, 11244-11251.

5. Heffern, M. C.; Matosziuk, L. M.; Meade, T. J., *Chem. Rev.* 2014, 8, 4496-4539.

6. Yang, Y.; da Costa, R. C.; Fuchter, M. J.; Campbell, A. J., *Nat. Photonics* 2013, 8, 634-638.

7. Maeda, H.; Bando, Y.; Shimomura, K.; Yamada, I.; Naito, M.; Nobusawa, K.; Tsumatori, H.; Kawai, T., *J. Am. Chem. Soc.* 2011, 24, 9266-9269.

8. Kim, Y.; Yeom, B.; Arteaga, O.; Jo Yoo, S.; Lee, S.-G.; Kim, J.-G.; Kotov, N. A., *Nat Mater* 2016, 4, 461-468.

9. Han, J.; You, J.; Li, X.; Duan, P.; Liu, M., *Adv. Mater.* 2017, 19, 1606503.

10. Zhao, B.; Pan, K.; Deng, J., *Macromolecules* 2018, 18, 7104-7111.

11. Kumar, J.; Nakashima, T.; Kawai, T., *J. Phys. Chem. Lett* 2015, 17, 3445-3452.

12. Jiang, Q.; Xu, X.; Yin, P.-A.; Ma, K.; Zhen, Y.; Duan, P.; Peng, Q.; Chen, W.-Q.; Ding, B., *J. Am. Chem. Soc.* 2019, 24, 9490-9494.

Chapter 7 Experimental

7.1. Materials

4-(Dimethylamino)pyridine (≥98%, DMAP), L-menthol, poly(ethylene glycol) methyl ether (M_n ~ 550 g·mol^{-1}, mPEG$_{12}$-OH), 2,3,4,5,6-pentafluorophenol, 4-chloropyridine, 2-(methylamino)ethanol, hex-1-yne, diethylamine (Et_2NH), bis(triphenylphosphine)palladium(II) dichloride ($Pd(PEt_3)_2Cl_2$), triethylamine (NEt_3), nickel(II) chloride hexahydrate ($NiCl_2·6H_2O$), 1,2-(diphenylphosphino)ethane (dppe), *o*-tolylmagnesium chloride (1.0 M in THF), 1-ethyl-3-(3-dimethylaminopropyl)carbodiimide (EDC), palladium on carbon loading 10 wt% (Pd/C 10%), propan-2-ol (*i*-PrOH), ethanolamine, 2-methoxy propene, *N*-(2-hydroxyethyl)-phthalimide acetic anhydride, 1-phenly-1-ethanol, 1-phenly-1-propanol, *N*,*N*-diisopropylethylamine (*i*-Pr_2NEt), butyric anhydride and dimethyl sulfoxide (DMSO) anhydrous (≥99%) were purchased from Sigma-Aldrich. DMSO was dried over molecular sieves overnight before use. Ethyl formate, dichloromethane (CH_2Cl_2), sodium hydroxide (NaOH), *p*-toluenesulfonic acid and molecular sieves 4Å were purchased from Fisher Scientific. Tetrahydrofuran (HPLC grade, THF), copper (I) chloride (CuCl) and methanol (MeOH) were purchased from VWR Chemicals. THF was purified *via* passage through a column of basic alumina prior to use. 4-nitrobenzoyl chloride, 2,2,2-trifluoroethylamine (98%) and trifluoroacetic acid (TFA) were purchased from Alfa Aesar. Phosphorus (V) oxychloride ($POCl_3$) was obtained from Acros Organics. Formvar-carbon coated (300 mesh), graphene oxide (GO)-coated (300 mesh) and lacey-carbon coated (400 mesh) copper grids were purchased from EM Resolutions.

7.2. Characterisation techniques

Circular Dichroism Spectroscopy. Circular dichroism (CD) spectra were recorded on a JASCO J810-150S spectropolarimeter with Quartz cells (path length 1 mm, 170 - 2000 nm) from Hellma. For the spectra range 650-450 nm, the following parameters were used: bandwidth 5 nm, data pitch 0.1 nm, scanning speed 100 $nm \cdot s^{-1}$, D.I.T. 4 s. For the spectra range 650-200 nm, the following parameters were employed: bandwidth 5 nm, data pitch 0.2 nm, scanning speed 200 $nm \cdot s^{-1}$, D.I.T. 1 s. 3 accumulations were taken in all cases.

Dynamic Light Scattering. Hydrodynamic diameters (D_h) and size distributions (PD) of nano-objects were determined by dynamic light scattering (DLS) with a Malvern Zetasizer Nano ZS with a 4 mW He-Ne 633 nm laser module which operated at 25 °C. Measurements were carried out at an angle of 173° (back scattering), and results were analysed with the Malvern DTS v7.03 software. All determinations were repeated 5 times with at least 10 measurements recorded for each run. D_h values were calculated with the Stokes-Einstein equation where particles are assumed to be spherical.

Flash Chromatography. Flash chromatography was performed on a Teledyne ISCO CombiFlash Rf+ Lumen equipped with two UV detectors (254 nm and 280 nm) and an internal evaporative light scattering detector (ELSD). Samples were purified with RediSep RF normal phase columns.

Gas chromatography mass spectrometry. GCMS was performed on a Shimadzu GCMS QP2010 SE system with a (CP-Chirasil-Dex CB 25 × 0.25). The temperature programming was set to 120 °C for 5 min then a gradient to 200 °C for 16 min. The injector temperature was (150 °C) with 5.0 μL injection volume

(90 split ratio). The helium carrier gas flow rate was set at (1 mL/min). MS detection was used selective ion scanning *m/z* 1.5-1000 amu. The EI source temperature was (200 °C).

High-Resolution Mass Spectrometry. HRMS spectra were recorded by the MS Analytical Facility Service at the University of Birmingham on a Waters Xevo G2-XS QTof Quadrupole Time-of-Flight mass spectrometer.

Infrared Spectroscopy. Infrared spectra were recorded (neat) on an Agilent Technologies Cary 630 FTIR spectrometer. 16 Scans from 600 to 4000 cm^{-1} were taken at a resolution of 4 cm^{-1}, and the spectra were corrected for background absorbance.

Multiple Angle Light Scattering. Light scattering data was collected over the whole angular range, $15 < \vartheta < 150^{\circ}$ with the sample maintained at 25°C. Autocorrelation functions calculated by the ALV LSE-5004 correlator unit were recorded at each (ϑ, c) and the REPES algorithm was used to determine relaxation times, $\tau(\vartheta, c)$. The data set $\tau(\vartheta, c)$ was then analysed to estimate the mean translational diffusion coefficient with the Stokes-Einstein equation. An empirical measurement was made of the refractive index increment for the polymer with a differential refractometer, model DnDc1260 supplied by PSS GmbH.

NMR Spectroscopy. ^{1}H NMR,^{13}C NMR, ^{19}F NMR and ^{31}P NMR spectra were recorded at 300 MHz or 400 MHz on a Bruker DPX-300 or a Bruker DPX-400 spectrometer, with deuterated chloroform ($CDCl_3$), dimethyl sulfoxide ($(CD_3)_2SO$) or methanol (CD_3OD) as the solvent. Chemical shifts of protons are reported as δ in parts per million (ppm) and are relative to $CHCl_3$ at δ =

7.26 ppm, $(CH_3)_2SO$ at δ = 2.50 ppm or CH_3OH at δ = 3.31 ppm. The multiplicity is specified as singlet (s), doublet (d), triplet (t), quartet (q) and quintet (p).

Size Exclusion Chromatography. Size exclusion chromatography (SEC) analysis was performed on a system composed of an Agilent 1260 Infinity II LC system equipped with an Agilent guard column (PLGel 5 μM, 50 × 7.5 mm) and two Agilent Mixed-C columns (PLGel 5 μM, 300 × 7.5 mm). The mobile phase used was THF (HPLC grade) that contained 2% v/v NEt_3 at 40 ºC at flow rate of 1.0 $mL{\cdot}min^{-1}$ (polystyrene (PS) standards were used for calibration). Number average molecular weights (M_n), weight average molecular weights (M_w) and dispersities ($Đ_M = M_w/M_n$) were determined with the Agilent GPC/SEC software. The calibration range was comprised between 200 and 1,069,000 $g{\cdot}mol^{-1}$.

Spectrophotometry. FL spectra were recorded on an Edinburgh Instruments FS5 spectrofluorometer equipped with Xenon lamp with 10 mm path length quartz cuvettes with four transparent polished faces (Starna Cells, type: 3-Q-10).

Transmission Electron Microscopy. Dry-state stained transmission electron microscopy (TEM) imaging was performed on a JEOL JEM-1400 microscope which operated at an acceleration voltage of 80 kV. All dry-state samples were diluted with deionised water or DMSO to appropriate analysis concentration and then deposited onto formvar-coated or GO-coated copper grids. After roughly 1 min, excess sample was blotted from the grid and the grid was stained with an aqueous 1 wt% uranyl acetate (UA) solution for 1 min. The excess stain solution was blotted and the sample was dried prior to microscopic

analysis. The size statistical data for the histograms were collected from 3-5 images and 300-500 particles.

UV/Vis Spectroscopy. UV/Vis spectroscopy was performed on Evolution 350 UV-Vis spectrophotometer equipped with Xenon Flash Lamp light source and Dual Matched Silicon Photodiodes detector. Quartz cells (path length 1 cm, 170 - 2000 nm) from Hellma with two polished sides were used and the absorption spectral data were analysed with the Thermo INSIGHT-2 v.10.0.30319.1 software.

7.3. Experimental protocols for Chapter 2

7.3.1. Menthyl 4-isocyanobenzoate (MAIC) synthesis

Compound MAIC was prepared in accordance with previously reported synthetic methods.[1]

7.3.1.1. Menthyl 4-nitrobenzoate synthesis

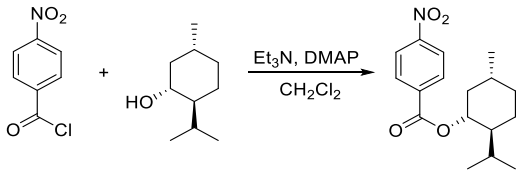

Scheme 7.1. Menthyl 4-nitrobenzoate synthesis.

A 500 mL round-bottom flask was charged with *L*-menthol (12 g, 77 mmol, 1.0 equiv.), DMAP (0.70 g, 5.7 mmol, 0.10 equiv.), NEt_3 (35 mL, 250 mmol, 3.3 equiv.) and CH_2Cl_2 (100 mL). The solution was cooled down to 0 °C in an ice bath before slow addition *via* syringe of a solution of 4-nitrobenzoyl chloride (15 g, 82 mmol, 1.1 equiv.) in CH_2Cl_2 (100 mL). The reaction mixture was stirred for 1 h while it warmed up to room temperature. The solution was concentrated *in vacuo*, and the resulting residue was re-dissolved in Et_2O (200 mL). The solution was filtered over celite and the filtrate was concentrated *in vacuo*, which yielded the crude product as a yellow solid which was used without further purification. ^{1}H NMR (400 MHz, $CDCl_3$): δ (ppm) 8.28 (d, $^3J_{H\text{-}H}$ = 9.1 Hz, 2H), 8.20 (d, $^3J_{H\text{-}H}$ = 9.1 Hz, 2H), 4.97 (td, 1H), 2.16-2.10 (m, 1H), 1.92 (pd, $^3J_{H\text{-}H}$ = 7.0, 2.7 Hz, 1H), 1.78-1.73 (m, 2H), 1.61-1.54 (m, 2H), 1.20-1.09 (m, 2H), 0.93 (dd, $^3J_{H\text{-}H}$ = 6.7, 6.0 Hz, 7H), 0.80 (d, $^3J_{H\text{-}H}$ = 7.0 Hz , 3H). ^{13}C NMR (100 MHz, $CDCl_3$): δ (ppm) 164.2 (*C*=O), 136.2 (*C*NO_2), 130.7 (O_2NC*C*H, aromatic), 123.5 (O_2NCCH*C*H, aromatic), 76.2 (O*C*H), 47.2 (*C*$CH(CH_3)_2$), 40.9 (OCH*C*H_2), 34.2 (H_3CC*C*H_2), 31.5 (H_3C*C*HCH_2), 26.6 (*C*$H(CH_3)_2$), 23.6 (HCC*C*H_2), 22.0 (C*C*H_3), 20.7 (CH*C*H_3), 16.5 (CH*C*H_3). Characterisation was consistent with that reported previously.[1]

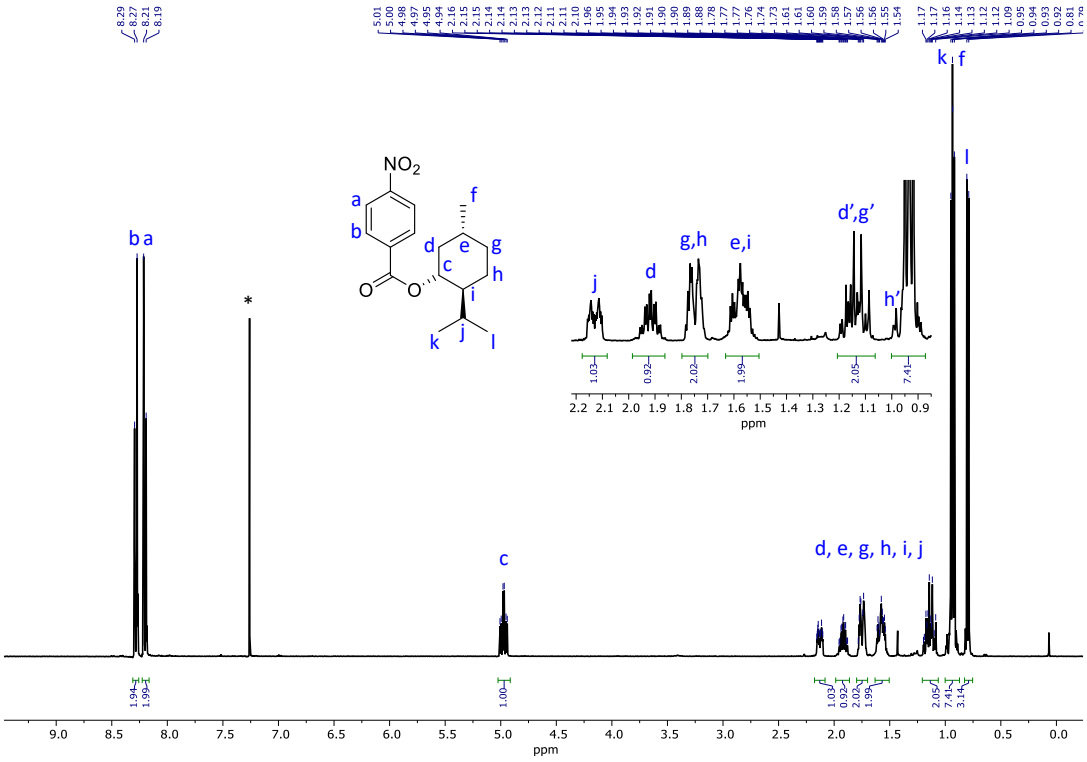

Figure 7.1 ^{1}H NMR spectrum of menthyl 4-nitrobenzoate in $CDCl_3$ (400 MHz, 298 K).

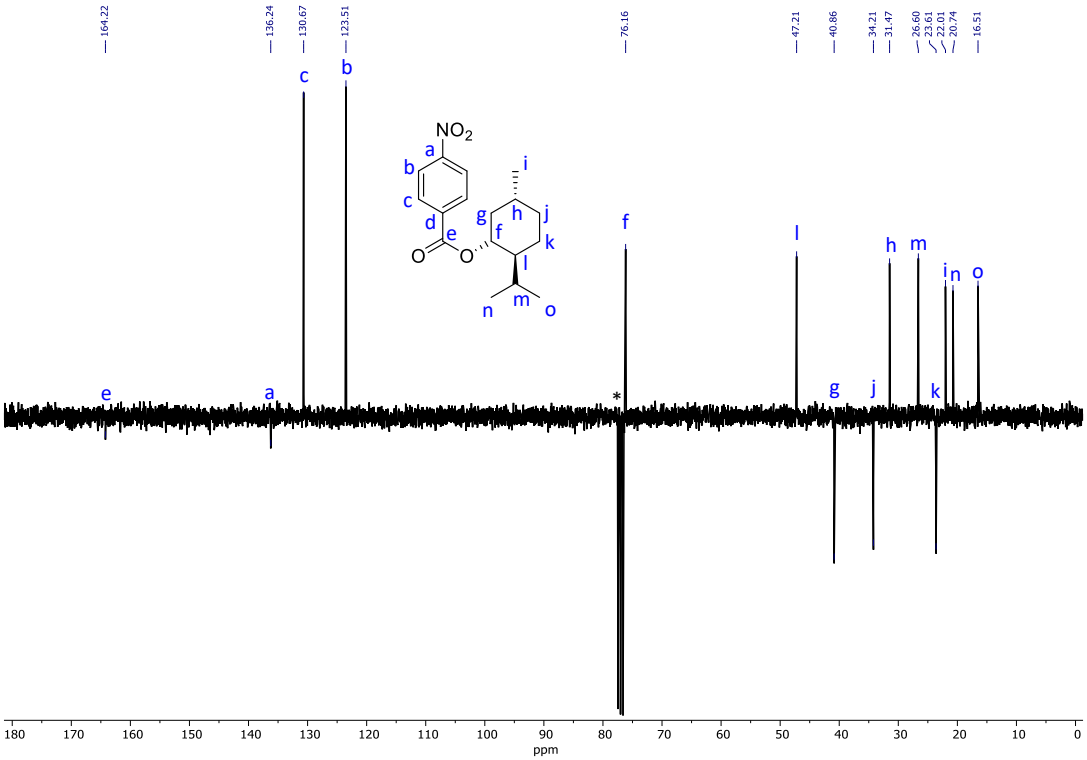

Figure 7.2 ^{13}C NMR spectrum of menthyl 4-nitrobenzoate in $CDCl_3$ (100 MHz, 298 K).

7.3.1.2. Menthyl 4-aminobenzoate synthesis

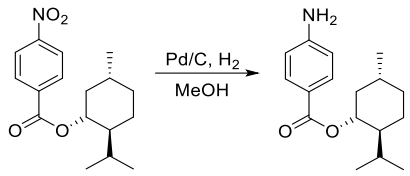

Scheme 7.2. Menthyl 4-aminobenzoate synthesis.

A 2-necked 500 mL round-bottom flask was charged with menthyl 4-nitrobenzoate (23 g, 75 mmol, 1.0 equiv.), Pd/C (10 wt%, 0.5 g, 0.75 mmol, 0.010 equiv.) and MeOH (250 mL). The flask was sealed with septa. H_2 was bubbled from a balloon for 1 h under vigorous stirring, then stirring was continued under a static hydrogen atmosphere overnight. The reaction mixture was filtered over celite and the filtrate was concentrated *in vacuo* which yielded the product as a white solid (15 g, 72% over two steps). ^{1}H NMR (400 MHz, $CDCl_3$): δ (ppm) 7.85 (d, $^3J_{H\text{-}H}$ = 8.8 Hz, 2H), 6.64 (d, $^3J_{H\text{-}H}$ = 8.8 , 2H), 4.87 (td, $^3J_{H\text{-}H}$ = 10.9, 4.4 Hz, 2H), 4.05 (bs, 1H), 2.11 (dtd, $^3J_{H\text{-}H}$ = 12.0, 4.3, 1.9 Hz, 1H), 1.96 (pd, $^3J_{H\text{-}H}$ = 7.0, 2.8 Hz, 1H), 1.73-1.68 (m, 2H), 1.58-1.48 (m, 2H), 1.16-1.02 (m, 2H), 0.94-0.89 (m, 7H), 0.78 (d, $^3J_{H\text{-}H}$ = 7.0 Hz, 3H). ^{13}C NMR (100 MHz, $CDCl_3$): δ (ppm) 166.0 (*C*(O)O), 148.9 (*C*NH_2, aromatic), 131.6 (O=CC*C*H, aromatic), 114.8 (H_2NC*C*H, aromatic), 74.2 (O*C*H), 47.4 (*C*CH$(CH_3)_2$), 41.1 (OCH*C*H_2), 34.4 (H_3CC*C*H_2), 31.5 (H_3C*C*HCH_2), 26.5 (*C*H$(CH_3)_2$), 23.7 (HCC*C*H_2), 22.1 (CH*C*H_3), 20.8 (CH*C*H_3), 16.6 (CH*C*H_3). Characterisation was consistent with that reported previously.[1]

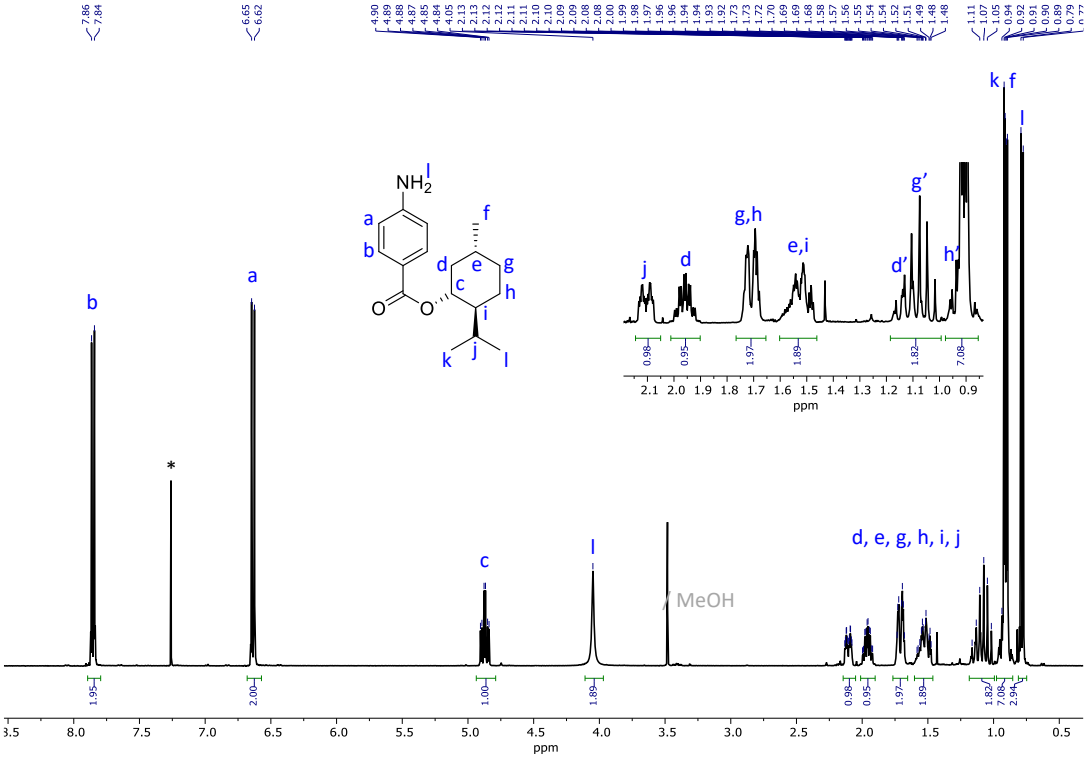

Figure 7.3. ^{1}H NMR spectrum of menthyl 4-aminobenzoate in $CDCl_3$ (400 MHz, 298 K).

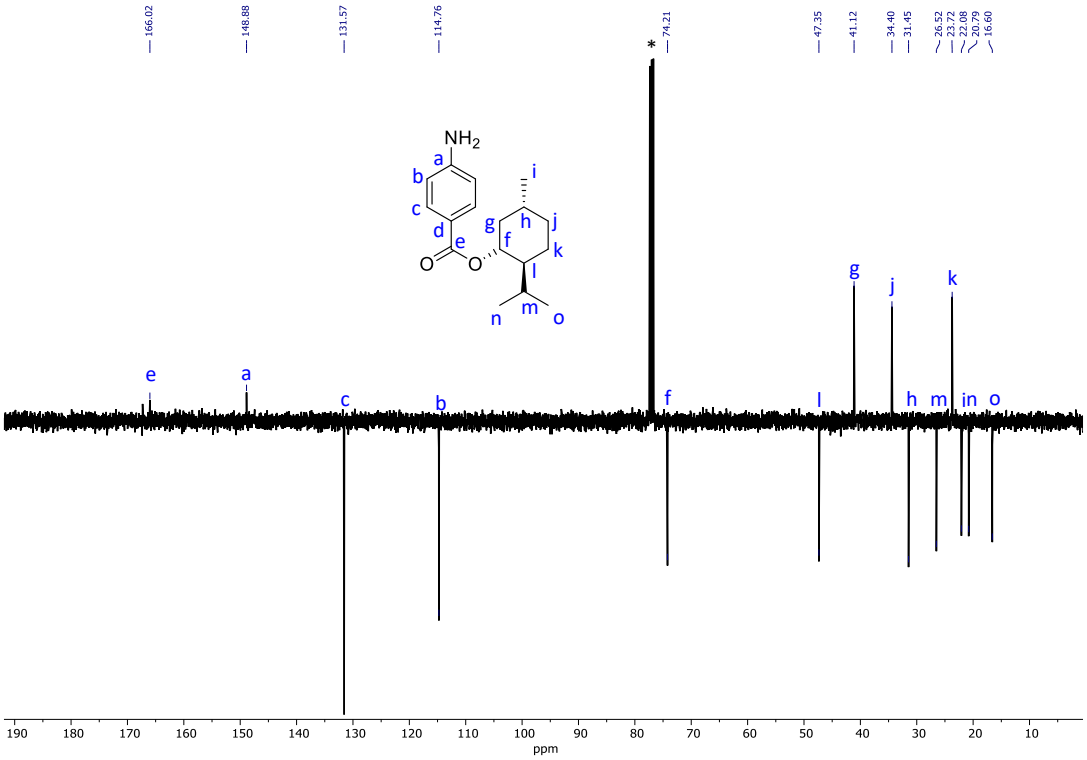

Figure 7.4. ^{13}C NMR spectrum of menthyl 4-aminobenzoate in $CDCl_3$ (100 MHz, 298 K).

7.3.1.3. Menthyl 4-formamidobenzoate synthesis

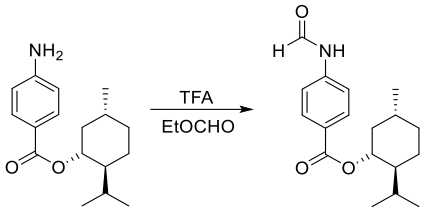

Scheme 7.3. Menthyl 4-formamidobenzoate synthesis.

In a 500 mL round-bottom flask, menthyl 4-aminobenzoate (15 g, 54 mmol, 1.0 equiv.) was suspended in ethyl formate (250 mL) with TFA (0.50 mL, 6.5 mmol, 0.10 equiv.). The reaction mixture was heated at reflux (70 °C) overnight. The reaction mixture was concentrated *in vacuo* and the resulting orange foam was purified by flash chromatography (5:1 v/v CH_2Cl_2/ethyl acetate) which gave the product as a white solid (14 g, 84%). ^{1}H NMR (400 MHz, $CDCl_3$): δ (ppm) 8.83 (bs, 1H), 8.43 (s, 0.55H), 8.07-8.00 (m, 2H), 7.93 (s, 0.45H), 7.64 (d, $^3J_{H\text{-}H}$ = 8.1 Hz, , 1.1H), 7.15 (d, $^3J_{H\text{-}H}$ = 8.0 Hz, 0.9H), 4.91 (t, $^3J_{H\text{-}H}$ = 10.8 Hz, 1H), 2.10 (d, $^3J_{H\text{-}H}$ = 11.9 Hz, 1H), 1.97-1.85 (m, 1H), 1.72 (d, $^3J_{H\text{-}H}$ = 11.6 Hz, 2H), 1.54 (t, $^3J_{H\text{-}H}$ = 10.9 Hz, 2H), 1.11 (p, $^3J_{H\text{-}H}$ = 11.8 Hz, 2H), 0.96-0.91 (m, 7H), 0.78 (d, $^3J_{H\text{-}H}$ = 6.8 Hz, 3H). ^{13}C NMR (100 MHz, $CDCl_3$): δ (ppm) 162.5 (*C*(O)O), 159.0 (H*C*=O), 131.7 (*C*NH, aromatic), 131.0 (O=CC*C*H, aromatic), 119.2 (HNC*C*H, aromatic), 117.4 (*C*C(O)O), 75.0 (O*C*H), 47.4 (*C*CH$(CH_3)_2$), 41.1 (OCH*C*H_2), 34.4 (H_3CC*C*H_2), 31.6 (H_3C*C*HCH_2), 26.7 (*C*H$(CH_3)_2$), 23.8 (HCC*C*H_2), 22.2 (CH*C*H_3), 20.9 (CH*C*H_3), 16.7 (CH*C*H_3). Characterisation was consistent with that reported previously.[1]

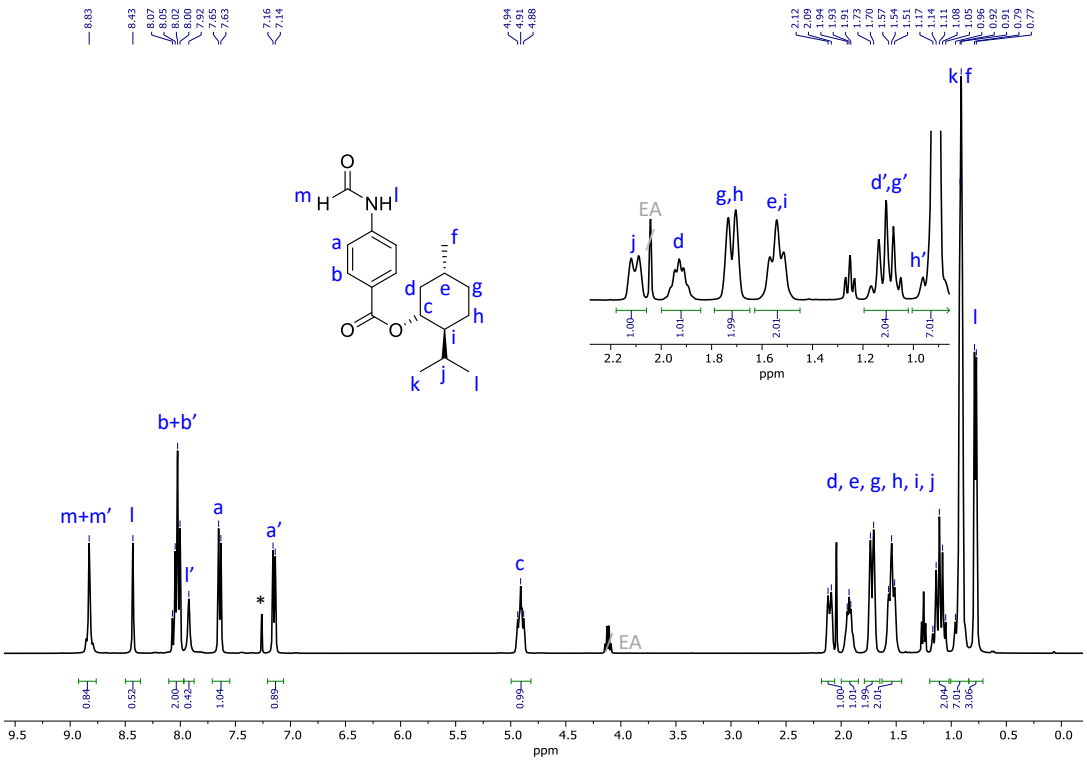

Figure 7.5. ^{1}H NMR spectrum of menthyl 4-formamidobenzoate in $CDCl_3$ (300 MHz, 298 K).

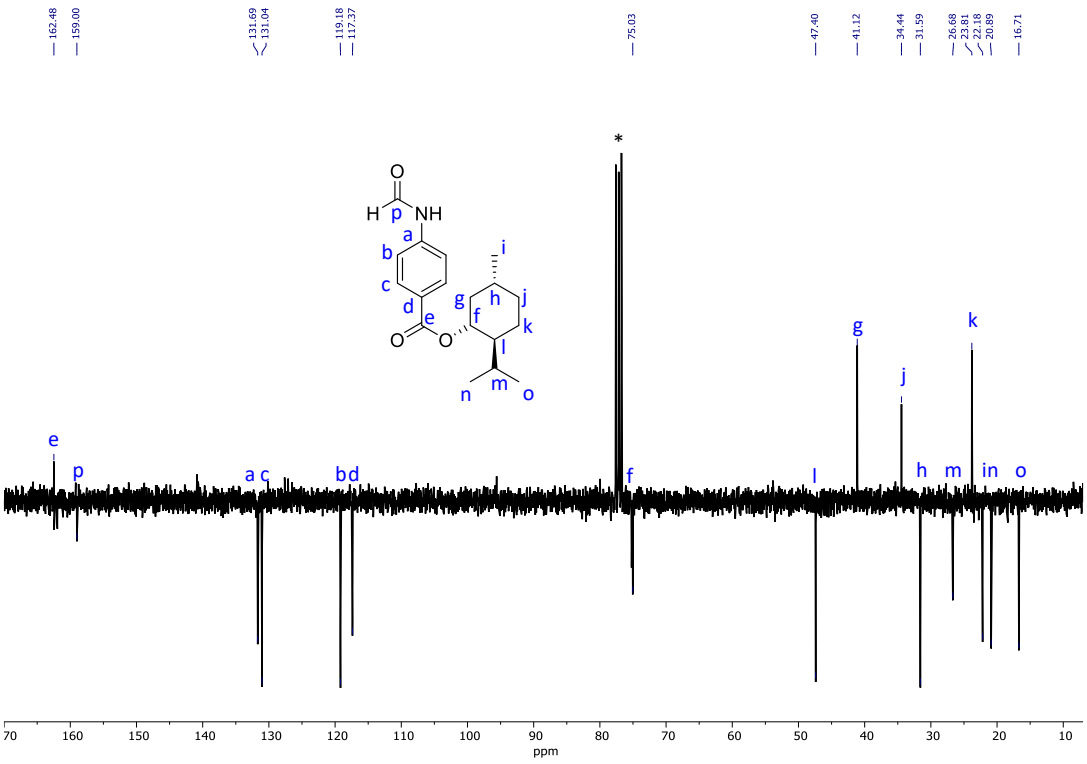

Figure 7.6. ^{13}C NMR spectrum of menthyl 4-formamidobenzoate in $CDCl_3$ (100 MHz, 298 K).

7.3.1.4. Menthyl 4-isocyanobenzoate (MAIC) synthesis

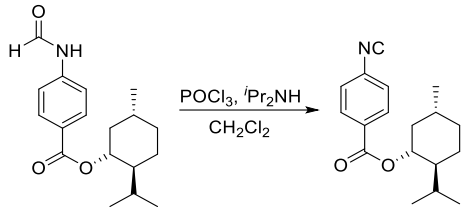

Scheme 7.4. Menthyl 4-isocyanobenzoate synthesis.

A 100 mL Schlenk flask (dried in the oven and under N_2) was charged with menthyl 4-formamidobenzoate (6.0 g, 20 mmol, 1.0 equiv.), diisopropylamine (11 mL, 78 mmol, 4.0 equiv.) and THF (dry, 30 mL). The solution was cooled down to 0 °C in an ice bath, then $POCl_3$ (2.0 mL, 22 mmol, 1.1 equiv.) was added dropwise with a syringe over 15 min. The reaction was stirred at 0 °C for 1 h before cold Na_2CO_3 (sat. 50 mL) was added to the solution. The reaction mixture was stirred for 10 min before the two phases were separated and the aqueous phase was extracted with Et_2O (3 × 50 mL). The combined Et_2O extracts were dried over $MgSO_4$ and filtered. The filtrate was concentrated *in vacuo* and purified by flash chromatography (4:1 v/v Hexane/CH_2Cl_2). The resulting fractions were dried *in vacuo* while the solution between was kept -78°C and -10 °C which yielded a white solid (4.3 g, 76%). ^{1}H NMR (400 MHz, $CDCl_3$): δ (ppm) 8.06 (d, $^3J_{H\text{-}H}$ = 8.8 Hz, 2H), 7.42 (d, $^3J_{H\text{-}H}$ = 8.6 Hz, 2H), 4.92 (td, $^3J_{H\text{-}H}$ = 10.9, 4.4 Hz, 2H), 2.09 (d, $^3J_{H\text{-}H}$ = 12.0 Hz, 1H), 1.89 (pd, $^3J_{H\text{-}H}$ = 7.0, 2.8 Hz, 1H), 1.75-1.67 (m, 2H), 1.60-1.47 (m, 2H), 1.18-1.02 (m, 2H), 0.90 (dd, $^3J_{H\text{-}H}$ = 6.9, 5.1 Hz, 7H), 0.77 (d, $^3J_{H\text{-}H}$ = 7.0 Hz, 3H). ^{13}C NMR (100 MHz, $CDCl_3$): δ (ppm) 166.0 (*C*(O)O), 163.4 (N≡*C*), 130.6 (*C*N≡C), 129.8 (O=CC*C*H, aromatic), 128.7 (*C*C(O)O), 125.4 (C≡NC*C*H, aromatic), 74.6 (O*C*H), 46.2 (*C*CH$(CH_3)_2$), 39.9 (OCH*C*H_2), 33.2 (H_3CC*C*H_2), 30.4 (H_3C*C*HCH_2), 25.5 (*C*H$(CH_3)_2$), 22.6 (HCC*C*H_2), 21.0 (CH*C*H_3), 19.7 (CH*C*H_3), 15.5 (CH*C*H_3). FT-IR (neat): 2943, 2116, 1710, 1602, 1270, 1099 cm^{-1}. Characterisation was consistent with that reported previously.[1]

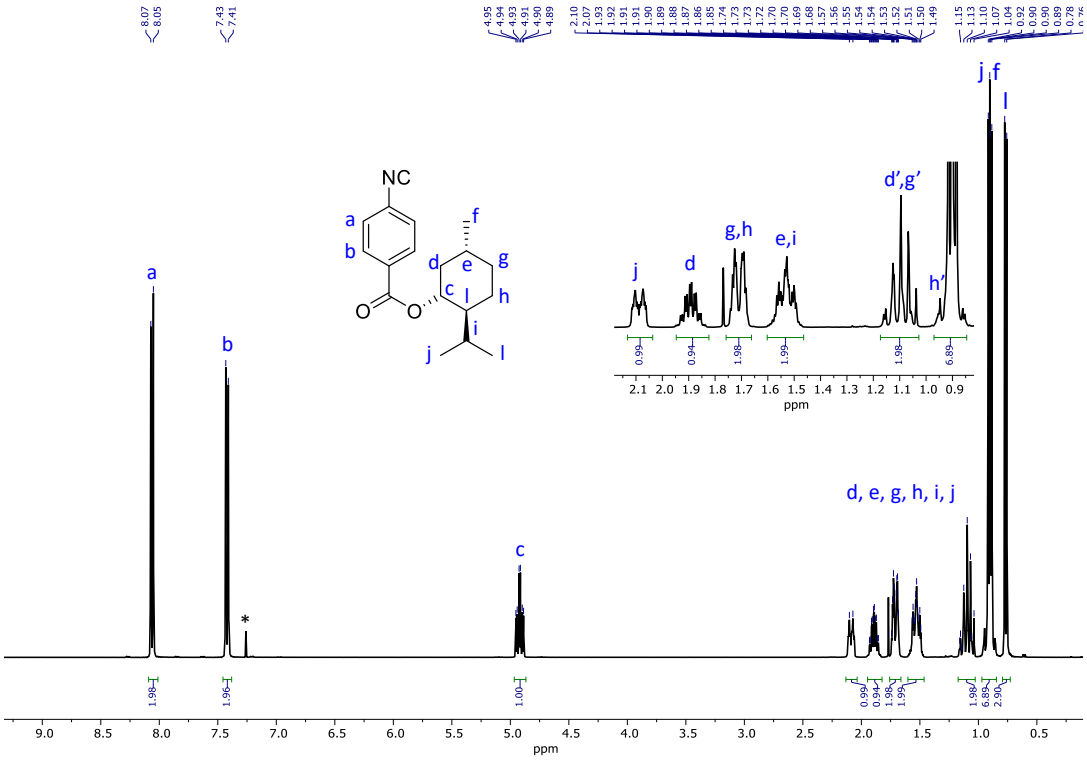

Figure 7.7. ^{1}H NMR spectrum of MAIC in $CDCl_3$ (400 MHz, 298 K).

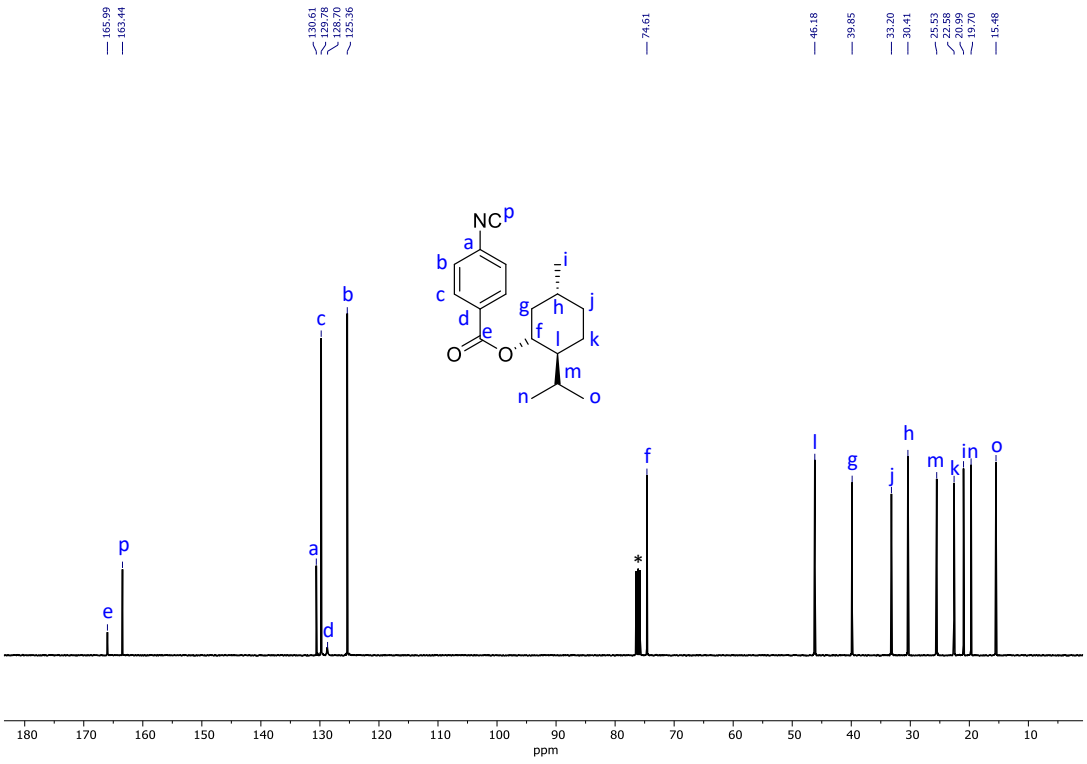

Figure 7.8. ^{13}C NMR spectrum of MAIC in $CDCl_3$ (100 MHz, 298 K).

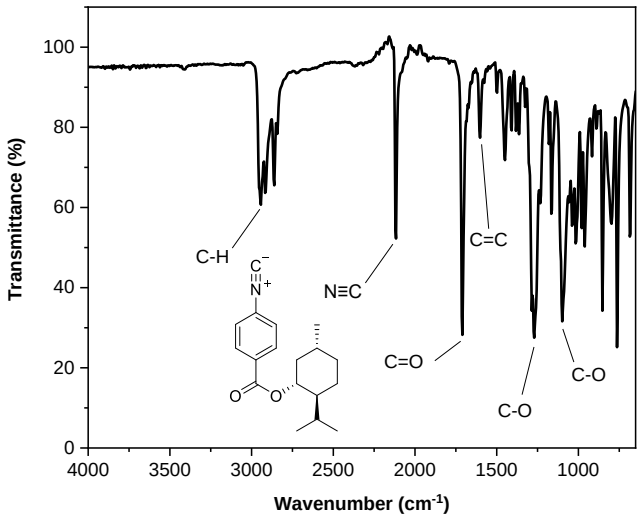

Figure 7.9. FT-IR spectrum of MAIC.

7.3.2. mPEGyl 4-isocyanobenzoate (PAIC) synthesis

7.3.2.1. mPEGyl 4-nitrobenzoate ($mPEG_{12}$-Ar-NO_2) synthesis

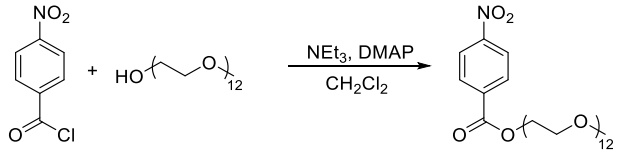

Scheme 7.5. mPEGyl 4-nitrobenzoate synthesis.

A 500 mL round-bottom flask was charged with $mPEG_{12}$-OH (25 g, 45 mmol, 1.0 equiv.), DMAP (0.55 g, 4.5 mmol, 0.10 equiv.), NEt_3 (25 mL, 180 mmol, 4.0 equiv.) and CH_2Cl_2 (150 mL). The solution was cooled down to 0 °C in an ice bath before slow addition *via* syringe of a solution of 4-nitrobenzoyl chloride (9.3 g, 49 mmol, 1.1 equiv.) in CH_2Cl_2 (15 mL). The reaction mixture was stirred for 3 h at to room temperature. The solution was concentrated *in vacuo*, and the resulting residue was re-dissolved in Et_2O and filtered over celite. The filtrate was purified by flash chromatography (gradient from 0 → 3% MeOH in CH_2Cl_2), which yielded a yellow oil as the product (28 g, 88%). ^{1}H NMR (400 MHz, $CDCl_3$): δ (ppm) 8.24 (d, $^3J_{H\text{-}H}$ = 9.0 Hz, 2H, O_2NCCH, aromatic), 8.18 (d, $^3J_{H\text{-}H}$ = 9.0 Hz, 2H, O=CCC*H*, aromatic), 4.48 (t, $^3J_{H\text{-}H}$ = 4.7 Hz, 2H,

C(O)OCH$_2$CH_2), 3.81 (t, $^3J_{H\text{-}H}$ = 4.8 Hz, 2H, C(O)OCH_2), 3.82-3.33 (m, 42H, OCH_2, PEG), 3.50 (dd, $^3J_{H\text{-}H}$ = 5.9, 3.3 Hz, 2H, OCH_2, PEG), 3.31 (s, 3H, CH_3). ^{13}C NMR (100 MHz, $CDCl_3$): δ (ppm) 164.7 (*C*(O)O), 150.6 (O_2NC, aromatic), 135.5 (O=C*C*, aromatic), 130.9 (O=CC*C*H, aromatic), 123.5 (O_2NCCH, aromatic), 72.5 (O*C*H$_2$, PEG), 71.7 (O*C*H$_2$, PEG), 70.6 (O*C*H$_2$, PEG), 68.7 (OCH$_2$, PEG), 64.8 (C(O)OCH$_2$*C*H$_2$), 61.7 (C(O)O*C*H$_2$CH$_2$), 59.1 (CH_3). SEC (THF + 2% v/v NEt_3, 40 °C): $M_{n,\,SEC}$ = 0.80 kDa ($Đ_{M,\,SEC}$ = 1.22). HRMS: *m/z* [$C_{32}H_{55}NO_{16}$+NH_4] $^+$ calc. 727.3865 g·mol^{-1}, exp. 727.3865 g·mol^{-1}. FT-IR (neat): 2862 (C-H stretch), 1723 (C=O stretch), 1526 (N-O stretch), 1455 (C-H bend), 1347 (C-N stretch), 1273 (C-O stretch, ester), 1094 (C-O stretch, ether), 945 (C=C bend) cm^{-1}.

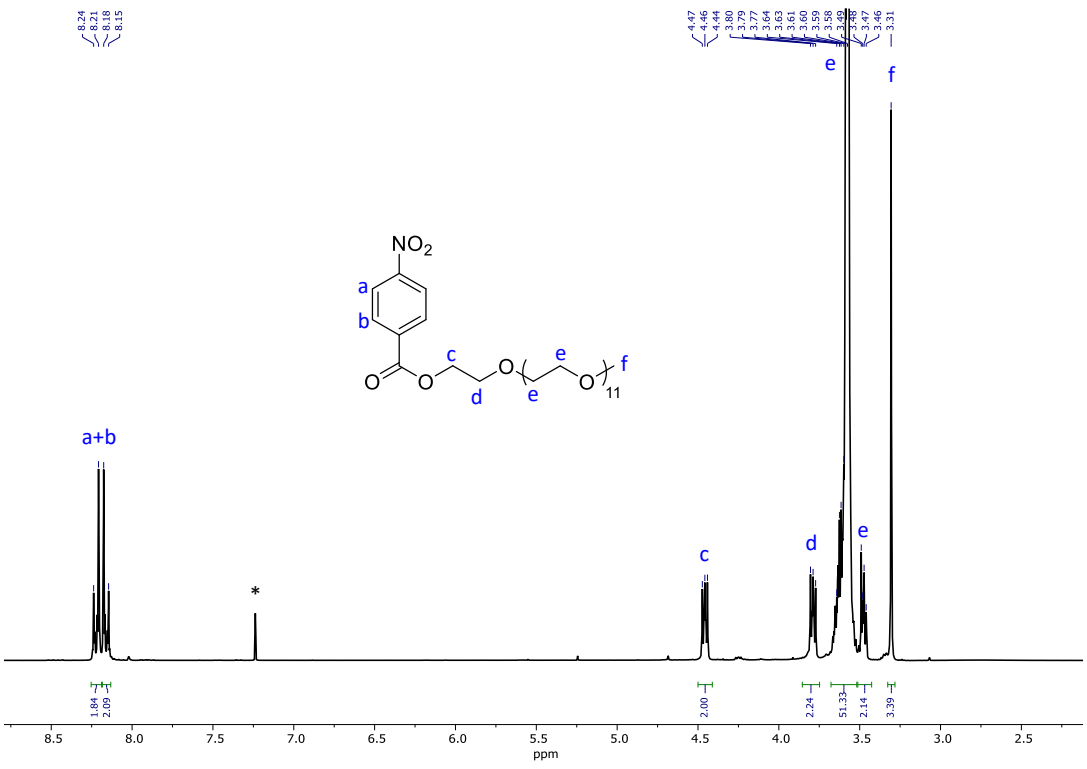

Figure 7.10. ^{1}H NMR spectrum of mPEG-Ar-NO_2 in $CDCl_3$ (400 MHz, 298 K).

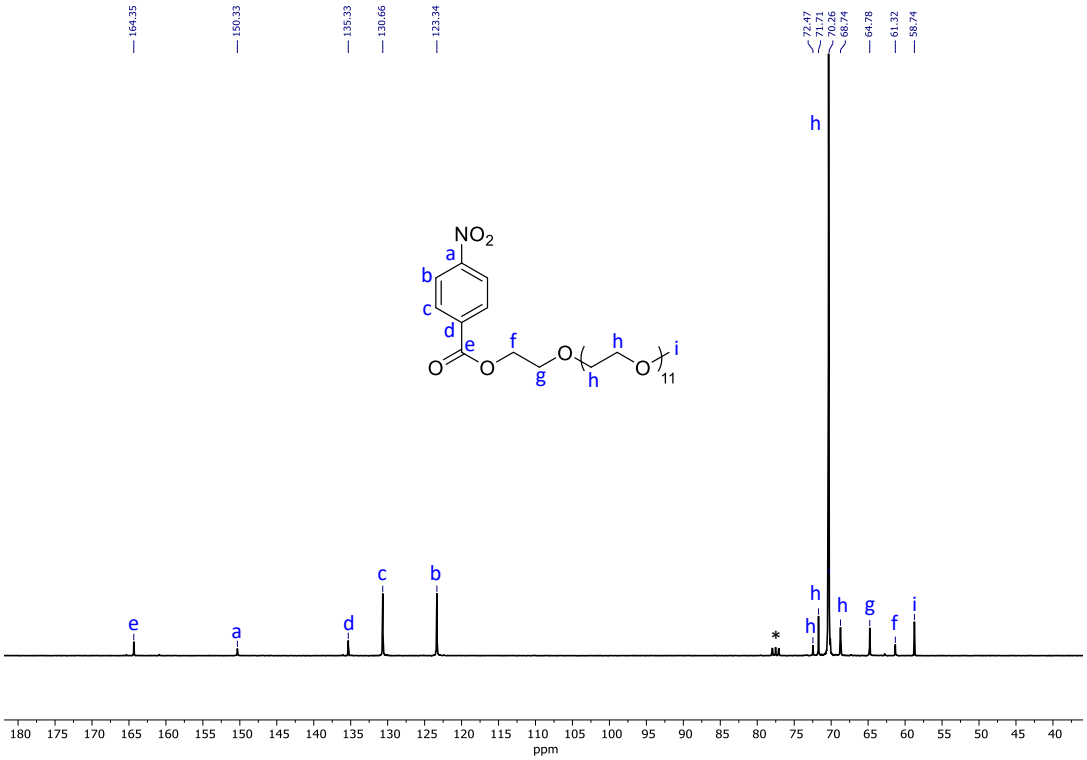

Figure 7.11. ^{13}C NMR spectrum of mPEG-Ar-NO_2 in $CDCl_3$ (100 MHz, 298 K)

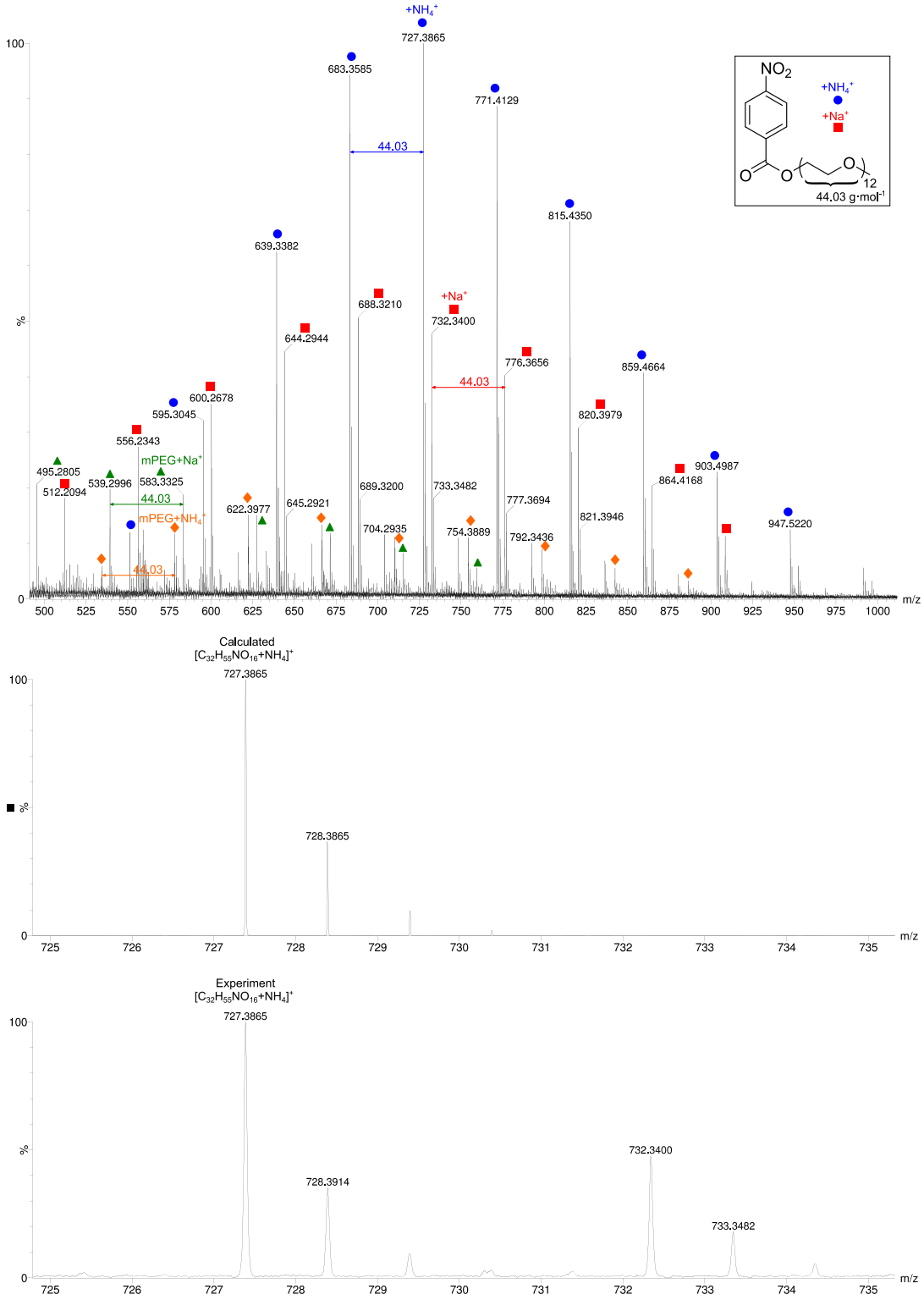

Figure 7.12. *Top:* Mass spectra of the mPEG-Ar-NO_2 collected by ESI-MS. *Top*: Expanded spectrum (500-1000 *m/z*) with NH_4^+ (blue circles), Na^+ (red squares) adduct of the product $mPEG_{12}$-Ar-NO_2 and NH_4^+ (orange diamonds), Na^+ (green triangles) adduct of the mPEG-OH starting material. *Bottom*: Calculated *vs* experimental *m/z* value for $mPEG_{12}$-Ar-NO_2+NH_4^+ adduct.

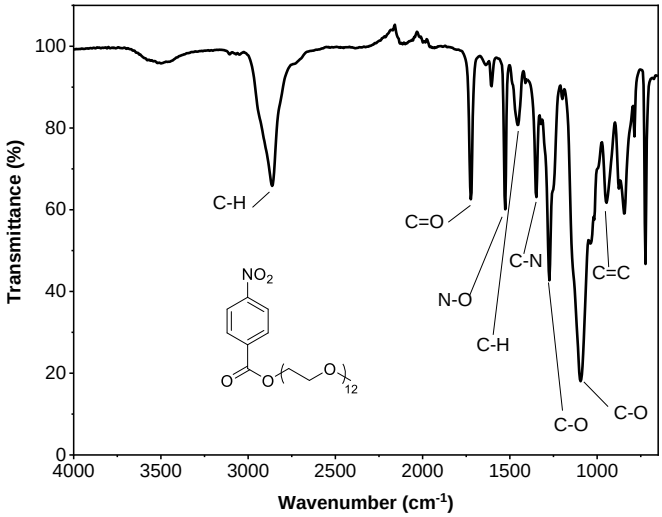

Figure 7.13. FT-IR spectrum of mPEG-Ar-NO_2.

7.3.2.2. mPEGyl 4-aminobenzoate ($mPEG_{12}$-Ar-NH_2) synthesis

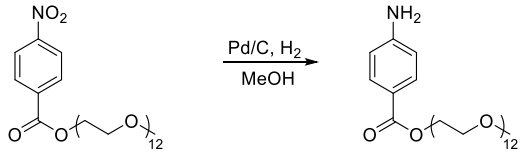

Scheme 7.6. mPEGyl 4-aminobenzoate synthesis.

A 2-necked 500 mL round-bottom flask was charged with nitro-PEG (30 g, 42 mmol, 1.0 equiv.), Pd/C (10 wt%, 0.45g, 0.40 mmol, 0.010 equiv.) and MeOH (250 mL). The flask was sealed with rubber septa. H_2 was bubbled from a balloon for 1 h under vigorous stirring, then stirring was continued under a static hydrogen atmosphere overnight. The reaction mixture was filtered over celite and the filtrate was concentrated *in vacuo* to give the product as a yellow oil (29 g, >99%) which was employed as obtained, without further purification, in the next step. ^{1}H NMR (400 MHz, $CDCl_3$): δ (ppm) 7.78 (d, $^3J_{H\text{-}H}$ = 8.6 Hz, 2H, O=CCC*H*, aromatic), 6.56 (d, $^3J_{H\text{-}H}$ = 8.7 Hz, 2H, H_2NCC*H*, aromatic), 4.34 (t, $^3J_{H\text{-}H}$ = 4.8 Hz, 2H, C(O)OCH_2), 4.23 (bs, 1H, NH_2), 3.73 (t, $^3J_{H\text{-}H}$ = 4.9 Hz, 2H, C(O)OCH_2CH_2), 3.61-3.46 (m, 42H, OCH_2, PEG), 3.47 (dd, $^3J_{H\text{-}H}$ = 5.6, 3.2 Hz, 2H, OCH_2, PEG), 3.30 (s, 1H, CH_3). ^{13}C NMR (100 MHz, $CDCl_3$): δ (ppm) 166.4 (*C*(O)O), 152.5 (H_2N*C*, aromatic), 131.1

(O=CC*C*H, aromatic), 117.4 (O=C*C*, aromatic), 113.1 (H_2NC*C*H, aromatic), 72.5 (O*C*H_2, PEG), 71.2 (O*C*H_2, PEG), 70.2 (O*C*H_2, PEG), 69.1 (O*C*H_2, PEG), 63.1 (C(O)OCH$_2$*C*H_2), 61.1 (C(O)O*C*H_2), 58.6 (*C*H_3). SEC (THF + 2% v/v NEt_3, 40 °C): $M_{n,\ SEC}$ = 0.85 kDa ($Đ_{M,\ SEC}$ = 1.18). HRMS: *m/z* $[C_{32}H_{55}NO_{16}+H]^+$ calc. 680.3857 g·mol^{-1}, exp. 680.3875 g·mol^{-1}. FT-IR (neat): 3439 (N-H stretch), 2866, (C-H stretch) 1697 (C=O stretch), 1604 (C=C stretch), 1452 (C-H bend), 1347 (C-N stretch), 1273 (C-O stretch, ester), 1091 (C-O stretch, ether), 945 (C=C bend) cm^{-1}.

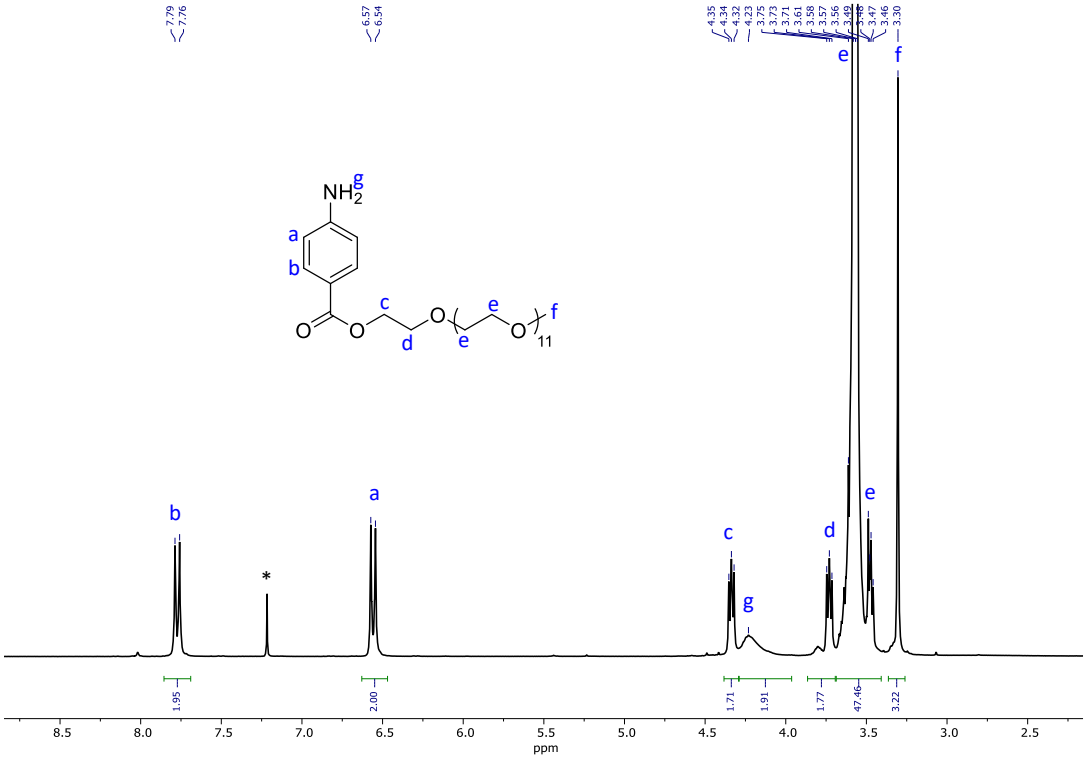

Figure 7.14. ^{1}H NMR spectrum of mPEG-Ar-NH_2 in $CDCl_3$ (400 MHz, 298 K).

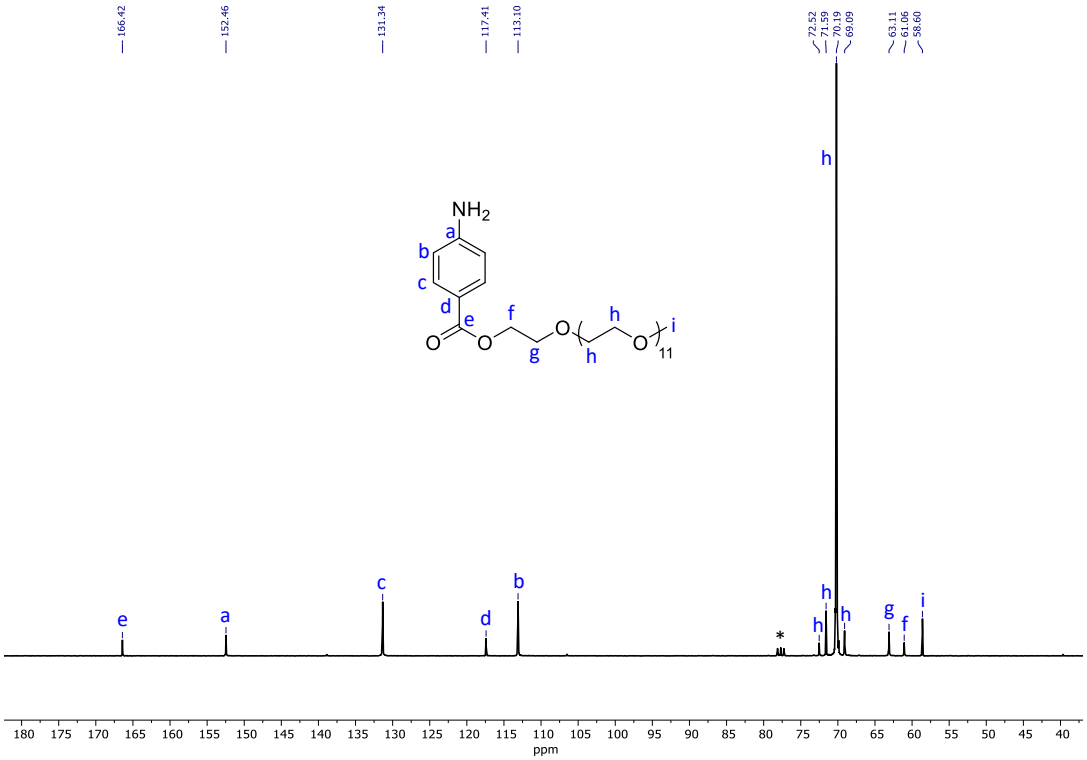

Figure 7.15. ^{13}C NMR spectrum of mPEG-Ar-NH_2 in $CDCl_3$ (100 MHz, 298 K).

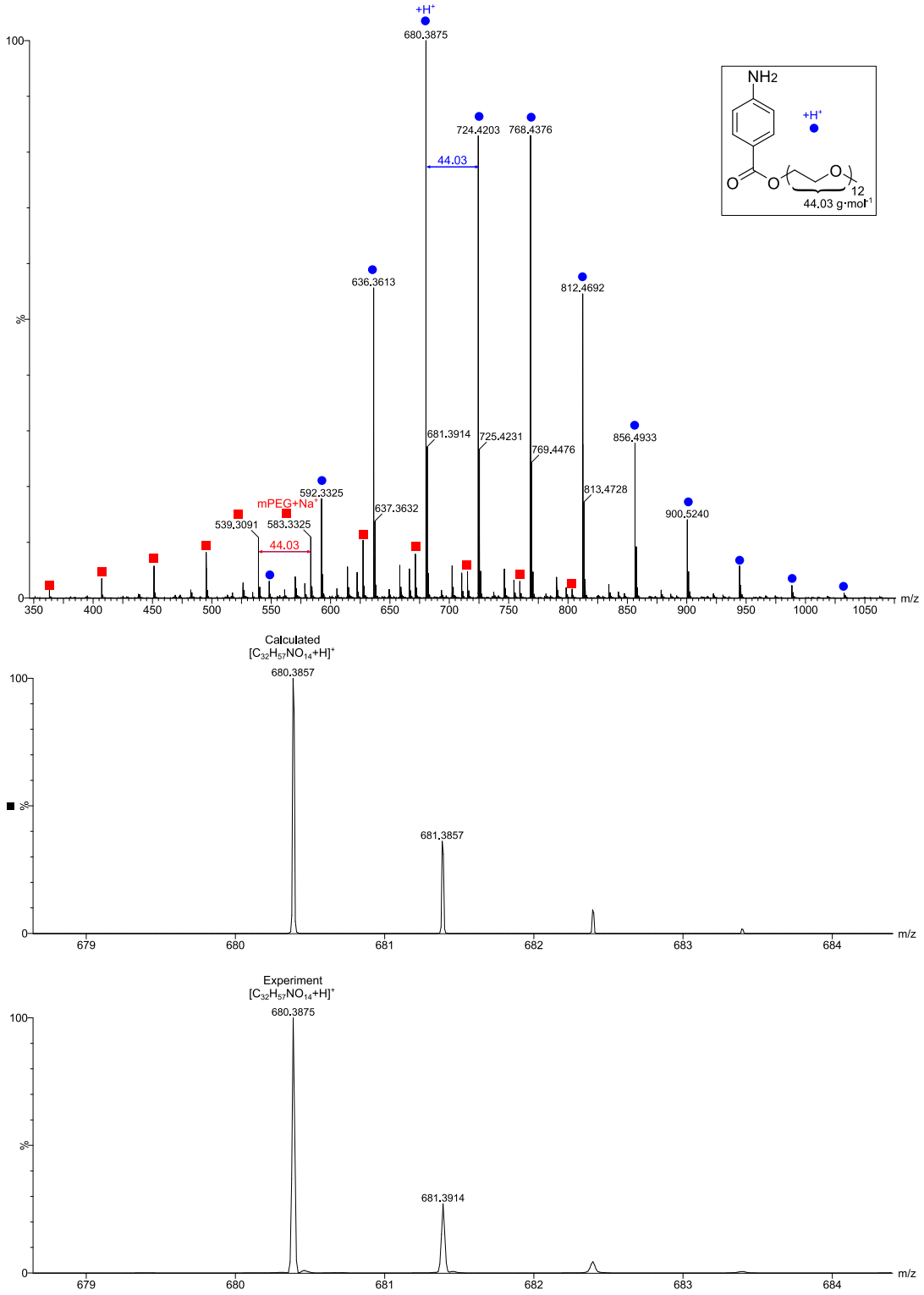

Figure 7.16. *Top:* Mass spectra of mPEG-Ar-NH_2 collected by ESI-MS. *Top*: Expanded spectrum (350-1000 *m/z*) with H^+ (blue circles) adduct of the product $mPEG_{12}$-Ar-NO_2 and Na^+ (red squares) adduct of the mPEG-OH starting material. *Bottom*: Calculated *vs* experimental *m/z* value for $mPEG_{12}$-Ar-NH_2+H^+ adduct.

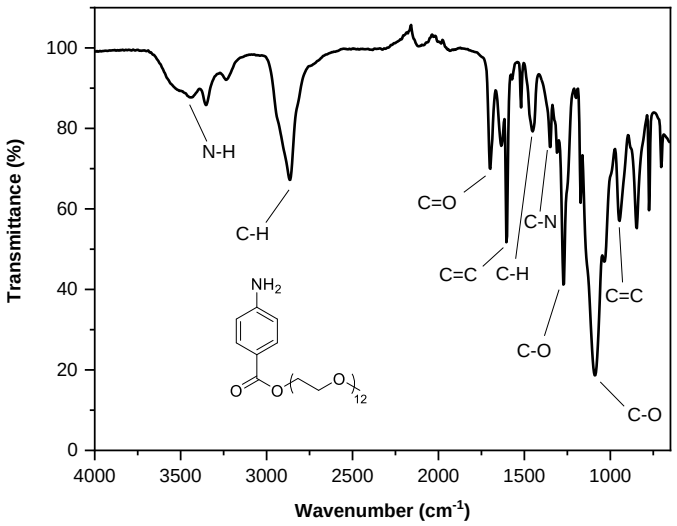

Figure 7.17. FT-IR spectrum of mPEG-Ar-NH_2.

7.3.2.3. mPEGyl 4-formamidobenzoate ($mPEG_{12}$-Ar-NHCHO) synthesis

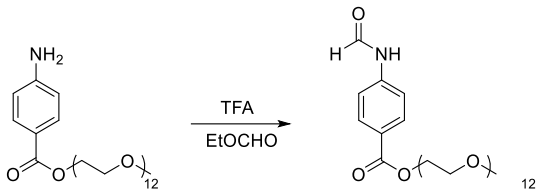

Scheme 7.7. mPEGyl 4-formamidobenzoate.

A 500 mL round-bottom flask was charged with amino-PEG (20 g, 29 mmol, 1.0 equiv.), TFA (0.23 mL, 2.9 mmol, 0.10 equiv.) and ethyl formate (200 mL). The reaction mixture was heated at reflux (65 °C) overnight. The solution was concentrated *in vacuo* and purified by flash chromatography (gradient from 0 → 3% MeOH in CH_2Cl_2), which yielded the product as an orange oil (24 g, 85%). ^{1}H NMR (400 MHz, $CDCl_3$): δ (ppm) 9.15-9.06 (m, 1H, *H*C=O, cis, and N*H*, trans), 8.61 (d, $^3J_{H\text{-}H}$ = 11.0 Hz, 0.15H, *H*C=O, trans), 8.12 (s, 0.85H, N*H*, cis), 7.69 (d, $^3J_{H\text{-}H}$ = 7.9 Hz, 2H, O=CCC*H*, cis and trans, aromatic), 7.45 (d, $^3J_{H\text{-}H}$ = 8.4 Hz, 1.7H, HNCC*H*, cis, aromatic), 6.95 (d, $^3J_{H\text{-}H}$ = 8.3 Hz, 0.3H, HNCC*H*, trans, aromatic), 4.15 (s, 1.7H, C(O)OCH_2, cis), 4.00 (t, $^3J_{H\text{-}H}$ = 4.5 Hz, 0.3H, C(O)OCH_2, trans), 3.53 (s, 2H, C(O)OCH_2CH_2), 3.41-3.24 (m, 44H,

OC*H*$_2$, PEG), 3.05 (s, 3H, C*H*$_3$). ^{13}C NMR (100 MHz, $CDCl_3$): δ (ppm) 165.6 (*C*(O)O, cis), 161.8 (*C*(O)O, trans), 160.9 (H*C*=O, trans), 160.2 (H*C*=O, cis), 142.1 (*C*NH, aromatic), 131.2 (O=CC*C*H, trans, aromatic), 130.5 (O=CC*C*H, trans, aromatic), 125.4 (HNC*C*H, trans, aromatic), 124.9 (HNC*C*H, cis, aromatic), 118.8 (*C*C(O)O, cis, aromatic), 116.8 (*C*C(O)O, trans, aromatic), 71.6 (O*C*H$_2$, PEG), 70.2 (O*C*H$_2$, PEG), 68.9 (O*C*H$_2$, PEG), 68.6 (O*C*H$_2$, PEG), 63.7 (C(O)OCH$_2$*C*H$_2$), 62.7 (C(O)O*C*H$_2$), 58.6 (*C*H$_3$). SEC (THF + 2% v/v NEt_3, 40 °C): $M_{n,\ SEC}$ = 0.85 kDa ($Đ_{M,\ SEC}$ = 1.14). HRMS: *m/z* $[C_{32}H_{55}NO_{16}+H]^+$ calc. 708.3806 g·mol^{-1}, exp. 708.3834 g·mol^{-1}. FT-IR (neat): 3270 (N-H stretch), 2862 (C-H stretch), 1697 (C=O stretch), 1600 (C=C stretch), 1455 (C-H bend), 1351 (C-N bend), 1273 (C-O stretch, ester), 1091 (C-O stretch, ether), 945 (C=C bend) cm^{-1}.

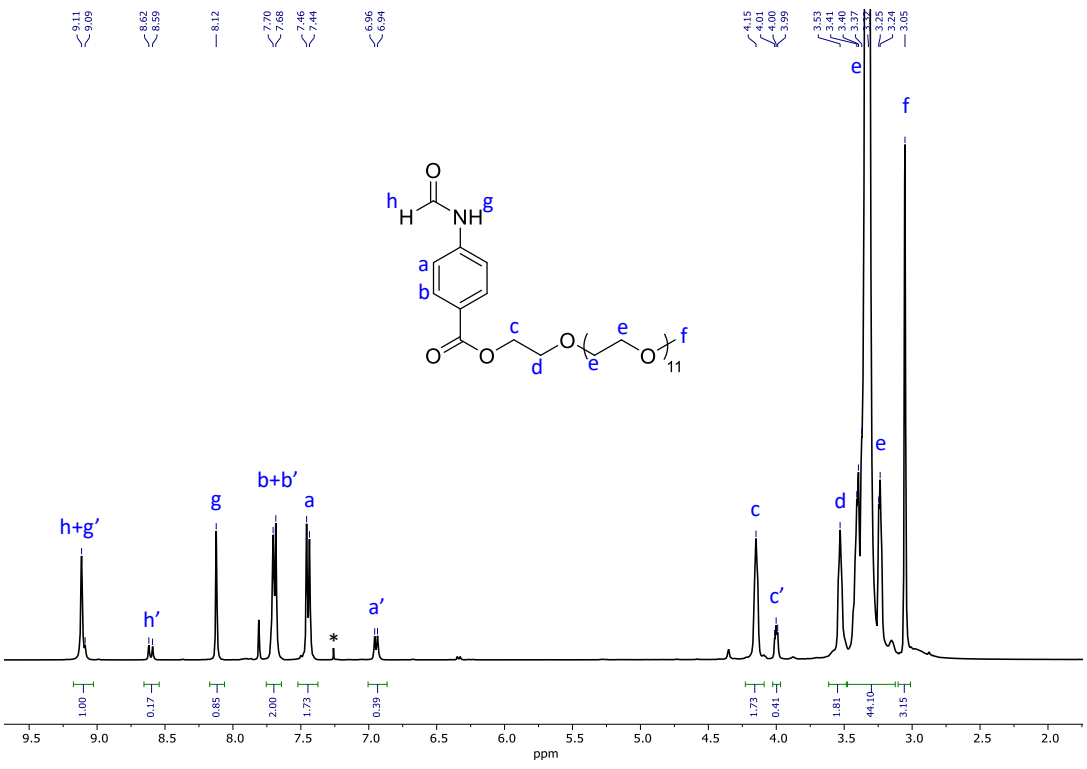

Figure 7.18. ^{1}H NMR spectrum of mPEG-Ar-NHCHO in $CDCl_3$ (400 MHz, 298 K).

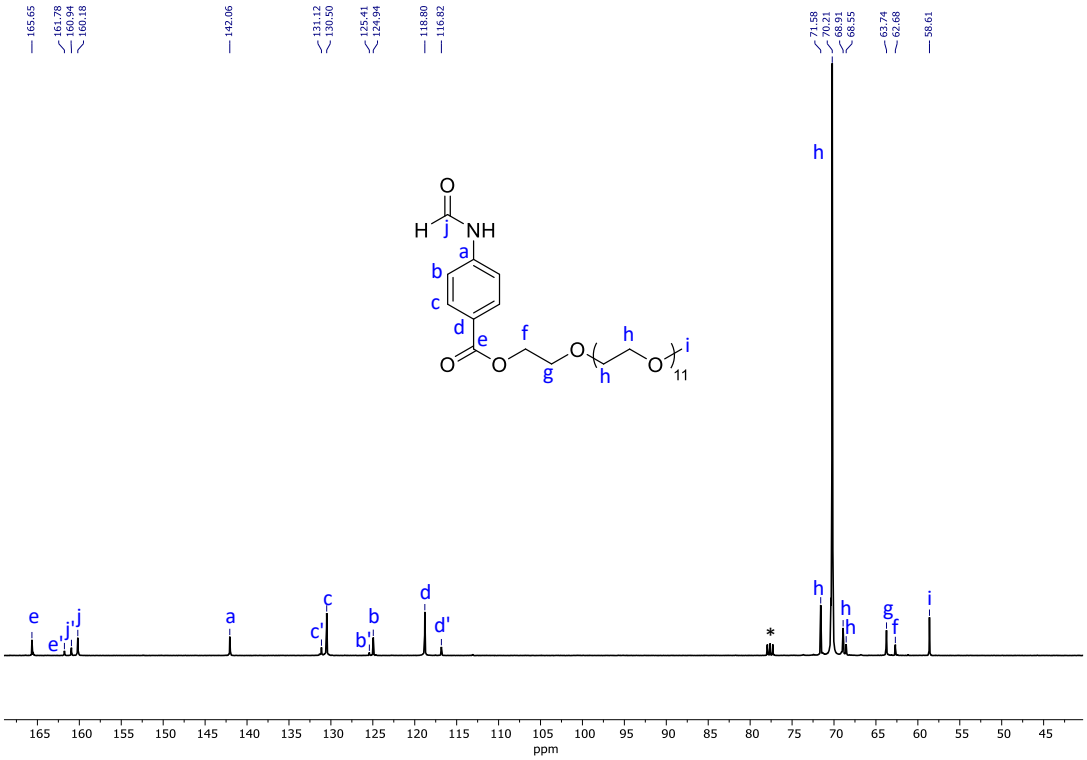

Figure 7.19. ^{13}C NMR spectrum of mPEG-Ar-NHCHO in $CDCl_3$ (100 MHz, 298 K).

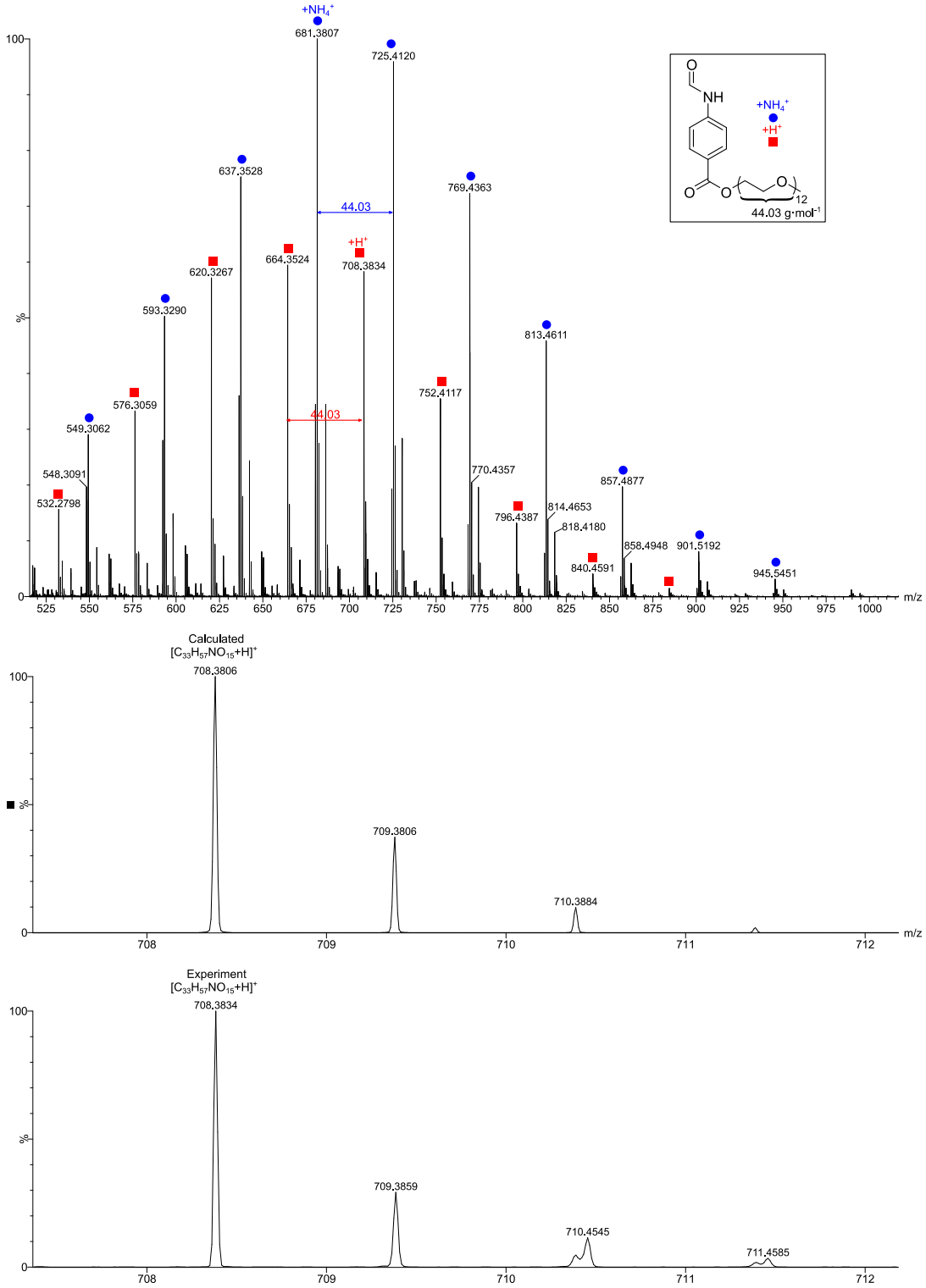

Figure 7.20. *Top:* Mass spectra of mPEG-Ar-NHCHO collected by ESI-MS. *Top*: Expanded spectrum (350-1000 *m/z*) with NH_4^+ (blue circles) and H^+ (red squares) adduct of the product $mPEG_{12}$-Ar-NHCHO. *Bottom*: Calculated *vs* experimental *m/z* value for $mPEG_{12}$-Ar-NHCHO+H^+ adduct.

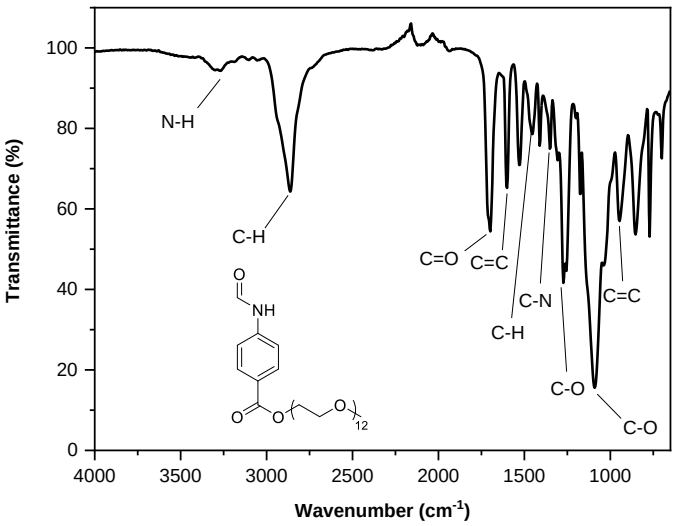

Figure 7.21. FT-IR spectrum of mPEG-Ar-NHCHO.

7.3.2.4. mPEGyl 4-isocyanobenzoate (PAIC) synthesis

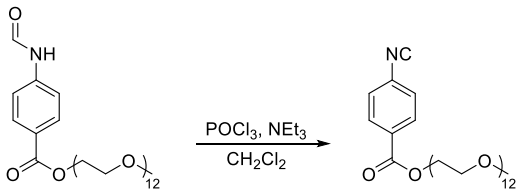

Scheme 7.8. mPEGyl 4-isocyanobenzoate synthesis.

A 100 mL Schlenk flask (dried in the oven and under N_2) was charged with formamide-PEG (3.3 g, 4.7 mmol, 1.0 equiv.), Et_3N (2.6 mL, 19 mmol, 4.0 equiv.) and CH_2Cl_2 (dry, 50 mL). The solution was cooled down to 0 °C in an ice bath, then $POCl_3$ (0.50 mL, 5.4 mmol, 1.2 equiv.) was added dropwise with a syringe over 15 min. The reaction was stirred at 0 °C for 1 h before cold Na_2CO_3 (sat. 10 mL) was added to the solution. The reaction mixture was stirred for 10 min before the two phases were separated and the aqueous phase was extracted with Et_2O (3 × 10 mL). The combined Et_2O extracts were dried over $MgSO_4$ and filtered. The filtrate was concentrated *in vacuo* and purified by flash chromatography (gradient from 0 → 3% MeOH in CH_2Cl_2), which yielded a yellow oil (1.6 g, 51%). ^{1}H NMR (400 MHz, $CDCl_3$): δ (ppm) 8.09 (d, $^3J_{H\text{-}H}$ = 8.8 Hz, 2H, C≡NCC*H*, aromatic), 7.44 (d, $^3J_{H\text{-}H}$ = 8.7 Hz, 2H,

O=CCC*H*), 4.47 (t, $^{3}J_{\text{H-H}}$ = 4.8 Hz, 2H, C(O)OC*H*$_2$), 3.82 (t, $^{3}J_{\text{H-H}}$ = 4.8 Hz, 2H, C(O)OCH$_2$C*H*$_2$), 3.68-3.62 (m, 42H, OC*H*$_2$, PEG), 3.54-3.52 (m, 2H, OC*H*$_2$, PEG), 3.36 (s, 3H, C*H*$_3$). ^{13}C NMR (100 MHz, CDCl$_3$): 167.2 (*C*(O)O), 164.8 (N≡*C*), 160.0 (*C*N≡C), 130.9 (O=CC*C*H, aromatic), 126.4 (NC*C*H, aromatic), 113.3 (*C*C(O)O), 71.8 (O*C*H$_2$, PEG), 70.5 (O*C*H$_2$, PEG), 68.9 (O*C*H$_2$, PEG), 64.6 (C(O)OCH$_2$*C*H$_2$), 62.9 (C(O)O*C*H$_2$), 58.9 (*C*H$_3$). SEC (THF + 2% v/v NEt$_3$, 40 °C): $M_{\text{n, SEC}}$ = 0.90 kDa ($Đ_{\text{M, SEC}}$ = 1.08). HRMS: *m/z* [C$_{33}$H$_{55}$NO$_{14}$+Na]$^+$ calc. 712.3521 g·mol^{-1}, exp. 712.3539 g·mol^{-1}. FT-IR (neat): 2858 (C-H stretch), 2118 (C≡N stretch), 1720 (C=O stretch), 1604 (C=C stretch), 1452 (C-H bend), 1347 (C-N stretch), 1273 (C-O stretch, ester), 1091 (C-O stretch, ether), 954 (C=C bend) cm^{-1}.

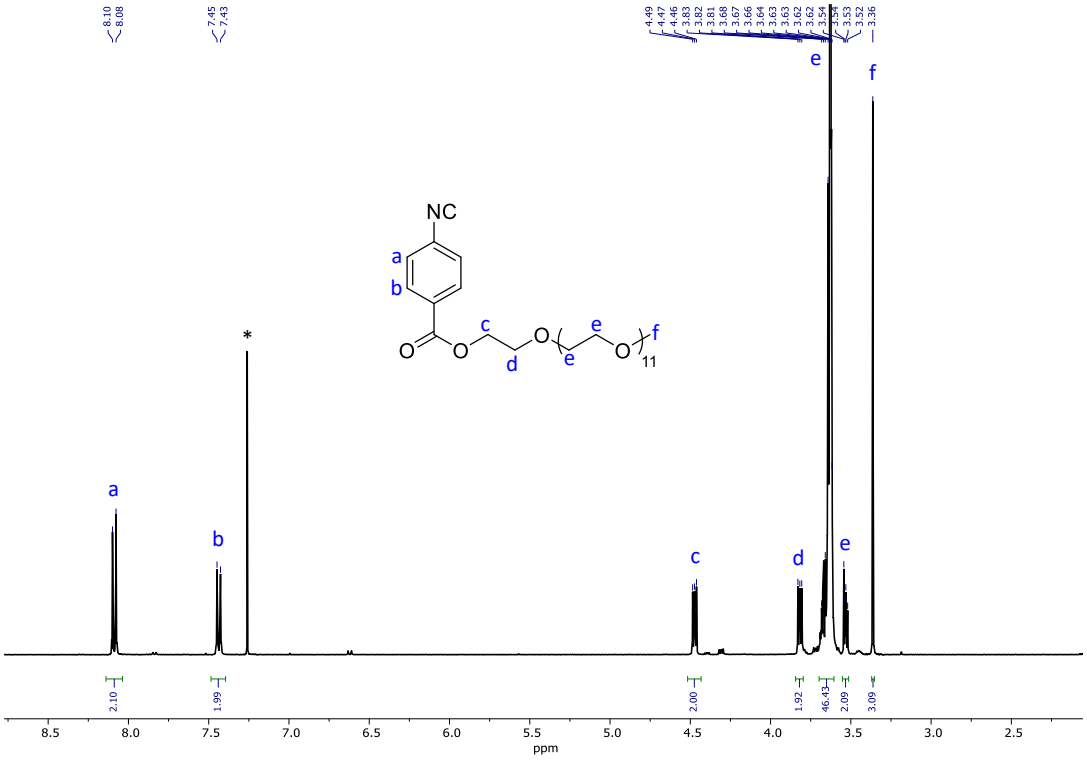

Figure 7.22. ^{1}H NMR spectrum of PAIC in $CDCl_3$ (400 MHz, 298 K).

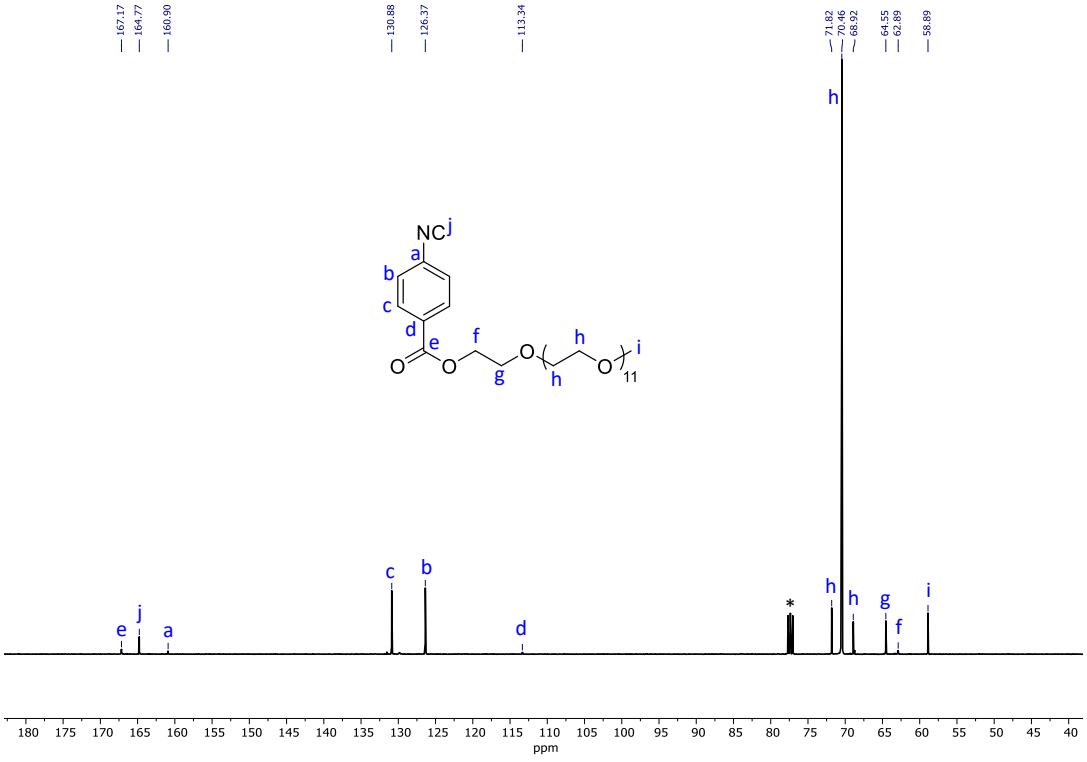

Figure 7.23. ^{13}C NMR spectrum of PAIC in $CDCl_3$ (100 MHz, 298 K)

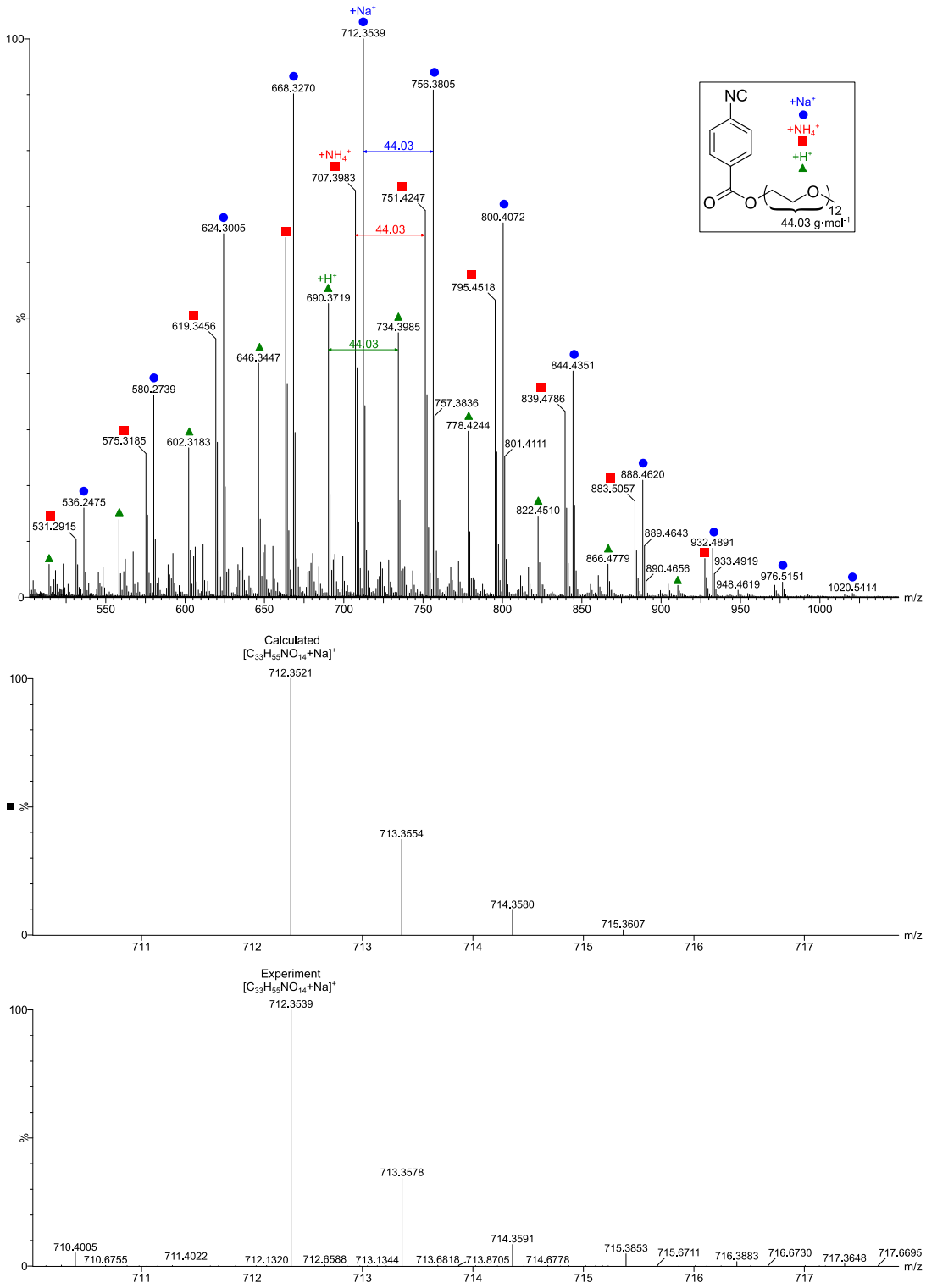

Figure 7.24. *Top:* Mass spectra of PAIC collected by ESI-MS. *Top*: Expanded spectrum (500-1000 m/z) with Na^+ (blue circles), NH_4^+ (red squares) and H^+ (green triangles) adduct of the product PAIC. *Bottom*: Calculated *vs* experimental m/z value for PAIC+Na^+ adduct.

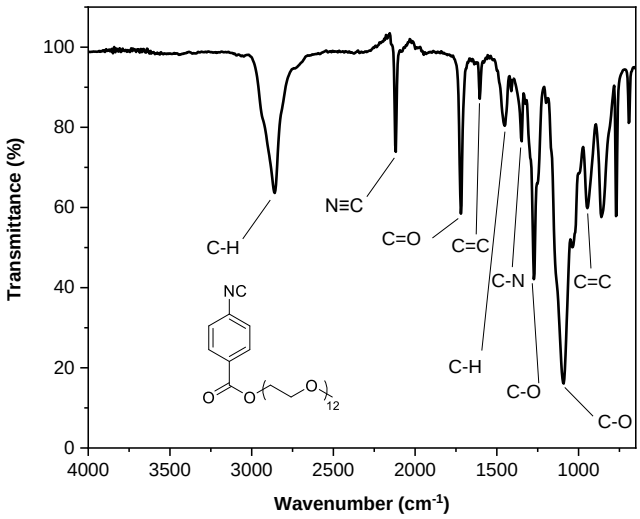

Figure 7.25. FT-IR spectrum of PAIC.

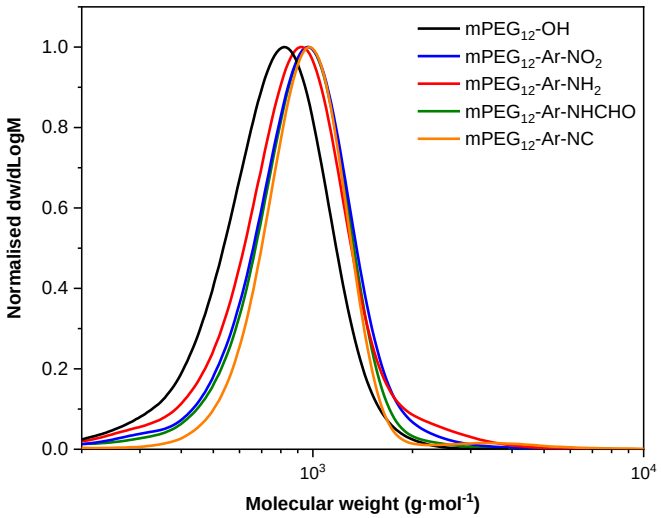

Figure 7.26. Size exclusion chromatograms (THF + 2 v/v% NEt_3, 40 °C, PS standards) of the starting material $mPEG_{12}$-OH and the different intermediates and the product: $mPEG_{12}$-Ar-NO_2, $mPEG_{12}$-Ar-NH_2, $mPEG_{12}$-Ar-NHCHO and $mPEG_{12}$-Ar-NC (PAIC).

Table 7.1. Characterisation by SEC of the different intermediates and the product: mPEG$_{12}$-Ar-NO$_2$, mPEG$_{12}$-Ar-NH$_2$, mPEG$_{12}$-Ar-NHCHO, mPEG$_{12}$-Ar-NC.

Polymer[a]	M_n (kDa)[b]	$Đ_M$[b]
mPEG$_{12}$-OH	0.70	1.17
mPEG$_{12}$-Ar-NO$_2$	0.80	1.22
mPEG$_{12}$-Ar-NH$_2$	0.85	1.18
mPEG$_{12}$-Ar-NCHO	0.85	1.14
mPEG$_{12}$-Ar-NC (PAIC)	0.90	1.08

[a]All conversions were > 99%, determined by ^{1}H NMR spectroscopy in CDCl$_3$.
[b]Determined by SEC (THF + 2% v/v NEt$_3$) with polystyrene (PS) standards.

7.3.3. *o*-tol(dppe)NiCl synthesis

Compound *o*-tol(dppe)NiCl was prepared in accordance with previously reported synthetic methods.[2]

7.3.3.1. (dppe)NiCl$_2$ synthesis

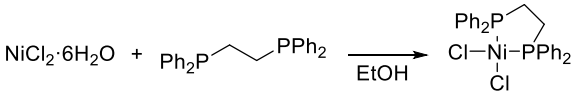

Scheme 7.9. (dppe)NiCl$_2$ synthesis.

In a 50 mL round-bottom flask, NiCl$_2$·6H$_2$O (2.3 g, 9.7 mmol, 1.0 equiv.) was dissolved in EtOH (30 mL). The flask was sealed with a rubber septum and the solution was purged with N$_2$ for 15 min. After removal of the septum, dppe (3.9 g, 9.7 mmol, 1.0 equiv.) was added and the reaction mixture was refluxed (85 °C) for 30 min. After the solution cooled down to r.t., the flask was put in an ice bath (0 °C) for 10 min. The suspension was filtered, and the filter was washed with EtOH (3 × 20mL) which yielded the product as a bright red powder (4.1 g, 81%). ^{1}H NMR (400 MHz, CDCl$_3$): δ (ppm) 7.99 (q, $^3J_{H\text{-}H}$ = 7.0 Hz, 8H, PCC*H*, aromatic), 7.56 (t, $^3J_{H\text{-}H}$ = 7.4 Hz, 4H, PCCHCHC*H*, aromatic), 7.48 (t, $^3J_{H\text{-}H}$ = 7.4 Hz, 8H, PCCHC*H*, aromatic), 2.13 (d, $^3J_{H\text{-}H}$ = 17.8 Hz, 4H, PC*H*$_2$). ^{13}C NMR (100 MHz, CDCl$_3$): δ (ppm) 133.6 (t,

PC*C*H, aromatic), 131.8 (s, PCCHCH*C*H, aromatic), 129.0 (t, PCCH*C*H, aromatic), 128.4 (t, P*C*CH, aromatic), 27.6 (t, P*C*H_2). Characterisation was consistent with that reported previously.[2]

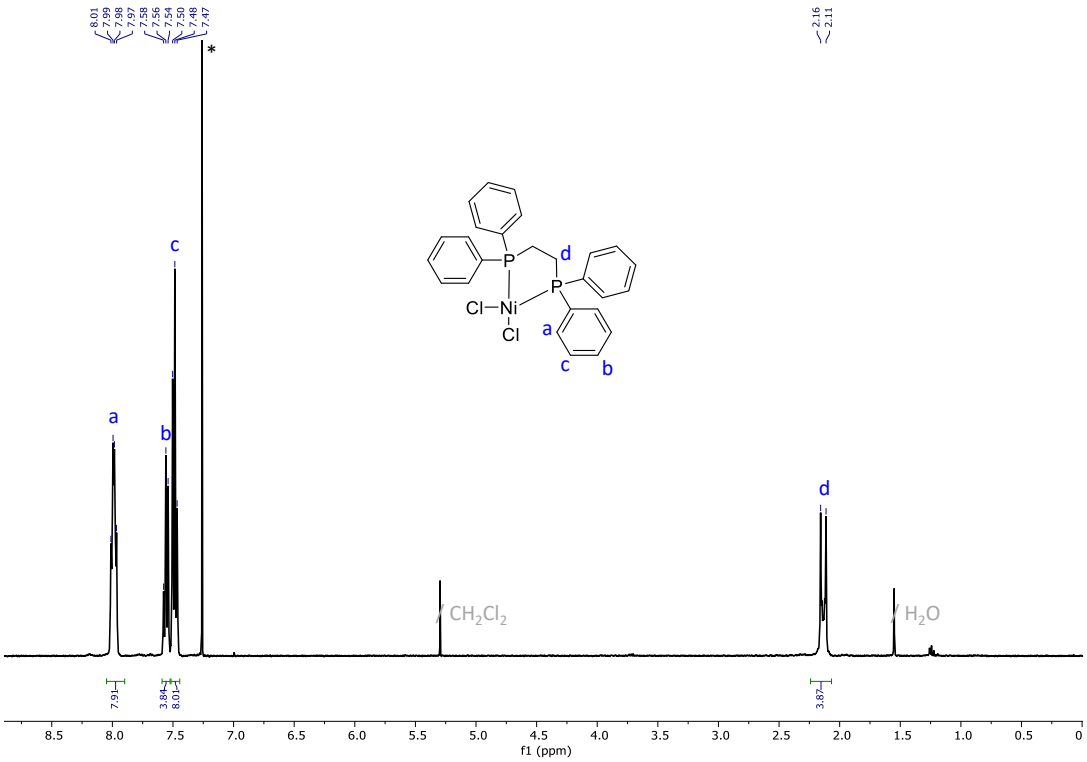

Figure 7.27. ^{1}H NMR spectrum of (dppe)$NiCl_2$ in $CDCl_3$ (400 MHz, 298 K).

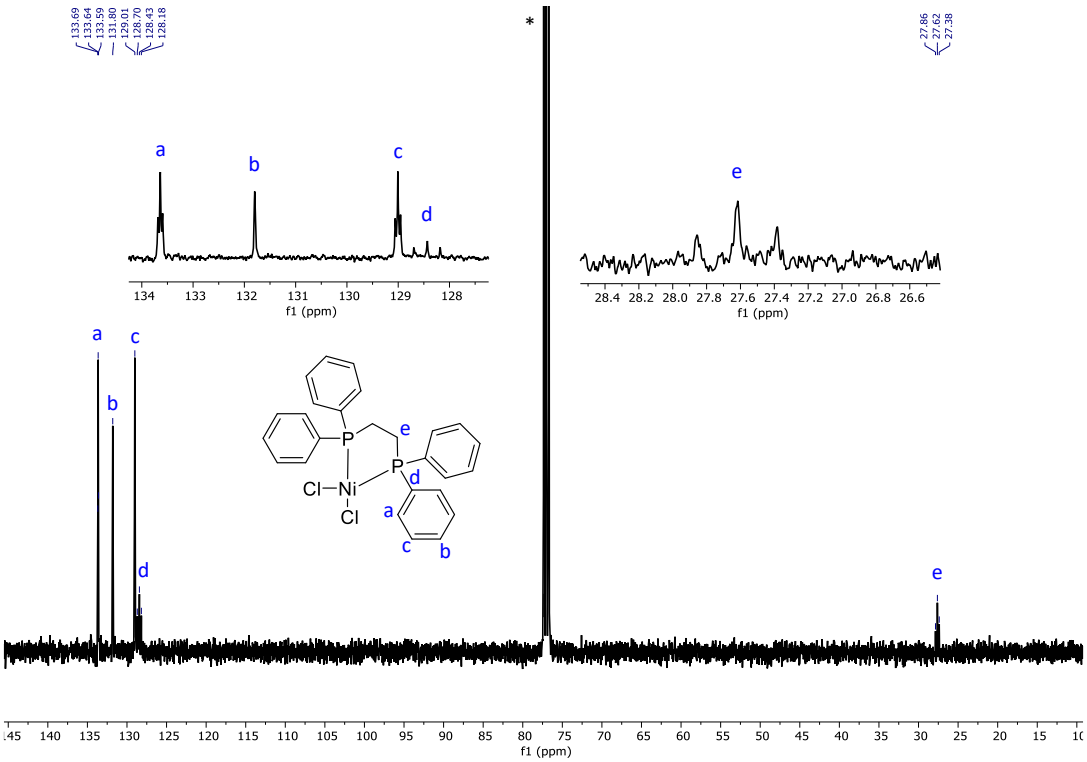

Figure 7.28. ^{13}C NMR spectrum of (dppe)$NiCl_2$ in $CDCl_3$ (100 MHz, 298 K).

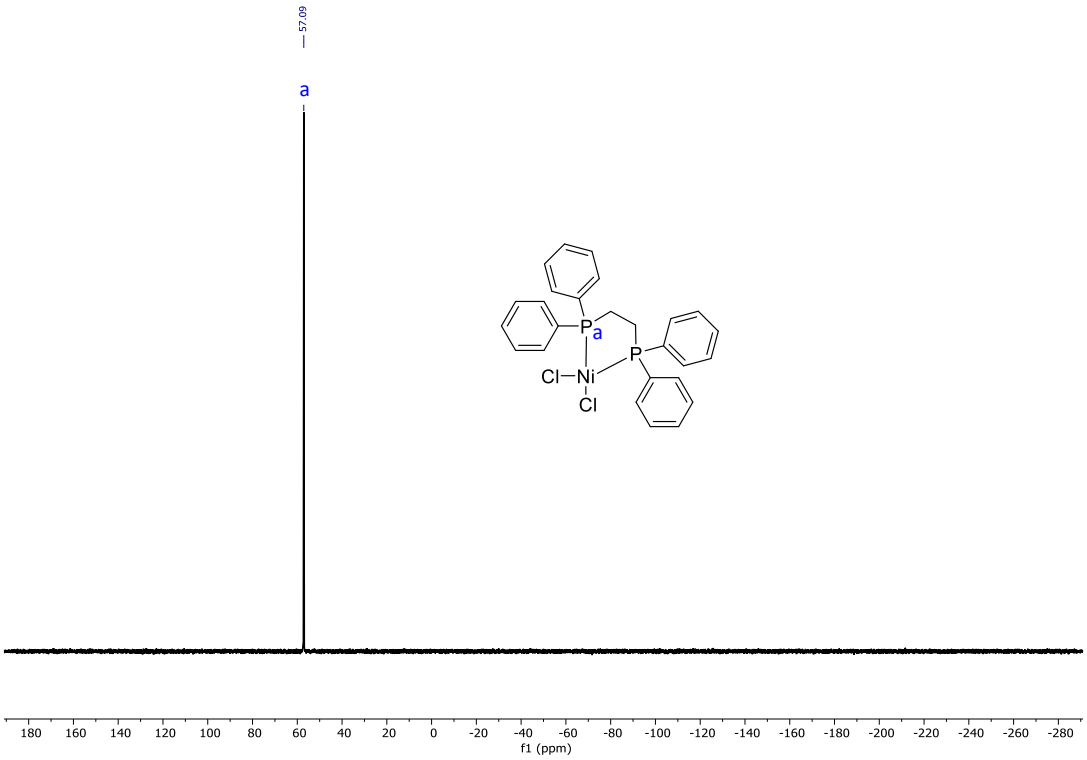

Figure 7.29. ^{31}P NMR spectrum of (dppe)$NiCl_2$ in $CDCl_3$ (100 MHz, 298 K).

7.3.3.2. *o*-Tol(dppe)$NiCl_2$ synthesis

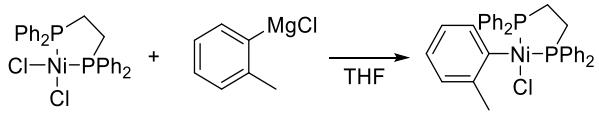

Scheme 7.10. *o*-Tol(dppe)$NiCl_2$ synthesis.

In a 250 mL Schlenk flask (oven-dried), (dppe)$NiCl_2$ (1.1 g, 2.1 mmol, 1.0 equiv.) was suspended in dried THF (100 mL) and cooled down to 0 °C. *o*-tolylmagnesium chloride (1.0 M in THF, 2.1 mL, 1.0 equiv.) was added slowly over 15 min and the reaction mixture was stirred for 15 min before concentration *in vacuo*. The residue was suspended in MeOH (20 mL) and sonicated for 10 min. The suspension was cooled down to 0 °C before filtration on Büchner. The filter was washed with cold MeOH (2 × 20mL) which gave the product as a yellow solid (0.62 g, 51%). ^{1}H NMR (400 MHz, $CDCl_3$): δ (ppm) 8.11 (t, $^{3}J_{H\text{-}H}$ = 9.5 Hz, 4H), 7.72 (t, $^{3}J_{H\text{-}H}$ = 8.0 Hz, 2H), 7.46-7.34 (m, 10H), 7.24-7.14 (m, 1H), 6.99 (td, $^{3}J_{H\text{-}H}$ = 7.8, 2.4 Hz, 2H), 6.63 (t, $^{3}J_{H\text{-}H}$ = 8.0 Hz, 2H), 6.52 (p, $^{3}J_{H\text{-}H}$ = 8.0 Hz, 2H), 6.34 (d, $^{3}J_{H\text{-}H}$ = 7.7 Hz, 1H), 2.43-2.33 (m, 2H), 2.28-2.19 (m, 3H), 2.08 (m, 1H), 1.53-1.46 (m, 1H) . ^{13}C NMR (400 MHz, $CDCl_3$): δ (ppm) 153.8 (s), 134.7 (d), 133.7 (d), 132.8 (d), 131.8 (d), 131.5 (s), 130.9 (s), 130.4 (s), 130.0 (s), 129.1 (d), 128.9 (d), 128.7 (d), 127.6 (d), 123.6 (d), 122.7 (s), 25.4 (s). Characterisation was consistent with that reported previously.[2, 3]

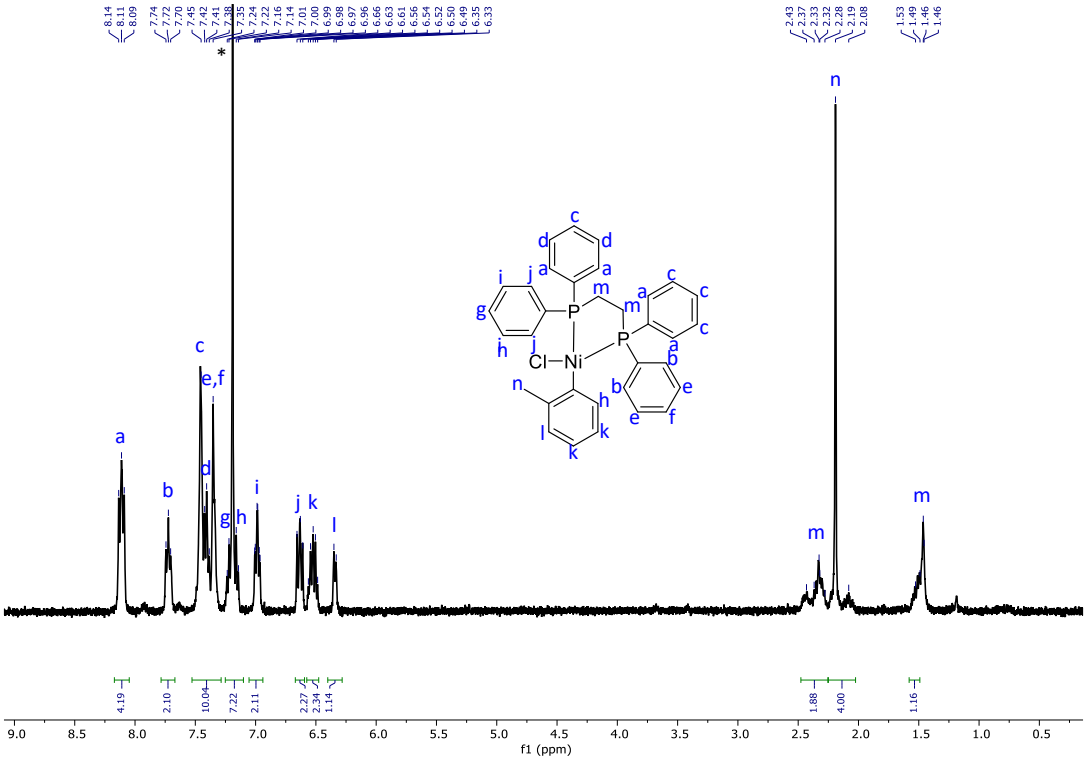

Figure 7.30. ^{1}H NMR spectrum of *o*-tol(dppe)NiCl$_2$ in CDCl$_3$ (400 MHz, 298 K).

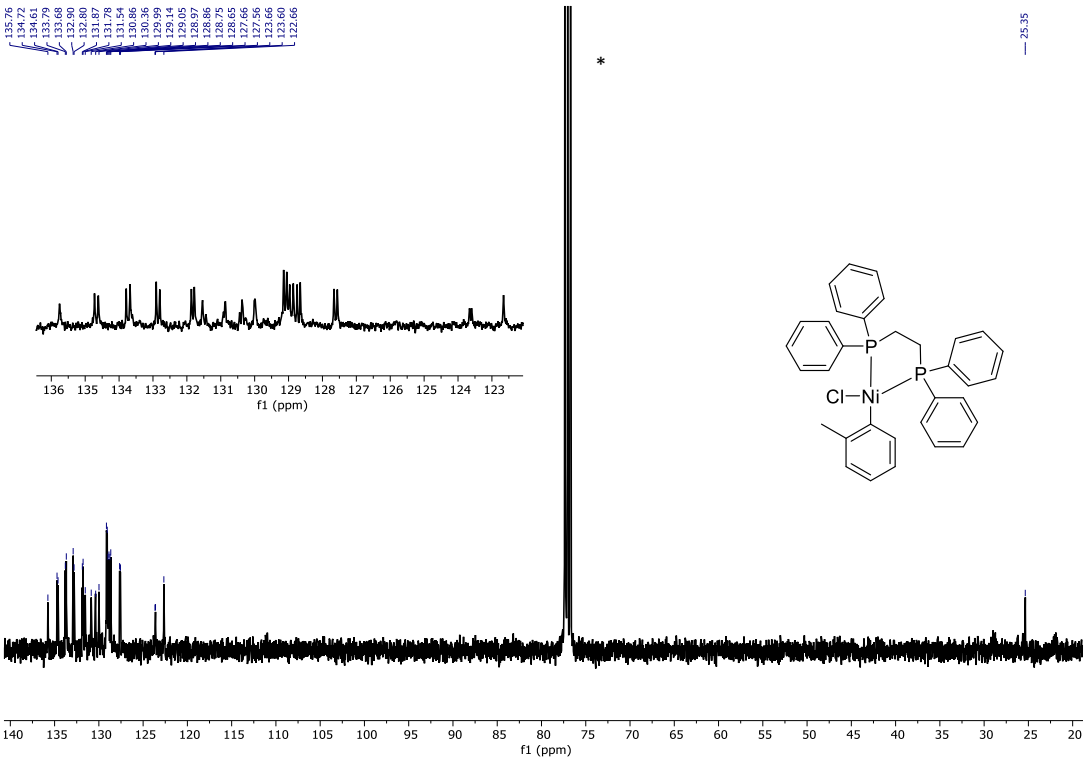

Figure 7.31. ^{13}C NMR spectrum of *o*-tol(dppe)NiCl$_2$ in CDCl$_3$ (100 MHz, 298 K).

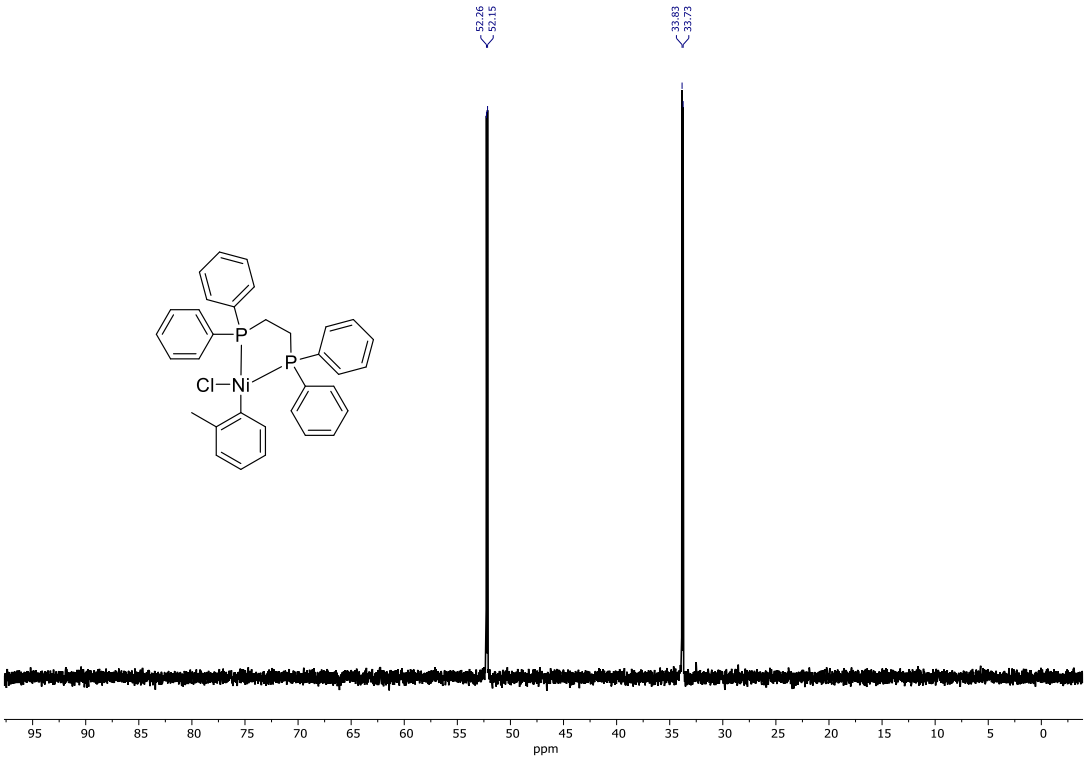

Figure 7.32. ^{31}P NMR spectrum of *o*-tol(dppe)NiCl$_2$ in CDCl$_3$ (100 MHz, 298 K).

7.3.4. General procedure for the homopolymerisation of MAIC

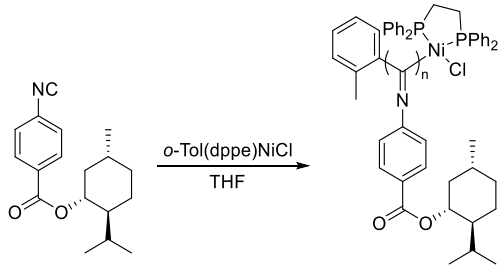

Scheme 7.11. Homopolymerisation of MAIC.

Example for P(MAIC)$_{50}$

A 7 mL scintillation vial (dried in the oven and under N$_2$) was charged with *o*-Tol(dppe)NiCl (2.5 mg, 0.070 mmol, 1.0 equiv.) and THF (dry, 1.8 mL). The MAIC (3.5 mmol, 0.20 M, 50 equiv.) was added and stirred for 10 min. The resulting dark orange solution was precipitated in a mixture of cold MeOH/H$_2$O (2:1) to yield the product as a light orange powder. ^{1}H NMR (300 MHz, CDCl$_3$): δ (ppm) 8.14-6.66 (m, 2H, NCC*H*, aromatic), 6.64-5.14 (m, 2H,

O=CCC*H*, aromatic), 5.13-4.08 (bs, 1H, OC*H*), 2.31-0.23 (m, 18H). SEC (THF + 2% v/v NEt_3, 40 °C): $M_{n,\,SEC}$ = 7.1 kDa ($Đ_{M,\,SEC}$ = 1.10).

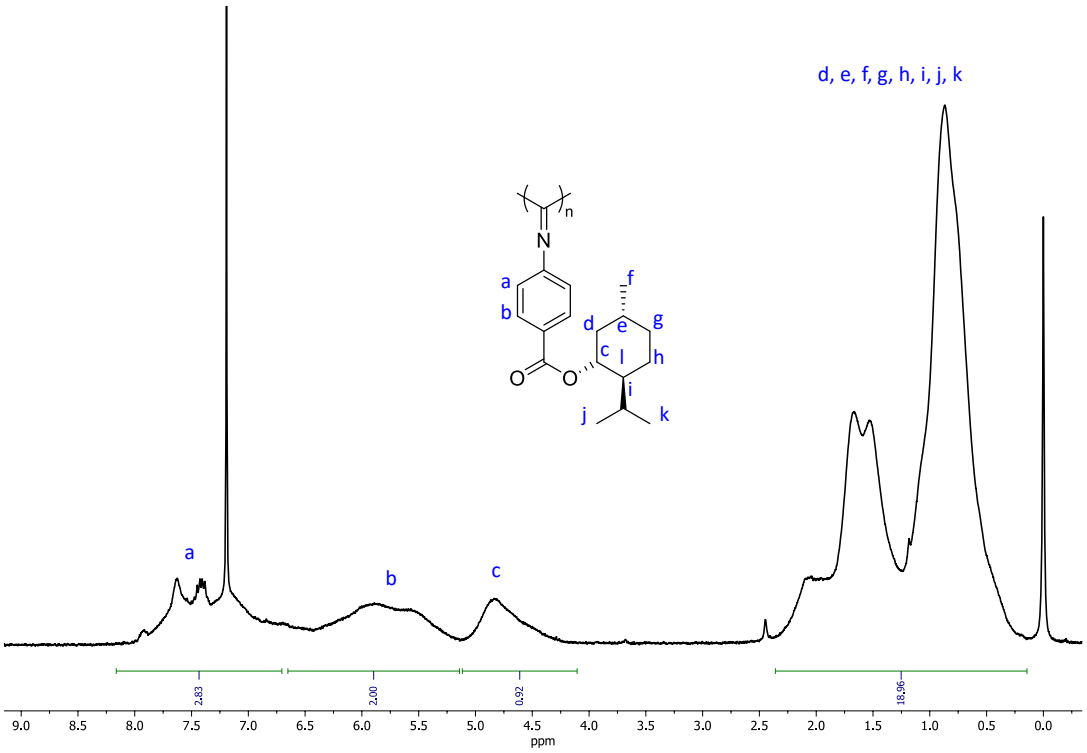

Figure 7.33. ^{1}H NMR spectrum of P(MAIC)$_{30}$ homopolymer in $CDCl_3$ (300 MHz, 298 K).

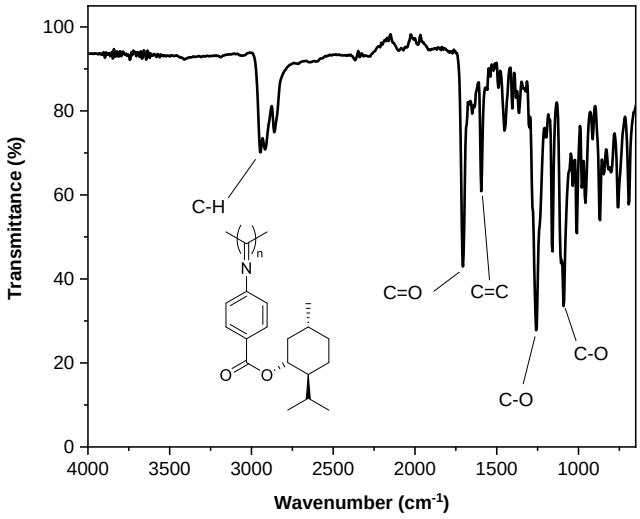

Figure 7.34. FT-IR spectrum of P(MAIC)$_{30}$ homopolymer.

7.3.5. General procedure for the homopolymerisation of PAIC

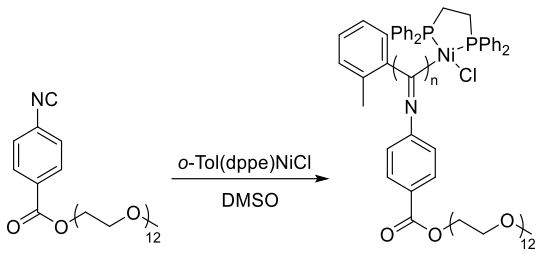

Scheme 7.12. Homopolymerisation of PAIC.

Example for P(PAIC)$_{50}$

A 7 mL scintillation vial (dried in the oven and under N_2) was charged with *o*-Tol(dppe)NiCl (2.5 mg, 0.070 mmol, 1.0 equiv.) and DMSO (dry, 1.75 mL). PAIC (3.5 mmol, 0.20 M, 50 equiv.) was added and stirred for 10 min. The resulting dark orange solution was stirred in a mixture of cold hexane to yield the product as a dark orange oil. ^{1}H NMR (300 MHz, $CDCl_3$): δ (ppm) 8.09-6.65 (m, 2H, NCC*H*, aromatic), 6.40-5.45 (m, 2H, O=CCC*H*, aromatic), 4.67-4.03 (bs, 2H, C(O)OCH_2), 4.01-3.01 (m, 49H). SEC (THF + 2% v/v NEt_3, 40 °C): $M_{n,\,SEC}$ = 16.8 kDa ($Đ_{M,\,SEC}$ = 1.16).

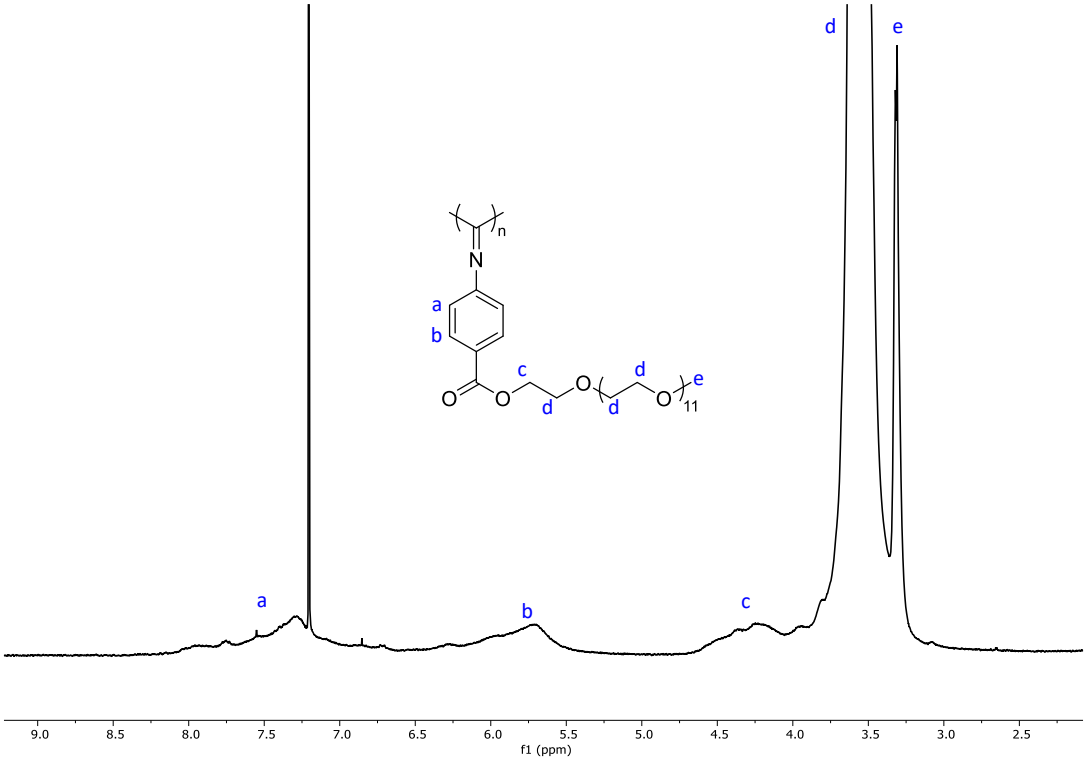

Figure 7.35. ^{1}H NMR spectrum of P(PAIC)$_{20}$ homopolymer in $CDCl_3$ (300 MHz, 298 K).

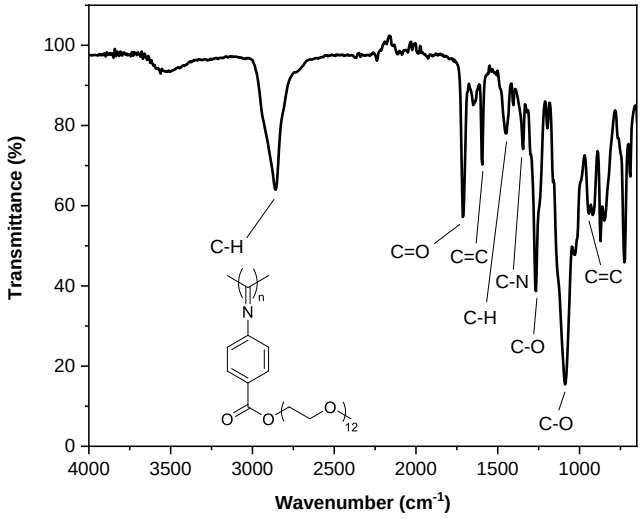

Figure 7.36. FT-IR spectrum of P(PAIC)$_{20}$ homopolymer

7.3.6. General procedure for the NiCCo-PISA of P(PAIC)$_x$-*b*-P(MAIC)$_y$ diblock copolymers

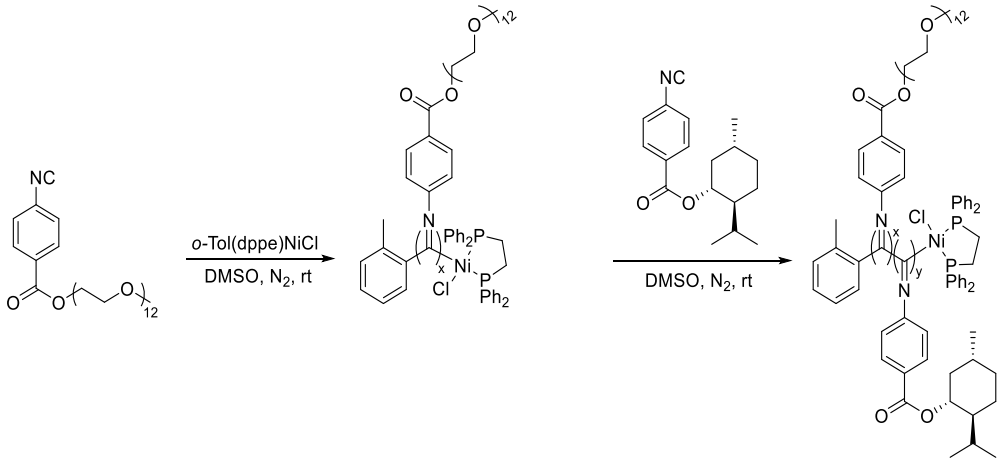

Scheme 7.13. NiCCo-PISA of P(PAIC)$_x$-*b*-P(MAIC)$_y$ diblock copolymers catalysed by *o*-Tol(dppe)NiCl in DMSO.

Example for P(PAIC)$_{20}$-*b*-P(MAIC)$_{30}$

A 2.5 mL scintillation vial (dried in the oven and under N_2) was charged with *o*-Tol(dppe)NiCl (2.5 mg, 0.070 mmol, 1.0 equiv.) and DMSO (dry, 0.10 mL). PAIC (1.4 mmol, 20 equiv.) in DMSO (dry, 0.50 mL) was added. After 5 min, MAIC (2.1 mol, 30 equiv.) in DMSO (dry, 0.40 mL) was added. After 10 min, the dark orange solution was opened to air to stop the reaction.

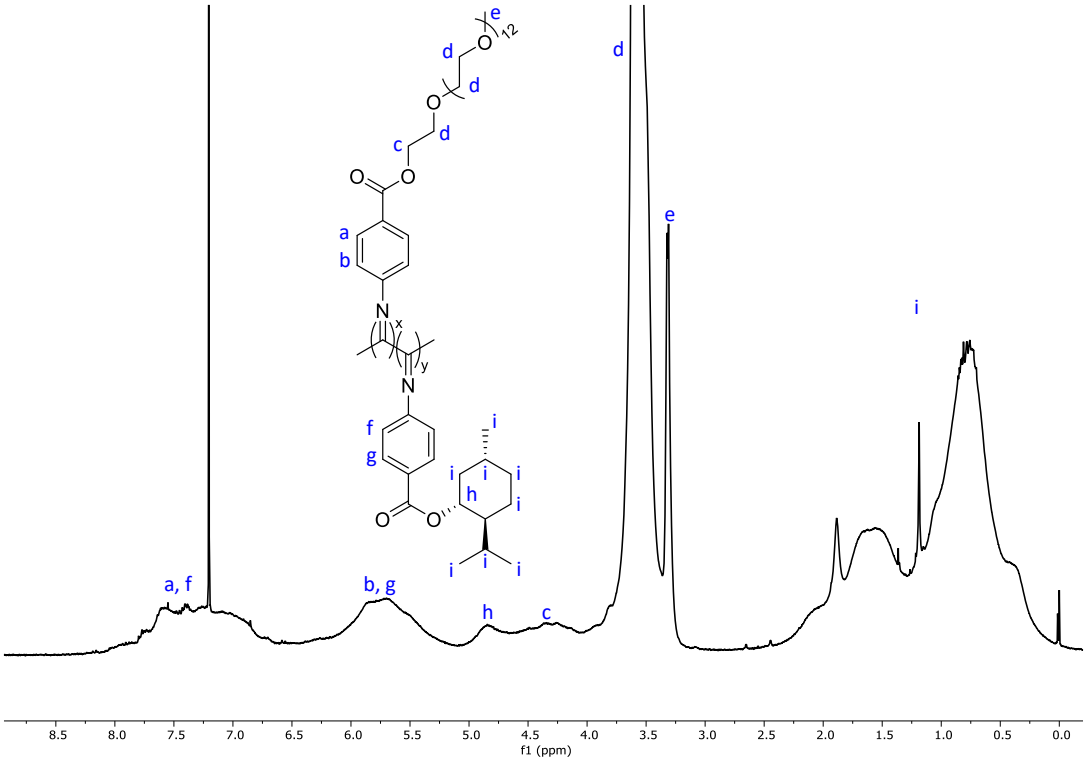

Figure 7.37. ^{1}H NMR spectrum of P(PAIC)$_{20}$-*b*-P(MAIC)$_{30}$ in $CDCl_3$ (300 MHz, 298 K).

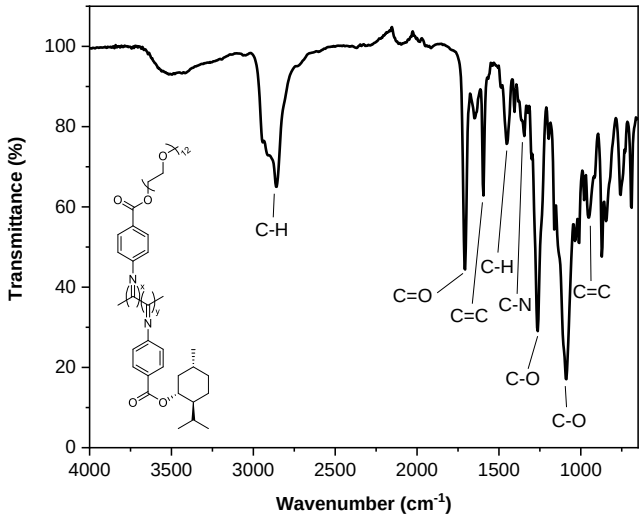

Figure 7.38. FT-IR spectrum of P(PAIC)$_{20}$-*b*-P(MAIC)$_{30}$.

7.3.7. General procedure for the encapsulation of Nile Red

NiCCo-PISA was conducted as described above with Nile Red mixed with the initial *o*-Tol(dppe)NiCl solution. The resulting solution was diluted to 0.5 wt% with DMSO and dialysed (4 kDa cutoff) in deionised water for 3 days (the water was changed every 6 h). The suspension was centrifuged and filtered (0.22 µm Nylon filter) to remove the precipitated Nile Red which yielded a purple solution.

7.4. Experimental protocols for Chapter 3

7.4.1. Pentafluorophenyl 4-isocyanobenzoate (FAIC) synthesis

The FAIC monomer was synthesised in accordance with the literature methodology.[4, 5]

7.4.1.1. 4-Formamidobenzoic acid synthesis

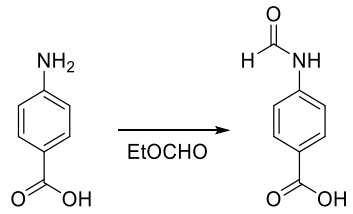

Scheme 7.14. 4-Formamidobenzoic acid synthesis.

In a 250 mL round-bottom flask, 4-aminobenzoic acid (10 g, 73 mmol) was suspended in ethyl formate (100 mL). The reaction mixture was heated at reflux (70 °C) overnight. The suspension was filtered on Büchner and washed with CH_2Cl_2 (2 × 200mL) which gave the product as an off-white solid (11 g, 90%). ^{1}H NMR (400 MHz, $(CD_3)_2SO$): δ (ppm) 12.74 (bs, 1H, C(O)O*H*), 10.48 (s, 0.75H, *H*C=O, cis), 10.42 (d, $^3J_{H\text{-}H}$ = 10.8 Hz, 0.25H, *H*C=O, trans), 8.94 (d, $^3J_{H\text{-}H}$ = 10.7 Hz, 0.25H, N*H*, trans), 8.34 (s, 0.75H, N*H*, cis), 7.93-7.87 (m, 2H, O=CCC*H*, aromatic, trans and cis), 7.70 (d, $^3J_{H\text{-}H}$ = 8.6 Hz, 1.5H, HNCC*H*, aromatic, cis), 7.28 (d, $^3J_{H\text{-}H}$ = 8.4 Hz, 0.5H, HNCC*H*, aromatic, trans). ^{13}C NMR (100 MHz, $(CD_3)_2SO$): δ (ppm) 167.0 (*C*(O)OH), 162.7 (H*C*=O, trans), 160.2 (H*C*=O, cis), 142.7 (*C*NH, aromatic, trans), 142.3 (*C*NH, aromatic, cis), 131.1 (O=CC*C*H, aromatic, trans), 130.7 (O=CC*C*H, aromatic, cis), 125.7 (*C*C(O)OH, aromatic, trans), 125.6 (*C*C(O)OH, aromatic, cis), 118.7 (HNC*C*H, aromatic, cis), 116.5 (HNC*C*H, aromatic, trans). Characterisation was consistent with that reported previously.[4]

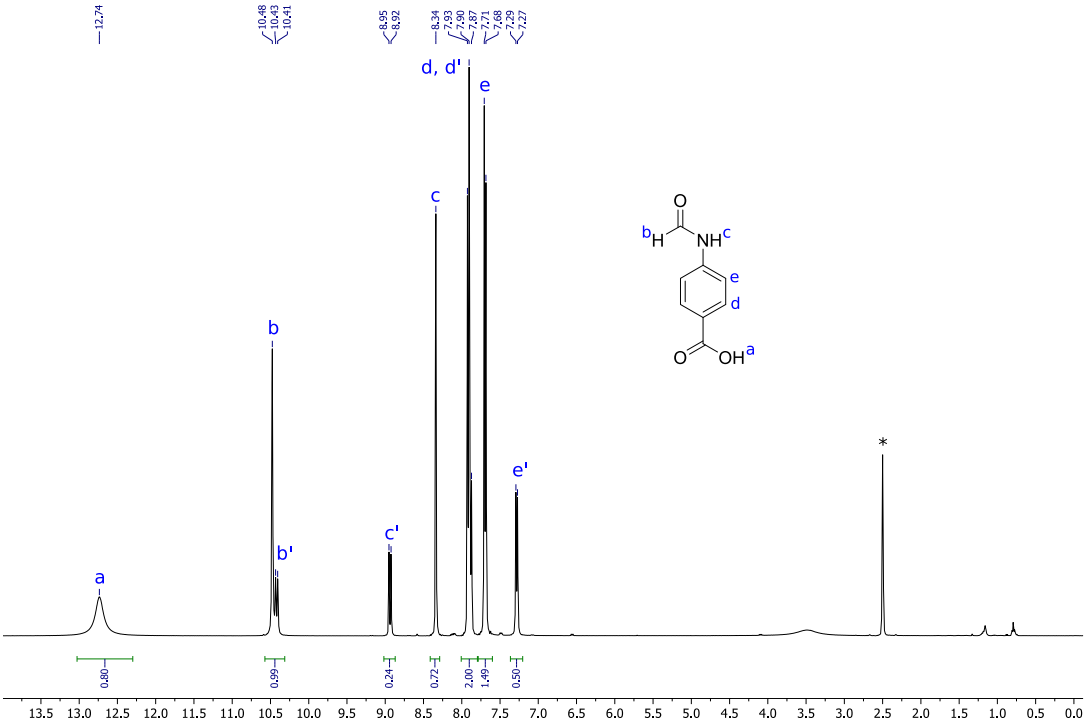

Figure 7.39. ^{1}H NMR of 4-formamidobenzoic acid in $(CD_3)_2SO$ (400 MHz, 298 K)

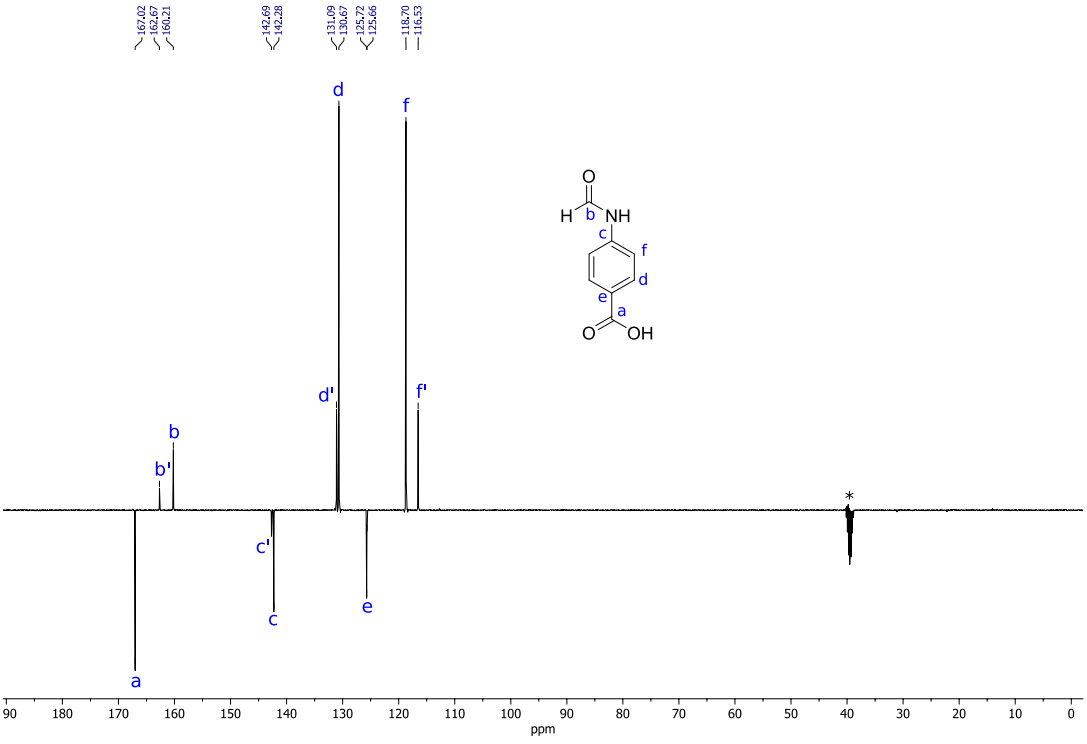

Figure 7.40. ^{13}C NMR 4-formamidobenzoic acid of in $(CD_3)_2SO$ (100 MHz, 298 K)

7.4.1.2. Pentafluorophenyl 4-formamidobenzoate synthesis

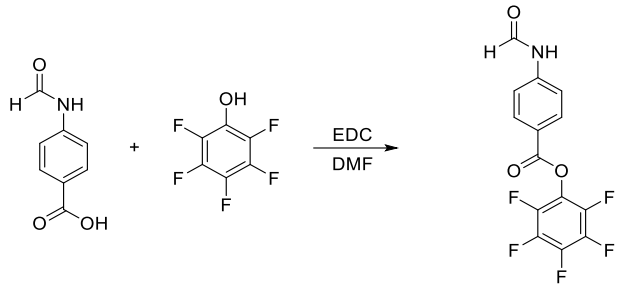

Scheme 7.15. Pentafluorophenyl 4-formamidobenzoate synthesis.

In a 250 mL round-bottom flask, 4-formamidobenzoic acid (5.0 g, 30 mmol, 1.0 equiv.) and 2,3,4,5,6-pentafluorophenol (6.1 mL, 33 mmol, 1.1 equiv.) were dissolved in DMF (80 mL). EDC (7.0 g, 37 mmol, 1.2 equiv.) was slowly added to the reaction mixture. The solution was stirred overnight before the reaction mixture was concentrated *in vacuo*. The residue was dissolved in ethyl acetate (250 mL) and the solution was washed with NH_4Cl (2 × 200 mL). The organic phase was dried on $MgSO_4$ and filtered. The solution was concentrated *in vacuo* and the residue was washed with cold ethyl acetate (3 × 20 mL) which yielded the product as a white solid (8.1 g, 81%). ^{1}H NMR (400 MHz, $(CD_3)_2SO$): δ (ppm) 10.74 (s, 0.75H, *H*C=O, cis), 10.66 (d, $^{3}J_{H\text{-}H}$ = 10.6 Hz, 1H, *H*C=O, trans), 9.07 (d, $^{3}J_{H\text{-}H}$ = 10.5 Hz, 0.25H, N*H*, trans), 8.41 (s, 0.75H, N*H*, cis), 8.15 (m, 2H, O=CCC*H*, aromatic, cis and trans), 7.85 (d, $^{3}J_{H\text{-}H}$ = 8.6 Hz, 1.5H, HNCC*H*, aromatic, cis), 7.46 (d, $^{3}J_{H\text{-}H}$ = 8.4 Hz, 0.5H, HNCC*H*, aromatic, trans). ^{13}C NMR (100 MHz, $(CD_3)_2SO$): δ (ppm) 161.7 (*C*(O)O), 160.5 (H*C*=O), 144.4 (*C*N, aromatic), 132.3 (O=CC*C*H, aromatic, trans), 132.0 (*C*H, aromatic, cis), 120.2 (*C*CO, aromatic), 119.1 (*C*H, aromatic, cis), 116.8 (*C*H, aromatic, trans). ^{19}F NMR (377 MHz, $(CD_3)_2SO$): δ (ppm) -153.6 (d, 2F, C*F*, aromatic), -157.8 (t, 1F, C*F*, aromatic), -162.5 (t, 2F, C*F*, aromatic). Characterisation was consistent with that reported previously.[4]

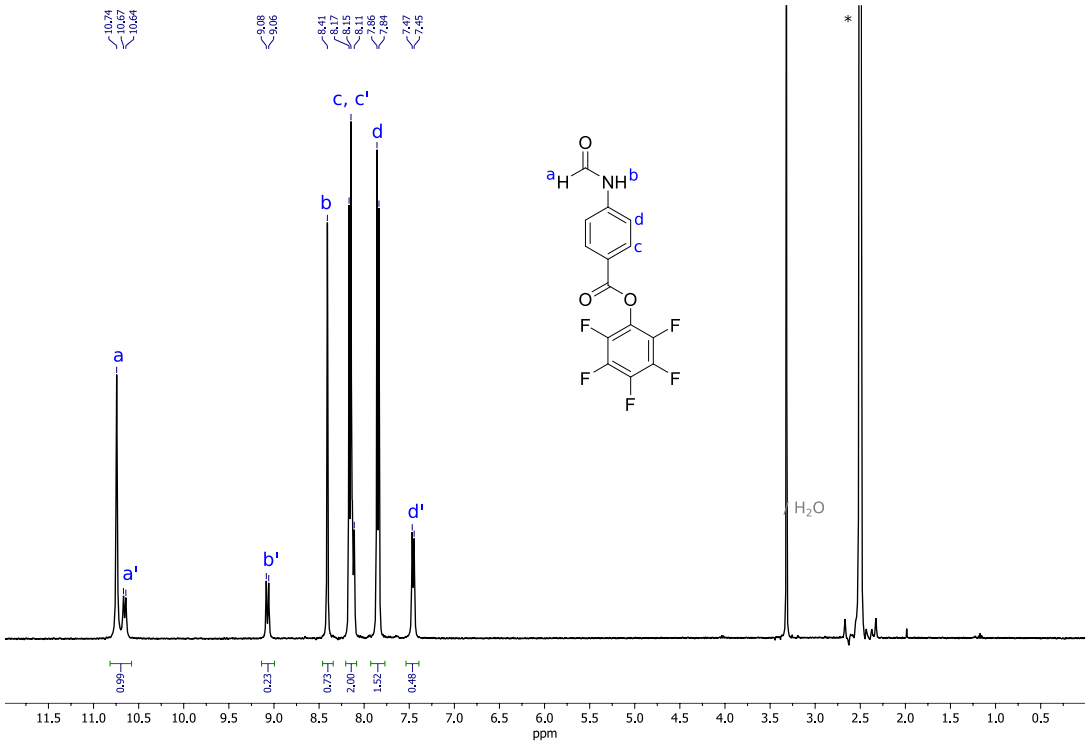

Figure 7.41. ^{1}H NMR of pentafluorophenyl 4-formamidobenzoate in $(CD_3)_2SO$ (400 MHz, 298 K)

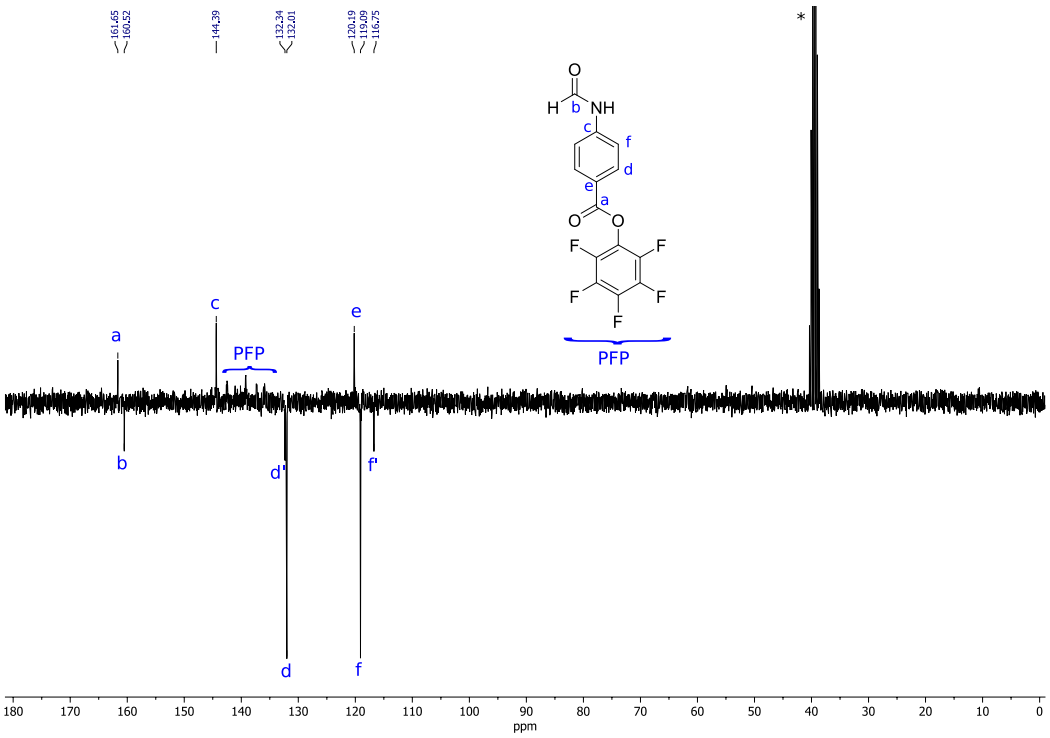

Figure 7.42. ^{13}C NMR of pentafluorophenyl 4-formamidobenzoate in $(CD_3)_2SO$ (100 MHz, 298 K)

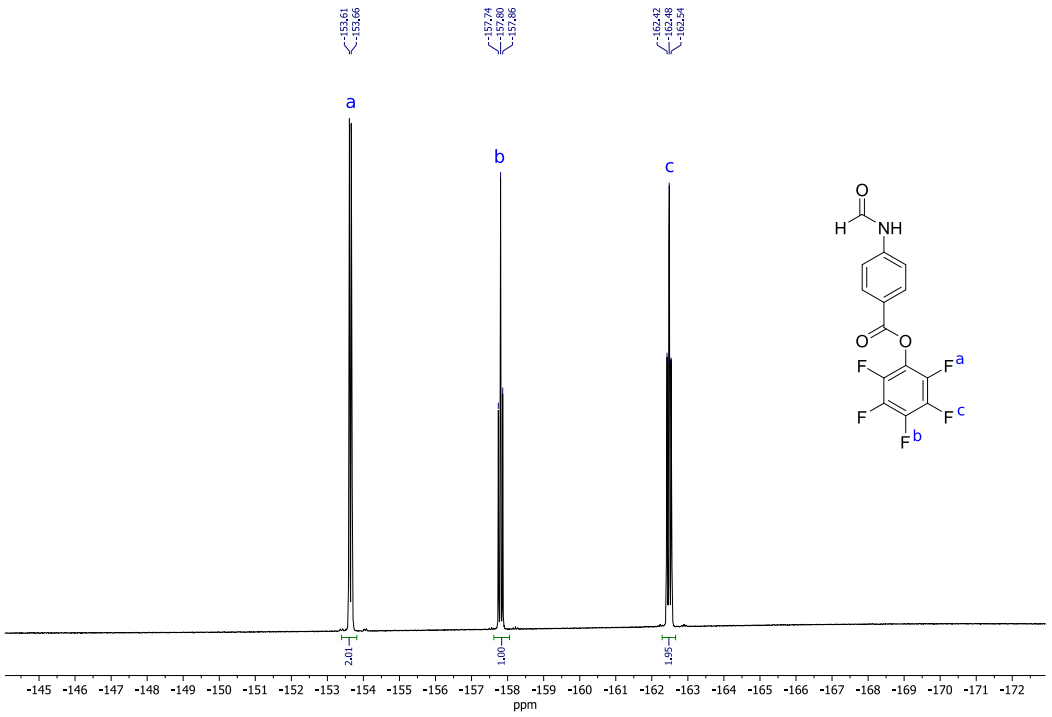

Figure 7.43. ^{19}F NMR of pentafluorophenyl 4-formamidobenzoate in $(CD_3)_2SO$ (377 MHz, 298 K)

7.4.1.3. Pentafluorophenyl 4-isocyanobenzoate (FAIC) synthesis

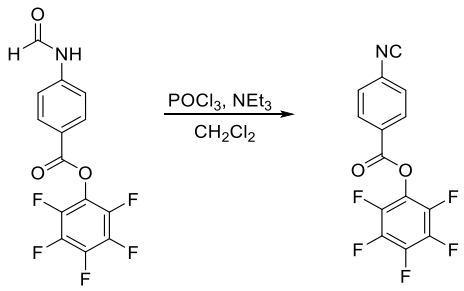

Scheme 7.16. Pentafluorophenyl 4-isocyanobenzoate (FAIC) synthesis.

A 100 mL Schlenk flask (dried in the oven and under N_2) was charged with pentafluorophenyl 4-formamidobenzoate (2.0 g, 5.9 mmol, 1.0 equiv.), NEt_3 (4 mL, 28 mmol, 4.8 equiv.) and CH_2Cl_2 (dry, 50 mL). The solution was cooled down to 0 °C in an ice bath, then $POCl_3$ (0.80 mL, 8.6 mmol, 1.4 equiv.) was added dropwise with a syringe over 15 min. The reaction was stirred at 0 °C for 1 h before cold Na_2CO_3 (sat. 100 mL) was added to the solution. The reaction mixture was stirred for 10 min before the two phases were separated and the aqueous phase was extracted with Et_2O (3 × 100 mL). The combined

Et_2O extracts were dried over $MgSO_4$ and filtered. The filtrate was concentrated *in vacuo* and purified by flash chromatography (CH_2Cl_2), which yielded an off-white solid (1.5 g, 78%). ^{1}H NMR (400 MHz, $CDCl_3$): δ (ppm) 8.26 (d, $^3J_{H\text{-}H}$ = 8.8 Hz, 2H, C≡NCC*H*, aromatic), 7.56 (d, $^3J_{H\text{-}H}$ = 8.8 Hz, 2H, O=CCC*H*, aromatic). ^{13}C NMR (100 MHz, $CDCl_3$): δ (ppm) 168.7 (*C*(O)O), 161.1 (*C*≡N, isocyanide), 142.4 (*C*N≡C, aromatic), 139.9 (*C*O, aromatic), 139.3 (*C*F, aromatic), 138.6 (*C*F, aromatic), 136.7 (*C*F, aromatic), 132.0 (*C*H, aromatic), 127.7 (*C*CO, aromatic), 127.0 (*C*H, aromatic). ^{19}F NMR (377 MHz, $CDCl_3$): δ (ppm)-152.4 (d, 2F, Ar–*F*), -157.0 (t, 1F, C*F*), -161.8 (t, 2F, C*F*). FT-IR (neat): 2120 (C≡N stretch), 1751 (C=O stretch), 1598 (C=C stretch, benzoate), 1509 (C=C stretch, PFP), 1248 (C-O stretch), 1054 (C-F stretch) cm^{-1}. Characterisation was consistent with that reported previously.[5]

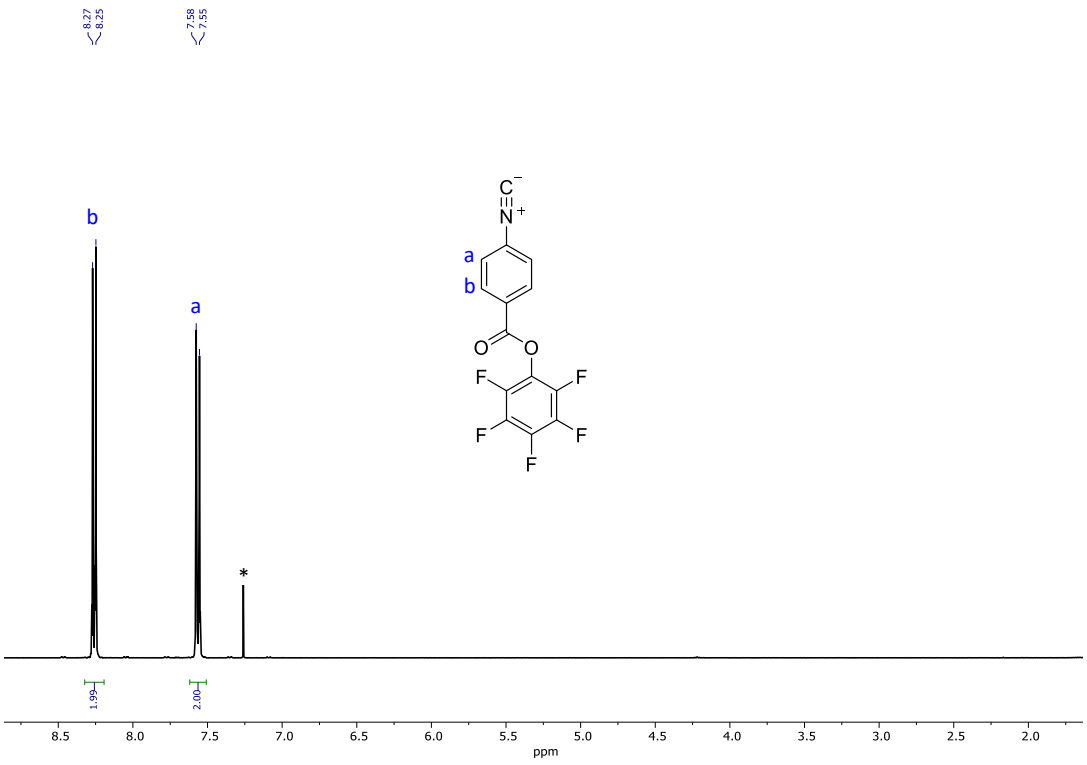

Figure 7.44. ^{1}H NMR of FAIC in $CDCl_3$ (400 MHz, 298 K)

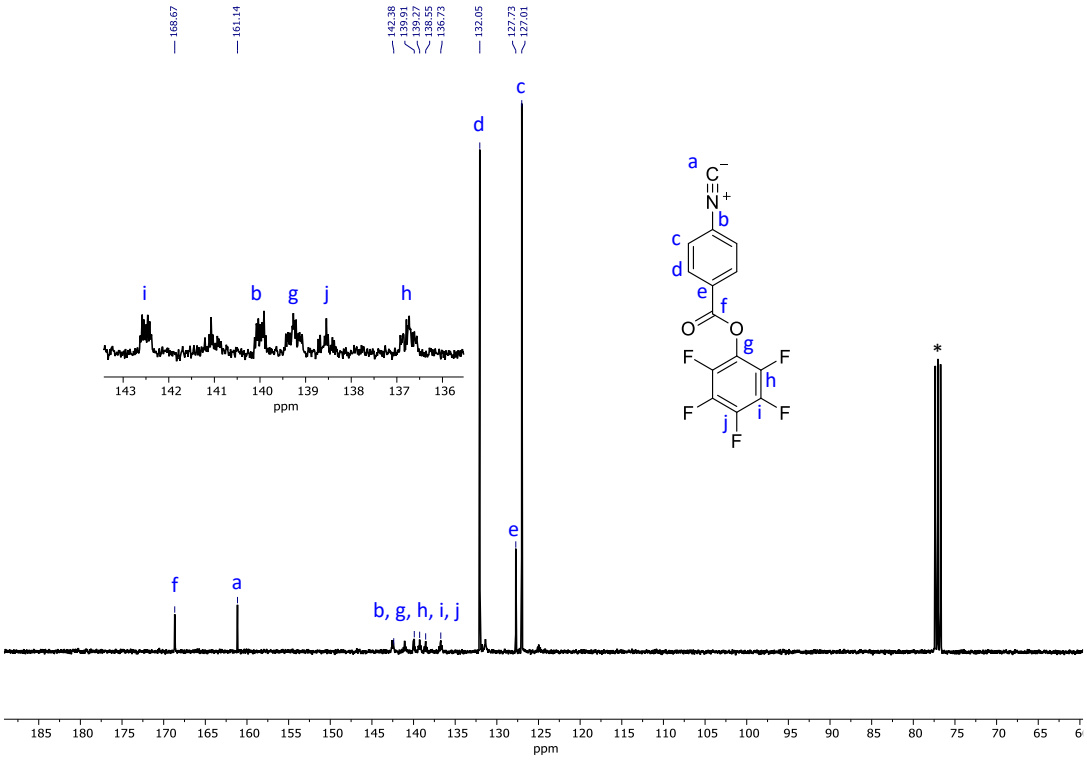

Figure 7.45. ^{13}C NMR of FAIC in $CDCl_3$ (100 MHz, 298 K)

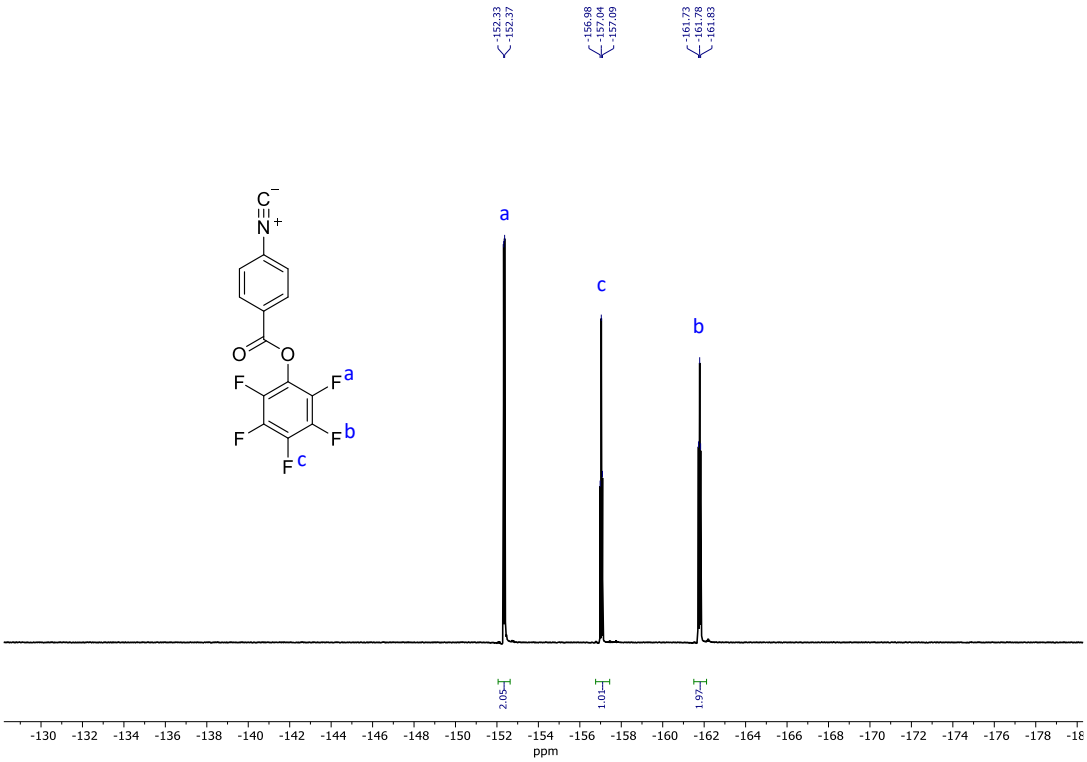

Figure 7.46. ^{19}F NMR of FAIC in $CDCl_3$ (377 MHz, 298 K)

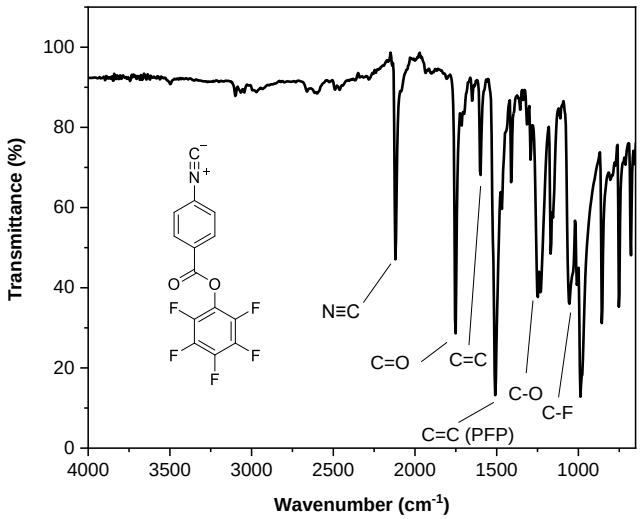

Figure 7.47. FT-IR spectrum of FAIC.

7.4.2. Aminochloridemaleimide dye (ACM) synthesis

The maleimide dye was synthesised in accordance with the literature methodology.[6]

7.4.2.1. 3,4-Dichloro-1-methyl-1H-pyrrole-2,5-dione synthesis

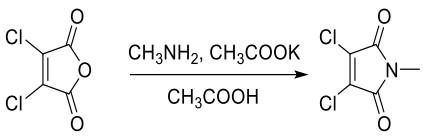

Scheme 7.17. 3,4-dichloro-1-methyl-1H-pyrrole-2,5-dione synthesis.

In a 50 mL round-bottom flask, 3,4-dichloromaleic anhydride (1.0 g, 6.0 mmol, 1.0 equiv.), methylamine hydrochloride (0.60 g, 9.0 mmol, 1.5 equiv.), and potassium acetate (1.2 g, 9.0 mmol, 1.5 equiv.) were added to a solution of acetic acid (10 ml). The reaction mixture was stirred for 4 h under reflux (120 °C). The solution turned yellow and was cooled to 25-30 °C before it was slowly poured into a cold sodium bicarbonate solution (1 M, 50 mL) until no effervescence was observed. The suspension was stirred for 1 h then, the solids were filtered, washed with n-hexane (2 × 30 mL) and dried *in vacuo* to obtain the product (0.732 g, 68%). The product was employed as obtained, without further purification, in the next step.

7.4.2.2. Boc-protected maleimide dye synthesis

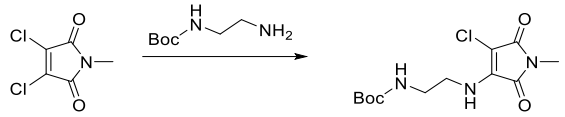

Scheme 7.18. Boc-protected maleimide dye synthesis.

2,3-chloromethylmaleimide (1.0 equiv.), sodium carbonate (2.5 equiv.) and *N*-Boc-ethylenediamine (1.1 equiv.) were mixed in THF (20 mL). Consumption of 2,3-chloromethylmaleimide was monitored by TLC, and was complete within 30 min. The solvent was then evaporated *in vacuo* and the residue was dissolved in CH_2Cl_2 (150 mL). The solution was washed with water (2 × 150 mL), dried with Na_2SO_4 and purified *via* column chromatography on silica gel (petroleum ether/ethyl acetate 4:1 v/v) which yielded the product as a yellow solid (47%). ^{1}H NMR (400 MHz, CD_3OD): δ (ppm) 3.66 (t, $^3J_{H\text{-}H}$ = 5.8 Hz, 2H, H_2CNHC(O)O), 3.29 (t, $^3J_{H\text{-}H}$ = 5.8 Hz, 2H, H_2CNHC), 2.95 (s, 3H, NCH_3), 1.44 (s, 9H, C(CH_3)$_3$). ^{13}C NMR (100 MHz, CD_3OD): δ (ppm) 42.6 (H_2CNHC(O)O), 40.5 (H_2CNHC), 27.3 (C(CH$_3$)$_3$), 22.7 (NCH$_3$). HRMS: *m/z* $[C_{12}H_{18}ClN_3O_4+Na]^+$ calc. 326.0883 g·mol^{-1}, exp. 326.0887 g·mol^{-1}.

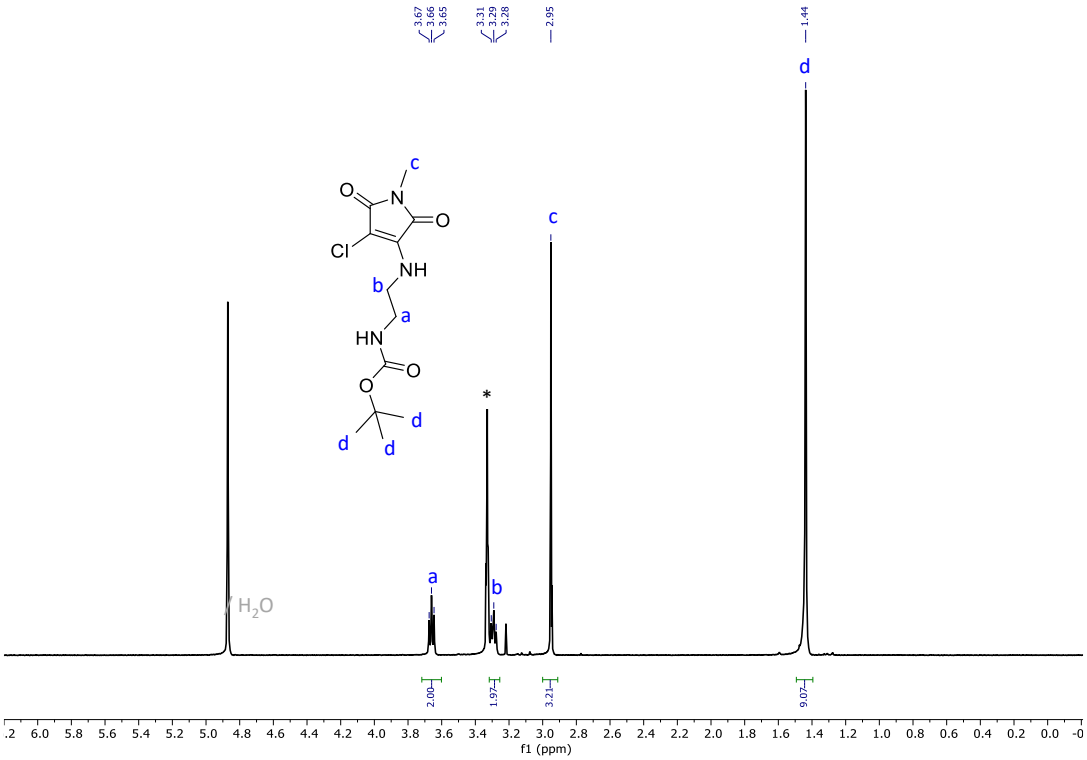

Figure 7.48. ^{1}H NMR of the Boc-protected maleimide dye in CD_3OD (400 MHz, 298 K)

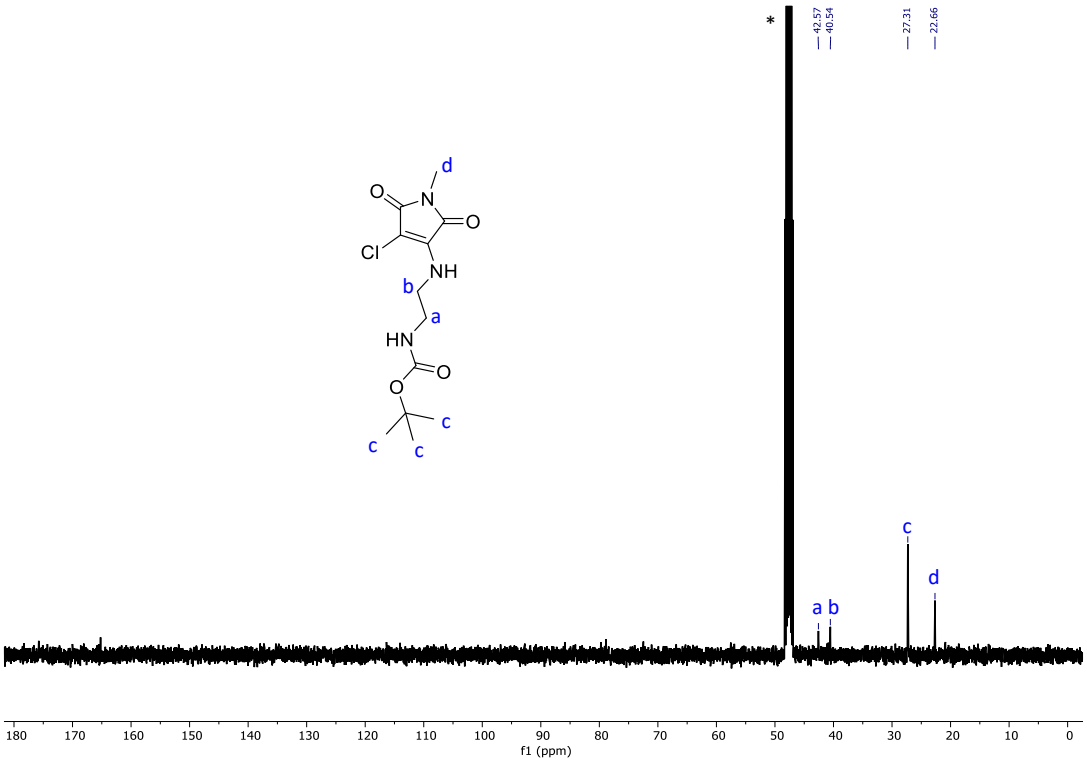

Figure 7.49. ^{13}C NMR of the Boc-protected maleimide dye in CD_3OD (100 MHz, 298 K)

7.4.2.3. Aminochloridemaleimide dye (ACM) synthesis

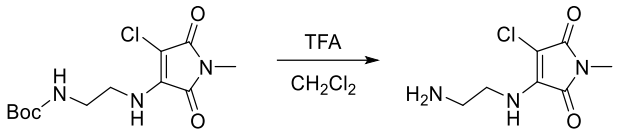

Scheme 7.19. Aminochloridemaleimide dye synthesis.

The Boc-protected maleimide dye was reacted for 2 h in a DCM/TFA (10:1 v/v) solution at room temperature before the rection mixture was dried *in vacuo*. The crude product was purified *via* column chromatography on silica gel (petroleum ether/ethyl acetate 1:2 v/v) which yielded the product as a yellow solid (86%). ^{1}H NMR (400 MHz, CD_3OD): δ (ppm) 3.90 (t, $^{3}J_{H\text{-}H}$ = 6.1 Hz. 2H, H_2NCH_2), 3.21 (t, $^{3}J_{H\text{-}H}$ = 6.1 Hz, 2H, $HNCH_2$), 2.97 (s, 3H, CH_3). ^{13}C NMR (100 MHz, CD_3OD): δ (ppm) 167.9 ($ClCC{=}O$), 165.1 ($HNCC{=}O$), 141.4 (CNH), 118.3 (CCl), 39.8 (H_2NCH_2), 39.7 ($HNCH_2$), 22.7 (NCH_3). HRMS: *m/z* $[C_7H_{10}ClN_3O_2{+}H]^{+}$ calc. 204.0540 g·mol^{-1}, exp. 7204.0535 g·mol^{-1}.

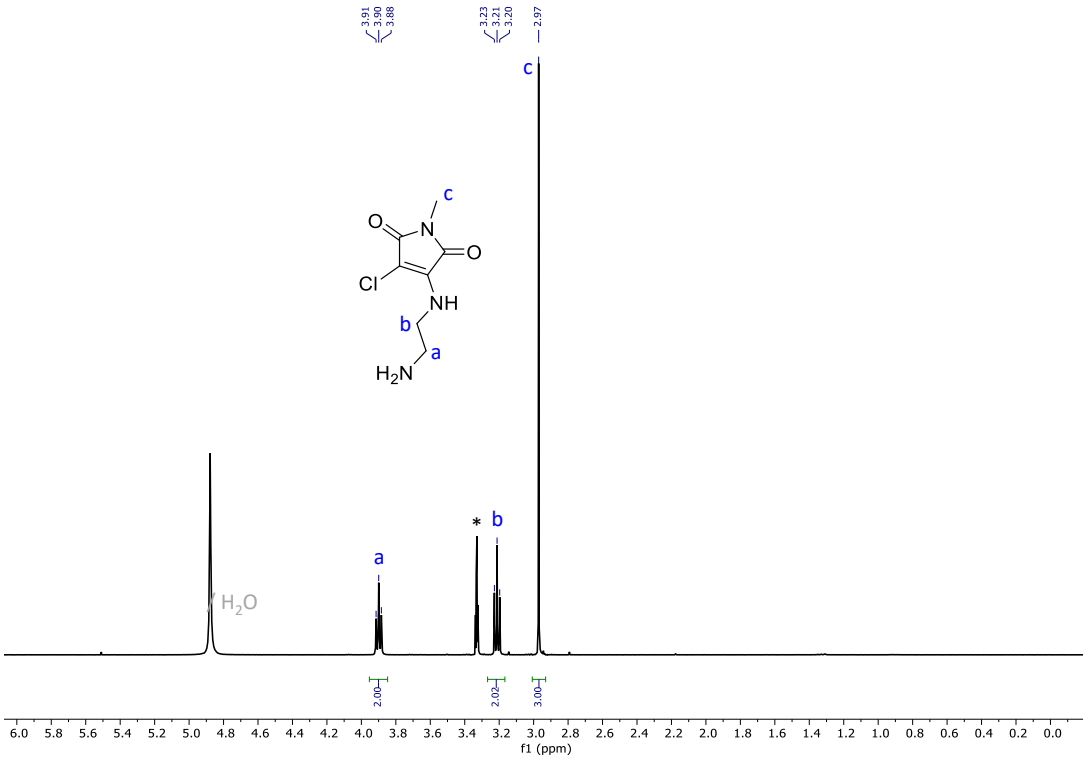

Figure 7.50. ^{1}H NMR of the maleimide dye in CD_3OD (400 MHz, 298 K)

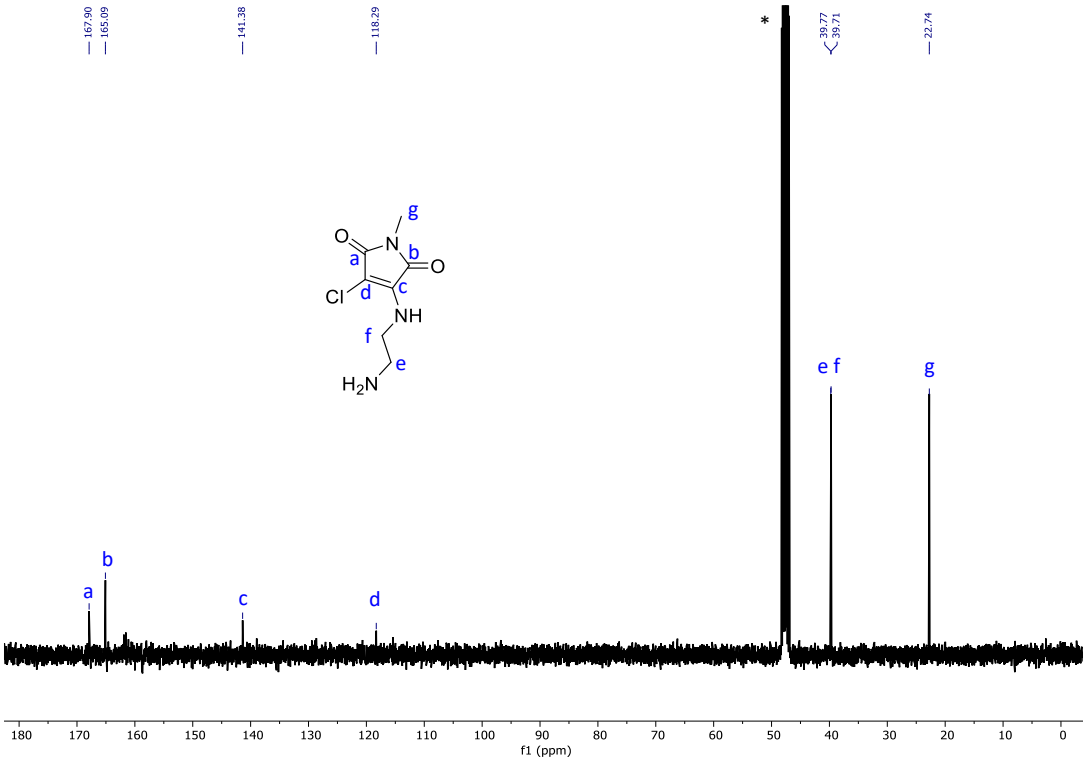

Figure 7.51. ^{13}C NMR of the maleimide dye in CD_3OD (100 MHz, 298 K)

7.4.3. General procedure for the copolymerisation of P(MAIC)$_x$-*co*-P(FAIC)$_y$ copolymers.

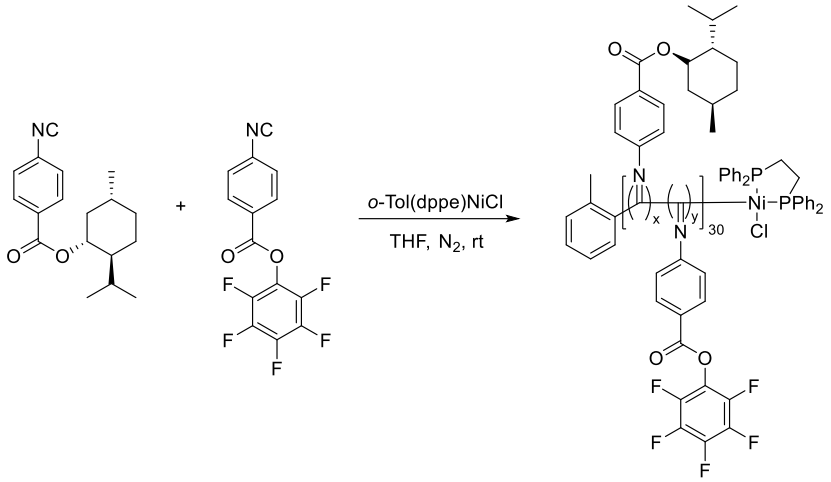

Scheme 7.20. Copolymerisation of P(MAIC)$_x$-co-P(FAIC)$_y$ copolymers catalysed by *o*-Tol(dppe)NiCl in THF.

In a 7 mL vial, under inert atmosphere, a solution of the MAIC and FAIC monomers in THF (0.5 mL) was added to the *o*-tol(dppe)NiCl catalyst in THF and stirred for 2 min before it was opened to atmosphere. The resulting copolymer was precipitated in MeOH three times before analysis.

Table 7.2. Quantities used for the copolymerisation of MAIC and FAIC.

FAIC (%)	MAIC (mg)	FAIC (mg)	*o*-Tol(dppe)NiCl (µL)[a]
0%	25.0	-	99.5
10%	22.0	2.7	97.3
20%	19.5	5.4	97.0
30%	17.0	8.2	96.7
40%	14.5	10.8	96.2
50%	11.6	13.0	92.3
60%	9.2	15.5	91.7
70%	6.9	18.0	91.3
80%	4.6	20.5	91.0
90%	2.2	22.5	88.8
100%	-	25.0	88.8

[a] 17.5 mg·mL^{-1} of catalyst in THF

7.4.4. General procedure for the NiCCo-PISA copolymerisation of P(PAIC)$_x$-*b*-(P(MAIC)$_y$-*co*-P(FAIC)$_z$)

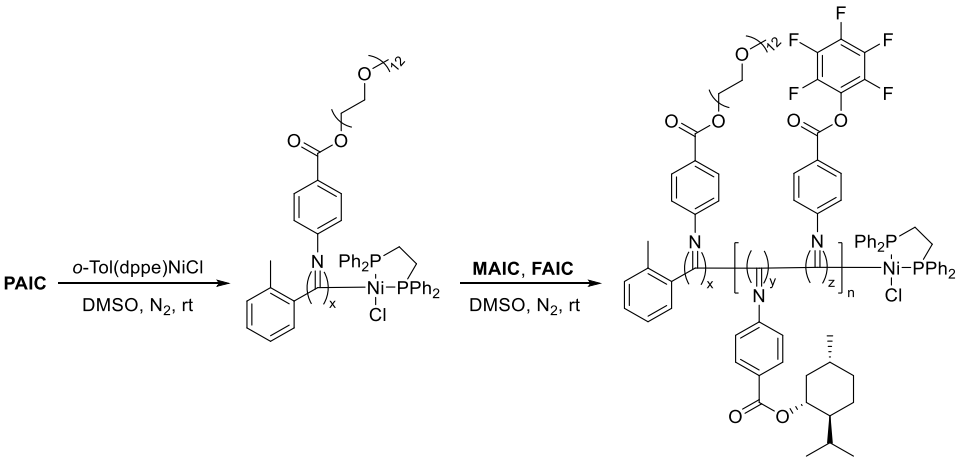

Scheme 7.21. NiCCo-PISA copolymerisation of P(PAIC)$_x$-*b*-(P(MAIC)$_y$-*co*-P(FAIC)$_z$) catalysed by *o*-Tol(dppe)NiCl in DMSO.,

In a 7 mL vial, under inert atmosphere, the PAIC monomer was added to the *o*-tol(dppe)NiCl catalyst (120 µL, 17.5 mg·mL^{-1} in DMSO) and stirred for 2 min. A solution of the MAIC and FAIC monomers in DMSO was added to

the reaction mixture and stirred for 2 min before it was opened to atmosphere. The final concentration of the reaction mixture was 50 mg·mL^{-1}.

Table 7.3. Quantities used for the copolymerisation of D0%, D20%, D50% and D100%.

Copolymer	PAIC (mg)	MAIC (mg)	FAIC (mg)	DMSO (mL)
D0%	59	30	-	1.8
D20%	59	24	7	1.8
D50%	59	15	17	1.9
D100%	59	-	34	1.8

7.4.5. General procedure for the post-polymerisation reaction

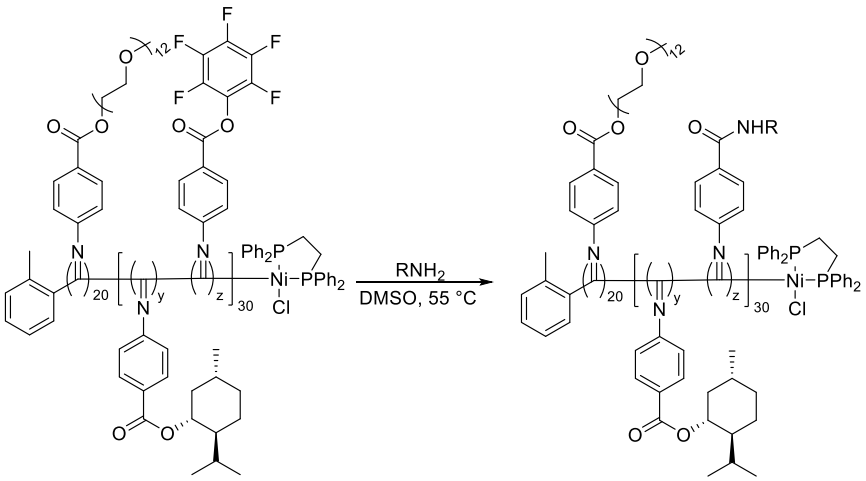

Scheme 7.22. Post-polymerisation reaction of PFP copolymers with amine nucleophiles.

In a 7 mL vial, a solution of the NiCCo-PISA nano-objects was diluted with DMSO to 10 mg·mL^{-1} and the nucleophile was added (5.0 equiv.). The reaction mixture was stirred for 24 h before analysis by DLS. The resulting solution was dialysed against water (6-8 kDa cut-off) then, freeze-dried and precipitated in hexane from THF. The resulting copolymer was analysed by FT-IR spectroscopy then, dissolved in THF or $CDCl_3$ for CD and NMR spectroscopy respectively.

7.5. Experimental protocols for Chapter 4

7.5.1. 2-[1-(2-Amino-ethoxy)-1-methyl-ethoxy]-ethylamine (AEE) synthesis

AEE was prepared in accordance with previously reported synthetic methods.[7]

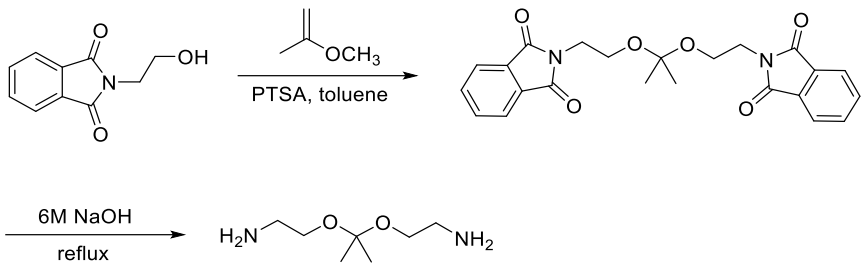

Scheme 7.23. 2-[1-(2-Amino-ethoxy)-1-methyl-ethoxy]-ethylamine synthesis

In a 500 round-bottom flask, *N*-(2-hydroxyethyl)-phthalimide (12 g, 65 mmol, 1.0 equiv.) was dissolved in dry benzene (200 mL). After the solution was cooled to 0 °C, 2-methoxy propene (6.5 mL, 68 mmol, 1.1 equiv.) and *p*-toluenesulfonic acid (120 mg, 0.010 equiv.) were carefully added to the solution. The reaction mixture was then stirred for 1 h at 0 °C. Then, the solution was dried *in vacuo* before acetic anhydride (7.5 mL) and Et_3N (15 mL) were added to the residue and the resulting suspension was stirred overnight. The crude product was precipitated in hexane (50 mL) before recrystallisation in ethyl acetate (200 mL) twice which gave the product as a yellow solid.

In a 100 mL round bottom flask, 2,2'-((propane-2,2-diylbis(oxy))bis(ethane-2,1-diyl))bis(isoindoline-1,3-dione) was solubilised in NaOH (6 M, 50 mL) and heated at reflux overnight. The reaction mixture was extracted with $CHCl_3$/*i*-PrOH (1/1, v/v, 3 × 50 mL), the combined organic layers were dried on $MgSO_4$, filtered and concentrated *in vacuo*. The crude product was washed with hexane which yielded the product as a yellow oil. ^{1}H NMR (400 MHz, $CDCl_3$): δ (ppm) 3.46 (t, $^3J_{H\text{-}H}$ = 5.4 Hz, 4H, CH_2NH$_2$), 2.84 (t, $^3J_{H\text{-}H}$ = 5.3 Hz, 4H, OCH_2), 1.70 (bs, 4H, NH_2), 1.37 (s, 6H, CH_3). ^{13}C NMR (100 MHz,

$CDCl_3$): δ (ppm) 99.6 (O*C*O), 62.7 (O*C*H_2), 42.0 (*C*H_2NH_2), 24.8 (*C*H_3). Characterisation was consistent with that reported previously.[7]

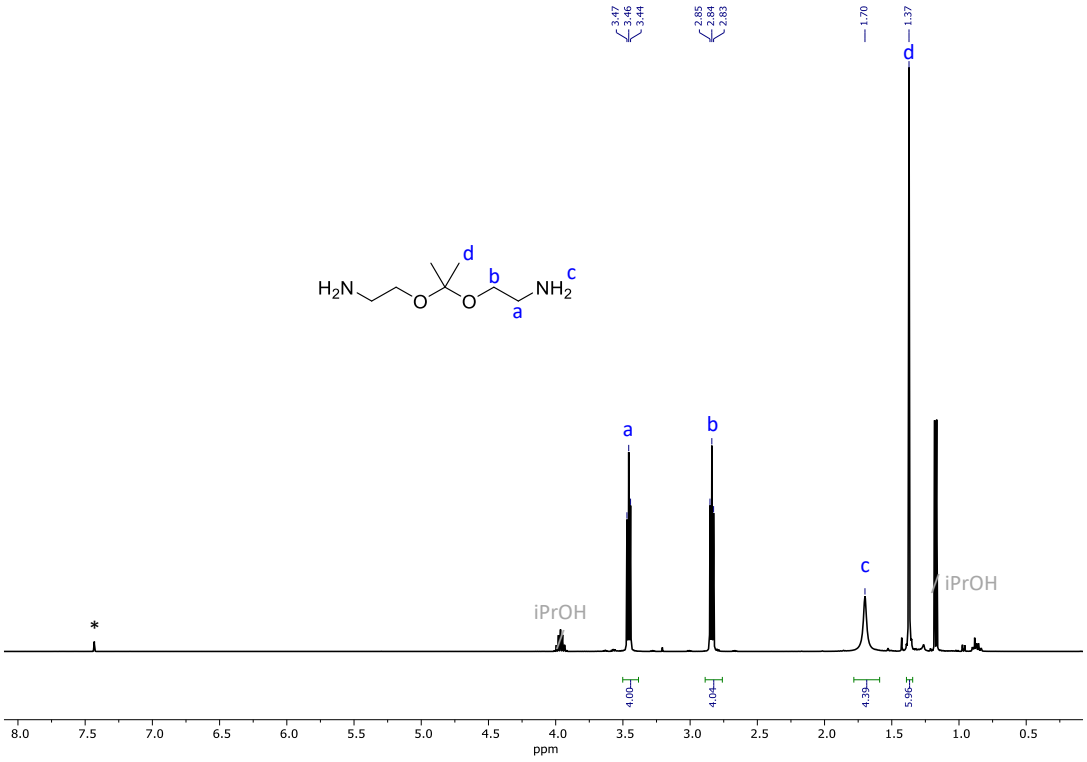

Figure 7.52. ^{1}H NMR of AEE in $CDCl_3$ (400 MHz, 298 K)

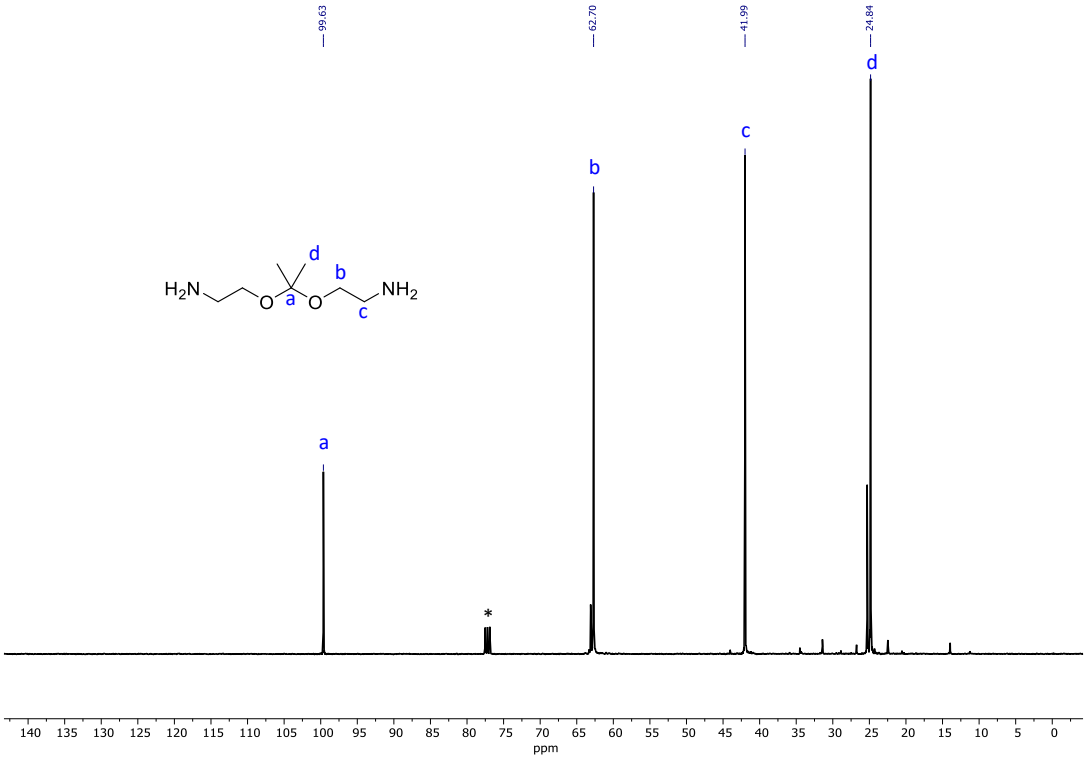

Figure 7.53. ^{13}C NMR of AEE in $CDCl_3$ (100 MHz, 298 K)

7.5.2. General procedure for the post-polymerisation cross-linking of the NiCCo-PISA micelles

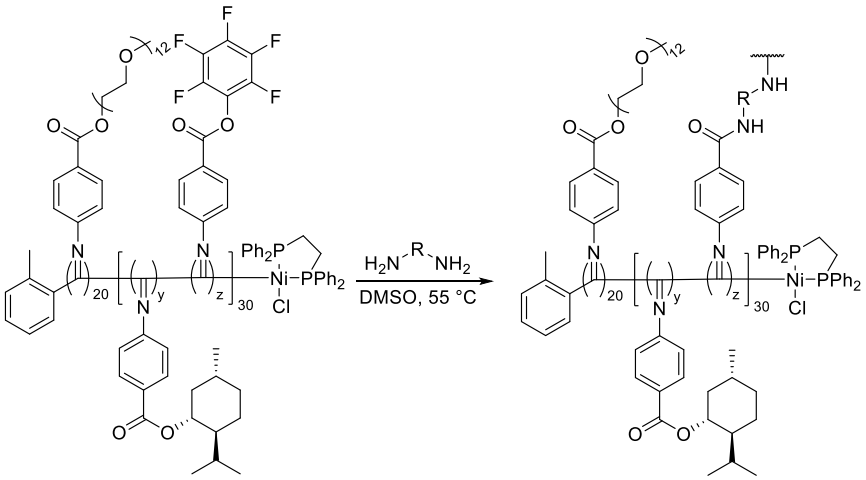

Scheme 7.24. Post-polymerisation cross-linking of the NiCCo-PISA micelles with diamine nucleophiles.

In a 7 mL vial, a solution of the NiCCo-PISA nano-objects was diluted with DMSO to 10 mg·mL^{-1} and the nucleophile was added (0.60 equiv.). The reaction mixture was stirred for 72 h at 55 °C. The resulting solution was analysed by DLS then, dialysed against water (6-8 kDa cut-off) before analysis by DLS. The solution was freeze-dried and precipitated in hexane from THF before analysis by FT-IR spectroscopy then, dissolved in THF for CD spectroscopy.

7.5.3. General procedure for the monitoring of the cross-linked particles responsiveness

A solution that contained 0.20 mg·mL^{-1-} of particles in water or THF was treated with GSH or HCl to obtain the desired concentration. The evolution of the nanostructures' size was monitored by DLS.

7.6. Experimental protocols for Chapter 5

7.6.1. $C_6H_9Pd(PEt_3)_2Cl$ (Palladium catalyst) synthesis

Compound $C_6H_9Pd(PEt_3)_2Cl$ was prepared in accordance with previously reported synthetic methods.[8]

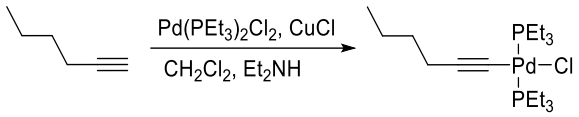

Scheme 7.25. $C_6H_9Pd(PEt_3)_2Cl$ (Palladium catalyst) synthesis.

A 250 mL Schlenk flask (dried in the oven and under N_2) was charged with $Pd(PEt_3)_2Cl_2$ (200 mg, 490 µmol, 1.0 equiv.), CuCl (6.9 mg, 70 µmol, 0.14 equiv.) in a solution of diethylamine (40 mL) and CH_2Cl_2 (dry, 10 mL). Hex-1-yne (60 µL, 520 µmol, 1.1 equiv.) was added slowly with a syringe and the reaction mixture was stirred at r.t. for 3 h. The solution colour changes from green to purple. The reaction mixture was concentrated *in vacuo* and the residue was purified by column chromatography (CH_2Cl_2) which yielded the product as an orange oil (160 mg, 71%). ^{1}H NMR (400 MHz, $CDCl_3$): δ (ppm) 2.23 (t, $^3J_{H\text{-}H}$ = 12.0, 2H, C≡CCH_2), 1.95-1.88 (m, 12H, PCH_2CH$_3$), 1.42-1.38 (m, 4H, CH_2CH_2CH$_3$), 1.16 (p, $^3J_{H\text{-}H}$ = 11.0 Hz, 18H, PCH$_2$CH_3), 0.88 (t, $^3J_{H\text{-}H}$ = 12.0 Hz, 3H, CH_3). ^{13}C NMR (100 MHz, $CDCl_3$): δ (ppm) 105.1 (Pd-*C*≡C), 77.8 (Pd-C≡*C*), 32.4 (*C*H$_2$CH$_2$CH$_3$), 22.1 (CH$_2$*C*H$_2$CH$_3$), 21.0 (C≡C*C*H$_2$), 15.3 (t, P*C*H$_2$CH$_3$), 13.7 (CH$_2$CH$_2$*C*H$_3$), 8.3 (P*C*H$_2$CH$_3$). Characterisation was consistent with that reported previously.[8]

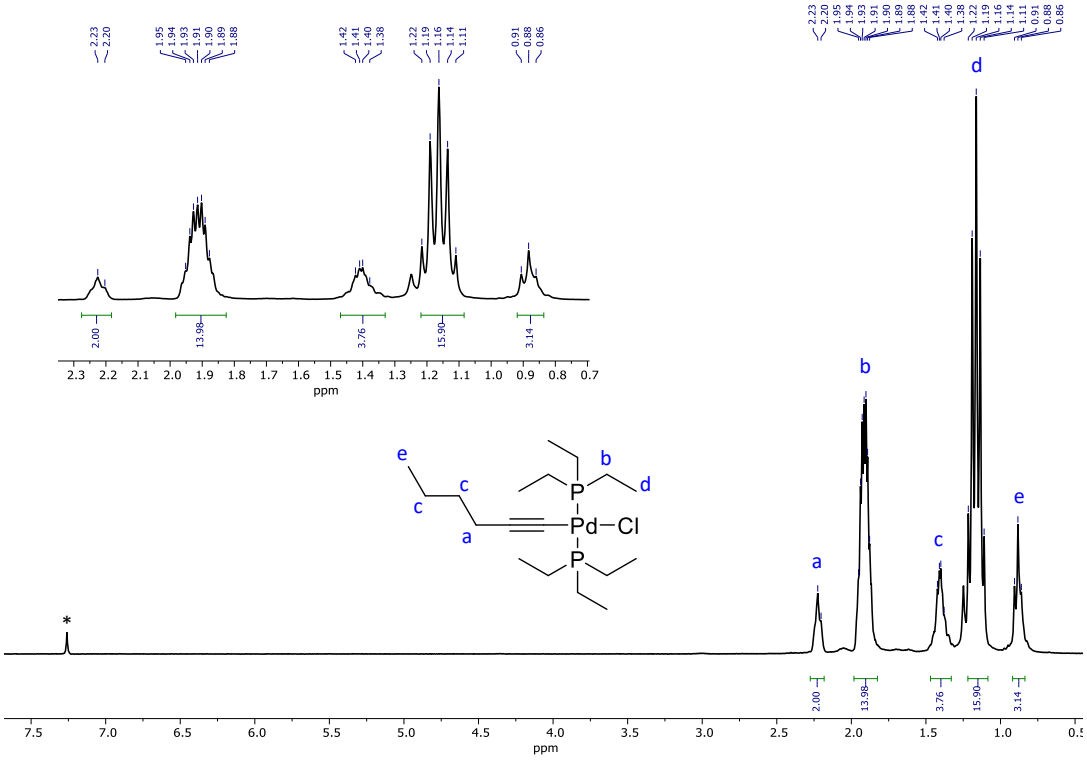

Figure 7.54. ^{1}H NMR spectrum of $C_6H_9Pd(PEt_3)_2Cl$ in $CDCl_3$ (400 MHz, 298 K).

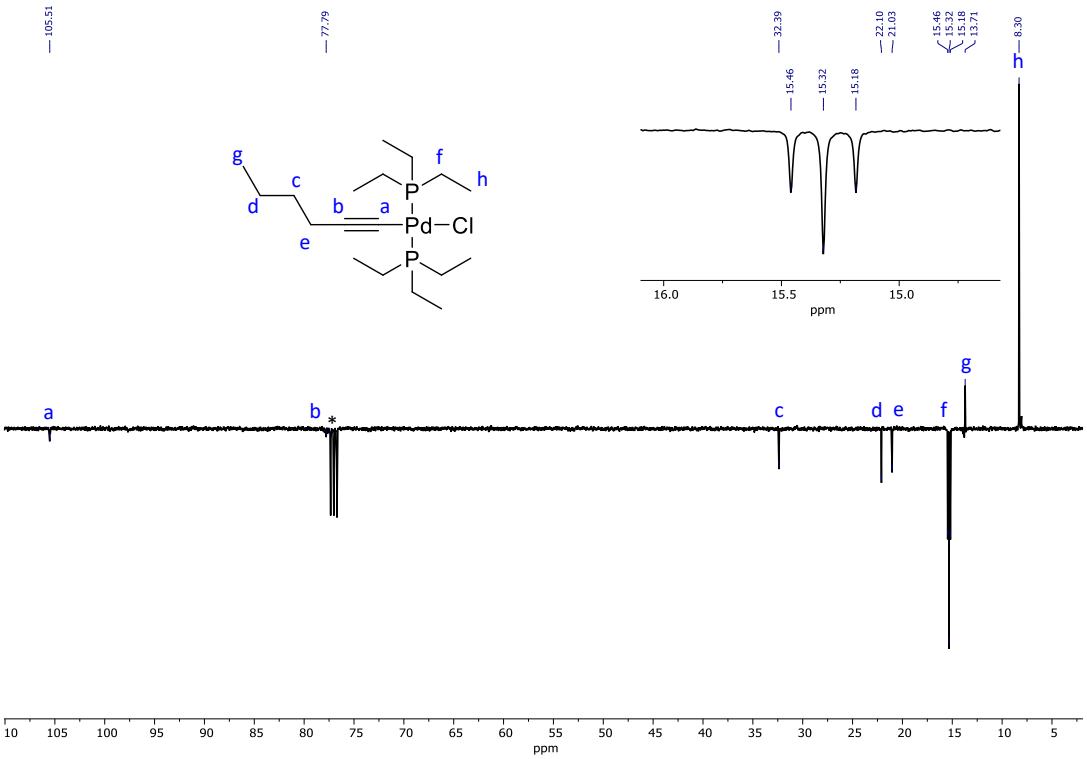

Figure 7.55. ^{13}C NMR spectrum of $C_6H_9Pd(PEt_3)_2Cl$ in $CDCl_3$ (100 MHz, 298 K).

7.6.2. General procedure for the copolymerisations with palladium catalyst

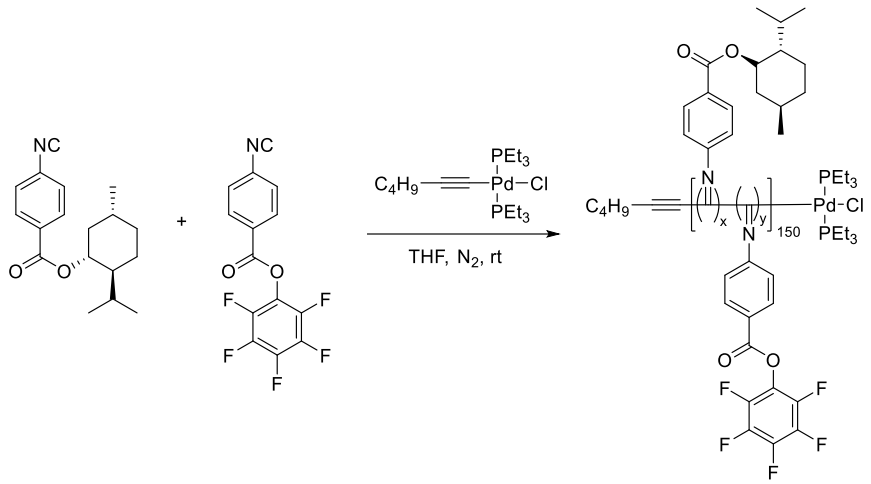

Scheme 7.26. Copolymerisation of $P(MAIC)_x$-co-$P(FAIC)_y$ copolymers catalysed by palladium catalyst in THF.

An ampoule (dried in the oven and under N_2) was charged with MAIC (280 mg, 840 µmol, 120 equiv.) and FAIC (66 mg, 270 µmol, 30 equiv.) in THF (dry, 9.6 mL). A solution of the catalyst $C_6H_9Pd(PEt_3)_2Cl$ (3.2 mg, 7.0 µmol, 1.0 equiv.) in THF (dry, 0.20 mL) was added. The reaction mixture was stirred at 55 °C overnight. The resulting solution was precipitated three times in MeOH which yielded the copolymer as an orange solid (280 mg, 80%).

7.6.3. General procedure for the self-assembly of block copolymers *via* solvent exchange

In a 20 mL vial, the copolymer (50 mg) was dissolved in THF (0.50 mL) before water (5.0 mL) was added with a syringe pump at 0.6 $mL \cdot h^{-1}$ under strong stirring. The resulting suspension was purified by dialysis against water (12-14 kDa cut-off) for 3 days.

7.6.4. 2-(Methyl(pyridin-4-yl)amino)ethan-1-ol (DMAP-OH) synthesis

DMAP-OH was synthesised in accordance with the literature methodology.[9]

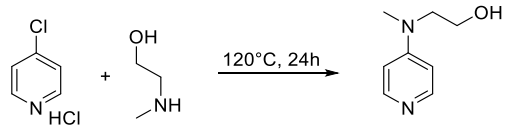

Scheme 7.27. 2-(Methyl(pyridin-4-yl)amino)ethan-1-ol synthesis.

In 100 mL three-necked round-bottom flask, 4-chloropyridine (5.0 g, 33 mmol) was dissolved in 2-(methylamino)ethanol (35 mL). The colour of the solution changed from colourless to red then yellow. The reaction mixture was heated at 120 °C for 24 h before the solvent was removed *in vacuo*. NaOH (1 M, 50mL) and CH_2Cl_2 (40 mL) were added to the yellow oil residue and the mixture was stirred overnight. The aqueous phase was separated and extracted with CH_2Cl_2 (2 × 50 mL). The combined organic phased were dried on $MgSO_4$ and filtrated before concentration *in vacuo* which gave the product as an off-white solid (3.6 g, 70%). ^{1}H NMR (300 MHz, $CDCl_3$): δ (ppm) 8.07 (d, $^3J_{H\text{-}H}$ = 5.6, 2H, NC*H*, aromatic), 6.47 (d, $^3J_{H\text{-}H}$ = 5.6, 2H, NCC*H*, aromatic), 3.80 (t, $^3J_{H\text{-}H}$ = 5.7, 2H, NCH_2), 3.51 (t, $^3J_{H\text{-}H}$ = 5.7, 2H, CH_2–OH), 3.02 (s, 3H, CH_3). ^{13}C NMR (100 MHz, $CDCl_3$): δ (ppm) 154.0 (*C*NCH_3, aromatic), 149.4 (N*C*HCH, aromatic), 106.8 (NCH*C*H, aromatic), 59.5 (N*C*H_2), 53.8(*C*H_2OH), 38.4 (N*C*H_3). Characterisation was consistent with that reported previously.[9]

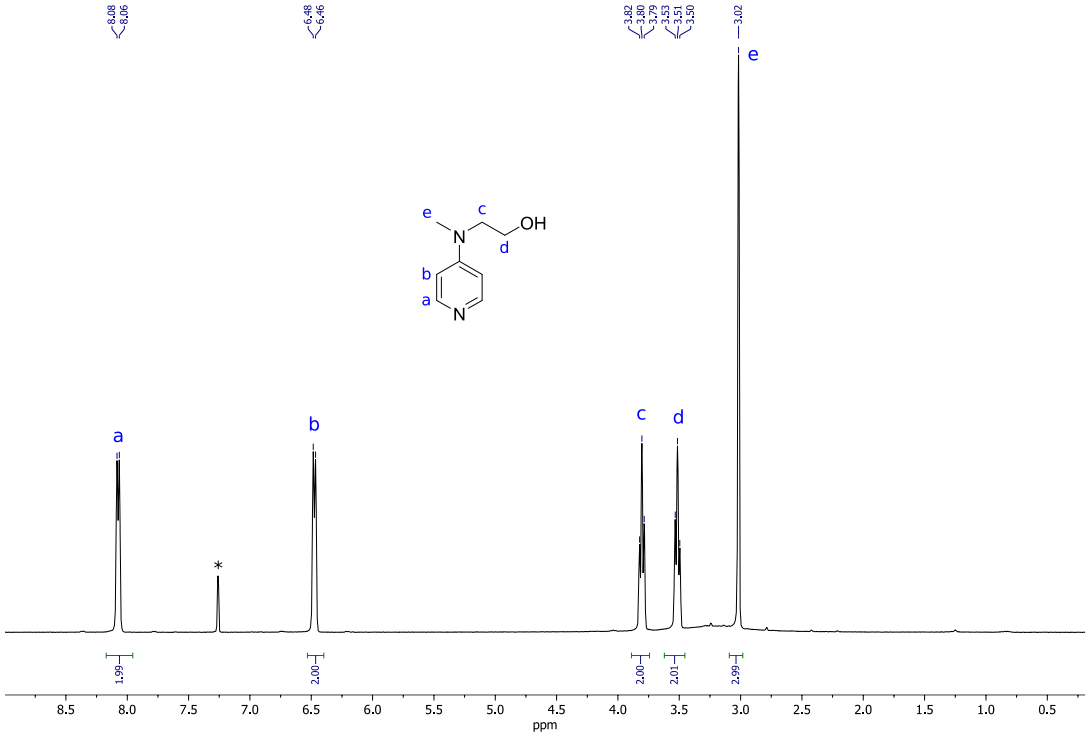

Figure 7.56. ^{1}H NMR of DMAP-OH in $CDCl_3$ (300 MHz, 298 K)

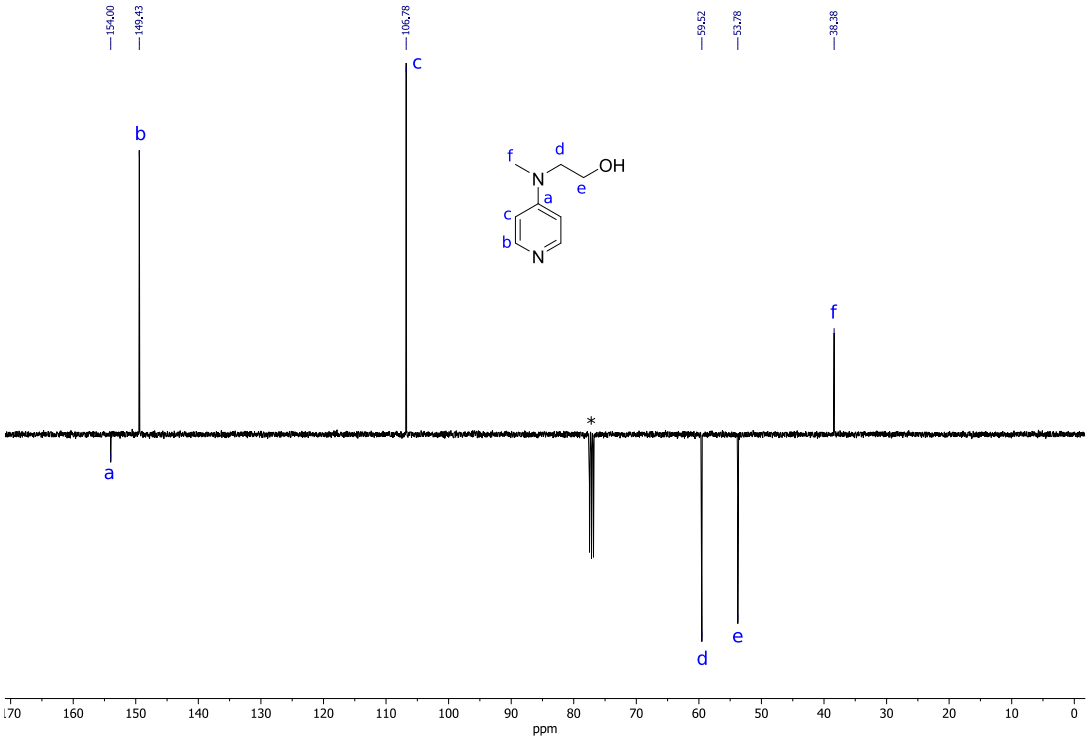

Figure 7.57. ^{13}C NMR of DMAP-OH in $CDCl_3$ (100 MHz, 298 K)

7.6.5. 2,2'-(Pyridin-4-ylazanediyl)bis(ethan-1-ol) ($DMAP(OH)_2$) synthesis

$DMAP(OH)_2$ was synthesised with a methodology modified from the literature.[10]

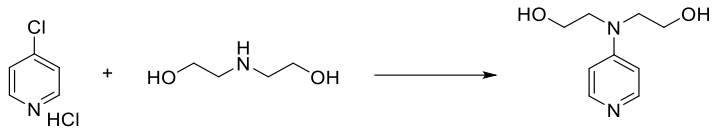

Scheme 7.28. 2,2'-(Pyridin-4-ylazanediyl)bis(ethan-1-ol) synthesis.

In an ampoule, 4-chloropyridine (3.2 g, 21 mmol, 1.0 equiv.) was dissolved in 2,2'-aminodiethanol (10 mL, 105 mmol, 5.0 equiv.). The colour of the solution changed from colourless to bright red. The reaction mixture was heated at 180 °C for 24 h before it was poured in a suspension of Na_2CO_3 (30 g) in *i*-PrOH (150 mL) and stirred for 30 minutes under reflux conditions (90 °C). After the reaction mixture cooled down to r.t., it was stored at -25 °C overnight. The suspension was filtered and the filtrate was concentrated *in vacuo*. The residue was distilled by Kugelrohr (230 °C, 0.03 mbar) which gave the crude product as a colourless oil. This was further purified by recrystallisation in cold acetone which yielded the product as colourless crystals (540 mg, 14%). ^{1}H NMR (400 MHz, $(CD_3)_2SO$): δ (ppm) 8.04 (d, $^3J_{H\text{-}H}$ = 6.6, 2H, NC*H*, aromatic), 6.58 (d, $^3J_{H\text{-}H}$ = 6.6, 2H, NCC*H*, aromatic), 4.81 (bs, 1H, O*H*), 3.54 (t, $^3J_{H\text{-}H}$ = 6.1, 2H, NCH_2), 3.44 (t, $^3J_{H\text{-}H}$ = 6.1, 2H, CH_2OH). ^{13}C NMR (100 MHz, $(CD_3)_2SO$): δ (ppm) 152.5 (*C*NCH_2, aromatic), 149.3 (N*C*H, aromatic), 106.5 (NC*C*H, aromatic), 57.9 (N*C*H_2), 52.2 (*C*H_2OH). HRMS: *m/z* $[C_9H_{13}N_2O_2\text{-}H]^-$ calc. 181.0977 g·mol^{-1}, exp. 181.0974 g·mol^{-1}. FT-IR (neat): 3323 (N-H stretch), 2663 (O-H stretch), 1595 (N=C stretch), 1520 (C=C stretch) cm^{-1}.

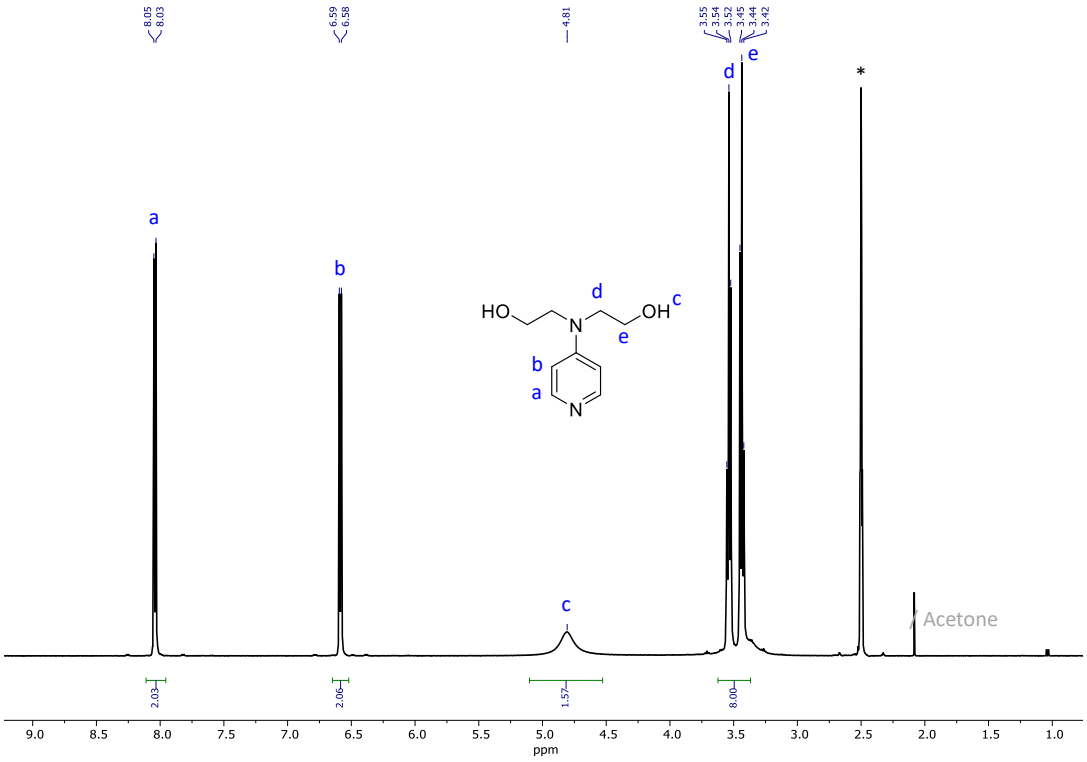

Figure 7.58. ^{1}H NMR of DMAP(OH)$_2$ in (CD$_3$)$_2$SO (400 MHz, 298 K)

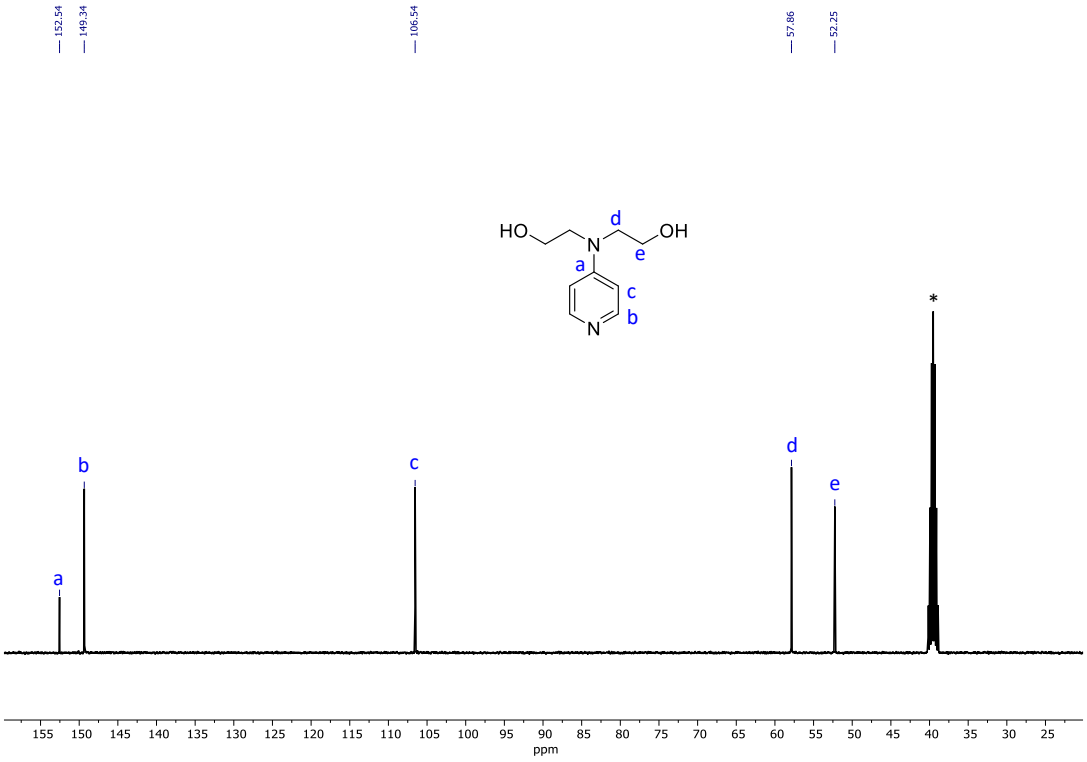

Figure 7.59. ^{13}C NMR of DMAP(OH)$_2$ in (CD$_3$)$_2$SO (100 MHz, 298 K)

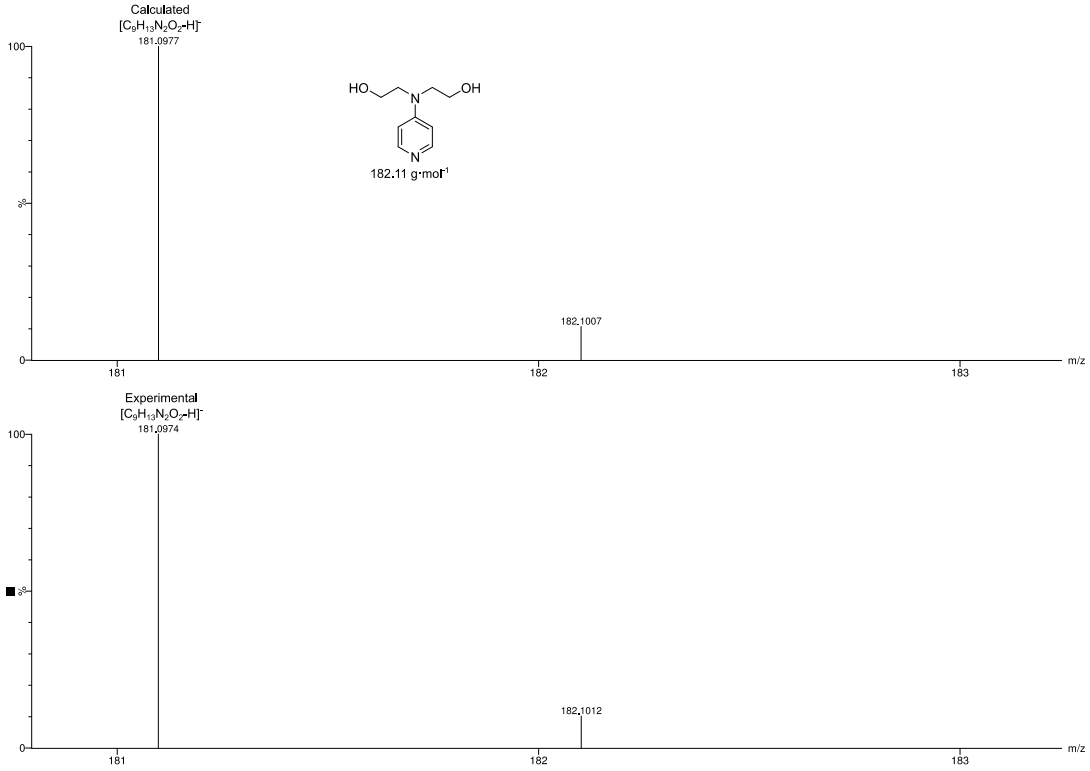

Figure 7.60. Mass spectrum of $DMAP(OH)_2$ collected by ESI-MS. Calculated *vs* experimental *m/z* value for $[DMAP(OH)_2 - H]^-$.

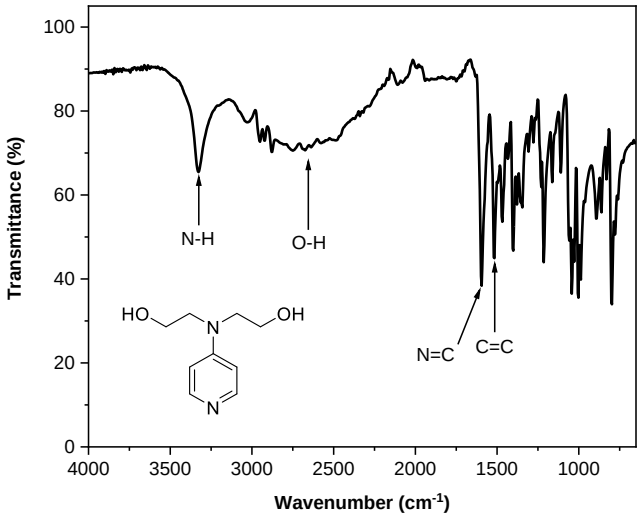

Figure 7.61. FT-IR spectrum of $DMAP(OH)_2$

7.6.6. General procedure for the monitoring of the acylation reactions

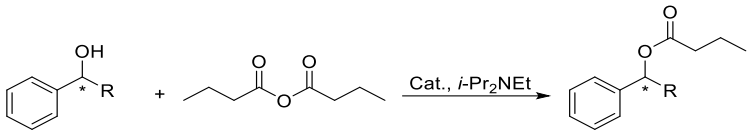

Scheme 7.29. Acylation reaction of phenyl alcohol with butyric acid under basic conditions.

In a 7 mL vial, the alcohol (40 µmol, 1.0 equiv.) was suspended in the solvent (2.0 mL). The catalyst (0.5 mol% or 1 mol%) was added with the *i*-Pr$_2$NEt (10 µL, 60 µmol, 1.5 equiv.), mesitylene (5.6 µL, 40 µmol, 1.0 equiv.) and butyric anhydride (20 µL, 120 µmol, 3.0 equiv.). The reaction was stirred at r.t. and aliquots (0.10 mL) were taken at regular time intervals. The aliquots were diluted in THF (1.0 mL) and filtered through a silica plug to remove the catalyst. The resulting solution was analysed by GC-MS to assess the reaction progress and enantioselectivity.

7.7. References

1. Asaoka, S.; Joza, A.; Minagawa, S.; Song, L.; Suzuki, Y.; Iyoda, T., *ACS Macro Lett.* 2013, 10, 906-911.
2. Standley, E. A.; Smith, S. J.; Müller, P.; Jamison, T. F., *Organometallics* 2014, 8, 2012-2018.
3. Ye, S.; Cheng, S.; Pollit, A. A.; Forbes, M. W.; Seferos, D. S., *J Am Chem Soc* 2020, 25, 11244-11251.
4. Xu, A.; Hu, G.; Hu, Y.; Zhang, X.; Liu, K.; Kuang, G.; Zhang, A., *Chem. - Asian J.* 2013, 9, 2003-2014.
5. Su, M.; Liu, N.; Wang, Q.; Wang, H.; Yin, J.; Wu, Z.-Q., *Macromolecules* 2016, 1, 110-119.
6. Xie, Y.; Husband, J. T.; Torrent-Sucarrat, M.; Yang, H.; Liu, W.; O'Reilly, R. K., *Chem. Commun.* 2018, 27, 3339-3342.
7. Paramonov, S. E.; Bachelder, E. M.; Beaudette, T. T.; Standley, S. M.; Lee, C. C.; Dashe, J.; Fréchet, J. M. J., *Bioconjugate Chem.* 2008, 4, 911-919.
8. Chen, J.-L.; Su, M.; Jiang, Z.-Q.; Liu, N.; Yin, J.; Zhu, Y.-Y.; Wu, Z.-Q., *Polym. Chem.* 2015, 26, 4784-4793.
9. Huber, F.; Kirsch, S. F., *Chem. Eur. J.* 2016, 17, 5914-5918.
10. Copp, F. C.; Timmis, G. M., *J. Chem. Soc.* 1955, 0, 2021-2027.